CONSTRAINING SCALAR-TENSOR THEORIES OF GRAVITY THROUGH OBSERVATIONS

by

David Sutton Anderson

A dissertation submitted in partial fulfillment
of the requirements for the degree

of

Doctor of Philosophy

in

Physics

MONTANA STATE UNIVERSITY
Bozeman, Montana

November 2018

DEDICATION

To my parents, Todd and Darlene, and my grandparents, Eleanor and Wade.

ACKNOWLEDGEMENTS

I would like to thank my Ph.D. advisor Nicolás Yunes for guiding me through my dissertation and providing invaluable advice and knowledge that has helped me become a professional. I would also like to extend my gratitude to Paulo Freire, Enrico Barausse, Neil Cornish, Travis Robson, and Blake Moore for supporting my research through collaboration, valuable discussion, and by keeping me focused.

TABLE OF CONTENTS

TABLE OF CONTENTS – CONTINUED

TABLE OF CONTENTS – CONTINUED

LIST OF TABLES

LIST OF FIGURES

LIST OF FIGURES – CONTINUED

Figure Page

ABSTRACT

Scalar-tensor theories of gravity have been among the most popular and well-studied alternatives to Einstein's General Relativity. These theories of gravity contain an extra scalar degree of freedom that allows them to rectify some of the limitations of General Relativity but also fail some of the cornerstone tests of gravity that General Relativity passes with flying colors. Because of these conflicting features, it becomes necessary to investigate if scalar-tensor theories can pass current tests of gravity while still allowing for possible deviations from General Relativity in regimes that are not as highly constrained. In this thesis, we present the first self-consistent study of scalar-tensor theories in which we study the effects and constraints from Solar System observations, cosmological evolution of the universe, and the precise timing of binary pulsar systems. We constrain the free parameters of a certain class of massless-scalar-tensor theories first through cosmology and Solar System tests, in which we investigate the consistency between cosmological evolution scenarios and current Solar System observations. We then study strong field tests involving binary pulsar systems and investigate the various constraints that can be placed from measurements of the Keplerian and post-Keplerian parameters that determine the orbits.

INTRODUCTION

Gravitational waves observations from the LIGO and Virgo collaborations [1–6] and the precise timing of binary pulsars (PSRs) [7–11] allow us to put General Relativity (GR) through the most strenuous tests in the most extreme gravitational environments [12, 13]. With more neutron star (NS) merger events, we will be able to tightly constrain the equation of state (EOS) and other properties of neutron stars (NS) [14, 15], hopefully resolving any degeneracies between these properties and gravitational theories. Furthermore, as radio astronomers continue to monitor binary pulsars systems, the errors in the timing model parameters will continue to decrease and help place tighter constraints on modified theories of gravity. General Relativity has been shown to be consistent with all of these observations and provides us with one of the best theories to understand gravitational physics [16]. Nonetheless, in order to compare GR's success to other theories and investigate how these future observations will help us further test gravity, we first must understand the precise details of how observable predictions are modified in different theories.

There are a few reasons to consider theories of gravity other than GR [12,17,18]. From an observational standpoint, the late time expansion of the universe [19, 20], rotation curves of galaxies [21,22], and other cosmological observations [23] suggest a need for modifications to GR to accurately account for such effects. General Relativity alone does not have adequately address such problems unless one ad hoc adds additional fields or exotic matter, suggesting that alternatives to GR could address these issues in a more consistent manner. From a theoretical point of view, GR's lack of compatibility with quantum field theory [24] has lead to many extensions that include string theory [25] and other higher-dimensional variations [26–28]. Therefore, it is important to study theories other than GR in an attempt to address the issues discussed above. Some of the most natural, yet simple, extensions to GR are scalar-tensor theories (STTs) [29–31] in which gravity is mediated by the metric tensor appearing in GR, as well as a long range scalar field that is non-minimally coupled. These theories are a well-motivated extension to GR because they are both well posed [32] and can naturally arise from the low energy limit of higher-dimensional theories [25], thus potentially addressing the issues with quantum field theory and cosmology.

While there have been many STTs proposed over the years, including a select few that have gained considerable attention in the literature, we restrict our focus to massless mono-scalar-tensor theories in which only a single scalar field is introduced. A particular STT is defined by a choice of conformal coupling that determines how the scalar field couples to matter, and thus also quantifies the level at which these theories violate the strong equivalence principle (SEP). This particular class of theories was first introduced by Jordan [33, 34], Fierz [35], Brans [36], and Dicke (JFBD) and consists of a scalar field, denoted by φ, that couples directly to matter through a constant, i.e. the coupling to matter takes the form $\alpha(\varphi) = \alpha_0$ in which α_0 becomes the free parameter of the theory. These theories were later extended by Damour and Esposito-Farése (DEF) [37–40] to include higher order terms in the action, leading to a coupling of the form $\alpha(\varphi) = \alpha_0 + \beta_0\varphi$, with β_0 entering as another free parameter, that in turn leads to more complicated interaction between matter and the scalar field. A more recent extension of these theories was introduced by Mends and Ortiz (MO) [41] in which the conformal coupling was constructed to replicate the effects of having a more fundamental action containing higher-order couplings between the scalar field and the curvature tensor [42–45]. In this work we focus our attention to studying the effects of DEF and MO theory and the various constraints that can be placed on these theories through observations.

Scalar-tensor theories of the DEF type predict a multitude of strong field effects [37, 38], even when the theory parameters have been chosen to satisfy Solar System constraints. One of the most interesting consequences of the non-linear coupling of DEF theory is that NSs can experience a phenomenon known as spontaneous scalarization. If the parameters of the theory are part of a particular region of parameter space then NSs can develop what is known as a scalar charge and lead to excitations of the scalar field above it's cosmologically [40] determined background value. This excitation of the scalar field is due to a tachyonic-like instability that occurs inside the NS once the the compactness of the star reaches some critical threshold. Scalarization leads to violations of the SEP and thus predicts modifications to observables in astrophysical systems containing NSs. In principle, one can map the parameters of the theory to these observable quantities, and once these quantities are measured constraints can then be placed on the theory.

Spontaneous scalarization occurs either in isolated NSs [12,38,46–48] or NSs that are in widely separated binary systems, like those of binary pulsars [39, 42, 49–51]. However, for tight binary systems, like NS mergers that would be observed by ground-based gravitational-wave detectors, there are two other types of scalarization that can occur, referred to as dynamical and induced scalarization [52,53]. Similar to how spontaneous scalarization occurs once the gravitational binding energy of an isolated NS reaches a critical value, dynamical scalarization occurs once the binding energy of the orbit becomes large enough to excite the instability in the scalar field. Induced scalarization, on the other hand, occurs when a NS in a binary system becomes scalarized under the influence of the companion star's scalar field. This typically would occur once one of the stars underwent spontaneous scalarization, whose scalar field would subsequently trigger the scalar field instability in it's companion. These phenomena directly affect the motion of the binary and thus leave an observable imprint on gravitational waves that are emitted from the system [52, 53].

At the level of the Solar System, GR has been shown to be consistent with all current observations. Thus, any theory that predicts modifications to GR must do so in a manner that is not in conflict with these observations. Solar System tests thus provide some of the tightest constraints on STTs because of the manner in which they modify the motion of bodies in a gravitational field. In particular, the perihelion shift of Mercury and the time delay of light measured by the Cassini spacecraft have verified the predictions of GR to high precision and thus places tight constraints on any modifications that are introduced at the Solar System level. These type of observations place extremely tight constraints on the STTs of JFBD because this theory produces direct modifications to the parameterized-post Newtonian parameters that quantify modifications to GR in the weak field, quasi-stationary regime. DEF theory, on the other hand, can avoid these types of constraints because modifications at the Solar System level can be suppressed due to the presence of the non-linear terms in the conformal coupling.

Although theories of the DEF variety predict modifications to GR in the generation of gravitational waves, there exists major theoretical problem when one self-consistently considers the cosmological implications of this type of scalar field: for choices of the free parameter β_0 that allow for scalarization, the cosmological evolution of the scalar field generically leads to local scalar field values *today* that are in violation of Solar-System constraints [40, 54, 55]. This means one must self-consistently choose theory parameters that allows Solar System constraints to be satisfied *after* the cosmological evolution of the scalar field. The equation of motion for the scalar field in cosmological contexts resembles that of a damped oscillator, whose potential is a function of the conformal coupling and the cosmological model [40, 55]. The DEF choice of the conformal coupling with $\beta_0 < 0$, which makes the potential unbounded from below, leading to a cosmological runaway attractor solution for the scalar field [54]. The only way to avoid this runaway behavior in these STTs is to choose $\beta > 0$, as shown by Damour and Nordtvedt [40, 55], but this is precisely the region of coupling parameter space that does not allow for any type of spontaneous scalarization.

Because Solar System tests do not probe the non-linear interactions of these theories to a sufficient level, it is difficult to place tight constrains on the higher order parameters of the theory. This means one must look to strong field systems, like those discussed above, that have the ability to probe such effects. To date, however, binary pulsar systems consistently place the tightest constraints on STTs. This is due to the fact that STTs introduce modifications directly to the timing model that is used to fit the observed times-of-arrival (TAO) of the pulses from pulsars. The timing model allows one to link the observed TOA at the observatory to the time of emission of the pulse, incorporating all relativistic effects and time delays up to first post-Newtonian order. Thus, the timing model allows us to accurately predict when the next pulse should arrive, providing a model that can be fit to the observed data and thus modification to the timing model predict modifications to the predicted TOAs. Binary pulsars can be timed so precisely that these measurements can accurately distinguish between GR and other theories of gravity. Typically, the tightest constraints come from the detection of gravitational radiation emitted from these systems from the observed orbital period decay that occurs as energy is removed from the system. General Relativity predicts quadrupolar radiation while STTs also predict dipole radiation that enter at lower post-Newtonian order, and thus is the dominant effect. However, the observed loss of energy from the system is consistent with GR, thus placing constraints on the dipolar radiation of STTs and in turn constraints on the theory.

Typically, when one attempts to constrain STTs, authors focus on solar system tests, cosmological tests, *or* binary pulsar tests. However, there has not been a self consistent study the incorporates *all* of these tests simultaneously. The goal of this study is to self-consistently investigate these constraints and determine which values of the coupling parameters are valid in all three scenarios. This part of our study involves understanding the cosmological evolution of the scalar field and how this affects current Solar System observations as well as those at the time of Big-Bang-Nucleosynthesis. Once we have determined which regions of parameter space are consistent will current weak-field observations we can consistently investigate the the strong-field modifications that these theories predict. The following paragraphs provide a summary of our work towards this end and gives an outline for the rest of this thesis.

In chapter 1 we investigate whether DEF theory can be modified such that the cosmological evolution leads to scalar field values that satisfy Solar System constraints *and* allow for spontaneous scalarization in NS systems. Thus, we generalize the conformal coupling to a higher-order polynomial in the scalar field, while keeping $\beta_0 < 0$. However, we find that even with a generalized conformal coupling, it is impossible to construct a theory that passes both Big-Bang nucleosynthesis (BBN) and Solar System constraints, while simultaneously allowing for scalarization in isolated/binary neutron stars. This is a result of the fact that the tachyonic instability that leads to spontaneous scalarization is no longer present once these modifications are made to the coupling function.

Our cosmological studies follow closely those performed in Refs. [40, 56, 57] where we make use of BBN constraints to set the initial conditions of the scalar field. Reference [56] performed a thorough investigation of DEF theory and how the BBN constraints on the speed-up factor affect the present day value of the scalar field after considering the entire cosmological evolution of the scalar field. These authors study the effects of mass thresholds as the universe is cooling and how this affects the evolution of the scalar field due to different species freezing out at different temperatures. While our study does not go into this in depth, we investigate different forms of the the conformal coupling and employ very similar techniques as those appearing in Ref. [40].

The initial conditions we use for the scalar field assume that BBN occurs in the radiation dominated era and that all species freeze out at the same time, providing a simpler scenario to consider when placing initial conditions. The BBN constraints we make use of come directly form the analyses in Refs. [58], which are summarized in [59] and references therein, and arise from the constraints on the gravitational constant placed from observations. This is ultimately achieved by translating bounds on the relativistic degrees of freedom that are inferred from BBN calculations, light element abundances, and Cosmic Microwave Background anisotropies [58,59] to bounds on the gravitational constant. These constraints, however, do not take into account issues with the synthesis of primordial Lithium [60], particularly that Lithium is typical overproduced by a factor of $\tilde{3}$ in these models, and thus may need to be improved upon in the future. In fact, it was shown in Ref. [56] that STTs leave the abundance of Lithium unaffected after BBN. Despite the uncertainty in these models and their predictions, we make use of these BBN constraints for our calculations as the general results will be qualitatively similar.

In chapter 2 we perform a similar study to the one in chapter 1 but in the context of both DEF and MO theory, with the goal of determining the valid regions of parameter space after cosmological evolution and the behavior of the scalar charges in these regions of parameter space. Rather than modifying the conformal coupling we simply enforce $\beta_0 > 0$ for these theories and find that Solar System tests are passed only in a very small subset of the coupling parameter space. Thus, even though the conformal potential is bounded from below here, it is still not guaranteed that Solar System tests are generically passed and is in fact sensitive to the initial conditions at the time of BBN. While NSs do not undergo spontaneous scalarization in this regime, it is possible for neutron stars to scalarize, but only once the coupling parameter is carefully selected under the restrictions above.

After thoroughly investigating the consequences of multiple STTs in the context of Solar System tests and cosmological evolution, we now consider the constraints that binary pulsars can place on these theories. Scalar-tensor theories will generically produce modifications to the timing model used when timing binary pulsars. These modifications require one to have knowledge of the various types of scalar charges that NSs will acquire in the presence of an external scalar field. Thus, in chapter 3 we calculate the scalar charges in DEF and MO theory for a large region of parameter space using 11 realistic equations of state (EOSs). While our cosmological study omits $\beta_0 < 0$, these constraints can avoided by fine tuning the present day value of the asymptotic value of the scalar field. Moreover, for completeness we study these theories in the entire parameter space and allow the our previous cosmological study to place constraints after the fact. We study these scalar charges and explore analytic scaling relations that allow us to predict their value in a substantial region of parameter space without costly numerical computations. These results allow for the quick evaluation of the scalar charges, which has applications for gravitational wave tests of scalar-tensor theories and binary pulsar experiments.

In chapter 4 we investigate binary pulsar constraints on STTs. As mentioned, one must make use of a timing model that predicts when a pulse will arrive at the observatory. Fitting this model to the data allows one to extract information about the pulsar's orbit and thus allow one to test the predictions made by a theory of gravity. We calculate the constraints that can be placed on STTs by saturating the current 1σ bounds on single post-Keplerian parameters, as well as employing Bayesian methods through Markov-Chain-Monte-Carlo simulations to explore the constraints that can be achieved when one considers all measured parameters simultaneously. Our results demonstrate that both methods are able to place similar constraints and that they are both indeed dominated by the measurements of the orbital period decay. The Bayesian approach, however, allows one to simultaneously explore the posterior distributions of not only the theory parameters but of the masses as well. Lastly, we conclude by summarizing our work and explaining some of the implications of our results.

An overview of the main results of our study can be found in Fig. 0.1. The top panel of Fig. 0.1 illustrates the constraints that can be placed on the $\{\alpha_0, \beta_0\}$ parameter space over large ranges of β_0. The red hatched region labeled "Unbounded Potentials" corresponds to functional forms of the scalar field coupling that inevitably lead to runaway scalar field solutions and are thus excluded by Solar System observations unless on wishes to fine tune the background value of the scalar field. The blue hatched region corresponds to constraints that are discussed in chapter 2 of this work, with the main conclusion being that many values of β_0 in this region of parameter space can be ruled out from Solar System observations unless, again, one wishes to carefully tune the initial conditions of the scalar field. The curves labeled γ_{PPN} and β_{PPN} correspond to the weak field constraints that can be placed from observations made in the Solar System, and we see that only a relatively small region of parameter space, in white between $\beta_0 = 0$ and $\beta \lesssim 17$, is consistent with all observations currently available. The bottom panel of Fig. 0.1 shows a smaller region of parameter space and also illustrates the constraints that binary pulsars can place. One finds that J1738+0333 has the ability to place even tighter constraints on the parameter space than the other tests we study here. Therefore, the solid white region appearing in Fig. 0.1 is the only region of parameter space found to be completely consist with *all* observations and does not require any fine tuning of the theories.

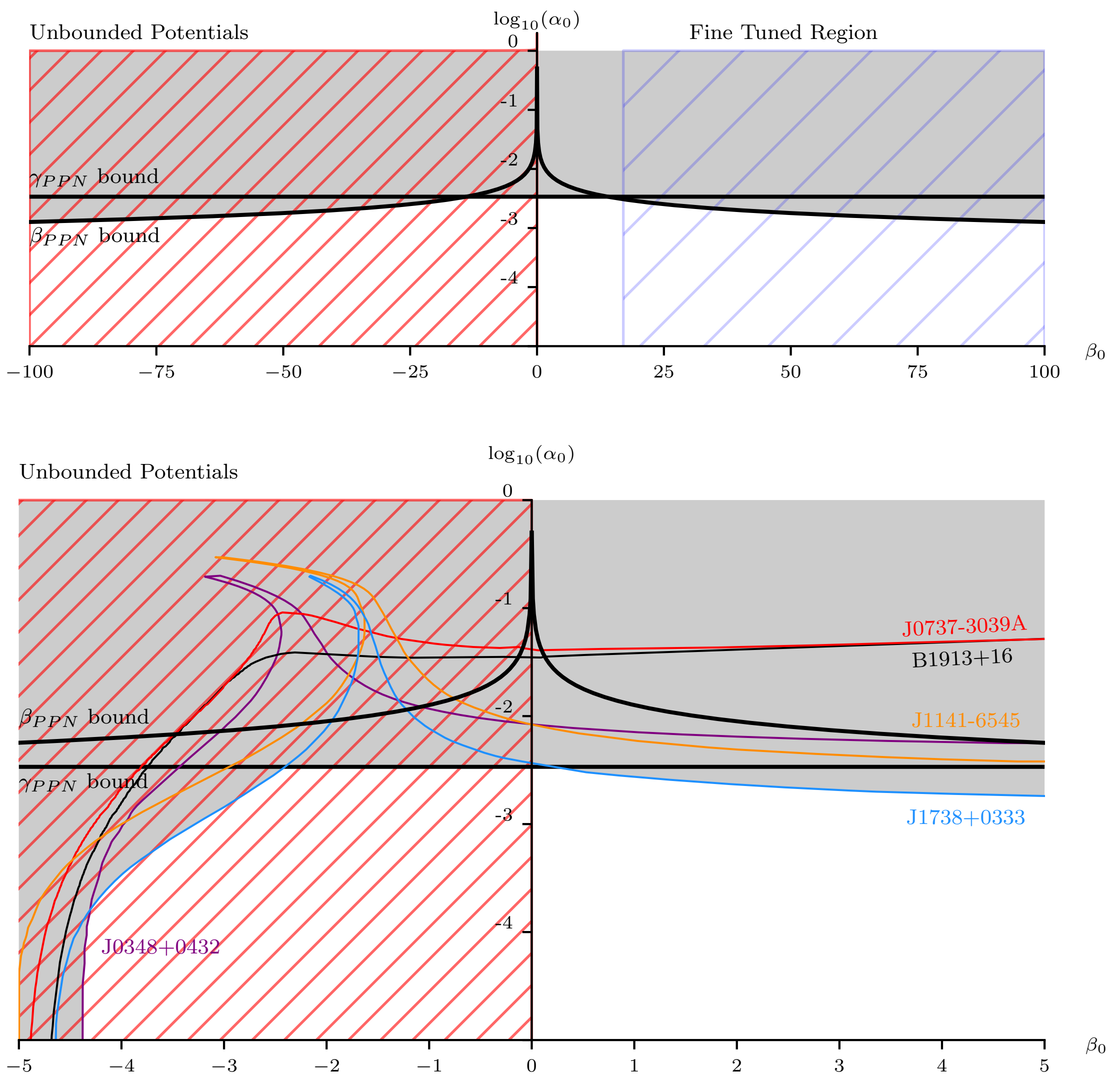

Figure 0.1: An overview of the constraints that can be placed on STTs after considering all effects studied in this work. This figure corresponds to MO theory but similar exclusion plots exists for DEF theory.

CHAPTER ONE

THE EFFECT OF COSMOLOGICAL EVOLUTION ON SOLAR SYSTEM CONSTRAINTS AND ON THE SCALARIZATION OF NEUTRON STARS IN MASSLESS SCALAR-TENSOR THEORIES

Contribution of Authors and Co-Authors

Manuscript in Chapter 2

Author: David Anderson

Contributions: Helped develop and implement the design study. Developed numerical code necessary for the project. Wrote the first draft of the manuscript.

Co-Author: Nicolás Yunes

Contributions: Helped develop design study and oversaw the completion of the project. Provided feedback on analysis and comments on draft of the manuscript.

Co-Author: Enrico Barausse

Contributions: Helped develop design study and provided original version of numerical code. Provided feedback on analysis and comments on draft of the manuscript.

Manuscript Information Page

David Anderson, Nicolás Yunes, Enrico Barausse

Physical Review D

Status of Manuscript:

____ Prepared for submission to a peer-reviewed journal

____ Officially submitted to a peer-reviewed journal

____ Accepted by a peer-reviewed journal

__x__ Published in a peer-reviewed journal

Published by the American Physical Society

Published on November 28, 2016, in volume 94, 104064

DOI: 10.1103/PhysRevD.94.104064

Abstract

Certain scalar-tensor theories of gravity that generalize Jordan-Fierz-Brans-Dicke theory are known to predict nontrivial phenomenology for neutron stars. In these theories, first proposed by Damour and Esposito-Farèse, the scalar field has a standard kinetic term, and couples conformally to the matter fields. The weak equivalence principle is therefore satisfied, but scalar effects may arise in strong-field regimes, e.g. allowing for violations of the strong equivalence principle in neutron stars ("spontaneous scalarization") or in sufficiently tight binary neutron-star systems ("dynamical/induced scalarization"). The original scalar-tensor theory proposed by Damour and Esposito-Farèse is in tension with Solar System constraints (for couplings that lead to scalarization), if one accounts for cosmological evolution of the scalar field and no mass term is included in the action. We here extend the conformal coupling of that theory, in order to ascertain if, in this way, Solar System tests can be passed, while retaining a non-trivial phenomenology for neutron stars. We find that even with this generalized conformal coupling, it is impossible to construct a theory that passes both Big-Bang nucleosynthesis and Solar System constraints, while simultaneously allowing for scalarization in isolated/binary neutron stars.

1.1 Introduction

The emission of gravitational waves by binary systems of compact objects is a key prediction of General Relativity (GR) and other relativistic gravitational theories [12, 13]. Their existence has been established indirectly (through their backreaction on the orbital motion) by timing the period of pulsar binaries [8, 10], and directly by Advanced LIGO [1,2] through the observation of the coalescence of black-hole binaries. Gravitational waves also allow for exquisite tests of gravitation in extreme gravity regimes [12, 13], since the binaries of compact objects that most copiously emit them involve strong and dynamical gravitational fields, and highly relativistic velocities. Therefore, these tests are qualitatively different than Solar System experiments [16], which probe gravity in the quasi-stationary, weak-field regime.

One of the most natural extensions of GR is the scalar-tensor theory class [29–31].

This class is defined (in the so-called Einstein frame) through the inclusion in the Einstein-Hilbert action of a scalar field φ with a canonical kinetic term, a potential and a (conformal) coupling to matter. Different members of this class are defined by the choice of potential and conformal coupling. For example, when the potential is chosen to be zero or to be a canonical mass potential, one obtains the so-called massless or massive scalar-tensor theory subclass. When, in addition, one chooses the logarithm of the conformal coupling to be linear in the scalar field, one obtains massless or massive Jordan-Fierz-Brans-Dicke (JFBD) scalar-tensor theory [33–36], while when one allows for a quadratic scalar field term (whose magnitude is controlled by a constant β), one obtains massless or massive Damour-Esposito-Farèse (DEF) scalar-tensor theory [37, 38].

Scalar-tensor theories are a natural choice of study because they arise in the low-energy limit of more fundamental quantum gravitational theories. For example, scalar-tensor theories arise in heterotic string theory upon 4-dimensional compactification [25], in higher-dimensional theories, such as Kaluza-Klein models [26] and braneworld models [27, 28], and in effective field theories of inflation [23]. Typically, these theories predict a multitude of scalar fields (not just one), with couplings that include the ones we focus on here, but also encompass more complicated functions of the curvature tensor.

Different scalar-tensor theories have been constrained to different degrees with different observations. JFBD theory predicts a modification to the Shapiro time delay of photons propagating on a curved background, which the Cassini probe has verified to be consistent with GR [61]; such an observation places a very stringent constraint on this theory [61, 62]. The coupling constants of DEF theory, on the other hand, can be tuned so that the theory reproduces exactly GR at first post-Newtonian (PN) order[1], thus evading this constraint, while still allowing for modifications to GR in more "extreme" gravity regimes. In particular, nonlinear interactions in this theory can lead to the sudden activation of the scalar field in spacetimes containing neutron stars (NSs), isolated or in binaries.

This sudden activation, usually referred to as *scalarization*, is an intrinsically nonlinear process that would be a smoking-gun deviation from Einstein's theory. Physically, this occurs when the gravitational binding energy in a matter configuration (e.g. a star) exceeds a certain threshold, which then amplifies the scalar inside matter, even if the asymptotic value of the field at spatial infinity is exponentially small. This phenomenon has been classified into *spontaneous*, *dynamical* and *induced scalarization*, depending on the specific systems involved. Spontaneous scalarization occurs in isolated and dense compact stars, e.g. neutron stars, when the compactness of the star exceeds a critical value [37, 38, 42, 64]. Induced scalarization occurs in a neutron-star binary, when one of the stars is exposed to the scalar field of its (already scalarized) companion [52, 53, 65, 66]. Dynamical scalarization also occurs in neutron-star binaries (even ones involving stars that do not spontaneously scalarize in isolation), when the binary's binding energy exceeds a certain critical value [52,53,65,66].

The activation of the scalar field typically produces large deviations from GR in the generation of gravitational waves by NS binaries. The dominant deviation is typically due to the consequent activation of scalar dipolar radiation, which increases the rate at which NSs in binaries spiral into each other. Binary pulsar observations, however, do not see such an increase [7], which then leads to constraints on scalarization. In more detail, binary pulsar observations exclude the presence of

[1]The PN approximation is one in which the field equations are expanded in small velocities and weak fields [63]. A term of NPN order is proportional to $(v/c)^{2N}$ with respect to its leading-order (controlling) factor.

spontaneous scalarization in a given (observed) pulsar mass range, which results in tight constraints on DEF theory [7]. Similarly, if the gravitational waves emitted by neutron-star binaries are detected by ground-based interferometers, they may constrain dynamical and induced scalarization [54][2].

Although DEF theory is a nice playground to explore modifications to GR in the generation of gravitational waves, its massless version at least has a major theoretical problem: for choices of the coupling constant β that allow for scalarization, the cosmological evolution of the scalar field generically leads to local scalar field values *today* that grossly violate Solar System constraints [40, 54, 55]. Indeed, the cosmological equation of motion for the scalar field resembles that of a damped oscillator, whose potential is a function of the conformal coupling and the cosmology [40,55]. The DEF choice of the conformal coupling with $\beta < 0$ makes the potential unbounded from below, leading to a cosmological runaway attractor solution for the scalar field [54]. The only way to avoid this runaway behavior in massless DEF theory is to choose $\beta > 0$, as shown by Damour and Nordtvedt [40, 55], but this is precisely the region of coupling parameter space that does not allow for any type of sudden scalarization (unless β is very large, i.e. $\beta \gtrsim 100$ [41]).

In this paper, we investigate whether massless DEF theory can be modified such that the cosmological evolution produces local scalar field values that both pass Solar System tests and which allow for scalarization in NS systems. For this purpose, we generalize the conformal coupling to include higher-order terms in the scalar field, while keeping $\beta < 0$ in the quadratic scalar field term. Based on the phenomenological oscillator picture discussed above, we must construct a conformal coupling such that the oscillator potential contains a global minimum, allowing the

[2]These gravitational tests may also be complemented by corresponding ones in the electromagnetic band [67], if an electromagnetic counterpart is detected.

field to settle there at late times. By choosing the higher-order terms such that this is guaranteed, this modified massless DEF theory can pass Solar System constraints upon cosmological evolution, while also (potentially) allowing the scalar field to have a non-trivial solution inside NSs[3].

We begin by considering the simple case of a cubic polynomial for the coupling: $\alpha(\varphi) = \beta\,\varphi + \delta\,\varphi^3$ with $\beta < 0$ and $\delta > 0$. This conformal coupling leads to a quartic oscillator potential (a "Mexican hat" potential) that contains two global minima and one local maximum. We use Big-Bang Nucleosynthesis (BBN) observations to restrict the values of the scalar field upon exiting the radiation era into two initial data sets. We then evolve each set and show that the modified theory evolves in such a way as to pass Solar System tests today provided (β, δ) are in the colored regions shown in Fig. 1.1, with the different colors corresponding to the different initial data sets. We note that, while not visible in the figure, the region near $\delta = 0$ is excluded, since then the conformal coupling potential is quadratic and concave down, so there is no minima. (Indeed, for $\delta = 0$ one recovers the original DEF theory.) We conclude this exploration by generalizing our argument to a wider class of polynomial coupling functions, showing in particular that conformal couplings that lead to unbounded oscillator potentials [i.e. those where the highest power of φ is odd, corresponding to even powers in $\alpha(\varphi)$] will generically always produce cosmological runaway solutions that violate Solar System constraints.

With that study in hand, we then investigate whether modified massless DEF theory (with coupling constants that allow the theory to pass Solar System constraints upon cosmological evolution) also leads to spontaneous scalarization in NSs. We numerically construct NS solutions in the modified theory, with non-vanishing

[3]An alternative approach we did not pursue in this paper is to allow the scalar field to be massive [68].

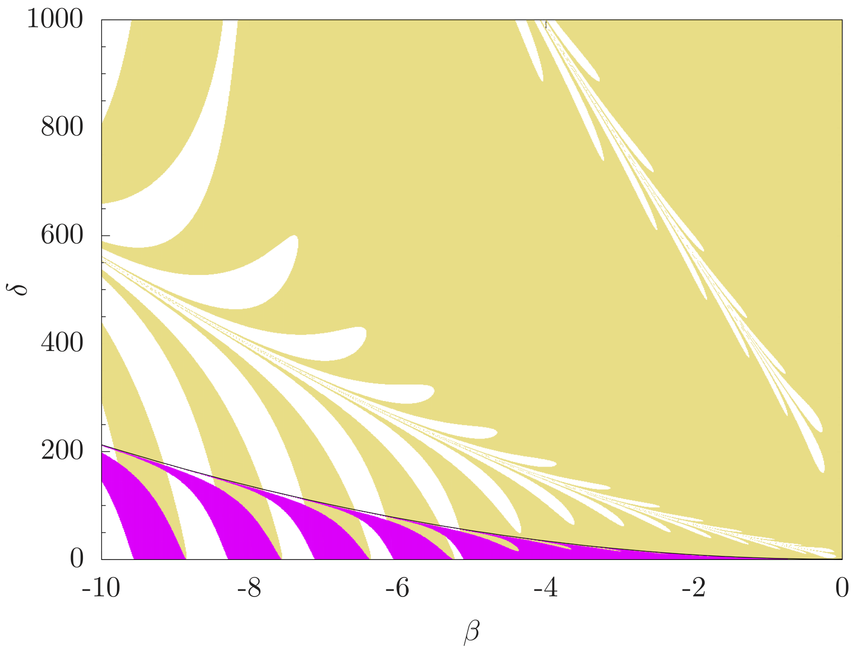

Figure 1.1: Regions of parameter space where modified DEF theory passes Solar System constraints, with blank space being regions that fail and yellow/magenta regions corresponding to different initial conditions at the beginning of matter domination. The region near $\delta = 0$ coinciding with DEF theory, while not visible, is ruled out for generic (i.e. not finely tuned) initial conditions during inflation.

asymptotic (at spatial infinity) values of the scalar field (φ_∞), as predicted by our cosmological evolutions at the present time. We find that spontaneous scalarization is not present in NSs in the modified theory. We have checked that if we artificially choose $\varphi_\infty = 0$, thus neglecting the cosmological evolution of the scalar field, then spontaneous scalarization is present.

As mentioned earlier, binary pulsar observations map the orbital motion of a binary system with at least one neutron star present. If a scalar field is present (i.e. if the scalar charge is non-zero), then the orbital motion will be different than that predicted in GR, the dominant effect being the activation of dipole radiation. Since the observed orbital motion is consistent with the predictions of GR, this places a constraint on the activation of the scalar field. In turn, this allows one to place constraints on the β parameter of standard DEF theory, where scalar charge is predicted. In modified DEF theory, however, we find that there is no charge in the first place, and thus, no modifications to the binary's orbital motion would be present. Therefore, binary pulsars cannot constrain any parameters that show up in modified DEF theory because no strong-field effects are present.

The rest of this paper will provide the details of the calculation described above. Section 1.2 introduces the basics of scalar-tensor theories and the constraints Solar System tests place on them. Section 1.3 covers the cosmological evolution of the scalar field in these theories and how we can constrain the δ parameter we introduce by using Solar System constraints. Section 1.4 discusses spontaneous scalarization in NSs and the results we arrive at using the allowed values of (β, δ) found in Sec. 1.3. Finally, Section 1.5 concludes by summarizing our results and discussing future work.

In the remainder of this paper, we use units in which $c = 1$. We also follow the conventions of [69], where Greek letters in index lists stand for spacetime indices. Other conventions and notation will be defined throughout the paper as they are introduced.

1.2 The Basics of Scalar-Tensor Theories

This section presents the class of theories we investigate in detail and establishes notation, following mostly [55]. The scalar-tensor theory class we consider in this paper can be defined by the action $S_{\rm J} = S_{{\rm J},g} + S_{\rm J,\, mat}[\chi, g_{\mu\nu}]$, where the gravitational part is

$$S_{{\rm J},g} = \int d^4x \frac{\sqrt{-g}}{2\kappa} \left[\phi R - \frac{\omega(\phi)}{\phi} \partial_\mu \phi \partial^\mu \phi \right] , \tag{1.1}$$

with g and R being the determinant and the Ricci scalar associated with the *Jordan-frame* metric $g_{\mu\nu}$, $\omega(\phi)$ is a kinetic coupling function for the *massless* scalar field ϕ, and $\kappa = 8\pi G$, with G the (bare) gravitational coupling constant. The matter action $S_{\,\mathrm{J,\,mat}}[\chi, g_{\mu\nu}]$ is a functional of the matter fields χ, which couple directly and only to the metric tensor $g_{\mu\nu}$. The latter implies that these scalar-tensor theories are *metric theories* of gravity.

One can rewrite the above action in a form reminiscent of the Einstein-Hilbert action through a conformal transformation. Let us then consider $g_{\mu\nu} = A(\varphi)^2 g^*_{\mu\nu}$, where we will refer to the conformal metric $g^*_{\mu\nu}$ as the *Einstein-frame* metric. With an appropriate choice of the conformal coupling A and by suitably defining the new scalar field φ, the action becomes

$$
\begin{aligned}
S_{\,\mathrm{E}} = &\int d^4x \frac{\sqrt{-g_*}}{2\kappa}\left[R_* - 2g_*^{\mu\nu}\partial_\mu\varphi\partial_\nu\varphi\right] \\
&+ S_{\,\mathrm{E,\,mat}}[\chi, A^2(\varphi)g^*_{\mu\nu}],
\end{aligned}
\tag{1.2}
$$

where g_* and R_* are the determinant and the Ricci scalar associated with the Einstein metric $g^*_{\mu\nu}$. In more detail, the transformation between the Jordan and Einstein frames is given by

$$
A^2(\varphi) = \phi^{-1}\,,
\tag{1.3}
$$

and

$$
\alpha(\varphi)^2 \equiv \left(\frac{d\ln A(\varphi)}{d\varphi}\right)^2 = [3 + 2\omega(\phi)]^{-1}\,,
\tag{1.4}
$$

the latter providing implicitly the relation between ϕ and φ. For later convenience we define $\alpha = \partial V_\alpha/\partial\varphi$ such that

$$
V_\alpha = \ln A(\varphi)\ ,
\tag{1.5}
$$

which plays the role of a conformal coupling potential in which the scalar field evolves cosmologically. Different choices of $\omega(\phi)$, or equivalently, different choices of $A(\varphi)$ define different members of this massless scalar-tensor class of theories.

Variation of the Einstein-frame action yields the Einstein-frame field equations

$$R^*_{\mu\nu} = \kappa \left(T^*_{\mu\nu} - \frac{1}{2} g^*_{\mu\nu} T^* \right) \; , \tag{1.6}$$

$$\Box_* \varphi = -\frac{\kappa}{2} \alpha(\varphi) T_{\,\mathrm{mat},*} \; , \tag{1.7}$$

where $\Box_*$ is the Einstein-frame covariant wave operator, and $T^{\,\mathrm{mat},*}$ is the trace of the Einstein-frame matter stress-energy tensor $T_{\mu\nu}^{\,\mathrm{mat},*}$. The latter is defined through

$$T_{\mu\nu}^{\,\mathrm{mat},*} \equiv \frac{2}{\sqrt{-g}} \frac{\delta S_{\,\mathrm{E,\,mat}}[\chi, A^2(\varphi) g^*_{\mu\nu}]}{\delta g^*_{\mu\nu}} \; , \tag{1.8}$$

and is therefore related to the Jordan-frame stress-energy tensor via $T^{\mu\nu}_{\mathrm{mat},*} = A^6 T^{\mu\nu}_{\mathrm{mat}}$. The field equations also depend on the total stress-energy tensor, which is simply the sum of the matter and scalar field stress-energy tensors, namely

$$T^*_{\mu\nu} = T_{\mu\nu}^{\,\mathrm{mat},*} + T_{\mu\nu}^{\varphi,*} \; , \tag{1.9}$$

where

$$\kappa \, T_{\mu\nu}^{\varphi,*} = 2 \left(\partial_\mu \varphi\right) \left(\partial_\nu \varphi\right) - g^*_{\mu\nu} \left(\partial_\sigma \varphi\right) \left(\partial^\sigma \varphi\right) \; . \tag{1.10}$$

Our study (both cosmological and in NSs) adopts a perfect fluid representation of matter in the Jordan frame. In the Einstein frame, we would like to write

$$T^{\mu\nu}_{\mathrm{mat},*} = (\rho_* + p_*) u^\mu_* u^\nu_* + p_* g^{\mu\nu}_* \; , \tag{1.11}$$

where ρ_* is the density, p_* is the pressure, and u_*^μ is the fluid four-velocity in the Einstein frame. Using the normalization of the four-velocity ($g^*_{\mu\nu} u^\mu_* u^\nu_* = -1 = g_{\mu\nu} u^\mu u^\nu$) one finds the relation $u^\mu_* = A u^\mu$ between Jordan- and Einstein-frame velocities. This result, combined with $T_*^{\mu\nu} = A^6 T^{\mu\nu}$, leads one directly to the relations $\rho_* = A^4 \rho$ and $p_* = A^4 p$ between Jordan- and Einstein-frame quantities.

Different choices of $A(\varphi)$ lead to different functionals $\alpha(\varphi)$, which in turn define different types of scalar-tensor theories. For example, one of the most well-known scalar-tensor theories is JFBD gravity [34–36], in which the conformal coupling takes the form $A_{\rm BD}(\varphi) = \exp(\alpha_{\rm BD}\varphi)$, such that $\omega_{\rm BD}(\phi) = \text{const}$, and thus $\alpha_{\rm BD}(\varphi) = \text{const} = [1/(3+2\omega_{\rm BD})]^{1/2}$. Another example is DEF gravity [37], defined by the conformal coupling $A_{\rm DEF}(\varphi) = \exp(\beta_{\rm DEF}\varphi^2/2)$, such that $\alpha_{\rm DEF}(\varphi) = \beta_{\rm DEF}\varphi$, with $\beta_{\rm DEF}$ a constant[4]. This theory has attracted considerable attention in recent years, since it has been shown to lead to the excitation of a scalar field near sources with strong gravity [38, 52–54, 65, 66] when $\beta_{\rm DEF} < 0$, without exciting the scalar in the Solar System.

The functions $A(\varphi)$ and $\alpha(\varphi)$ play a critical role in tests of scalar-tensor theories, because they define the local value of Newton's gravitational constant G_N (entering, for example, Newton's Second Law)

$$G_N = G[A^2\,(1+\alpha^2)]_{\varphi_0}\ , \tag{1.12}$$

with φ_0 denoting the value of the scalar field today,and the values of the parameters of the parameterized post-Newtonian (ppN) framework [71, 72]. For example, the

[4] Technically, the theory introduced by DEF also includes a φ-independent term in α, just like in Brans-Dicke theory. However, that term can be set to zero without loss of generality, if one allows the scalar field φ to take asymptotically non-zero values far away from a system, c.f. discussion in [52, 70].

γ_{PPN} parameter, a measure of how much spatial curvature is produced by a unit rest mass [16, 73], is given in (massless) scalar-tensor theories by

$$\gamma_{\text{PPN}} - 1 = - \left. \frac{2\alpha^2}{1+\alpha^2} \right|_{\varphi_0} , \tag{1.13}$$

where the above expression is to be evaluated at today's value of φ; similar expressions hold for the other ppN parameters. All ppN parameters have been very well-constrained by Solar System experiments, and in particular, the most stringent constraint on γ_{PPN}, $|\gamma_{\text{PPN}} - 1| < 2.3 \times 10^{-5}$ [16], was placed through a verification of the Shapiro time delay of signals from the Cassini spacecraft [61].

1.3 Cosmological Evolution and Solar-System Constraints

In order to determine today's value of $\alpha(\varphi_0)$, we must first understand its cosmological evolution. Consider then the Einstein-frame field equations with a spatially flat Friedmann-Roberston-Walker (FRW) metric with the Einstein-frame scale factor a_*:

$$3H_*^2 = \kappa\rho_* + \dot{\varphi}^2 , \tag{1.14}$$

$$-3\frac{\ddot{a}_*}{a_*} = \frac{\kappa}{2}\rho_* (1 + 3\lambda) + 2\dot{\varphi}^2 , \tag{1.15}$$

$$\ddot{\varphi} + 3H_*\dot{\varphi} = -\frac{\kappa}{2}\alpha\rho_*(1 - 3\lambda) , \tag{1.16}$$

where $H_* = \dot{a}_*/a_*$ is the Einstein-frame Hubble parameter, the overhead dots stand for derivatives with respect to the Einstein-frame coordinate time t_*, p_* and ρ_* are the total pressure and density (in the Einstein frame) of all the components of the Universe (matter, radiation, dark energy, inflation, etc) and $\lambda = p_*/\rho_*$ is the usual cosmological equation of state (EoS) parameter. The Einstein-frame variables can be related to the Jordan-frame ones via the conformal transformation $g_{\mu\nu} = A^2 g^*_{\mu\nu}$ to give the relations $dt = Adt_*$ and $a = Aa_*$. Note that we assume that the energy density and pressure of φ are always negligible with respect to those of the other cosmological components, *i.e.* φ should not be interpreted as the inflaton or dark energy. In the matter epoch $\lambda \approx 0$, in the radiation epoch $\lambda \approx 1/3$, and $\lambda \approx -1$ during inflation or after the onset of dark energy domination. By introducing a new time coordinate $d\tau \equiv H_* dt_*$, the scalar field satisfies the following evolution equation:

$$\frac{2}{3-\varphi'^2}\varphi'' + (1-\lambda)\varphi' = -(1-3\lambda)\alpha(\varphi) \tag{1.17}$$

where primes denote differentiation with respect to τ.

To gain a better understanding of how τ varies over timescales we are familiar with, let us look at two cases: the time elapsed since the end of the radiation era until today and the time since the birth of GR (1915) until today. A difference in time $\Delta\tau$ corresponds to

$$\Delta\tau = \ln(a^*_f/a^*_i) = \ln\left(\frac{1+Z_i}{1+Z_f}\right) + (V_{\alpha,i} - V_{\alpha,f}) \ , \tag{1.18}$$

where Z_i and Z_f are the initial and final redshifts of a photon traveling a look-back time Δt corresponding to $\Delta\tau$. As we will explain later, the terms involving the conformal coupling potential are typically negligible, which allows the analysis to remain independent of the choice of scalar-tensor theory. Therefore, the redshift corresponding to the end of radiation domination is ~ 3600 ΛCDM model, thus, the τ-time that has passed since then is $\Delta\tau \approx 8.2$. From the lookback time, the redshift since 1915 is 7×10^{-9}, and thus $\Delta\tau \approx 7\times10^{-9}$. Thus, $\Delta\tau \sim 10^{-1}$ actually corresponds to a significant amount of look-back time, $t \sim 10^9$ years from today.

Whether scalar-tensor theories satisfy Solar System constraints today depends on the functional form of $\alpha(\varphi)$ and on the cosmological evolution of the scalar field. The latter resembles the evolution of an oscillator with the velocity-dependent mass $2/(3-\varphi'^2)$, the friction-like term $(1-\lambda)\varphi'$, and the forcing term proportional to $\alpha(\varphi)$. In DEF theory, Damour and Nordtvedt have shown that during the matter-dominated era, φ is driven exponentially to zero when $\beta_{\rm DEF} > 0$, such that $\gamma_{\rm PPN}$ approaches unity at late times [40, 55]. However, Ref. [54] (see also Refs. [40, 55]) has shown that when $\beta_{\rm DEF} < 0$ the opposite occurs: φ has a *linear* run-away attractor solution that approaches a limiting velocity $\varphi' = \sqrt{3}$. Such an evolution forces $\gamma_{\rm PPN} - 1$ in Eq. (1.13) to approach -2 at late times in the matter era, a value clearly in conflict with Solar System experiments. However, it is precisely when $\beta_{\rm DEF} < 0$ that strong-field, nonlinear effects become important inside NSs and allow for spontaneous/dynamical/induced scalarization, which in turn could lead to clear signatures of deviations from GR in astrophysical observations. Thus, *DEF theory is already ruled out by Solar System observations in the β_{DEF} range of interest ($\beta_{DEF} < 0$)* [40, 54, 55].

In this paper, we want to investigate whether one can relax the assumption of quadratic conformal coupling such that scalarization continues to occur, yet the theory passes Solar System constraints. Let us then begin by noting that the forcing term in Eq. (1.17) can be written as the gradient of a potential, namely the one given in Eq. 1.5. In the particle analogy described above, the scalar field starts its evolution in this potential with some initial velocity and position. One then expects that over time this particle will settle to a minimum, if one exists, provided the scalar does not reach the limiting velocity $\varphi' \approx \sqrt{3}$, which effaces the effect of the potential and leads to a run-away attractor solution. Finding a conformal coupling that allows the modified DEF theory to pass Solar System constraints then reduces to finding the appropriate choice of the conformal coupling potential V_α (one, in particular, that has a global minimum).

A word of caution, however, is due before proceeding. The above discussion depends somewhat on the choice of initial conditions for the evolution of the scalar field. Even with a conformal coupling potential that possesses a global minimum, not all initial conditions will lead to scalar field values today that pass Solar System constraints. This is simply because some initial conditions can be so close to the run-away attractor solution that they cannot escape its attraction. We will show below, however, that it is possible to construct a general class of DEF-like theories that can evade Solar System constraints after cosmological evolution for a large set of initial conditions, provided the conformal coupling is chosen appropriately.

1.3.1 Inflation and Radiation

During inflation ($\lambda = -1$), Eq. (1.17) becomes

$$\frac{1}{3 - \varphi'^2}\varphi'' + \varphi' = -2\alpha(\varphi) \ , \tag{1.19}$$

which still describes a damped oscillator with a forcing term. In order to study the evolution of the scalar during this era, one needs to prescribe initial conditions at the beginning of inflation. Since the latter are unknown, we will follow Damour and Nordtvedt [40, 55] and take a qualitative approach. Regardless of what the initial conditions are, there are only three possible outcomes upon leaving inflation:

1. the scalar can reach its terminal velocity $\varphi' = \sqrt{3}$, and therefore get caught by the attractor solution found in [54],
2. the scalar can end up near (but not necessarily at) a minimum of the potential,
3. the scalar can be in an intermediate solution (e.g. it may still be rolling down the potential).

The first possibility leads to theories that never pass Solar System tests today because, once the attractor solution is reached, all subsequent evolution remains on the attractor, regardless of λ or $\alpha(\varphi)$. The third outcome is possible in principle, but we find that it requires fine-tuning of the initial conditions, because the friction term efficiently damps any evolution far from the attractor in a short timescale. The second possibility is then the only that remains, and we thus adopt it henceforth to study how the scalar evolves into other cosmological eras.

Let us now consider the evolution of the scalar during the radiation-dominated era ($\lambda \approx 1/3$). In this era, the forcing term is suppressed, and Eq. (1.17) becomes

$$\frac{2}{3-\varphi'^2}\varphi'' + \frac{2}{3}\varphi' = 0 \ , \tag{1.20}$$

which notice is completely independent of the conformal coupling. Damour and Nordtvedt showed [40, 55] that, during the radiation era, the scalar field evolves according to

$$\varphi(\tau) = \varphi_r - \sqrt{3}\ln\left[Ke^{-\tau} + (1+K^2e^{-2\tau})^{1/2}\right] \ , \tag{1.21}$$

with

$$K = \frac{\varphi_i'\sqrt{3}}{\sqrt{1-\varphi_i'^2/3}} \ , \tag{1.22}$$

where φ_r is a constant and φ_i' is the particle's velocity upon leaving inflation. As long as the latter does not approach the limiting value of $\sqrt{3}$ of the run-away attractor solution (to prevent K from approaching infinity), then Eq. (1.21) tells us that the velocity at the end of radiation domination will be damped away. This can be seen by considering the amount of τ-time that elapses during the radiation-dominated era: the τ-time between the end of the radiation-dominated era (0.75 eV, $Z \approx 3600$) and the electroweak (EW) phase transition (100 GeV, $Z \approx 10^{15}$), the QCD phase transition (150 MeV, $Z \approx 10^{12}$), or electron/positron pair (e^-e^+) annihilation (500 keV, $Z \approx 10^9$) is $\tau_{EW} = 25.6$, $\tau_{QCD} = 19.1$, and $\tau_{e^-e^+} = 13.4$ respectively [from Eq. (1.18)]. Even the shortest of these τ-times is long enough to allow the scalar velocity to become exponentially damped by the end of the radiation era.

The evolution in the radiation era also determines the end position of the scalar in the conformal coupling potential at the beginning of the matter-domination era. Let us investigate this by considering the constraint on the gravitational constant from BBN, which took place at temperatures between 10 and 0.1 MeV in the radiation era. The speed-up factor $\xi_{\,\mathrm{BBN}} := H/H_{GR}$ quantifies deviations of the expansion rate from the GR prediction, caused by changes to the (standard) gravitational constant. Here, $H^2 = (8\pi/3)GA_R^2\rho_R$ is the observed expansion rate in scalar-tensor theory, where ρ_R and A_R are the Jordan-frame energy density and the conformal coupling during the radiation era [this can be derived from Eq. (1.14) with $\dot{\varphi} = 0$]. On the other hand, $H_{GR}^2 = (8\pi/3)G_N\rho_R$ is the expansion rate predicted by GR, where G_N is the (standard) gravitational constant we measure today given in Eq. (1.12). The speed-up factor then becomes

$$\xi_{\,\mathrm{BBN}} = \left(\frac{H}{H_{GR}}\right) = \left(\frac{GA_R^2}{G_N}\right)^{1/2} = \frac{1}{\sqrt{1+\alpha_0^2}}\frac{A_R}{A_0}\ , \tag{1.23}$$

where the R and 0 subscripts represent values at the end of the radiation era and the present values, respectively. Current tests relating the speed-up factor to the abundance of Helium [59] tell us that

$$|1 - \xi_{\,\mathrm{BBN}}| \leq \frac{1}{8}\ , \tag{1.24}$$

and Solar System tests limit α_0^2 to be $\lesssim 10^{-5}$. This leads to $\xi_{\,\mathrm{BBN}} \sim A_R/A_0$, which through Eq. (1.24) leads to a constraint on A_R given by

$$\left|1 - \frac{A_R}{A_0}\right| \leq \frac{1}{8} \ . \tag{1.25}$$

The largest deviations from the predictions of GR will be achieved by saturating this constraint, such that $A_R/A_0 = 7/8$ or $A_R/A_0 = 9/8$. Thus, using Eq. (1.5), we arrive at the requirement

$$V_{\alpha,0} + \ln(7/8) \ \leq \ V_{\alpha,R} \ \leq \ V_{\alpha,0} + \ln(9/8) \ . \tag{1.26}$$

In what follows, we will use these BBN-compatibility condition to determine the initial conditions for the evolution of the scalar field at the beginning of the matter-dominated era.

1.3.2 Matter and Dark Energy Domination

Let us now solve for the evolution of the scalar field during the matter-dominated era ($\lambda = 0$), during which Eq. (1.17) reduces to

$$\frac{2}{3 - \varphi'^2}\varphi'' + \varphi' = -\alpha(\varphi) \ . \tag{1.27}$$

Let us consider a generic scalar-tensor theory defined by

$$\alpha(\varphi) = \sum_{n=1}^{\infty} a_n \varphi^n = \beta\varphi + \gamma\, \varphi^2 + \delta\, \varphi^3 + \ldots \ , \tag{1.28}$$

where we have neglected the $n = 0$ term associated with JFBD gravity (c.f. footnote 4). For consistency with standard DEF theory, we define $a_1 = \beta$, and for later convenience, we define $a_2 = \gamma$ and $a_3 = \delta$. As we will show later, the γ term leads to a modified DEF theory that typically violates Solar System constraints, so let us ignore it for now. We then focus first on modified DEF theories defined by

$$\alpha(\varphi) = \beta\,\varphi + \delta\,\varphi^3\,, \tag{1.29}$$

$$V_\alpha(\varphi) = \frac{\beta}{2}\varphi^2 + \frac{\delta}{4}\varphi^4\,, \tag{1.30}$$

where we will take $\beta < 0$ and $\delta > 0$. (We will consider $\alpha(\varphi)$ with higher order φ terms later.) One recognizes that the conformal coupling potential presents a "Mexican-hat" shape, with negative curvature near the origin and two global minima that prevent the scalar from running off to infinity. For appropriate initial conditions and values of δ, one expects the scalar field to execute damped oscillatory motion about the global minima, without ever reaching the terminal velocity and the attractor solution, and eventually settling down near one of the minima by today.

1.3.2.1 Initial Conditions Before solving Eq. (1.27) we must first quantitatively determine the initial conditions for the scalar field evolution at the beginning of the matter era. To find these, we first determine where the scalar field could be today in the conformal coupling potential if the theory is to pass Solar System constraints, and then use the BBN constraint condition to determine where the field had to be at the beginning of the matter era. With our choice of $\alpha(\varphi)$ in Eq. (1.29) and noting the $\alpha(\varphi)^2$-dependence in Eq. (1.13), it is then clear that there are six possible values of φ today that saturate the Cassini bound $1 - \gamma_{\rm PPN} \leq 2.3 \times 10^{-5}$. These six values of φ are indicated by purple dashes in Fig. 1.2 near the extrema of the potential.

The next step requires that we apply the BBN constraint derived in Eq. (1.26) to map these possible values of φ today to possible initial values of the scalar field at the beginning of the matter era. Equation (1.26) tells us that, at the very most, the scalar field can sit no more than ln(7/8) below or ln(9/8) above where it sits in the

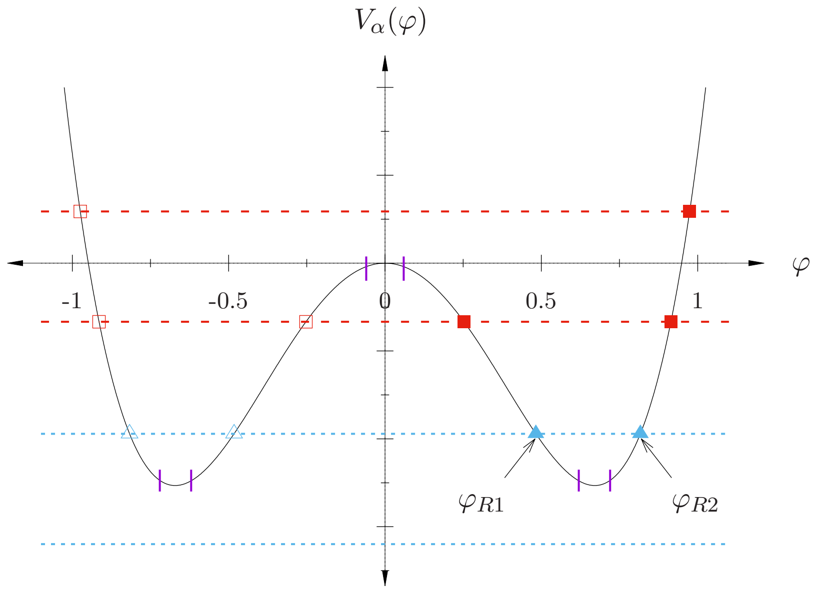

Figure 1.2: Schematic diagram of the conformal coupling potential, where we used $\beta = -4.5$ and $\delta = 10$. Purple dashes represent boundaries of the regions consistent with ppN constraints (determined by Eq. (1.13)). Horizontal dashed lines (as well as the squares and triangles marking their intersections with the potential) are a representation of BBN constraints on the speed-up factor and determine the regions in the potential consistent with nucleosynthesis at the end of the radiation era. Because of the symmetry of the potential, we shade in the squares/triangles on the right to indicate that one only needs to consider these initial conditions without loss of generality. φ_{R1} and φ_{R2} indicate the points we investigate in this paper.

conformal coupling potential today; this is indicated by the blue and red horizontal dashed lines in Fig. 1.2. In particular, the red dashed lines correspond to applying the BBN constraint to values of $V_{\alpha,0}$ that lie near zero, while the blue dashed lines were used for those that lie near the minimum of the potential. Figure 1.2 clearly shows that there are 10 possible initial conditions for the scalar field at the beginning of matter domination that can potentially lead to scalar field configurations that satisfy Solar System constraints today.

Not all of these initial conditions are physically well-motivated based on the previous arguments we presented. We have previously argued that inflation leaves the scalar field near the minimum of the potential and the radiation era effectively keeps it there, since the scalar velocity is damped away completely. The initial positions lying near $V(\varphi) = 0$ (red squares) in Fig. 1.2 are inconsistent with these physical arguments, since they *do not* lie near the minimum, and thus, they will be neglected in what follows. We now only need to consider initial positions near the minimum of the potential (blue triangles), and because of the symmetry of the potential we need only consider one of the two sets; the evolution of the scalar field that starts at the solid blue triangles will be identical to that which starts at the empty blue triangles, and thus, leads to the same conclusions.

The initial positions labeled φ_{R1} and φ_{R2} in Fig. 1.2 with initial velocity $\varphi' = 0$ at the end of the radiation era are the initial states of the scalar field we aim to investigate. Typically, one need to consider both, but for a sufficiently large δ (relative to β) only φ_{R2} exists. This is because when $\delta \gg \beta$, the conformal coupling potential becomes very shallow and the top blue line can be above the extremum at $V_\alpha(\varphi) = 0$, leading only to φ_{R2} (the other initial condition φ_{R1} becomes imaginary).

1.3.2.2 Cosmological Evolution The evolution of the scalar field during matter domination, as given in Eq. (1.27), is that of a damped oscillator. Provided the attractor solution is not reached, i.e. provided φ' does not reach its limiting value of $\sqrt{3}$, then the scalar will exhibit damped oscillatory motion in the potential. For Solar System tests to be passed, then, one needs $\alpha(\varphi_0)$ to be small enough after a time τ_0 has elapsed from the beginning of the matter-dominated era.

Let us begin by calculating what this τ_0 must be. Recalling that $d\tau = H_* dt_*$, one has that $\tau = \ln a_* + \text{const}$. If we set τ to zero at the end of the radiation era and recall that $a = A(\varphi)a_*$ and $V_\alpha = \ln A(\varphi)$, today corresponds to

$$\tau_0 = \ln a_{*,0} - \ln a_{*,R} = \ln(1 + Z_R) + (V_{\alpha,R} - V_{\alpha,0}) \ , \tag{1.31}$$

where $Z_R \approx 3600$ is the redshift of the end of the radiation era. For an evolution that satisfies Solar System constraints, the particle must settle toward a minimum of V_α, which means the last term above will always be a positive number. The most stringent constraints on these theories arise when we neglect this last term and demand that Solar System constraints be satisfied at least by $\tau_0 = \ln(1 + Z_R) \approx 8.2$. The inclusion of the last term would make τ_0 larger, which would then allow the scalar field more time to settle near the minimum of V_α, thus leading to weaker restrictions on δ.

One would then think that if the scalar is such as to pass Solar System tests after evolving by $\tau_0 \approx 8.2$, then such tests would also be passed for all later times, but this is not necessarily the case. The reason is that the scalar exhibits oscillatory motion, and thus, it is possible that φ is crossing the minimum right at τ_0. This is evident in Fig. 1.3, which shows the evolution of $1 - \gamma_{\,\mathrm{PPN}}$ as a function of τ for a set of (β, δ). At the beginning of the evolution Solar System constraints are clearly not satisfied since the slope of the potential, i.e. $\alpha(\varphi)$, is too large. Observe the oscillations about the minima of the potential signaled by the dips, which represent times at which $\alpha(\varphi) = 0$. Observe also that at $\tau = 8.2$ Solar System constraints are satisfied by both initial conditions φ_{R1} and φ_{R2}, but after evolving to later times (e.g. to $\tau \approx 8.3$) they are not. Notice, however, that although the τ difference during which tests are not passed seems small ($\Delta\tau \approx 10^{-1}$), this is a very long time interval Δt.

With no *a priori* knowledge of which initial condition the radiation era leaves the scalar in, we must consider theories for which the evolution of the scalar field with both

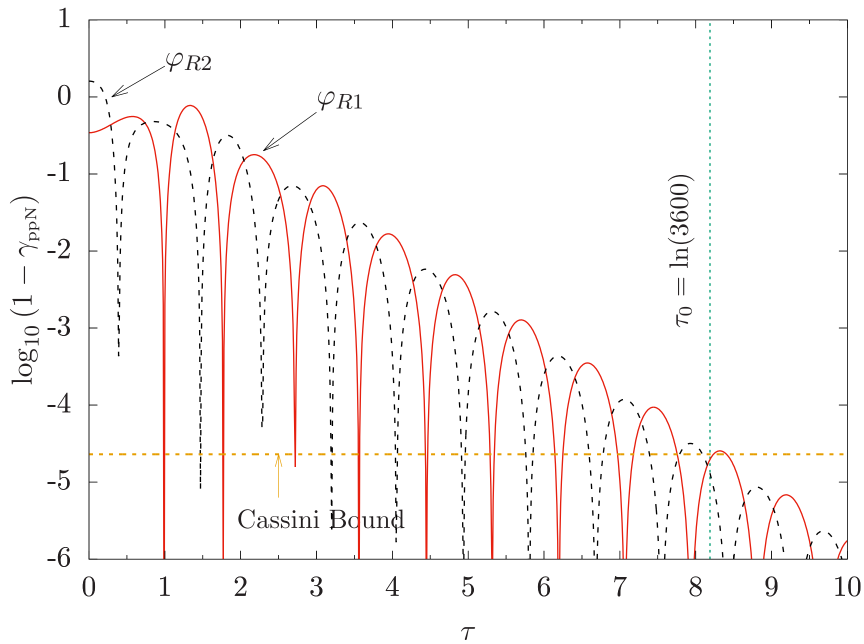

Figure 1.3: $|1-\gamma_{\,\rm PPN}|$ using both initial conditions (red solid for φ_{R1} and black dashed for φ_{R2}) with $\beta = -4.5$ and $\delta = 36$. The horizontal yellow dashed line marks the Cassini bound placed on these theories today, while the vertical line at $\tau_0 = \ln(3600) \approx 8.2$ corresponds to the present time. Observe that although the Solar System constraint is passed for both initial conditions at τ_0, it is not a little τ-time later.

initial conditions of the previous section leads to passing Solar System constraints. From an analysis of how each of the initial conditions evolves and demanding that $|1-\gamma_{\,\rm PPN}| \le 2.3 \times 10^{-5}$ for $\tau \ge 8.2$, stringent upper bounds can be placed on the (β, δ) coupling parameter space, as shown in Fig. 1.4. The green regions represent the values of (β, δ) where the cosmological evolution of the scalar field leads to scalar-field values that satisfy the current Cassini bound today and for all future times. Red regions in Fig. 1.4 represent the values of (β, δ) that satisfy the Cassini bound today but fail to do so in the future. Empty regions (white) correspond to all other values of (β, δ), i.e. those that do not satisfy the Cassini bound today and are thus ruled out. The black line running through the plot designates the separation between regions of parameters space where both φ_{R1} and φ_{R2} exist (below the line) and those where only φ_{R2} does (above the line). When considering values of (β, δ) below the line one must consider the intersection (see Fig. 1.1) of the two regions as being valid theories such that regardless of the initial condition (φ_{R1} or φ_{R2}) of matter domination, the theory remains consistent with Solar System tests.

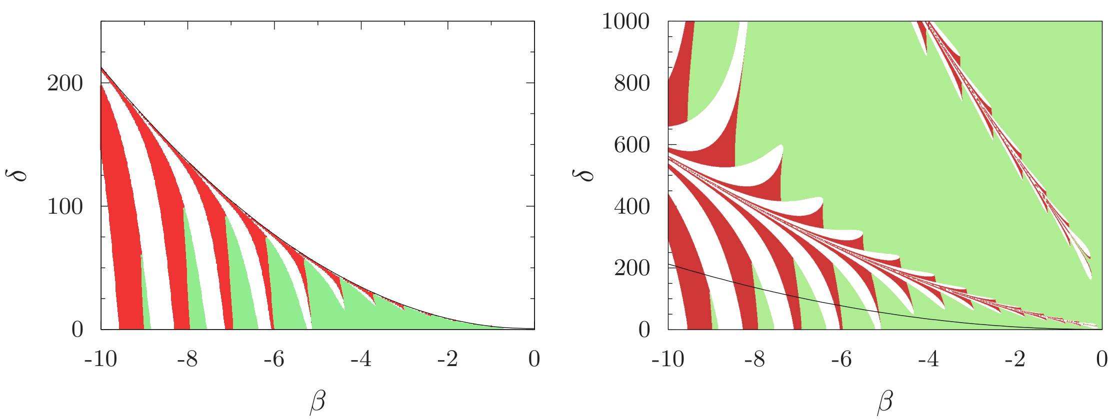

Figure 1.4: Left: (β, δ) parameter space for evolution with initial position φ_{R1}, the red region corresponding to points that satisfy the Cassini bound today but not for all future times, and the green to points that satisfy it today and all times in the future. The black line through the middle marks the boundary of the regions where φ_{R1} exists (below) and does not exist (above). Right: (β, δ) parameter space for evolution with initial position φ_{R2} with red/green regions having the same meaning as in the left panel. For reference we also include the black line to link the left and right panels.

For the regions in parameter space where Solar System tests are passed today but not in the future (red regions) we can determine a time scale at which the cosmological evolution will becomes inconsistent with future observations. Figure 1.5 shows a cumulative distribution of how long after today it takes these points in parameter space to violate Solar System tests. We find that 67% of them fail by a time $\Delta\tau = 0.19$ has passed and 95% failed after $\Delta\tau = 0.34$. In terms of coordinate time measured in years, i.e. on a human scale, however, these are enormous timescales on the order of 10^9 years which are in the very distant future. This means that requiring that all future Solar System tests be passed (green regions in Fig. 1.4) may be too conservative, and one may instead only require that tests be passed at least today (the union of green and red regions in Fig. 1.4). The region of parameter space which allows Solar System tests to be passed, at least today, is shown in Fig. 1.1 for both initial conditions.

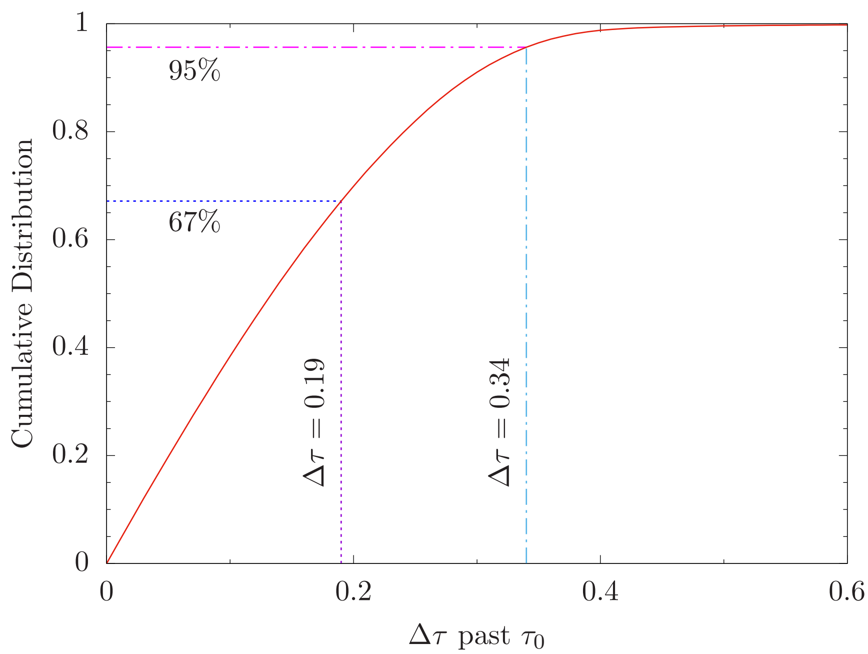

Figure 1.5: A cumulative distribution of the points in the (β, δ) parameter space that eventually break Solar System tests as a function of how long into the future this occurs. After $\Delta\tau = 0.19$ has passed we find that 67% of all cases now violate Solar System tests and 95% of all cases will fail by $\Delta\tau = 0.34$.

The analysis presented above, however, neglects the fact that for sufficiently small δ (and in particular, in the limit as $\delta \to 0$), Solar System constraints will *not* be passed, as the theory reduces to the original DEF theory with $\beta < 0$. This is because as δ becomes very small (relative to β), the potential becomes deeper and steeper, and it is thus easier for the scalar field to reach the attractor solution during inflation, which we know violates Solar System constraints. Of course, this solution is not reached if the initial conditions for the scalar field are highly fine-tuned close to the minimum of the potential. However, the level of fine-tuning required grows as δ decreases, making it more and more unlikely that random initial conditions at inflation would lead to a scalar field that satisfies Solar System constraints today. To avoid this fine-tuning problem, we set a minimum value for δ by requiring that none of the initial conditions on φ that fall between the zero crossings of the potential V_α (i.e. $|\varphi| = \sqrt{-2\beta/\delta}$) lead to the attractor solution[5]. For the range of β we considered, this places a lower-bound on δ of roughly unity, i.e. $\delta \gtrsim 1$.

1.3.2.3 Dark Energy Domination To determine the complete evolution of the scalar field one must also consider the dark energy dominated era that follows the matter-dominated one. In this case, the evolution of the scalar field is the same as during inflation [the scalar field evolves as given in Eq. (1.19)], and it will thus continue to be damped to the minimum of the potential. We neglect this era in our study because its effects only become significant for redshifts $Z \lesssim 1$, which corresponds to a small $\Delta\tau \lesssim 0.7$. Because the dynamics of the solutions we find occurs on much larger time scales and because the matter era damps the solutions as well, we expect our conclusions to hold, at least qualitatively, even in the presence of a dark energy dominated era.

1.3.3 General Coupling Potentials

We can now use the insights gained from the previous section to understand the evolution of the scalar field in theories with more generic conformal coupling

[5] Note that because the Planck mass is factored out in the action of Eq. (1.2), φ is dimensionless, and $|\varphi|$ of order unity (as is the case here) corresponds to Planck-scale excitations of φ. These are "natural" initial conditions at the beginning of inflation, hence our requirement on δ ensures that the scalar field is unlikely to be trapped in a runaway solution during inflation, i.e. outcome 1 discussed in Sec. 1.3.1 can never take place.

potentials. The key idea to remember about the potential in Eq. (1.30) is that it possessed global minima that the scalar could eventually settle to, i.e. the potential was bounded from below. Because of this feature, the scalar field could damp toward one of these minima and settle down so as to pass Solar System constraints. This idea can be extended to other polynomial forms of V_α and $\alpha(\varphi)$.

Let us first consider Eq. (1.28) with the highest power in φ even, such that the highest power in V_α is odd. Such a potential is not bounded from below at either $\varphi \to +\infty$ or $\varphi \to -\infty$, and thus, it will eventually diverge to negative infinity.[6] The BBN constraint in Eq. (1.26) still holds for all potentials, and will therefore determine the particle's initial position at the end of the radiation-dominated era. This constraint will always lead to at least one initial condition in the unbounded regime of the potential, leaving the scalar field no choice but to run away toward the attractor solution, rapidly violating Solar System constraints. Therefore, without *a priori* knowledge of the initial conditions at inflation or some argument that eliminates the initial condition that unavoidably leads to an attractor solution, all potentials of this form are immediately ruled out by requiring that initial conditions not be fine-tuned.

A similar argument also applies to coupling potentials whose highest power is even but with a negative coefficient. These potentials have two regions that approach $-\infty$, and thus, they will result in run-away solutions for the scalar field. By the same initial condition argument discussed above, these theories will not generically pass Solar System tests after cosmological evolution.

The probability that the scalar will find its way to the unbounded part the

[6]A potential unbounded from below would also be expected to lead to quantum mechanical instabilities as it allows no ground state. This forces unbounded potentials, such as the one considered in footnote 18 of Ref. [42], to be extremely fine tuned and therefore require a very specific set of initial conditions to pass Solar System tests.

potential only increases with the inclusion of multiple scalar fields. Of course, the scalar field might evolve in these potentials and never reach these regions, for some initial conditions. However, the only way to guarantee that this does not occur for generic initial conditions is to demand that the potential be bounded from below, and this is the simplest and safest assumption to make.

Moreover, all of our discussion in Sec. 1.3.1 and 1.3.2.2 can be extended to all other polynomial potentials whose highest power is even and has a positive coefficient. These potentials are qualitatively similar to the the quartic one we have considered thus far, in the sense that there exists a global minimum for the scalar field to settle near. Locally, near the minima, these potentials look nearly identical to the one we have considered here and thus one would expect qualitatively similar results. Considering these higher order potential, however, comes at the cost of adding more degrees of freedom and coefficients to constrain, unnecessarily complicating the problem even further.

1.4 Neutron Stars and Scalarization

In this section, we discuss the basics of scalarization and under what conditions it can occur. Note that we focus on spontaneous scalarization in isolated NSs, because one expects theories where the latter is not possible to not allow for dynamical/induced scalarization in binaries [52, 53]. In more detail, we first consider NSs in the original DEF theory. We then extend these calculations to the modified DEF theory with the cubic conformal coupling function presented in the previous section to show that scalarization cannot occur. We conclude by extending our arguments to more generic potentials.

1.4.1 DEF Theory

For a spherically symmetric, non-rotating star, we can write the Einstein-frame line element as

$$ds_*^2 = -e^{\nu(r_*)}dt_*^2 + \frac{dr_*^2}{1-2\mu(r_*)/r_*} + r_*^2 d\Omega_*^2 \ , \tag{1.32}$$

where μ and ν are functions of r_* and are determined from the field equations. The Jordan-frame line element is then given by $ds^2 = A^2 ds_*^2$ such that $dr = A dr_*$ in the equations that follow. The matter inside old and cold NSs can be described through a perfect fluid stress-energy tensor given in Eq. (1.11).

Using the line element above in Eqs. (1.6-1.7) and applying the stress-energy conservation condition in the Jordan frame, $\nabla_\mu T^{\mu\nu} = 0$, we arrive at the set of first-order differential equations [38]

$$\begin{aligned}
\mu' &= 4\pi G r_*^2 A^4(\varphi)\rho + \frac{1}{2} r_*(r_* - 2\mu)\psi^2 \ , \\
\nu' &= r_*\psi^2 + \frac{1}{r_*(r_*-2\mu)}\left[2\mu + 8\pi G r_*^3 A^4(\varphi)\rho\right] \ , \\
\varphi' &= \psi \ , \\
\psi' &= \frac{4\pi G A^4(\varphi)}{(r_*-2\mu)}\left[\alpha(\varphi)(\rho-3p) + r_*\psi(\rho-p)\right] \\
&\quad -2\psi\frac{(1-\mu/r_*)}{(r_*-2\mu)} \ , \\
p' &= -(\rho+p)\left(\nu'/2 + \alpha(\varphi)\psi\right) \ .
\end{aligned} \tag{1.33}$$

Note that the density and pressure in these equations are the Jordan-frame ones. To close the system of equations, we use a simple polytropic EoS in the Jordan frame:

$$p = K\,\bar{\rho}^{\Gamma} \ , \tag{1.34}$$

$$\rho = \bar{\rho} + \frac{p}{\Gamma - 1} \ , \tag{1.35}$$

with $\bar{\rho}$ the Jordan-frame baryonic density, and with $\Gamma = 2$ and $K = 123\, G^3 M_\odot^2$ following Ref. [53, 74]. The choice of EoS affects the mass and radius of the NS, as well as the exact compactness at which spontaneous scalarization occurs. However, within the set of realistic neutron-star EoSs, the particular equation-of-state choice made does *not* affect whether scalarization exists in the first place or not.

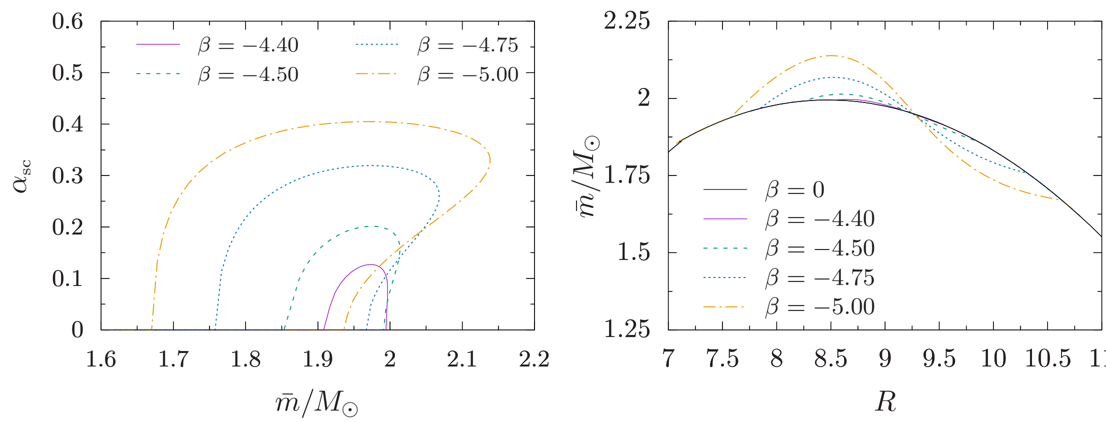

Figure 1.6: Left: Scalar charge as a function of baryonic mass in DEF theory [$\alpha(\varphi) = \beta\varphi$] with various values of β. For simplicity, we choose $\varphi_\infty = 0$, since this quantity is constrained to be close to zero by Solar System experiments. Observe that the scalar charge activates spontaneously when the mass exceeds a certain critical value, which depends on β. Right: Mass-radius curves in DEF theory with Jordan-frame quantities $\bar{m}$ and R, the same choices of β, and $\varphi_\infty = 0$. The GR curve is shown in black, and one can see that the more negative β becomes, the greater the deviation from GR.

We numerically solve the system of equations described above for a set of stars parameterized by their central density. In particular, we use `Mathematica`'s default integrator, which uses an LSODA approach, switching between a non-stiff Adams method and a stiff Gear backward differentiation formula method [75]. Inside the star, the pressure is given as a function of the density via the polytropic EoS of Eqs. (1.34)–(1.35), while outside the pressure and density vanish. The boundary of the interior and exterior region, i.e. the radius of the star, is defined by where the pressure vanishes. Our code integrates from the center of the star to an effective spatial infinity, thus fully determining the metric and the scalar field in the entire spacetime. Near spatial infinity, the scalar field decays as

$$\varphi \approx \varphi_\infty + \frac{\omega}{r^*} \, . \tag{1.36}$$

The quantity φ_∞ is the asymptotic (at spatial infinity) value of the scalar field (which we fix to a specified value as a boundary condition), while ω is related to the *scalar charge* of the star $\alpha_{\rm sc}$ via [38]

$$\alpha_{\rm sc} = \frac{\omega}{G m_*} \, , \tag{1.37}$$

where m_* is the Einstein-frame ADM mass of the star; notice that we add a subscript *sc* to the scalar charge to distinguish it from the conformal coupling α in Eq. (1.4). We find ω, and thus $\alpha_{\rm sc}$, by extracting the $1/r$ part of the scalar field by fitting its exterior solution from our numerical calculations.

Figure 1.6 shows the results of our numerical calculations for DEF theory, which reproduce old results from the literature [37, 38]. (We assume here $\varphi_\infty = 0$.) One can see that the scalar charge "spontaneously" turns on at a critical baryonic mass $\bar{m}_{\rm crit}$. One can also see in Fig. 1.6 that for $\bar{m} > \bar{m}_{\rm crit}$ there are two branches of solutions, one with $\alpha_{\rm sc} \neq 0$ and one with $\alpha_{\rm sc} = 0$. This second branch is unstable to perturbations, i.e. those solutions will either collapse or evolve to the stable branch. The more negative β becomes, the larger the maximum scalar charge. These results are quantitatively dependent on the EoS used and for our choice, scalarization occurs only when $\beta \lesssim -4.4$.

Let us now provide a physical explanation for why spontaneous scalarization occurs, following the arguments in [38]. Consider then the evolution equation of the scalar field in the weak-gravity static limit, such that $\Box \to \delta^{ij}\nabla_i\nabla_j$. Let us further consider a constant density star (with negligible pressure, following the weak-field assumption), such that $-4\pi G T^* \to 4\pi G \rho_* = 3GmR^{-3} = 3\mathcal{C}R^{-2}$, with $\mathcal{C} = Gm/R$ the compactness and R the stellar radius. This leaves us with the simple equation

$$\nabla^2 \varphi = \mathrm{sign}(\beta) K^2 \varphi \ , \tag{1.38}$$

where $K^2 = 3\ \mathcal{C}\ |\beta|\ R^{-2}$ when $r_* < R$ and $K = 0$ when $r_* > R$. The solution must be regular at the center, $\varphi(0) = \varphi_c =$ finite and $\varphi'(0) = 0$, and must be continuous and differentiable at the surface $r_* = R$. When $\beta < 0$, these conditions lead to the interior solution[7]

$$\varphi = \frac{\varphi_\infty}{\cos(KR)} \frac{\sin(K r_*)}{K r_*} \ . \tag{1.39}$$

One can see that when $KR = \pi/2$, the scalar field can be amplified inside the star, even when $\varphi_\infty \approx 0$. This is how spontaneous scalarization occurs in DEF-like theories. When $\beta > 0$, however, the solution can be obtained by replacing sin and cos with sinh and cosh respectively in Eq. (1.39). In this case, one typically finds a de-amplification of the scalar field inside the star which suppresses any deviations from GR.

A similar argument holds when $\beta > 0$ if one considers a NS whose trace of the stress-energy tensor, i.e. $T = -\rho + 3p$, is positive such that the overall sign on the right-hand side of Eq. (1.38) is still negative. This will lead to the same instability in the star and give a solution similar to Eq. (1.39), in which case the scalar field becomes amplified in the regions where $p > \rho/3$. Indeed, it has been shown that for β very large, i.e. $\beta \gtrsim 100$ [41], scalarization can occur in standard DEF theory for certain NS equations of state; note that we here restrict attention to the $\beta < 0$ case.

[7] Technically, the regularity conditions at the center lead to the interior solution $\varphi_{\rm int} = \varphi_c \sin(K r_*)/(K r_*)$, while the exterior solution is $\varphi_{\rm ext} = \varphi_\infty + \omega/r_*$. The matching conditions at the surface, $\varphi_{\rm int}(r_* = R) = \varphi_{\rm ext}(r_* = R)$ and $\varphi'_{\rm int}(r_* = R) = \varphi'_{\rm ext}(r_* = R)$, relate the central value of the field to its asymptotic value at spatial infinity $\varphi_c = \omega/\cos(KR)$.

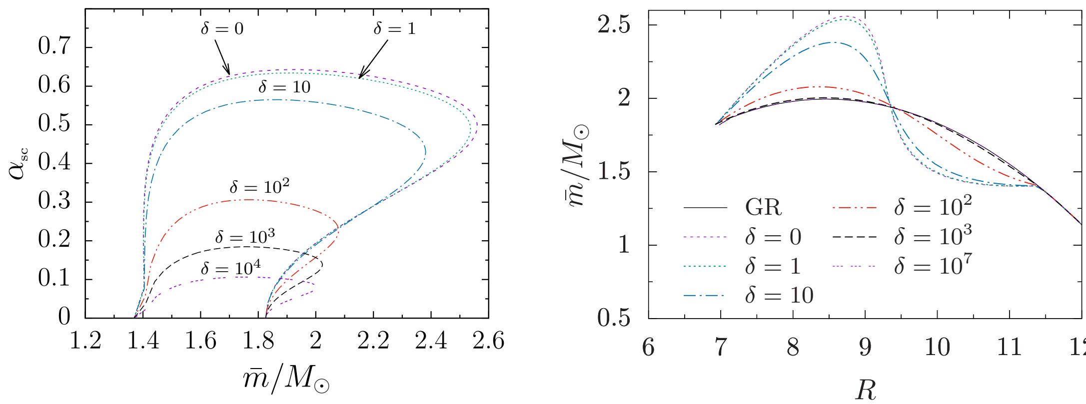

Figure 1.7: Left: Scalar charge as a function of baryonic mass in modified DEF theory [$\alpha(\varphi) = \beta\varphi + \delta\,\varphi^3$] with $\beta = -6$ and various values of δ. We again choose $\varphi_\infty = 0$ to see the effect that the δ term has on the previous DEF theory results. We see again that the scalar charge activates spontaneously when the mass exceeds a certain critical value, and a larger value of δ causes the charge to become smaller. Right: Mass-radius curves in modified DEF theory with Jordan-frame quantities $\bar{m}$ and R, $\beta = -6$, and the same choices of δ. With the black curve representing GR again, we see that the deviations away from GR are maximized when $\delta = 0$ (i.e. when the theory reduces to DEF theory), while larger values of δ decrease any deviations from GR.

1.4.2 Modified DEF Theory

To study NSs in modified DEF theory we must numerically solve the equations of the previous section but with $\alpha(\varphi)$ defined as in Eq. (1.29). As a first pass, we will continue to assume that $\varphi_\infty = 0$ to gain insight on how the inclusion of the δ term affects the results of the previous subsection. The left panel of Fig. 1.7 compares the scalar charge present for several orders of magnitude in δ. We see that spontaneous scalarization still occurs and it even "turns on/off" at the same values of $\bar{m}$ as in the ($\delta = 0$) DEF theory case. The δ independence of $\bar{m}$ in this case makes sense because $\varphi_\infty = 0$ and therefore the field is sitting in the region of the potential that is dominated by the DEF-like β term. One can see that adding the δ term suppresses the scalar charge of the star and drives the solution to that of GR in the limit $\delta \to \infty$.

These results are also evident in the right panel of Fig. 1.7 where mass-radius relations are plotted for a large range of δ for fixed β. The largest deviations from GR occurs when $\delta = 0$ (i.e. DEF theory) and again it is clear that as $\delta \to \infty$ the NS solutions reduce to those found in GR.

One can go even further and extract the maximum value of the scalar charge as a function of δ to explore a much broader region of parameter space, comparable to that in Fig. 1.1. In Fig. 1.8 we plot this quantity for different choices of fixed β . We find a clear monotonic decrease in the maximum scalar charge as δ increases. Also, not surprisingly, as β becomes more negative the (maximum) scalar charge increases, since the curvature of the potential becomes more negative and the potential has a steeper slope, thus allowing the field to become more amplified as a result.

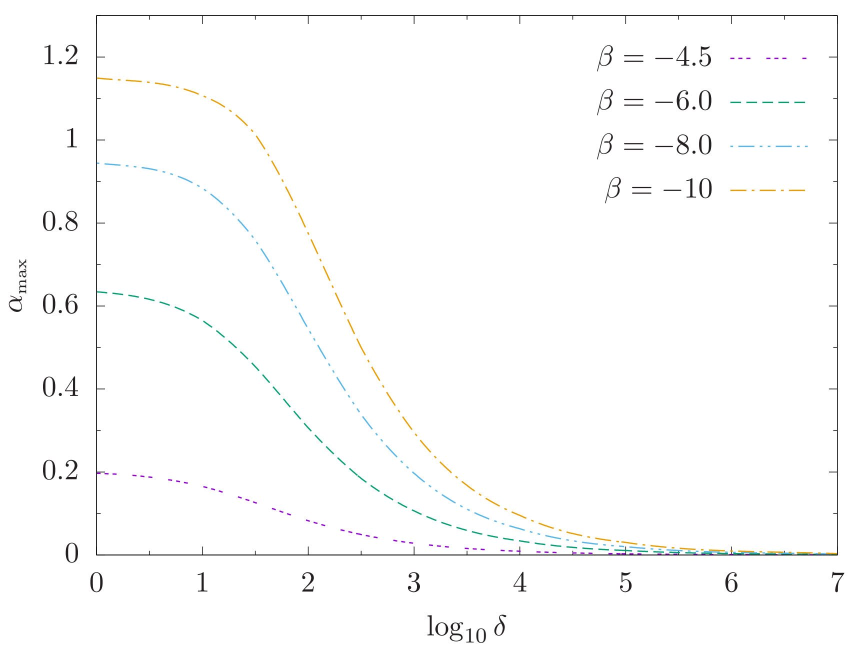

Figure 1.8: Maximum scalar charge as a function of δ for multiple values of β in modified DEF theory. Observe a uniform monotonic decrease as δ become large for a significant range of negative values of β.

We are now in a position to link the results from cosmological evolution and

Solar System tests to NSs and scalarization. So far, we have assumed $\varphi_\infty = 0$ in our NS solutions, but there is a problem with this assumption when we connect to our previous results in Fig. 1.4: φ_∞ does *not* vanish upon cosmological evolution, but rather it is near the minimum of the conformal potential if it is to satisfy Solar System constraints today. Thus, choosing $\varphi_\infty = 0$ *a priori* when building NS solutions (corresponding to the field sitting near the local maximum in Fig. 1.2) is completely inconsistent with Solar System observations. Instead, we must set $\varphi_\infty \sim \varphi_{\rm min}$ such that it is near the global minima.

Before proceeding numerically, let us take a step back and qualitatively explain what should happen when $\varphi_\infty \sim \varphi_{\rm min}$. The negative curvature of the potential in DEF theory ($V_\alpha = \beta\varphi^2/2$) leads to scalarization because the scalar field has the ability to roll in the potential. The same is true in modified DEF theory ($V_\alpha = \beta\varphi^2/2 + \delta\,\varphi^4/4$) when $\varphi_\infty = 0$, because the field sits near the local maximum of the potential and can roll when influenced by matter, which explains our previous numerical results on scalarization. However, if we now set the asymptotic value of the field to be near the minimum of the potential, such that Solar System tests are passed, the field now sits in a region of the potential where the curvature is positive. In regions of local positive curvature we would expect physics to reduce to the case of DEF theory with $\beta > 0$, in which case no scalarization occurs because the scalar field can no longer roll. As we will show, our numerical results are consistent with this qualitative idea. We stress that to determine if spontaneous scalarization occurs, the exact numerical value of $\varphi_{\rm min}$ is not an important factor, provided that $\varphi_\infty \approx \varphi_{\rm min}$ such that the scalar field sits near the minimum of the potential.

Allowing the asymptotic value of the scalar field to be *exactly* at the minimum gives zero scalar charge and all mass-radius curves reduce exactly to GR. This is what one expects, but it may not be the most complete conclusion to make. The

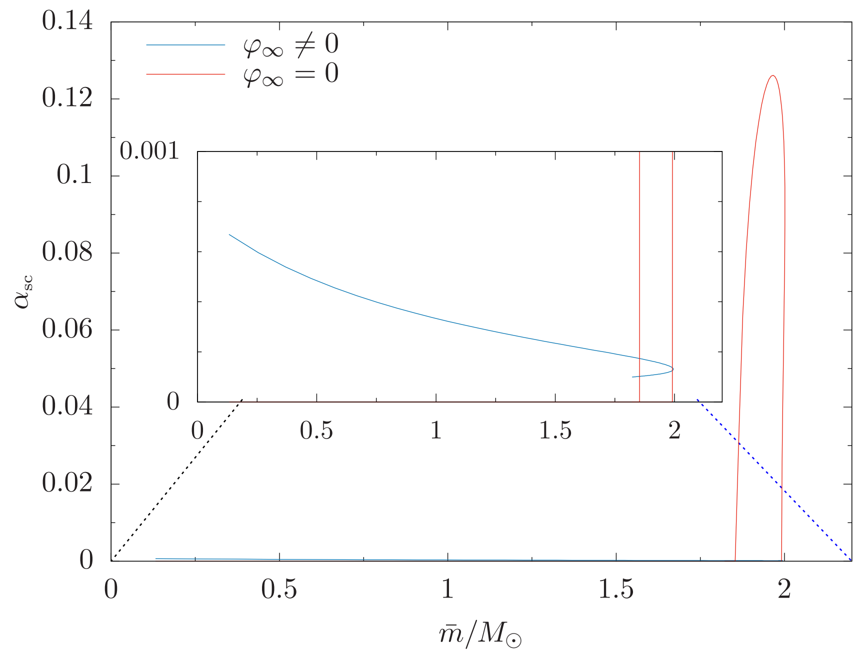

Figure 1.9: Scalar charge as a function of baryonic mass in modified DEF theory with $\beta = -4.5$ and $\delta = 100$. We plot the charge when $\varphi_\infty = 0$ and when φ_∞ lies near (but not exactly at) the minimum of the conformal potential (such that it saturates current Solar System bounds). In the second case (denoted by $\varphi_\infty \neq 0$) we see a scalar charge that is always present but never reaches a value greater than 10^{-3}. This shows that there is no "spontaneous" activation of the scalar field in the $\varphi_\infty \neq 0$ case.

Cassini bound requires that the scalar field sit *near* the minimum of the potential, corresponding to the region between the purple dashes in Fig. 1.2. The best chance of allowing for scalarization occurs when one saturates this bound and sets φ_∞ to coincide with one of these dashes near the minimum, giving the scalar field a very small region to roll in. Again, however, we find that spontaneous scalarization does not occur and that all mass-radius curves reduce approximately to that of GR. There does exist a small scalar charge in this case (just like in DEF theory with $\beta > 0$ or in JFBD theory), see Fig. 1.9, but exactly like in those cases (i) the charge is very small (on the order of 10^{-4}) and (ii) the charge does not turn on/off suddenly, as one would expect in spontaneous scalarization, but rather it is always present for all masses.

This behavior is shown in Fig. 1.9, which shows the scalar charge as a function of the baryonic mass for two different choices of φ_∞. In one case, the asymptotic value of the scalar charge φ_∞ is chosen to be near the minimum of the conformal potential, saturating Solar System constraints (i.e. φ is set equal to one of the dashes near the minimum in Fig. 1.2). In the other case, $\varphi_\infty = 0$, which allows for spontaneous scalarization, but as discussed earlier, is not consistent with the predictions of the cosmological evolution of the field at the present time. These results prove that if modified DEF theory is to remain consistent with Solar System tests after cosmological evolution, then the spontaneous scalarization of NSs is not a phenomenon that can occur.

Does this inconsistency between scalarization and Solar System tests persist for other forms of the conformal coupling potential? Previously we have argued that the only way Solar System tests can be passed (without a mass term in the scalar field action) is if the potential contains a minimum, preferably a global one to prevent the scalar field from diverging (see Sec. 1.3.3). Regardless of the exact form of the potential, however, one must require the the scalar field be near the minimum today in order to pass Solar System tests. This requirement then reduces the problem to a local analysis of the potential near the minimum, where the curvature is positive, thus making the analysis for NSs qualitatively similar to that of the potential that we have studied above. Thus, because the scalar field must sit near the minimum of the conformal potential today, the results of this section generalize to any polynomial coupling potential that passes Solar System tests upon cosmological evolution.

1.5 Conclusion

In this paper, we studied scalar-tensor theories of gravity and their cosmological evolution to determine whether such theories are able to pass Solar System tests today while still allowing for scalarization. As expected [40, 54, 55], the theory proposed by Damour and Esposito-Farèse does not pass these tests when $\beta < 0$, precisely the values of β that lead to spontaneous scalarization in strongly self-gravitating systems like NSs. This is because when $\beta < 0$, an attractor basin arises leading to a run-away scalar field solution that violates Solar System constraints today.

We have studied a generic modification to DEF theory by considering a conformal coupling function composed of a higher-order polynomial in the scalar field, such that the associated coupling potential is bounded from below. We show that this modification allows the theory to pass Solar System tests today upon cosmological evolution for a wide range of initial conditions. Any potential that *is not* bounded from below allows the scalar field to reach a runaway attractor solution (at least for some initial conditions), and thus, can never pass Solar System tests for generic initial conditions. Potentials that are bounded from below and pass Solar System constraints, however, do not allow for spontaneous scalarization. This is because cosmological evolution drives the scalar field to the minimum of the conformal potential, thus eliminating the ability of the field to roll when solving for NS configurations.

The results of this paper suggest that if one wishes to construct scalar-tensor theories that can simultaneously pass Solar System constraints and allow for spontaneous scalarization, then modifications to the conformal coupling of this form are not enough. One possibility is to consider the addition of a mass for the scalar field. Indeed, Ref. [68] has already shown that massive DEF theory still allows for spontaneous scalarization for a very light scalar (masses between 10^{-15} and 10^{-9} eV). Such massive scalar tensor theories could potentially pass Solar System constraints upon cosmological evolution, an investigation that is currently ongoing. Another possibility is to consider other, non-polynomial, functional forms for the coupling potential, such as that studied recently in [41]. Indeed, the latter reference has recently claimed that such a potential allows for spontaneous scalarization. Whether this model also passes Solar System constraints will also be analyzed in a forthcoming publication.

1.6 Acknowledgments

We thank Gilles Esposito-Farèse for insightful conversations on scalarization and scalar-tensor theories, and Norbert Wex and Thibaut Arnoulx de Pirey for reading our manuscript carefully and providing useful suggestions. N. Y. acknowledges support from the NSF CAREER Grant PHY-1250636. E. B. acknowledges support from the European Union's Seventh Framework Programme (FP7/PEOPLE-2011-CIG) through the Marie Curie Career Integration Grant GALFORMBHS PCIG11-GA-2012-321608. This project has received funding from the European Union's Horizon 2020 research and innovation programme under the Marie Sklodowska-Curie grant agreement No 690904.

CHAPTER TWO

SOLAR SYSTEM CONSTRAINTS ON MASSLESS SCALAR-TENSOR GRAVITY WITH POSITIVE COUPLING CONSTANT UPON COSMOLOGICAL EVOLUTION OF THE SCALAR FIELD

Contribution of Authors and Co-Authors

Manuscript in Chapter 2

Author: David Anderson

Contributions: Helped develop and implement the design study. Developed numerical code necessary for the project. Wrote the first draft of the manuscript.

Co-Author: Nicolás Yunes

Contributions: Helped develop design study and oversaw the completion of the project. Provided feedback on analysis and comments on draft of the manuscript.

Manuscript Information Page

David Anderson, Nicolás Yunes

Physical Review D

Status of Manuscript:

____ Prepared for submission to a peer-reviewed journal

____ Officially submitted to a peer-reviewed journal

____ Accepted by a peer-reviewed journal

__x__ Published in a peer-reviewed journal

Published by the American Physical Society

Published on September 22, 2017, in volume 96, 064037

DOI: 10.1103/PhysRevD.96.064037

Abstract

Scalar-tensor theories of gravity modify General Relativity by introducing a scalar field that couples non-minimally to the metric tensor, while satisfying the weak-equivalence principle. These theories are interesting because they have the potential to simultaneously suppress modifications to Einstein's theory on Solar System scales, while introducing large deviations in the strong field of neutron stars. Scalar-tensor theories can be classified through the choice of conformal factor, a scalar that regulates the coupling between matter and the metric in the Einstein frame. The class defined by a Gaussian conformal factor with negative exponent has been studied the most because it leads to spontaneous scalarization (i.e. the sudden activation of the scalar field in neutron stars), which consequently leads to large deviations from General Relativity in the strong field. This class, however, has recently been shown to be in conflict with Solar System observations when accounting for the cosmological evolution of the scalar field. We here study whether this remains the case when the exponent of the conformal factor is positive, as well as in another class of theories defined by a hyperbolic conformal factor.We find that in both of these scalar-tensor theories, Solar System tests are passed only in a very small subset of coupling parameter space, for a large set of initial conditions compatible with Big Bang Nucleosynthesis. However, while we find that it is possible for neutron stars to scalarize, one must carefully select the coupling parameter to do so, and even then, the scalar charge is typically two orders of magnitude smaller than in the negative exponent case.Our study suggests that future work on scalar-tensor gravity, for example in the context of tests of General Relativity with gravitational waves from neutron star binaries, should be carried out within the positive coupling parameter class.

2.1 Introduction

General Relativity (GR) has been shown to be consistent with all current observations, including those in the Solar System (SS) [16,61], with binary pulsars [7], and recently with gravitational waves through the merging of two black holes detected by advanced LIGO [1, 76]. Scalar-tensor theories (STTs) of gravity are among the most natural extensions to GR [29–31] because they are both well-posed [32] and well-motivated from string theory [25, 77], quantum field theory [24], and cosmology [17, 23, 78, 79]. These theories have seen a recent revival given that they can lead to large deviations from GR in strong-field scenarios, making them a natural theory choice to test GR with gravitational wave observations.

STTs modify GR by introducing a scalar field that couples to the metric non-minimally, thus forcing matter to respond both to the metric tensor and to the scalar field. The easiest way to see this is to (conformally) transform the metric tensor into the *Einstein frame*, in which the action looks identical to the Einstein-Hilbert one, but with the matter sector responding to the product of the conformally-transformed metric and the conformal factor. Therefore, STTs can be classified by the specific functional form of the conformal factor. One of the most studied classes is that originally proposed by Damour and Esposito-Farèse (DEF) [37, 38], in which the conformal factor is a Gaussian in the Einstein-frame scalar field with an exponent proportional to a coupling constant β, i.e. $A(\varphi) = \exp(\beta\varphi^2/2)$. Another class that has recently captured some attention is that in which the conformal factor is proportional to a certain power of a hyperbolic cosine with argument proportional to the product of the Einstein-frame scalar field and a constant β, i.e. $A(\varphi)^{3\beta} = \cosh(\sqrt{3}\beta\varphi)$ [41, 44, 45, 80]. In this paper, we will study both classes, referring to the former as *exponential* and the latter as *hyperbolic*.

Perhaps one of the most interesting consequences of STTs is that neutron stars (NSs) can undergo what is known as *scalarization* [37, 38], in which the scalar field is amplified above its background value inside the NS. Three types of scalarization processes have been discovered, which can be classified by the physical process that causes the activation of the scalar field. For isolated NSs, *spontaneous scalarization* occurs once a critical density is reached inside the star [37, 38, 42, 64]. In binary systems, NSs can undergo either *dynamical* or *induced* scalarization [52, 53, 65, 66]. The former occurs when the binding energy of the orbit reaches a critical value, causing the violent activation of the scalar field, while the latter occurs when one

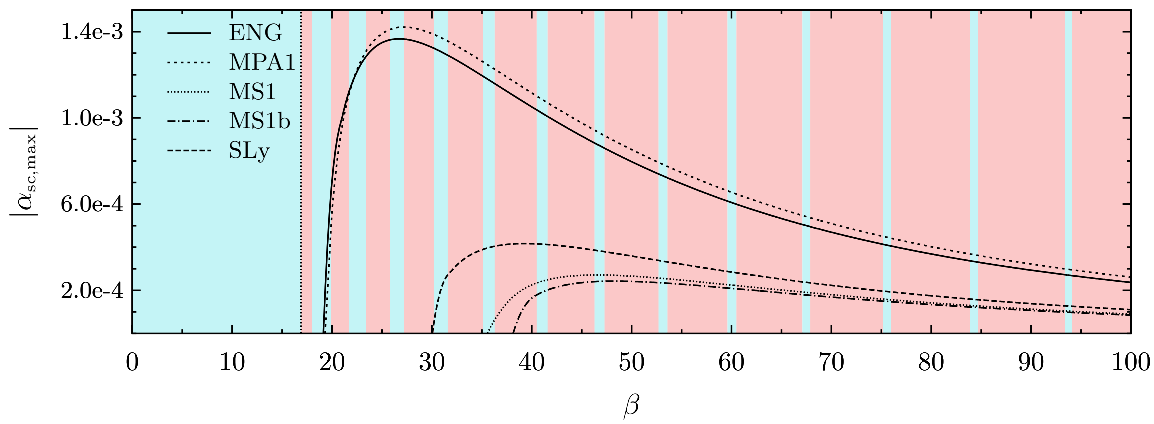

Figure 2.1: Maximum value of scalar charge $\alpha_{\rm sc}$ inside stable NSs as a function of the coupling parameter β in hyperbolic STTs with 5 different EoSs. In the background, blue (red) regions correspond to values of β that are consistent (inconsistent) with Solar System observations after cosmological evolution. Observe that the green regions become thinner and more sparse as β increases. The bounds shown here are the most stringent ones one can place with initial conditions that deviate from GR as much as possible by saturating BBN constraints.

member of the binary is already scalarized and it induces a scalar charge in its companion. Until recently, scalarization was thought to only occur in the exponential class of STTs if $\beta < 0$, because then a certain scalar instability can occur for most equations of state (EoSs). But recently, a non-vanishing scalar charge has also been shown to occur inside NSs when $\beta > 0$ in both exponential and hyperbolic STTs with certain EoSs [41, 80, 81]. In these cases, however, the activation of the scalar charge (for example, as a function of ADM mass) is not nearly as sudden as in the $\beta < 0$ case and the maximum scalar charge is typically significantly smaller.

STTs have also been popular because of the belief that they can be made to pass Solar System constraints by appropriately choosing the asymptotic value of the scalar field, but recently this belief was proven to be incorrect [40, 54, 55, 82]. Solar System observations place a very strict constraint on exponential STTs because the asymptotic value of the scalar field in the Solar System cannot be chosen freely, but rather it must be chosen consistently with the field's prior cosmological evolution. The cosmological evolution of the universe forces the scalar field to grow rapidly with redshift when $\beta < 0$ (for all but very fine-tuned initial conditions), leading to clear violations of Solar System tests today, most notably in the consistency of the Shapiro time delay and the perihelion shift of Mercury with the GR predictions [61]. A previous study [82] attempted to remedy this problem by modifying the form of the exponential conformal factor by adding a term of higher order in the Einstein frame scalar field. While this was enough to ensure Solar System tests are passed today, it reduced the scalar charge in NSs by orders of magnitude.

Theory	SS tests?	$\alpha_{\rm sc,max}$	Stable NS?
$\beta < 0$ exp.	$\times$	$\mathcal{O}(10^{-1})$	✓
$\beta > 0$ exp.	✓	$\mathcal{O}(10^{-3})$	$\times$
$\beta < 0$ hyp.	$\times$	$\mathcal{O}(10^{-1})$	✓
$\beta > 0$ hyp.	✓	$\mathcal{O}(10^{-3})$	✓

Table 2.1: A summary of the various properties of two classes of STTs. The columns correspond to the following: Do they pass Solar System tests after cosmological evolution? What is the typical magnitude of the maximum scalar charge they can support inside NSs? Do they allow for stable *and* scalarized NS solutions?

Given all of this, it is then natural to explore exponential and hyperbolic STTs with $\beta > 0$ in more detail to determine if Solar System constraints can be placed, and if so, the degree to which NSs continue to scalarize within the allowed region of parameter space. We first study Solar System constraints by exploring the cosmological behavior of STTs from the time of Big-Bang Nucleosynthesis (BBN) until today. For any particular value of β and any particular set of initial conditions consistent with BBN constraints, the value of the scalar field today will either be consistent with Solar System observations or it will violate them, therefore determining if that value of β is part of the viable region of parameter space for those initial conditions. There are two distinct sets of initial conditions that we consider in detail.

1. **BBN constraints on the scalar-field initial conditions are saturated such that deviations from GR are at a maximum.**

Figure 2.1 shows the β (blue) regions that allow hyperbolic STTs to pass Solar System tests when choosing initial conditions that saturate BBN constraints. For all viable initial conditions (including those that saturate BBN constraints), hyperbolic STTs pass Solar System tests when $0 < \beta \lesssim 17$, while exponential STTs pass when $0 < \beta \lesssim 24$ (not shown in the figure). Moreover, there are special values of the initial conditions for which both theories pass Solar System tests above these critical β values, which are shown as thin green regions in Fig. 2.1. This is because the cosmological evolution of the scalar field has damped oscillations with redshift, thus allowing for the possibility that today the field happens to be in a state in which Solar System tests are passed, although this may not be the case in the future.

2. **BBN constraints on the scalar-field initial conditions are relaxed such that deviations from GR are not at a maximum.**

The constraints reported above can be relaxed by fine-tuning the initial conditions at the time of BBN. Cosmological observations and the theory nucleosynthesis require that the scalar field at the time of BBN be in a small region near the minimum of an effective potential. Saturating current constraints on the speed-up factor, quantifying deviations of the gravitational constant G from GR at the time of BBN, put the scalar as far away from the minimum as possible. In principle, however, one can relax this assumption and place the scalar closer to the minimum, making it easier for the theory to satisfy current Solar System constraints. A random distribution of viable initial conditions relaxes the bounds reported above to $0 < \beta \lesssim 34$ and $0 < \beta \lesssim 25$ in the exponential and hyperbolic cases respectively. Larger values of β would typically require fine-tuning of initial conditions for Solar System tests to be passed. It is worth noting that if these assumption are completely relaxed such that there are no deviation from GR at the time of BBN, then one cannot place any constraints on the value of β because the cosmological evolution of the universe will be completely consistent with GR.

With this at hand, we then explore whether spontaneous scalarization still occurs in exponential and hyperbolic STTs within the viable β regimes of parameter space. In the exponential STT case, scalarized NSs have already been shown to be unstable to gravitational collapse for such values of β [41]. In the hyperbolic case, however, scalarized NSs can be stable for certain EoSs, but the scalar charge is typically two orders of magnitude smaller than typical charges in the $\beta < 0$ exponential STT case. Figure 2.1 plots the maximum scalar charge for stable NSs in hyperbolic STTs for a large range of β using different EoSs. None of the EoSs that we consider here give stable scalarized NS solutions for $\beta \lesssim 17$, but they do allow for stable scalarized stars when $\beta \gtrsim 20$. Moreover, there exist (small) periodic regions of viable parameter space that allow for scalarized NSs (green regions that have non-zero scalar charge in them), although these separate and become thinner as β increases. These general conclusions are summarized in Table 2.1. The results in Table 2.1 only holds for *massless* STTs and the addition of a potential term for the scalar field could allow the theories to completely avoid any constraints we place here.

Our results are directly relevant to studies that constrain deviations from GR in the strong field, for example with gravitational waves. Most of the latter have so far focused on the massless exponential class of STTs with $\beta < 0$, but these have already been shown to be incompatible with Solar System observations [54, 82]. We will here show that the massless exponential class of STTs with $\beta > 0$ does pass Solar System tests for a range of β, but these theories have already been shown to disallow for stable scalarized NSs [41]. We will also show that the hyperbolic class of STTs with $\beta > 0$ also passes Solar System tests for a range of β, and these theories do allow for stable scalarized stars [41] making them much more appropriate for gravitational wave studies. Our results, however, also indicate that the amount of scalar charge in such theories is drastically smaller than what is obtained in the massless exponential case with $\beta < 0$. This raises the question of whether such small charges can be constrained in practice with second-generation ground-based gravitational wave detectors. A more detailed analysis is required to address this last question.

The rest of this paper will address the points above in more detail. We first lay out our notation and the background of STTs in Sec. 2.2. We next go into details of the cosmological evolution of the scalar field in both theories in Sec. 2.3 and place constraints on β from Solar System observations. Section 2.4 addresses NS solutions in detail, first for $\beta < 0$ to build a foundation and then for $\beta > 0$. Finally, we end with our conclusions in Sec. 2.5 and discuss the implications of our results. We adopt units in which $c = 1$ but restore cgs units in our discussion of NSs when appropriate.

2.2 The Basics of Scalar-Tensor Theories

In this section we present the details of the class of theories we investigate and establish notation, following mostly the presentation in [82]. The STTs we consider in this paper can be defined by the action $S_{\rm J} = S_{{\rm J},g} + S_{\rm J,\,mat}$, where the gravitational part is given by

$$S_{\mathrm{J},g} = \int d^4x \frac{\sqrt{-g}}{2\kappa}\left[\phi R - \frac{\omega(\phi)}{\phi}\partial_\mu\phi\,\partial^\mu\phi\right] , \tag{2.1}$$

and where g and R are the determinant and Ricci scalar associated with the Jordan-frame metric $g_{\mu\nu}$, $\omega(\phi)$ is a coupling function for the scalar field ϕ, and $\kappa = 8\pi G$ with G the bare gravitational constant. The matter action $S_{\mathrm{J,\,mat}}[\chi, g_{\mu\nu}]$ is a functional of the matter fields χ, which couple directly to the Jordan frame metric $g_{\mu\nu}$, meaning that STTs of this form are metric theories of gravity.

One can take the action in Eq. (2.1) and write it in a form resembling the Einstein-Hilbert action in GR through a conformal transformation $g_{\mu\nu} = A^2(\varphi)g^*_{\mu\nu}$ where we refer to $g^*_{\mu\nu}$ as the Einstein-frame metric. By choosing the conformal factor $A(\varphi)$ such that

$$A^2(\varphi) = \phi^{-1} , \tag{2.2}$$

and providing an explicit relationship between φ and ϕ via

$$\alpha^2(\varphi) = \left(\frac{d\ln A(\varphi)}{d\varphi}\right)^2 = \frac{1}{3+2\omega(\phi)} , \tag{2.3}$$

the Einstein-frame action becomes

$$\begin{aligned} S_{\mathrm{E}} = &\int d^4x \frac{\sqrt{-g_*}}{2\kappa}\left[R_* - 2g_*^{\mu\nu}\partial_\mu\varphi\,\partial_\nu\varphi\right] \\ &+ S_{\mathrm{E,\,mat}}\left[\chi, A^2(\varphi)g^*_{\mu\nu}\right] , \end{aligned} \tag{2.4}$$

where g_* and R_* are the determinant and Ricci scalar associated with the Einstein-frame metric $g^*_{\mu\nu}$. Notice that the matter degrees of freedom χ now couple to the product of the conformal factor $A(\varphi)$ and the Einstein-frame metric. For later convenience, we define a conformal coupling potential via $\alpha = \partial V_\alpha/\partial\varphi$, such that

$$V_\alpha(\varphi) \;=\; \ln A(\varphi) \;, \tag{2.5}$$

and note that the curvature of this potential is then given by

$$\beta(\varphi) \;=\; \frac{\partial^2 V_\alpha}{\partial \varphi^2} \;=\; \frac{\partial \alpha(\varphi)}{\partial \varphi} \;. \tag{2.6}$$

The potential in Eq. (2.5) will later play the role of an effective potential that the scalar field evolves in cosmologically. For the rest of this paper we will strictly refer to $A(\varphi)$ as the conformal factor, $\alpha(\varphi)$ as the (conformal) coupling, and $V_\alpha(\varphi)$ as the (conformal) coupling potential.

Variation of the Einstein-frame action yields the field equations

$$R^*_{\mu\nu} \quad = \quad \kappa\left(T^*_{\mu\nu} - \frac{1}{2} g^*_{\mu\nu} T^*\right) \;, \tag{2.7}$$

$$\Box_* \varphi \quad = \; -\frac{\kappa}{2}\alpha(\varphi) T^{\;\mathrm{mat},*} \;, \tag{2.8}$$

where $\Box_*$ is the Einstein-frame covariant wave operator and $T^{\;\mathrm{mat},*}$ is the trace of the Einstein-frame matter stress-energy tensor defined by

$$T^{\;\mathrm{mat},*}_{\mu\nu} \equiv \frac{2}{\sqrt{-g_*}} \frac{\delta S_{\;\mathrm{E,\,mat}}\left[\chi, A^2(\varphi) g^*_{\mu\nu}\right]}{\delta g_*^{\mu\nu}} \;. \tag{2.9}$$

One can see that the Einstein-frame stress-energy tensor is related to the Jordan-frame one via $T^{\mu\nu}_{\mathrm{mat},*} = A^6 T^{\mu\nu}_{\mathrm{mat}}$ by applying the conformal transformation to Eq. (2.9). The field equations also depend on the total stress-energy tensor, which is the sum of the matter and scalar field stress-energy tensors

$$T^*_{\mu\nu} \;=\; T^{\;\mathrm{mat},*}_{\mu\nu} + T^{\varphi,*}_{\mu\nu} \;, \tag{2.10}$$

where

$$\kappa T^{\varphi,*}_{\mu\nu} \;=\; 2(\partial_\mu\varphi)(\partial_\nu\varphi) - g^*_{\mu\nu}(\partial_\sigma\varphi)(\partial^\sigma\varphi) \; . \tag{2.11}$$

Our entire study, both cosmologically and for NSs, adopts a perfect fluid representation of the matter in the Jordan frame. However, this is also true in the Einstein frame since they are related through a conformal transformation, and thus we use

$$T^{\,\mathrm{mat},*}_{\mu\nu} \;=\; (\epsilon_* + p_*)u^*_\mu u^*_\nu + p_* g^*_{\mu\nu} \; , \tag{2.12}$$

where ϵ_* is the energy density of the fluid, p_* is the pressure, and u^* is the 4-velocity, all in the Einstein frame. Normalization of the 4-velocity $g^*_{\mu\nu}u^\mu_* u^\nu_* = -1 = g_{\mu\nu}u^\mu u^\nu$ leads to the relationship $u^\mu_* = Au^\mu$. Using this result in conjunction with $T^{\mu\nu}_* = A^6 T^{\mu\nu}$ allows one to derive the direct relations $\epsilon_* = A^4\epsilon$ and $p_* = A^4 p$ between the Einstein and Jordan frame density and pressure.

The choice of $A(\varphi)$, or consequently $\alpha(\varphi)$, defines a particular theory and therefore plays a critical role in testing that theory with observations. Specifically, these functions determine the local value of Newton's gravitational constant [30]

$$G_N \;=\; G\big[A^2\,(1+\alpha^2)\big]_{\varphi_0} \; , \tag{2.13}$$

where φ_0 is the value of the scalar field today determined cosmologically. They also determine the local value of the parameterized post-Newtonian (PPN) parameters [71, 72]. The $\gamma_{\,\mathrm{PPN}}$ parameter, which measures the spatial curvature due to a unit rest mass [16, 73], is given in massless STTs by

$$|1-\gamma_{\,\mathrm{PPN}}|_{\varphi_0} \;=\; \frac{2\alpha_0^2}{1+\alpha_0^2} \; , \tag{2.14}$$

where α_0 is the conformal coupling evaluated at the present day value of the scalar field φ_0. There exist another such expression for the $\beta_{\,\mathrm{PPN}}$ parameter which is given by

$$|1-\beta_{\,\mathrm{PPN}}|_{\varphi_0} \;=\; \frac{1}{2}\frac{\beta_0\alpha_0^2}{(1+\alpha_0^2)^2}\ , \tag{2.15}$$

where $\beta_0 = \partial\alpha/\partial\varphi|_{\varphi_0}$. In GR $\gamma_{\,\mathrm{PPN}} = \beta_{\,\mathrm{PPN}} = 1$, and the constraints $|1-\gamma_{\,\mathrm{PPN}}| \lesssim 2.3\times10^{-5}$ and $|1-\beta_{\,\mathrm{PPN}}| \lesssim 8\times10^{-5}$ [16], from the verification of the Shapiro time delay by the Cassini spacecraft and the perihelion shift of Mercury respectively [73], provide the weak field constraints on the theories we consider in this paper.

2.3 Cosmological Evolution and Solar-System Constraints

To determine if a particular theory is consistent with Solar System tests, we must first understand the cosmological evolution of the scalar field. We here review the cosmological evolution equations originally presented in Refs. [40, 55] and continue to establish notation, following again mostly the presentation in [82]. We adopt a spatially flat Friedmann-Roberston-Walker (FRW) metric in the Einstein-frame

$$ds_*^2 = -dt_*^2 + a_*^2(dr_*^2 + r^2 d\Omega_*^2)\ , \tag{2.16}$$

where a_* is the Einstein-frame scale factor. The Einstein-frame field equations then become

$$3H_*^2 = \kappa\epsilon_* + \dot{\varphi}^2\ , \tag{2.17}$$

$$-3\frac{\ddot{a}_*}{a_*} = \frac{\kappa}{2}\epsilon_*\,(1+3\lambda) + 2\dot{\varphi}^2\ , \tag{2.18}$$

$$\ddot{\varphi} + 3H_*\dot{\varphi} = -\frac{\kappa}{2}\alpha\epsilon_*(1-3\lambda)\ , \tag{2.19}$$

where overhead dots stand for derivatives with respect to Einstein-frame coordinate time t_*, $H_* = \dot{a}_*/a_*$ is the Einstein-frame Hubble parameter, ϵ_* and p_* are the energy density and pressure of all components of the universe (matter, radiation, dark energy), and $\lambda = p_*/\epsilon_*$ is the usual cosmological EoS parameter. The Einstein-frame variables can be transformed to Jordan-frame variables via the conformal transformation mentioned earlier: $g_{\mu\nu} = A^2(\varphi)g^*_{\mu\nu}$ which yields $dt = A(\varphi)dt_*$ and $a = A(\varphi)a_*$. Following Ref. [82], we assume that any pressure and energy density associated with φ will be negligible compared to other energy components of the universe.

Equations (2.17)–(2.19) do not lend themselves to a simple analytic solution for the evolution of the scalar field φ. However, by defining a new time coordinate $d\tau = H_* dt_*$, one can decouple the evolution equations. Under this time transformation one finds that the time derivatives become

$$
\begin{aligned}
\dot{\varphi} &= H_*\varphi' \ , & (2.20)\\
\ddot{\varphi} &= H_*^2\varphi'' + \dot{H}_*\varphi' \ , & (2.21)\\
\frac{\ddot{a}}{a} &= \dot{H}_* + H_*^2 \ , & (2.22)
\end{aligned}
$$

where primes denote derivative with respect to τ. Using these redefinitions, Eqs. (2.17)–(2.19) can be simplified into a single equation for the evolution of the scalar field

$$\frac{2}{3-\varphi'^2}\varphi''\epsilon_* + \epsilon_*(1-\lambda)\varphi' = -\alpha(\varphi)\epsilon_*(1-3\lambda) \ . \tag{2.23}$$

It is important to note here that if one wishes to consider more than a single component universe, ϵ_* must not be divided out of the equation. In general, each term containing ϵ_* and λ will be a sum over all components of the universe, and therefore, ϵ_* cannot simply be removed from the equation.

To have a complete description of Eq. (2.23) one must understand its evolution in τ. From conservation of energy in the Jordan-frame one finds

$$d(\epsilon a^3) = -p(\epsilon)d(a^3) \ , \tag{2.24}$$

which, using $\lambda = p/\epsilon$, can be written as

$$\epsilon = a^{-3(1+\lambda)}\epsilon_0 \ , \tag{2.25}$$

where ϵ_0 is the value of the Jordan-frame energy density measured today (i.e. when $a = 1$). To transform Eq. (2.25) to the Einstein frame we make use of the fact that $d\tau = H_* dt_*$ to write $a_* = e^\tau$ and then use $a = A(\varphi)a_*$ to write

$$a = A(\varphi)e^\tau \ . \tag{2.26}$$

We can then use $\epsilon_* = A^4\epsilon$ in combination with Eq. (2.26) to write the Einstein-frame energy density as

$$\epsilon_* = \epsilon_0 e^{-3(1+\lambda)\tau} A^{1-3\lambda} \ . \tag{2.27}$$

If we divide Eq. (2.23) by the critical density $\epsilon_{\rm crit}$ and use the result of Eq. (2.27) the scalar field evolution equation becomes

$$\frac{2\varphi''}{3-\varphi'^2}C_1(\varphi,\tau) + \varphi' C_2(\varphi,\tau) = -\alpha(\varphi)C_3(\varphi,\tau) \ , \tag{2.28}$$

where we have defined

$$
\begin{aligned}
C_1(\varphi,\tau) &= \sum_i \Omega_{i,0}\, e^{-3(1+\lambda_i)\tau}\, A^{(1-3\lambda_i)} \ , && (2.29)\\
C_2(\varphi,\tau) &= \sum_i \Omega_{i,0}(1-\lambda_i)\, e^{-3(1+\lambda_i)\tau}\, A^{(1-3\lambda_i)} \ , && (2.30)\\
C_3(\varphi,\tau) &= \sum_i \Omega_{i,0}(1-3\lambda_i)\, e^{-3(1+\lambda_i)\tau}\, A^{(1-3\lambda_i)} \ , && (2.31)
\end{aligned}
$$

where $\Omega_{i,0} = \epsilon_{i,0}/\epsilon_{\rm crit}$ is the standard density parameter as seen today for the ith energy component.

The evolution described in Eq. (2.28) is reminiscent of a damped oscillator. Assuming the density functions C_1, C_2, and C_3 only contain a single energy component for simplicity, it becomes apparent that there is a velocity dependent mass appearing in front of the second derivative, a damping term proportional to the velocity, and on the right-hand side of the equations there is a potential gradient influencing the overall evolution of the scalar field, as first pointed out in [40, 55]. Even if the density functions are not constant in τ or φ, the damped oscillator picture still holds, as we will show numerically later in this section, and it will thus provide a useful analogy to extract a physical understanding from our numerical calculations.

2.3.1 Two Scalar-Tensor models

Thus far we have remained model independent and have not made any assumptions about the form of $\alpha(\varphi)$. In this section we define the two STTs that we study in this paper. The first model we consider is the standard DEF theory, defined by

$$
\begin{aligned}
A(\varphi) &= e^{\frac{1}{2}\beta\varphi^2} \;, && (2.32)\\
V_\alpha(\varphi) &= \frac{1}{2}\beta\varphi^2 \;, && (2.33)\\
\alpha(\varphi) &= \beta\varphi \;, && (2.34)\\
\beta(\varphi) &= \beta \;, && (2.35)
\end{aligned}
$$

which we will refer to as the *exponential model.* The other model we consider is that introduced by Mendes [41, 80], defined by

$$
\begin{aligned}
A(\varphi) &= \left[\cosh(\sqrt{3}\beta\varphi)\right]^{\frac{1}{3\beta}} \;, && (2.36)\\
V_\alpha(\varphi) &= \frac{1}{3\beta}\ln\left[\cosh(\sqrt{3}\beta\varphi)\right] \;, && (2.37)\\
\alpha(\varphi) &= \frac{\tanh(\sqrt{3}\beta\varphi)}{\sqrt{3}} \;, && (2.38)\\
\beta(\varphi) &= \beta\,\mathrm{sech}^2(\sqrt{3}\beta\varphi) \;, && (2.39)
\end{aligned}
$$

which we will refer to as the *hyperbolic model.* Notice that β enters both models as a free parameter that will quantify the degree of departure from GR (with $\beta = 0$ reducing the theory to GR). The conformal factor here is motivated as an analytic approximation to the conformal factor one would find if the action also included terms proportional to $R\,\varphi^2$ in the Einstein frame [41, 44, 45, 80], motivated by quantum field theory considerations [24].

In the context of an oscillator, V_α is the potential that sources the scalar field evolution through its gradient $\alpha(\varphi)$. In the case of exponential STTs, this is simply a parabola, cf. the left panel of Fig. 2.2, and therefore the scalar field evolves analogously to a damped harmonic oscillator in τ. In the case of hyperbolic coupling,

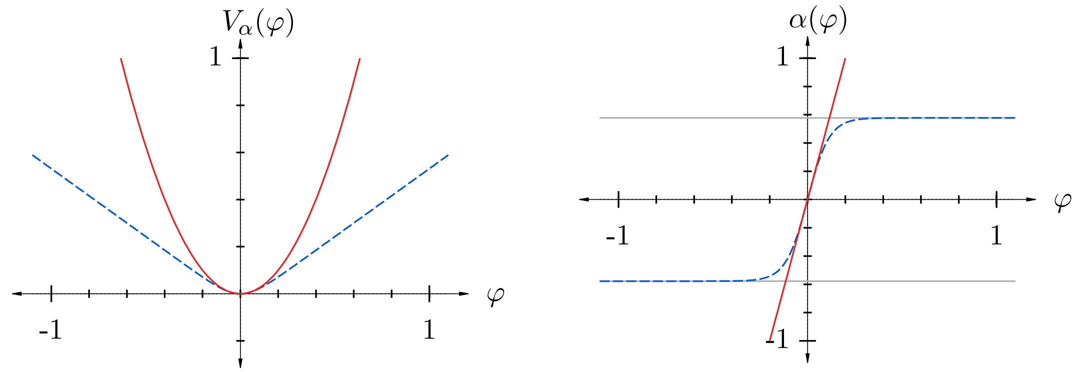

Figure 2.2: Schematic diagrams for both the conformal coupling potential V_α (left) and the conformal coupling $\alpha(\varphi)$ (right). The exponential STT is represented by solid red curves and the hyperbolic theory by dashed blue curves. The horizontal gray lines at $\pm 1/\sqrt{3}$ in the right panel correspond to the limiting values of $\alpha(\varphi)$ in the hyperbolic theory. These figures were constructed with $\beta = 5$, but the qualitative features remain the same for all positive values of β.

however, that potential is no longer a simple parabola and while we expect the evolution of the scalar field to still be oscillatory, it should be quantitatively different than in the exponential STT case. The key difference between the potentials in these theories lies in their behavior away from their minima ($\varphi = 0$). In the exponential case, the gradient of the potential grows linearly as we increase φ (or β for that matter) where for hyperbolic coupling the gradient becomes constant; both behaviors can be seen in the right panel of Fig. 2.2. The behavior of these potentials away from their minima plays a key role in the behavior of the scalar field, both in cosmology and in NSs, as we will show in the following sections.

2.3.2 BBN Constraints and Initial Conditions

To determine the evolution of the scalar field one must first determine a set of initial conditions that it must obey at some point in the past. The natural first choice is to determine initial conditions at the very beginning of the universe, or at the very least at the end of inflation. However, there is substantial uncertainty in the true physics of the early universe, and thus, any constraints would be subject to this uncertainty. Following the work in [82], we will use the observational constraints from Big-Bang-Nucleosynthesis (BBN) to determine the behavior of the scalar field at matter-radiation equality ($Z \sim 3600$), which we will use as our "initial" point in time for our numerical integrations.

Consider an era in which the universe is radiation dominated, as was the case in the early universe after inflation, when $a \sim 10^{-5}$. In this case we can neglect the energy density contributions from matter and dark energy and write Eqs. (2.28)–(2.31) as simply

$$\frac{2}{3-\varphi'^2}\varphi'' + \frac{2}{3}\varphi' = 0 \ , \tag{2.40}$$

where we have divided out the common energy density terms. Notice that the coupling function $\alpha(\varphi)$ does not appear in this equation, meaning that the scalar field evolution during a purely radiation dominated universe will always be the same, regardless of the coupling function of the theory. Equation (2.40) has a solution of the form (following the notation in Refs. [40, 55])

$$\varphi(\tau) = \varphi_r - \sqrt{3}\ln\left[Ke^{-\tau} + (1 + K^2e^{-2\tau})^{1/2}\right] \ , \tag{2.41}$$

where

$$K = \frac{\varphi_i'\sqrt{3}}{\sqrt{1-\varphi_i'^2/3}} \ , \tag{2.42}$$

with φ_r a constant and φ_i' the scalar velocity upon exiting inflation. The only necessary assumption that we must make here is that the scalar velocity not be very close to its limiting value of $\sqrt{3}$. This assumption is valid because if the scalar velocity ever does reach $\sqrt{3}$ then all dynamics of the evolution are removed, which can be seen from Eq. (2.28). When $\varphi' = \sqrt{3}$ the only solution to Eq. (2.28) is one in which the field grows linearly in time, which certainly violates Solar System constraints today since the right-hand side of Eq. (2.14) would asymptote to two. Thus, we can conclude that $\varphi' < \sqrt{3}$ for *all times* in the past and from Eq. (2.41) we can conclude that $\varphi'(\tau)$ is exponentially damped to zero during the radiation domination era.

To constrain the initial value of the scalar field we use BBN constraints on the gravitational constant. The speed-up factor $\xi_{\text{ BBN}} := H/H_{GR}$ quantifies any differences between the actual Hubble parameter H and the the Hubble parameter predicted by GR, H_{GR}; these differences are caused by deviations from the standard gravitational constant. The observed Hubble parameter can be derived from Eq. (2.17) with $\dot{\varphi} = 0$ (as we have just argued to be true immediately after the radiation era), and is given by $H = (8\pi/3)GA_R^2\epsilon_R$ where ϵ_R and A_R are the Jordan-frame energy density and conformal factor, respectively, evaluated at the time of BBN. The expansion rate predicted in GR takes the form $H_{GR}^2 = (8\pi/3)G_N\epsilon_R$, with G_N given in Eq. (2.13) with $\alpha_0 = 0$. The speed-up factor then becomes

$$\xi_{\text{ BBN}} = \left(\frac{H}{H_{GR}}\right) = \left(\frac{GA_R^2}{G_N}\right)^{1/2} = \frac{1}{\sqrt{1+\alpha_0^2}}\frac{A_R}{A_0}\ , \tag{2.43}$$

where the R and 0 subscripts indicate values at the end of the radiation era (or at the time of BBN more specifically) and today respectively.

Observational bounds on the abundances of Helium place constraints on the expansion rate of the universe [56, 57, 59], which then implies that

$$|1 - \xi_{\text{ BBN}}| \leq \frac{1}{8}\ , \tag{2.44}$$

which is a one σ constraint. On the other hand, Solar System tests restrict $\alpha_0^2 \sim 10^{-5}$ which means that to a good approximation we can neglect its contributions in

Eq. (2.43) and write $\xi_{\,\mathrm{BBN}} \sim A_{R}/A_0$. A constraint on A_{R} can be placed through Eq. (2.44), giving

$$\left|1 - \frac{A_{R}}{A_0}\right| \leq \frac{1}{8} \ . \tag{2.45}$$

Saturating this constraint gives $A_{R}/A_0 = 7/8$ or $A_{R}/A_0 = 9/8$.

From here the particle analogy can be used to understand what exactly this constraint tells us. Relating the constraint on the conformal factor A to the conformal coupling potential V_α via Eq. (2.5) one finds

$$V_{\alpha,0} + \ln(7/8) \ \leq \ V_{\alpha,R} \ \leq \ V_{\alpha,0} + \ln(9/8) \ . \tag{2.46}$$

This tells us that the scalar field can, at most, be $\ln(9/8)$ higher in the potential than where it is today or $\ln(7/8)$ lower. However, both conformal potentials we consider here, Eqs. (2.33) and (2.37), have a global minimum which the scalar field *must* be near to today in order to satisfy the Cassini bound. Such a condition means the the scalar field cannot be lower in the potential than it is today and therefore only $V_{\alpha,R} \leq \ln(9/8)$ is a valid constraint (because $V_{\alpha,0} \approx 0$). For our calculations we will use

$$V_{\alpha,R} = \zeta \ln(9/8) \ , \tag{2.47}$$

where ζ is a parameter that ranges from 0 to 1 and will scale the BBN constraint to allow us to sample the full range of possible initial conditions.

Now we must apply the BBN constraint in Eq. (2.47) to the conformal coupling potentials we consider in this paper. By equating Eq. (2.33) and Eq. (2.47) we find the initial conditions for the exponential STT to be

$$\varphi_{R,\text{ DEF}} = \sqrt{\frac{2}{\beta}\zeta \ln\left(\frac{9}{8}\right)} \ , \tag{2.48}$$

$$\varphi'_{R,\text{ DEF}} = 0 \ . \tag{2.49}$$

Likewise, in the hyperbolic case we have

$$\varphi_{R,\text{ hyp}} = \frac{1}{\sqrt{3\beta}} \cosh^{-1}\left[\left(\frac{9}{8}\right)^{3\beta\zeta}\right] \ , \tag{2.50}$$

$$\varphi'_{R,\text{ hyp}} = 0 \ . \tag{2.51}$$

The constraints on the conformal factor from BBN also provide information on how far in the past BBN occurred in τ-time. Consider the definition $d\tau = H_* dt_*$ and integrate it to get $\tau = \ln a_*$. Transformation back to the Jordan-frame scale factor via $a = A(\varphi)a_*$ gives

$$\tau = \ln\left(\frac{1}{1+Z}\right) - \ln(A) \ , \tag{2.52}$$

where Z is the Jordan-frame redshift related to the Jordan-frame scale factor through $a = 1/(1+Z)$. Because we set $a = 1$ today, the value of τ today must be zero, i.e. $\tau_0 = 0$. Finding the difference in τ-time between now and when BBN occurred is simply $\tau_0 - \tau_R$, or

$$\tau_R = \ln\left(\frac{1}{1+Z_R}\right) - \zeta \ln\left(\frac{A_R}{A_0}\right) \ , \tag{2.53}$$

where we have made use of the fact that the redshift today is zero. Notice that the ratio A_R/A_0 is the same ratio that is constrained from BBN, and thus $A_R/A_0 \leq 9/8$, which is valid for all values of β. Therefore, using $Z_R = 3600$ and $\zeta = 1$, one finds that BBN occurred at most $\tau = \tau_R \sim -8.306$. The value of τ_R determined in Eq. (2.53) with $Z_R = 3600$ and a given ζ will mark the initial time of our numerical calculations.

2.3.3 Exponential Theory

We study the cosmological evolution of the scalar field in detail and place bounds on β. We start by considering the $\zeta = 1$ case, i.e. saturating the BBN constraints on the speed-up factor, to understand the nature of the evolution for $1 < \beta < 1000$. From there, we relax this assumption on ζ and allow $0 < \zeta < 1$, and we use these results to place bounds on β by avoiding fine-tuning scenarios. In order to avoid confusion, we point out that, in general, Solar System constraints on $\gamma_{\rm PPN}$ and $\beta_{\rm PPN}$ place relatively independent constraints on the value of β. For completeness, we present both results but in the end our conclusions will be based off of the PPN parameter that places the tightest constraints on β; in every case that we study, we find that $\beta_{\rm PPN}$ consistently places the tightest constraints.[1]

2.3.3.1 Scalar-Field Evolution

We solve Eq. (2.28) numerically from the end of the radiation dominated era ($Z \sim 3600$) to the present day. Describing the energy density of the universe as a piecewise function in τ-time would only require one to consider a single energy component of the universe at a time and thus only keep a single term in Eqs. (2.29)–(2.31)(this leads to a rather simple analytic solution for the scalar field [40, 54, 55, 82]). Treating the energy densities in this manner, however, forces sharp transitions between different cosmological eras (i.e. from matter domination to dark energy domination). To avoid any sharp transition and ensure a smooth evolution, we simply consider all energy components of the universe for all time and evolve the full form of Eqs. (2.28)–(2.31) numerically.

The left panel of Fig. 2.3 shows the evolution of $1 - \gamma_{\rm PPN}$ in the exponential

[1] Technically, constraints on $\dot{G}_N/G_N$, as appearing in Eq. (2.13), can also constrain these theories because the oscillating scalar field induces an oscillating value of G_N. However, we find that these constraints are insignificant when compared to $\gamma_{\rm PPN}$ and $\beta_{\rm PPN}$ in the range of parameter space that we explore.

theory for the entire integration time and three different values of $\beta > 0$. A general

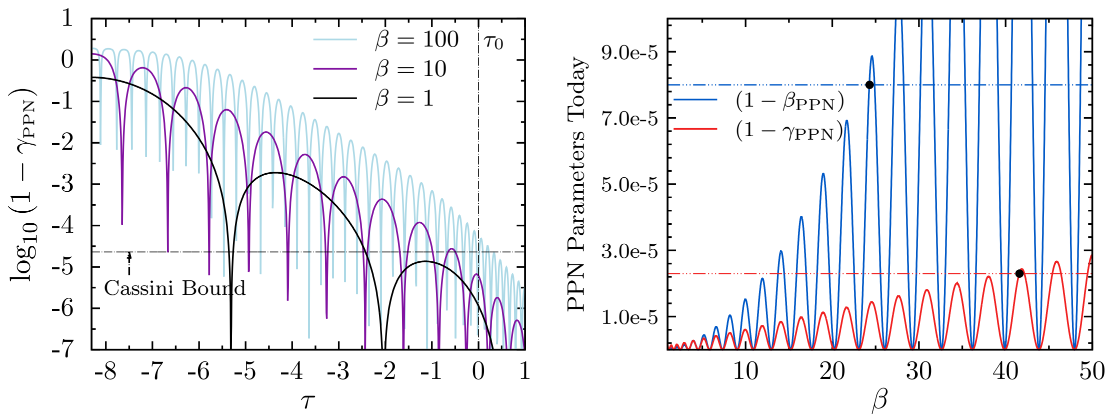

Figure 2.3: **Left:** $1 - \gamma_{\mathrm{PPN}}$ evaluated during the evolution of the scalar field, with $\zeta = 1$ here, to show that an increase in β makes it harder to satisfy the Cassini bound today at $\tau_0 = 0$. The dips here physically go to zero but due to finite numerical precision this is not reflected here. **Right:** $1 - \gamma_{\mathrm{PPN}}$ (red) and $1 - \beta_{\mathrm{PPN}}$ (blue) evaluated today at $\tau_0 = 0$ for a range of β.

feature of the evolution regardless of β is that there are oscillations inside of a decaying envelope, which should not come as a surprise. The scalar field starts at some height in the potential and oscillates about the minimum. Because there is a damping term in the evolution equation, the amplitude of the oscillations must decrease in time. The dips in this plot, which go to zero, are points when the scalar field passes through the minimum of the potential, i.e. when $\alpha(\varphi) = 0$, and the peaks correspond to turning points in the evolution where φ' instantaneously vanishes.

There are a few features of note that are present for different values of β. As β increases, the period of oscillations about the minimum becomes smaller and therefore the motion is more rapid. This is primarily due the steepness of the corresponding potential, i.e. when β is large the potential is steep and narrow, allowing the velocity to be large. This accounts for two features of the evolution: 1) the period of oscillation is shorter and 2) the damping is weaker so the decay is slower in τ-time. The first point above is obvious: starting from a higher point in the potential means there is more "potential energy", which converts to "kinetic energy", leading to a faster velocity and therefore faster oscillations, but the second point may seem counterintuitive. Recalling Eq. (2.28), as φ' becomes larger the term $3-\varphi'^2$ becomes smaller, meaning that the damping term proportional to φ' alone holds less significance during the evolution. This velocity-dependent mass term is what is responsible for the decreased damping at the beginning of the evolution as β increases.

A final feature of the evolution worth noting is the different decay rates that occur in the left panel of Fig. 2.3 (most apparent for $\beta = 100$). One would expect to see different decay rates for different intervals of τ during the evolution because damping is determined by the value of C_2 in Eq. (2.30). As time passes, the dominant energy density of the universe also changes, which causes C_2 to be dominated by that energy and results in a distinct decay rate. Before $\tau = -6$ the effects of both radiation and matter are important, until about $\tau = -1$ matter seems to completely dominate the damping, and for $\tau \gtrsim -0.5$ the effect of dark energy becomes dominant causing the fastest decay. Although we do not show it explicitly, similar conclusions can be drawn from the behavior of $\beta_{\,\mathrm{PPN}}$ throughout the evolution of the scalar field.

The right panel of Fig. 2.3 shows the value of $|1-\gamma_{\,\mathrm{PPN}}|$ (red) and $|1-\beta_{\,\mathrm{PPN}}|$ (blue) today for a subset of β that we considered. As one may expect from the previous results, as β becomes larger the damping becomes weaker and as a result the field may not settle to the minimum of the potential by today. There are, however, periodic values of β that do allow for Solar System tests to be passed even when β is large. These values of β lead to an evolution where the scalar field just happens to be passing by the minimum of the potential today and thus the Solar System bounds are satisfied. However, as time continues to progress the scalar field will leave the minimum of the potential in the future and may eventually fail to satisfy Solar System constraints. Such an outcome becomes unavoidable for $\beta \gtrsim 30$.

The apparent linear β dependence of $(1-\gamma_{\,\mathrm{PPN}})_{\varphi 0}$ can be explained by an approximate analytic solution to Eq. (2.28). For simplicity, consider an era that is dominated by matter and assume $\varphi' \ll \sqrt{3}$ such that the scalar-field evolution can be approximated by

$$\frac{2}{3}\varphi'' + \varphi' = -\beta\varphi \ , \tag{2.54}$$

which is a classical damped harmonic oscillator. With the initial conditions in Eqs. (2.48)-(2.49), with $\zeta = 1$, the solution becomes

$$\varphi(\tau) = \varphi_{R}\, e^{-T(\tau)} \left[\cos(B\,T(\tau)) + \frac{\sin(B\,T(\tau))}{B}\right] \tag{2.55}$$

where $T(\tau) = 3(\tau + \tau_R)/4$, $B = \sqrt{(8/3)\beta - 1}$, and $\tau_R = -8.306$. Note that this solution is valid only for the under-damped case such that $\beta > 3/8$, which is precisely the region of parameter space we are interested in. For a more detailed discussion of the critically- and over-damped cases see Ref. [55]. Because $\alpha^2 = \beta^2\varphi^2$ is small today (it is of the same order as $1-\gamma_{\,\mathrm{PPN}}$ in most cases) we can approximate Eq. (2.14) as

$$1 - \gamma_{\,\mathrm{PPN}} = 2\alpha^2 = 2\beta^2\varphi^2 \ . \tag{2.56}$$

Evaluating φ in Eq. (2.55) today and averaging over the small oscillations to extract the secular terms, one finds

$$(1-\gamma_{\,\mathrm{PPN}})_{\varphi 0} \propto \beta^2\varphi_R^2 \propto \beta \ , \tag{2.57}$$

using Eq. (2.48) for φ_R. In other words, the overall growth of $1-\gamma_{\,\mathrm{PPN}}$ today is linear in β, as we see in the right panel of Fig. 2.3. Likewise, $1-\beta_{\,\mathrm{PPN}}$ has an extra factor of

β in the numerator, making it quadratic, and thus grows even faster than $1-\gamma_{\,\mathrm{PPN}}$, leading to a stronger violation of Solar System constraints for large β.

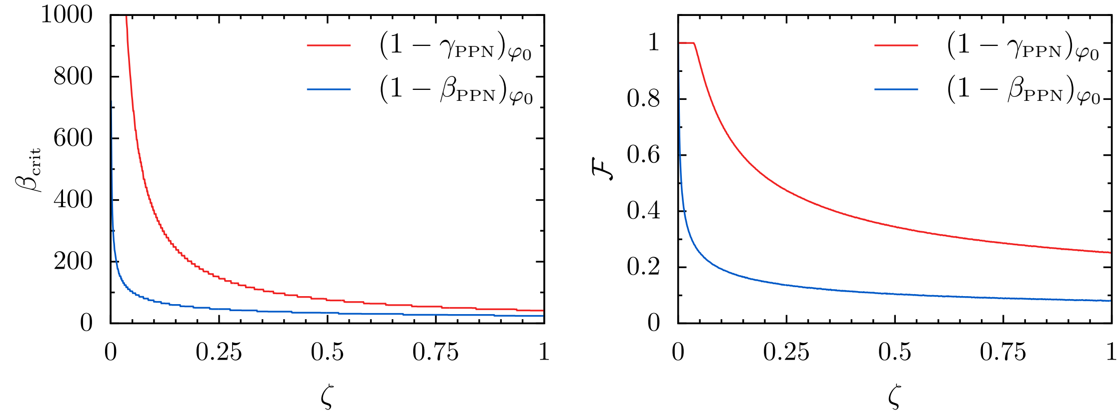

Figure 2.4: **Left:** Value of $\beta_{\,\mathrm{crit}}$, as defined in the text, for every value of ζ which corresponds to the the entire range of possible initial scalar positions at the time of BBN. **Right:** The total fraction out of all β values sampled $(1 < \beta < 1000)$ that allow Solar System tests to be passed at $\tau = 0$, as a function of the initial conditions determined by ζ. The general trend of the top right panel tells us that this fraction would continue to decrease as we increase the upper bound of our sample size.

2.3.3.2 Constraints on β We now turn our attention to placing quantitative constraints on β from the results of our numerical calculations. Because of the oscillatory nature of the scalar field, there are different types of constraints that can be placed, which differ in their generality:

- $\beta_{\,\mathrm{crit}}$, where all $\beta < \beta_{\,\mathrm{crit}}$ pass Solar System at the present time but not necessarily at all future times,
- $\beta_{\,\mathrm{fail}}$, where all $\beta < \beta_{\,\mathrm{fail}}$ pass Solar System tests at the present time, and generically also at all future times (this is the method used in Ref. [82]),
- $\beta_{\,\mathrm{all\ fail}}$, where *all* $\beta > \beta_{\,\mathrm{all\ fail}}$ will generically fail Solar System tests either today or at some future time.

In general, one finds that $\beta_{\text{all fail}} > \beta_{\text{crit}} > \beta_{\text{fail}}$ and all of these possibilities lead to constraints that are consistent with each other, but for completeness we present all of them in our analysis. Furthermore, we will show below that these constraints are relatively insensitive to the value of ζ, i.e. the initial conditions chosen at the time of BBN, provided that they are not finely tuned to be close to $\zeta = 0$ ($\varphi = 0$).

The discussion in the previous section specifically applied to the $\zeta = 1$ case only, so now we will focus on the consequences of allowing $0 < \zeta < 1$. For every set of initial conditions determined by ζ in Eqs. (2.48)-(2.51) there exists a critical value of β, denoted by β_{crit}, for which all $\beta < \beta_{\text{crit}}$ lead to a value of φ_0 that is consistent with Solar System observations. In general, there is a β_{crit} associated with each PPN parameter, corresponding to the intersections of the constraints (red/blue horizontal lines) and corresponding curves (red/blue curves) in the right panel of Fig. 2.3. The smaller of these two will be the value of β_{crit} reported in this paper, since it places the tightest constraint. For $\zeta = 1$, one can see from the right panel of Fig. 2.3 that $\beta_{\text{crit}} = 24$, corresponding to the black point where the blue horizontal line intersects the curve for $|1 - \beta_{\text{PPN}}|$. The left panel of Fig. 2.4 shows the behavior[2] of β_{crit} for all values of ζ, associated with both γ_{PPN} and β_{PPN}. Small values of ζ lead to large values of β_{crit}, such that $\beta_{\text{crit}} \to \infty$ in the limit that $\zeta \to 0$ for both PPN parameters. This should indeed be the case because when $\zeta \to 0$ the scalar field is sitting at the minimum of the potential at the time of BBN. If the field is at the minimum in the past, with no velocity, then it will certainly be at the minimum today, and thus it will satisfy Solar System tests with ease. Our results show that regardless of the value of ζ, current constraints on β_{PPN} place the tightest constraints on the value of β_{crit}. The values of β_{fail} and $\beta_{\text{all fail}}$ are determined in a similar fashion and have a very

[2]The step-like nature of β_{crit} is related to the oscillatory behavior of the scalar field shown in Fig. 2.3, and it is not an artifact of numerical resolution.

similar dependence on ζ as β_{crit} does. We list all of these values in Table 2.2.

Ultimately we want to place bounds on values of β and use those in our NS calculations, but considering $\zeta \sim 0$ does not restrict β at all according to the arguments presented above. We therefore restrict our calculations to $\zeta > 0.05$ as a way of avoiding a large amount of fine-tuning; the choice of 0.05 as the lower bound is because in a randomly selected sample of ζ there is only a 5% chance that $\zeta < 0.05$ would be selected. In another effort to avoid a finely tuned bound, we take a random distribution of ζ and select the median of the resulting distribution of β_{crit} to represent a measure of the "most probable" value of β_{crit}, denoted by $\beta_{\text{crit,med}}$, if ζ were chosen randomly. We find that in the exponential theory this median value is $\beta_{\text{crit,med}} \sim 34$.

The quantities β_{crit} and $\beta_{\text{crit,med}}$ still do not necessarily tell the entire story of which values of β should be considered feasible because, as Fig. 2.3 shows, there is a (small) subset of $\beta > \beta_{\text{crit}}$ (or $\beta > \beta_{\text{crit,med}}$ in the case of more finely-tuned initial conditions) that do indeed pass Solar System tests today. To quantify this, we define

$$\mathcal{F} = \frac{\#\text{ of }\beta\text{ that pass Solar System tests}}{\#\text{ of }\beta\text{ sampled}} \tag{2.58}$$

and present these results as a function of ζ in the right panel of Fig. 2.4. The scalar $\mathcal{F}$ depends on the sampling of β and ζ, and thus, on their prior probability distribution. We here assume that all β and ζ are equally likely and choose flat distributions for their sampling, which is equivalent to discretizing the β and ζ spaces linearly; we are not aware of any theoretical argument to prefer any particular value of these couplings over others[3]. As a reminder, $\zeta = 1$ corresponds to the solutions displayed

[3] If a theoretical mechanism is devised in the future that suggests, for example, that ζ must be close to zero at the time of BBN, then the scalar $\mathcal{F}$ can be recalculated and the conclusions found here revised.

in Fig. 2.3 where $\beta_{\text{crit}} \sim 24$, as determined by constraints on β_{PPN}, and in this case $\mathcal{F}$ is only slightly over 8%. We point out that for this calculation we sample both β and ζ linearly. This means that there is roughly an 8% chance that a randomly selected value of β between 1 and 1000 will allow Solar System tests to be passed. Interestingly, $\mathcal{F}$ changes very slowly with ζ, such that even for very small values of ζ, i.e. for $\zeta > 0.05$, $\mathcal{F}$ is still $\lesssim 25\%$.

The above results may seem to indicate that there is a decent number of possible values of β above the critical or the median one for which Solar System tests are passed, provided that we sample larger values of β, but this conclusion would be premature. We have here greatly narrowed the scope of our study by only focusing on $\beta < 1000$, but in principle, β could take on any value between zero and infinity. Considering values of $\beta > 1000$, say up to $\beta = 10^6$ for definiteness, would lead to two consequences: (i) the # of β that pass Solar System tests would increase slightly, and (ii) the # of β sampled would increase dramatically. Because of these effects, the relative fraction $\mathcal{F}$ would decreases significantly leaving a very small probability of passing Solar System tests without a very fine-tuned choice of β.

Let us wrap up this subsection by summarizing the main results we have obtained, all of which can be inferred from Fig. 2.3 and Fig. 2.4. For the $\zeta = 1$ case, we see that for all $\beta \lesssim \beta_{\text{crit}} \sim 24$ the scalar field will evolve such that Solar System tests are passed today. For $\beta \gtrsim \beta_{\text{crit}} \sim 24$ the solutions for which Solar System tests are passed is periodic in nature, but in general they do not pass Solar System tests. Moreover, the ones that do pass Solar System tests today do not generically do so in the future. In fact, all $\beta \gtrsim 29$ that happen to pass Solar System tests today will eventually fail them in the future. The monotonic growths seen in the right panel of Fig. 2.3 imply that this trend will continue as β increases and there will never be a turnover such that larger ranges of β will generally pass Solar System tests. Such

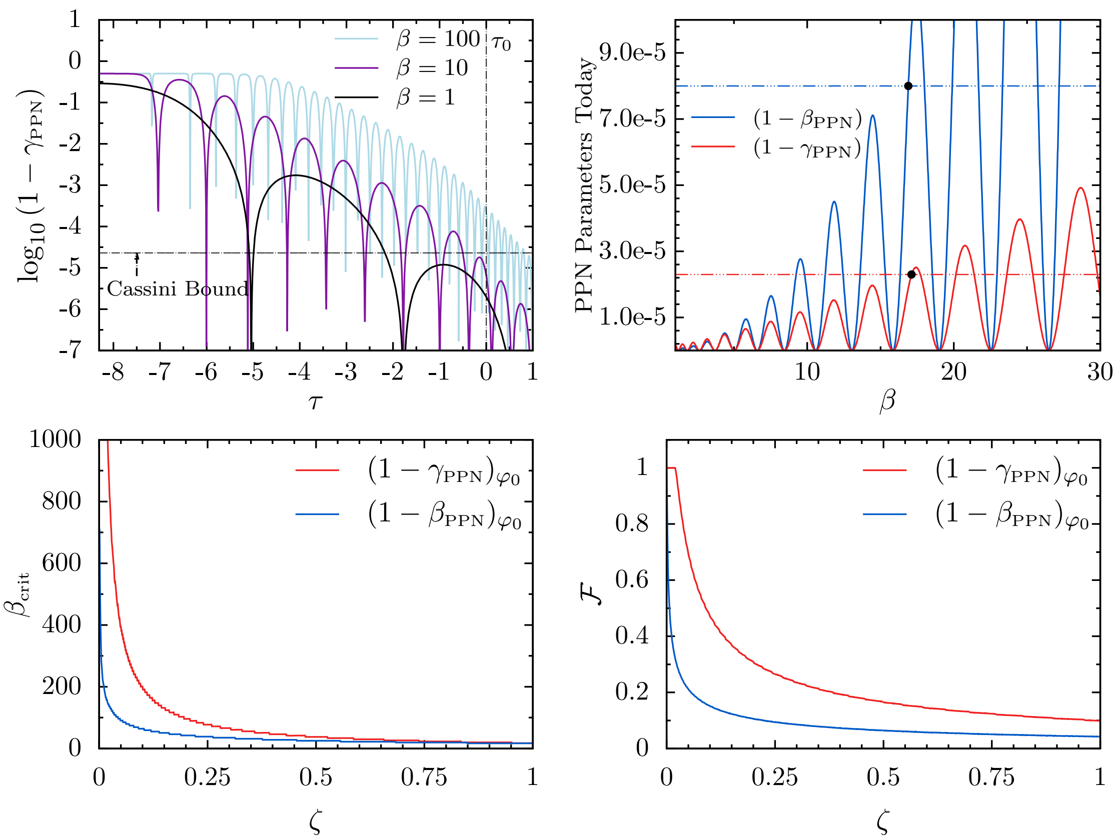

Figure 2.5: Same as Fig. 2.3 and 2.4 but for the hyperbolic class of STTs.

conclusions turn out to be valid for all values of $\zeta > 0$. A summary of these results can be found in Table 2.2.

2.3.4 Hyperbolic Theory

We now repeat the analysis described above but using the hyperbolic theory instead of the exponential one. The numerical results for the evolution of the scalar field are displayed in Fig. 2.5. There are several similar features in the scalar field evolution to what we found in the exponential case, as well as a few features exclusive to hyperbolic coupling that we discuss below.

The upper panels of Fig. 2.5 show the evolution of the scalar field for $\zeta = 1$. As β increases, there is a distinct increase in the frequency of oscillation about the minimum of the potential. In the exponential theory, this was attributed to the fact that the potential became steeper with increasing β, generating steeper gradients and therefore larger accelerations. The potential gradient $\alpha(\varphi)$ in the hyperbolic theory exponentially asymptotes to a value of $1/\sqrt{3}$ for large values of $\beta\varphi$, cf. Fig. 2.2. This behavior limits the maximum value of $1-\gamma_{\,\text{PPN}}$ via Eq. (2.14), and also restricts the coupling between the scalar field and matter, effectively placing an upper limit on the sourcing term of the oscillator. As a result, the scalar field does not gain as much velocity as quickly here, and therefore, it spends more time away from the minimum of the potential initially, leading to minimal amounts of oscillatory motion and the saturation of $1-\gamma_{\,\text{PPN}}$ occurring in Fig. 2.5 at early times. Again, while we do not show the time evolution of $1-\beta_{\,\text{PPN}}$, its behavior is similar and ultimately leads to identical qualitative conclusions.

Once enough time has passed and the scalar field has been damped enough to remain near the minimum of the potential, it finally begins to behave as in the exponential theory, but this has a significant effect on whether or not Solar System tests are passed today. Because $\alpha(\varphi)$ remains at its limiting value for a substantial amount of time, which is evident for example when $\beta > 10$, the friction terms do not have a significant effect until later in the evolution, making it harder for the field to decay to a small enough value in order for either PPN parameter to be consistent with Solar System constraints. This is made clear in the top, right panel of Fig. 2.5 where we see that $\beta_{\,\text{crit}} \sim 17$, a value smaller than that found in the exponential case. We also see that it becomes even more difficult to pass Solar System tests for large β, i.e. the regions falling below the Solar System bounds become smaller the larger β becomes. We also find that all $\beta \gtrsim 19$ that allow Solar System tests to be passed today will ultimately fail to do so at some point in the future, if Solar System tests continue to show that the constraints on PPN parameters are time-independent.

Similar to the analysis in the previous section we can study what effect the initial conditions, parameterized via ζ, have on the scalar-field evolution, with the bottom panels of Fig. 2.5 showing β_{crit} and $\mathcal{F}$ as functions of ζ. The overall behavior of β_{crit} is similar to that in the exponential theory but it is always significantly lower. Just like we did previously, we can quantify a median value of β_{crit} corresponding to the median of the distribution appearing in the bottom, left panel of Fig. 2.5 and we find that $\beta_{\text{crit,med}} \sim 25$ for the hyperbolic theory. The fraction $\mathcal{F}$ is also smaller and is only around half of what it is in the exponential theory. As we argued before, this fraction will only decrease with an increased sample size of β, and to avoid fine-tuning scenarios one should try to avoid considering value of β larger than β_{crit} that satisfy Solar System tests today because they just happen to have $\alpha(\varphi) = 0$ today. Table 2.2 contains a summary of all bounds on β from these calculations.

2.3.5 Constraints on β: Summary

Let us now briefly summarize our conclusions regarding the bounds we can place on β given Solar System observations and their implications. First, recall that we focused on the range $1 < \beta < 1000$ and $0 < \zeta < 1$, and that ζ close enough to zero, e.g. $\zeta < 0.05$, corresponds to a finely tuned choice of initial conditions, i.e. choosing $\varphi \sim 0$ at the time of BBN. Table 2.2 shows representative values of the bounds on β from the three choices discussed at the beginning of Sec. 2.3.3, for both PPN parameters in both the exponential and hyperbolic theories. Notice that in every case displayed, the bounds placed from β_{PPN} are all tighter than the ones placed by γ_{PPN}. This is consistent with the structure of the PPN constraints because β_{PPN} takes the curvature of the conformal potential into account, while γ_{PPN} does not. For any $\beta \gtrsim 10$ the curvature of the potential becomes significant near the minimum of the potential, in turn causing larger present day values of $|1 - \beta_{\text{PPN}}|$ which are

		Exponential		Hyperbolic	
		$(1-\gamma_{\text{PPN}})_{\varphi_0}$	$(1-\beta_{\text{PPN}})_{\varphi_0}$	$(1-\gamma_{\text{PPN}})_{\varphi_0}$	$(1-\beta_{\text{PPN}})_{\varphi_0}$
$\zeta = 0.05$	β_{crit}	722	104	395	91
	β_{fail}	722	103	394	91
	$\beta_{\text{all fail}}$	811	113	431	100
	$\mathcal{F}$	93%	25%	69%	21%
$\zeta = 1$	β_{crit}	42	24	17	17
	β_{fail}	41	24	17	17
	$\beta_{\text{all fail}}$	60	29	25	19
	$\mathcal{F}$	25%	8%	10%	4%
Median Values	β_{crit}	76	34	38	25
	$\beta_{\text{all fail}}$	99	40	49	27
$\beta_{\text{crit}} = 50$		$\zeta < 0.843$	$\zeta < 0.229$	$\zeta < 0.393$	$\zeta < 0.162$
		$\varphi_R < 0.063$	$\varphi_R < 0.032$	$\varphi_R < 0.088$	$\varphi_R < 0.041$
$\beta_{\text{crit}} = 100$		$\zeta < 0.376$	$\zeta < 0.051$	$\zeta < 0.196$	$\zeta < 0.043$
		$\varphi_R < 0.029$	$\varphi_R < 0.011$	$\varphi_R < 0.044$	$\varphi_R < 0.013$

Table 2.2: Bounds on β using different initial conditions (determined by ζ) and both PPN parameters (γ_{PPN} and β_{PPN}) in both the exponential and hyperbolic theories. The parameters β_{crit}, β_{fail}, $\beta_{\text{all fail}}$, and $\mathcal{F}$ are those defined in the text. The first row shows data for lowest value of ζ we consider, i.e. $\zeta = 0.05$. The second row shows the data for saturating BBN constraints ($\zeta = 1$). We present the median values of certain parameters in the third row, given by the definitions defined in the text. The last two rows illustrate the amount of fine tuning of ζ, or alternatively φ_R, that would be necessary to force β_{crit} to either 50 or 100.

inconsistent with Solar System observations. We therefore focus explicitly on the bounds placed by β_{PPN}.

Let us first focus on the $\zeta = 1$ portion of Table 2.2 and recall the definitions of β_{crit}, β_{fail}, and $\beta_{\text{all fail}}$ presented in Section 2.3.3. For both theories, β_{crit}, β_{fail}, and $\beta_{\text{all fail}}$ all place nearly identical upper bounds on β. Furthermore, $\mathcal{F}$ is 8% and 4% for the exponential and hyperbolic theory respectively. Such small values of $\mathcal{F}$ suggest that it is extremely hard to randomly select a value of $\beta > \beta_{\text{crit}}$ that will be consistent with Solar System constraints, and in fact this value only becomes smaller by considering values of $\beta > 1000$. This suggest that one would have to very precisely select a $\beta > \beta_{\,\mathrm{crit}}$ if one wants to remain consistent with Solar System observations, leading to a fine-tuning problem. Therefore, in order to naturally avoid this, one should only consider $\beta < \{\beta_{\,\mathrm{crit}}, \beta_{\,\mathrm{fail}}, \beta_{\,\mathrm{all\ fail}}\}$, all of which are ~ 20 in both theories.

Let us now discuss the fine-tuning issue in a bit more detail, by focusing on the rest of Table 2.2. First, notice that considering $\zeta = 0.05$ brings the upper bounds on β up to ~ 100 and $\mathcal{F}$ up to $\sim 25\%$ for both theories. While this increases the viable range of β, one should remember that forcing ζ to be small is equivalent to forcing $\varphi \to 0$ at the time of BBN, resulting in a carefully selected set of initial conditions. To avoid this fine tuning issue, we calculated the median value of the distribution of $\beta_{\,\mathrm{crit}}$ and $\beta_{\,\mathrm{all\ fail}}$, which represent the β's that would be *likely* to pass Solar System tests if ζ were chosen randomly (these are located in the rows label "Median Values" in Table. 2.2). Ultimately, we see that this type of analysis only slightly relaxes the bounds on β relative to what is found when $\zeta = 1$, meaning that for a large subset of $0 < \zeta < 1$ the bounds on β are around ~ 40 and ~ 25 for the exponential and hyperbolic theory respectively.

Lastly, let us quantify the amount of fine-tuning that would be needed in order to raise $\beta_{\,\mathrm{crit}}$ to a region containing non-zero scalar charge in Fig. 2.1. This information is shown in the bottom two rows of Table 2.2, but let us here only focus on the hyperbolic theory since we only find stable NSs with non-zero scalar charge there. In order to raise $\beta_{\,\mathrm{crit}}$ to 50 (100), ζ would have to be smaller than 0.162 (0.043). To achieve this one needs to demand that the scalar field be close to the minimum of the conformal potential and therefore be very similar to GR on cosmological scales. While allowing STTs to reduce to GR ($\zeta \sim 0$) on these scales would allow Solar System tests to be passed it is effectively a set of measure zero. For the reasons above, we conclude that the most natural way to evade Solar System constraints today is to consider bounds on β corresponding to $\zeta = 1$, and we note that only under a carefully selected set on initial conditions at BBN and β is it possible to pass Solar System tests otherwise.

2.4 Neutron Stars and Scalarization

In this section we describe NSs in STTs and introduce the basics of scalarization. To reiterate the argument made in Ref. [82], we only study isolated NSs here because theories that do not allow for spontaneous scalarization are also not likely to allow for dynamical/induced scalarization. We first present the equations of structure and then describe the piecewise polytropic EoSs we use to model realistic tabulated EoSs [83]. Finally, once the framework for the numerics has been laid out we present results for NSs in the exponential theory and the hyperbolic theory, first for $\beta < 0$ and then for $\beta > 0$.

For our study, we focus explicitly on isolated, static, and spherically symmetric spacetimes, which in general can be described by the Einstein-frame line element

$$ds_*^2 = -e^{\nu(r_*)} dt_*^2 + \frac{dr_*^2}{1 - 2\mu(r_*)/r_*} + r_*^2 d\Omega_*^2 \,, \tag{2.59}$$

where ν and μ are only functions of the Einstein-frame coordinate radius r_* and $d\Omega_*^2$ is the line element on the two-sphere. To a good approximation, the matter inside cold NSs can be represented as a perfect fluid and therefore we use the form of the matter stress-energy tensor given in Eq. (2.12). Applying conservation of stress energy in the Jordan frame, $\nabla_\nu T^{\mu\nu} = 0$, along with the line element and perfect fluid assumptions above yield a set of first order differential equations governing the structure of the

NSs [37, 38]

$$\mu' = 4\pi G r_*^2 A^4(\varphi)\epsilon + \frac{1}{2} r_*(r_* - 2\mu)\psi^2 , \tag{2.60}$$

$$\nu' = r_*\psi^2 + \frac{1}{r_*(r_* - 2\mu)}\left[2\mu + 8\pi G r_*^3 A^4(\varphi) p\right] , \tag{2.61}$$

$$\varphi' = \psi , \tag{2.62}$$

$$\psi' = \frac{4\pi G r A^4(\varphi)}{(r_* - 2\mu)}\left[\alpha(\varphi)(\epsilon - 3p) + r_*\psi(\epsilon - p)\right] - 2\psi\frac{(1 - \mu/r_*)}{(r_* - 2\mu)} , \tag{2.63}$$

$$p' = -(\epsilon + p)\left(\nu'/2 + \alpha(\varphi)\psi\right) , \tag{2.64}$$

where primes denote derivatives with respect to r_*, and all occurrences of p and ϵ are explicitly in the Jordan frame. [4]

EoS	$\log(p_1)$	Γ_1	Γ_2	Γ_3	$\rho_{\rm crit}/\rho_0$	$\beta_{\rm min}$	$\beta_{\rm max}$	$\alpha_{\rm sc,max}$
ENG	34.437	3.514	3.130	3.168	4.544	19.1	26.7	$\sim 1.4\times10^{-3}$
MPA1	34.495	3.446	3.572	2.887	3.683	19.3	27.2	$\sim 1.4\times10^{-3}$
MS1	34.858	3.224	3.033	1.325	3.067	35.6	46.3	$\sim 2.7\times10^{-4}$
MS1b	34.855	3.456	3.011	1.425	3.092	35.8	48.3	$\sim 2.4\times10^{-4}$
SLy	34.384	3.005	2.988	2.851	5.349	30.0	39.3	$\sim 4.2\times10^{-4}$

Table 2.3: Parameters of the piecewise polytropes $\{\log(p_1), \Gamma_1, \Gamma_2, \Gamma_3\}$ from Ref. [83] for the 5 EoSs we use for NS calculations and the values of $(\beta_{min}, \beta_{max}, \alpha_{\rm sc,max})$ found here. For clarity, all $\rho > \rho_{\rm crit}$ allow $T_{\rm mat} > 0$ in the core, β_{min} is the lowest value of β allowing for stable scalarized solutions, β_{max} is where the maximal stable scalar charge occurs, and $\alpha_{\rm sc,max}$ is the maximal scalar charge, corresponding to the peak values of the curves in Fig. 2.1.

To close the system of equations we need to prescribe an EoS. We use the piecewise polytropic EoSs studied in Ref. [83] in which the authors developed a four

[4] There is a missing factor of r_* in the Eq. (2.63) equivalent appearing in Reference [82].

parameter polytopic model that accurately approximates 34 tabulated EoSs. Let us briefly discuss this parameterization of the EoS. In each baryonic density region inside the star $\rho_{i-1} < \rho < \rho_i$ the pressure is given by the standard polytropic form

$$p = K_i \rho^{\Gamma_i} , \tag{2.65}$$

where Γ_i is the adiabatic index of the fluid in that region and K_i is the polytropic constant chosen to ensure continuity at the boundary between density regions. The energy density ϵ appearing in the structure equations is then found by integrating the first law of thermodynamics

$$d\frac{\epsilon}{\rho} = -p\, d\frac{1}{\rho} , \tag{2.66}$$

to find

$$\epsilon = \rho + \frac{p}{\Gamma - 1} . \tag{2.67}$$

We adopt a low-density crust region described by a degenerate relativistic gas with adiabatic constant $\Gamma_0 = 4/3$ and match it to a polytrope with adiabatic index Γ_1. The polytropic constant K_0 for this crust region is determined by forcing the crust to match the SLy EoS at a baryonic density of $\rho_0 = 2.7 \times 10^{14}$ g/cm^3. A different choice of a fixed crust EoS only affects the physical quantities of the system by a few percent. More importantly, scalarization will only occur in the dense regions of the star, which are unaffected by the choice of crust used, so the simple choice we make here will suffice for our study. The boundary between the crust and the next polytropic region will therefore depend on the value of Γ_1. At a fixed baryonic density of $\rho_1 = 10^{14.7}$ g/cm^3 and pressure $p_1 = p(\rho_1)$ the EoS is matched to another polytrope with adiabatic index Γ_2 and constant K_2. Another boundary is set at $\rho_2 = 10^{15}$ g/cm^3 where the EoS is matched yet again to another polytrope with index

Γ_3 and constant K_3. The set of parameters $\{\log(p_1), \Gamma_1, \Gamma_2, \Gamma_3\}$ determines the best fit to tabulated EoSs and were determined in Ref. [83], which we refer the reader to for a more detailed description. Following Ref. [80] we restrict the scope of our investigation to EoSs that allow for a maximum gravitational mass of more than two solar masses and do not violate causality. These constraints leave us with 5 EoSs, whose parameters are listed in Table 2.3 for convenience.

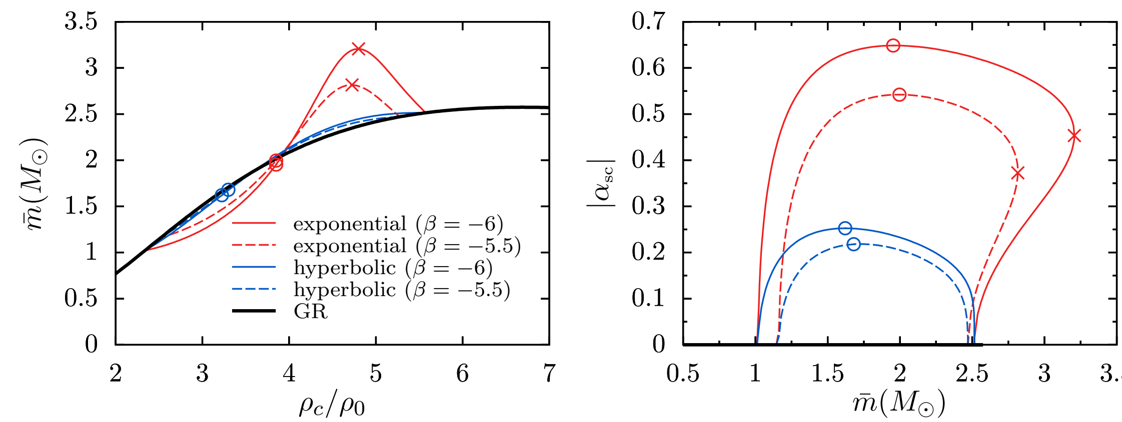

Figure 2.6: **Left:** Baryonic mass of the NS as a function of central baryonic density. Deviations from GR occur above some critical density which depends on β. A more negative β leads to larger deviations from GR, but notice that the exponential theory has more of an effect than the hyperbolic theory does. **Right:** Scalar charge as a function of the total baryonic mass. The "spontaneous" activation of the scalar field occurs at a particular mass, while the dependence on β appears to be independent of the theory. Again we see that the exponential theory causes a larger activation of the scalar field than the hyperbolic theory. The circles in both panels correspond to the solutions that have maximum scalar charge and the crosses indicate the maximum mass solutions, which also mark an instability in these branches of solutions [64, 84].

We numerically solve the system of equations above parameterized by central density ρ_c and coupling constant β. Following the methods employed in Ref. [82] we use `Mathematica`'s default integrator which makes use of an LSODA approach (a variant of the Livermore Solver for Ordinary Differential Equations) [75]. Inside the star the pressure is governed by the piecewise polytropic EoS, while the pressure vanishes outside the star with the boundary where the pressure vanishes marking the surface of the star. We integrate the equations from the center of the star to an effective infinity that is far from the surface of the star, which allows us to determine the metric and the scalar field in the entire spacetime. Far from the star, the scalar field behaves as

$$\varphi = \varphi_\infty + \frac{\omega}{r_*} + \mathcal{O}\left(\frac{1}{r_*^2}\right) , \tag{2.68}$$

where φ_∞ is the asymptotic value of the scalar field determined from cosmology (which we fix to a small value and enforce as a boundary condition) and ω is a constant that is proportional to the scalar charge. We define the scalar charge via

$$\alpha_{\rm sc} = \frac{\omega}{G m_*} , \tag{2.69}$$

where m_* is the Einstein-frame ADM mass of the star and the subscript "sc" is used to distinguish the scalar charge from the conformal coupling $\alpha(\varphi)$. Physically, the scalar charge is a measure of the effective coupling between the scalar field and the star, with a larger value meaning stronger coupling. The scalar charge is then determined by ω which we find by extracting the $1/r$ piece of the external solution of the scalar field.

2.4.1 $\beta < 0$: Standard Spontaneous Scalarization

Choosing a sufficiently negative value of β ($\lesssim -4$ for most EoS) leads to an instability in the star that causes an activation of the scalar field above its background cosmologically-determined value, a process known as spontaneous scalarization [37, 38,42]. In the context of cosmology, however, all massless STTs with $\beta < 0$ generically lead to drastic disagreement with Solar System observations [54, 82], at least for the subset of symmetric, monotonically increasing coupling potentials that we consider here. Thus, the NS solutions presented in this section should be strictly seen as a stepping stone towards giving a better understanding of what will be presented for the $\beta > 0$ cases.

Figure 2.6 shows the results of our numerical calculations using both exponential and hyperbolic couplings for $\beta = -6$ and $\beta = -5.5$ as examples. For these calculations we employ the ENG piecewise polytropic EoS with parameters given in Table 2.3, but it should be noted that the qualitative behavior seen here is general among all EoS that we consider. At low densities, only the GR solution exists and the scalar field remains at its background value. There exists a critical density at which the scalar field begins to "turn on" and produces sudden deviations from GR as can be seen in the left panel of Fig. 2.6. The critical density at which this happens depends on the EoS and the value of β, but as we stated earlier, it is a generic feature among all EoS considered here. Larger central densities eventually lead back to the GR solution and a trivial scalar field profile, just as in the low density case.

A more negative value of β, which in these theories explicitly means a stronger coupling to matter, leads to larger deviations from GR and therefore larger values of scalar charge $\alpha_{\rm sc}$ (cf. the right panel of Fig. 2.6). This is consistent with the idea that scalar charge is the effective coupling between the star and the scalar field. Notice, however, that the exponential theory predicts larger deviations from GR than the hyperbolic theory does (i.e. the charge is roughly three times larger), regardless of what value of β we choose. This can be understood by looking at the first term in square bracket in Eq. (2.63), or more explicitly the fact that $\psi' \propto \alpha(\varphi)$, which provides a type of feedback loop. In the exponential theory, large values of φ produce large values of $\alpha(\varphi)$ relative to the hyperbolic theory, which is obvious from the right panel of Fig. 2.2. Larger values of $\alpha(\varphi)$ thus lead to a larger positive feedback into ψ' and so on, explaining why the exponential theory leads to larger activation of the scalar field for given values of central density.

It is useful to provide an analytic explanation behind this spontaneous activation of the scalar field. In both theories, $\alpha(\varphi) = \beta\varphi + \mathcal{O}(\varphi^2)$ for small values of $\beta\varphi$, which must be true due to the arguments presented in Sec. **??**. Following arguments and notation presented in Refs. [38, 82], consider then the evolution of the scalar field in a weakly gravitating, spherically symmetric system such that $\Box \to \delta_{ij}\nabla_i\nabla_j \to \nabla_r^2$, where ∇_r^2 is the radial part of the Laplacian in spherical coordinates. For simplicity we will assume $T^*_{\rm mat}$ is constant and while weakly gravitating systems would be expected to have $T^*_{\rm mat} < 0$ we allow it to remain arbitrary in the interest of generality. These assumptions reduce the field equation for the scalar field to

$$\nabla_r^2\varphi = -K^2\varphi\,\mathrm{sign}(\beta T^*_{\rm mat}) \; , \tag{2.70}$$

where $K^2 = (\kappa/2)|\beta T^*_{\rm mat}|$ for $r_* < R$ and must vanish outside the star. The solution to this must still obey the physical boundary conditions of the scalar field, i.e. $\varphi(0) = \varphi_c$ and $\varphi'(0) = 0$ to ensure regularity at the center and the solution must be continuous and differentiable at the surface $r_* = R$. When the product $\beta T^*_{\rm mat}$ is positive the solution becomes

$$\varphi = \frac{\varphi_\infty}{\cos(KR)}\frac{\sin(Kr)}{Kr} \; . \tag{2.71}$$

Even when $\varphi_\infty \approx 0$, which we emphasize is the case here, a nontrivial scalar-field solution can arise when $KR \approx \pi/2$. This type of "resonance" between the scalar field and matter explains why spontaneous scalarization occurs in DEF-like theories and why there exist deviations from GR in Fig. 2.6. However, when $\beta T^*_{\rm mat}$ is negative the scalar field is exponentially suppressed to its background value, which can be seen by replacing the trig functions in Eq. (2.71) with their corresponding hyperbolic counterparts. It is then reasonable to expect that only certain ranges of density, which ultimately controls $T^*_{\rm mat}$, will lead to an activation of the scalar field for any given β, and why for relatively small and large central densities we only see the GR solution in Fig. 2.6.

We here focused explicitly on the the sign of $\beta T^*_{\rm mat}$ rather than just β for a reason. Indeed, for the weakly gravitating system used in the example above $T^*_{\rm mat} < 0$ and the sign in Eq. (2.71) would be completely determined by the sign of β. However, cosmological constraints force $\beta > 0$, so unless $T^*_{\rm mat}$ were also positive one would not expect scalarization to occur. This was studied recently in Refs [41, 80, 81] and will be the focus of the next section.

2.4.2 $\beta > 0$: Go Big or Go Home

Studying NSs in STTs with $\beta > 0$ is important because this is the region of parameter space that is consistent with Solar System constraints upon cosmological evolution of the scalar field. Luckily, NSs are extremely dense and there can exist regions near the core where $T^*_{\rm mat}$ is indeed positive, allowing for possible scalarized branches of solutions. Reference [41], however, demonstrated that NSs that scalarize in the exponential theory lead to gravitational collapse. We will start our discussion by summarizing the results presented in Refs. [41, 81] and then present the results of our numerical study of NSs in the hyperbolic theory with $\beta > 0$.

2.4.2.1 Gravitational Collapse in Exponential Theory The instability of the exponential theory can be understood through a linear stability analysis of Eq. (2.8). By allowing $\varphi = \varphi_0 + \delta\varphi$ and keeping terms up to first order one finds

$$\Box_* \, \delta\varphi \; = \; -\frac{\kappa}{2}\beta_0 T^*_{\rm mat} \, \delta\varphi \; , \tag{2.72}$$

where $\beta_0 = (\partial\alpha/\partial\varphi)_{\varphi_0}$ is like the curvature of the coupling potential[5], and the box operator and the stress-energy tensor are those of GR. Reference [41] performed a numerical search for solutions to Eq. (2.72) of the form $\delta\varphi = e^{\Omega t} f(r)$ with a spherically symmetric background, a perfect fluid stress-energy tensor, and a polytropic EoS (in general, the location of the instability regions will depend on the EoS used). The results of this search are presented in Fig. 2 of Ref. [41] and we provide a *rough* schematic drawing of those results in Fig. 2.7.[6] The results of the stability analysis are independent of the theory being studied and only depend on the value of β_0 defined above.

The red/blue regions in Fig. 2.7 correspond to regions that are unstable to scalar field perturbations, which could lead to a non-trivial scalar-field profile inside the star. White regions, on the other hand, are regions in the parameter space where only the GR solution is present and no excitations of the scalar field would be expected inside the star. We mark a line at $\beta = -6$ to clearly show that as central density increases the instability arises but then as density continues to rise the instability eventually turns off. The turn on/off of the instability in the $\beta < 0$ regime is consistent with the results we previously presented in Fig. 2.6 for both theories. Recall that the instability is related to the sign of $(\beta T^*_{\rm mat})$ as we argued in the previous section. For small ρ_c and $\beta < 0$ the sign of $(\beta T^*_{\rm mat})$ is positive, causing the amplification of the scalar field inside the star. As ρ_c grows larger eventually $T^*_{\rm mat}$ becomes positive, causing $(\beta T^*_{\rm mat})$ to become negative, ultimately suppressing the scalar field rather than amplifying it, which is why the instability eventually vanishes as ρ_c increases.

In the $\beta > 0$ region of the parameter space the behavior of the instability is

[5]Notice that Eq. (2.72) encompasses a large class of STTs, not just the exponential model. This analysis applies to STTs whose coupling functions $\alpha(\varphi)$ can be approximated by $\beta\varphi + \mathcal{O}(\varphi^2)$.

[6]Figure 2.7 is indeed a quantitatively replication of the results formally presented in Ref. [41]. We adjusted the regions to match those of the ENG EoS studied here. We only present this figure here for completeness and to act as a visual aid to explain the behavior of the scalar instability.

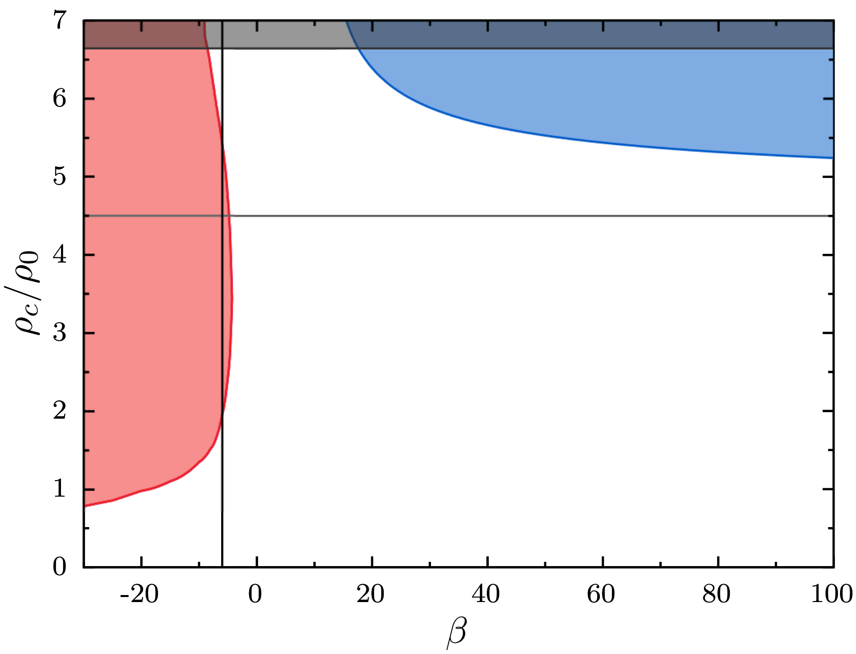

Figure 2.7: A rough schematic representation of the instability regions from linear stability analysis carried out in Ref. [41]. Red/Blue regions are unstable to scalar-field perturbations and the black region corresponds to solutions that are unstable to gravitational collapse. The horizontal line marks the density above which $T^*_{\text{mat}} > 0$ at the center of the NS. We mark a vertical line at $\beta = -6$ (corresponding to an example scenario we used in Fig. 2.6) to help demonstrate the behavior of the instability.

slightly different. The instability to scalar perturbations no longer vanishes for larger values of ρ_c, meaning that once the central density becomes large enough, i.e. in the blue regions of Fig. 2.7, the instability will be present inside the star. The work in Refs. [41, 81] showed that the final fate of scalarized NSs existing in the $\beta > 0$ region of Fig. 2.7 in the exponential theory was always gravitational collapse. Our understanding of these results is that NSs can exist in the exponential theory with $\beta > 0$, provided that they live outside of the blue region of Fig. 2.7 and are identical to the trivial GR solutions. However, since these NSs would be identical to NSs in GR in these regions of parameter space no scalarized solutions would exist in nature. Because NSs in the exponential theory that could undergo scalarization would ultimately collapse to black holes we focus our attention to the study of NSs in the hyperbolic theory.

2.4.2.2 Scalarization in the Hyperbolic Theory Following the numerical procedure explained at the beginning of the section, we calculate NS solutions in all 5 EoSs given in Table 2.3 for $0 \leq \beta \lesssim 450$ and $\beta = 1000$. While we do not analyze the dynamical stability of the static solutions we find, we define stability based on a turning point criterion in a sequence of equilibrium configuration described in detail in Refs. [64, 84]. In short, every solution to the left of the maximum mass in a mass-density plot, like that in Fig. 2.8, would be considered stable and every solution to the right would be unstable. Figure 2.8 shows our numerical solutions using the ENG EoS for a small subset of β, with the top panel demonstrating stronger deviations from GR for larger values of β. There are three key features of note in these solutions:

1. there exist values of β that have no stable branch of solutions,
2. there appears to be an asymptotic branch of solution for large values of β,
3. there will exist a maximum mass and stable scalar charge $\alpha_{\text{sc,max}}$ for each β.

Let us investigate the first point above. From our turning point definition of stability, any solution existing on a branch to the right of the maximum will be unstable to gravitational collapse. Because small values of β do not lead to deviations from GR until after the maximum mass is reached, it stands to reason that there exists a β_{min} such that only values of $\beta > \beta_{\text{min}}$ allow for stable scalarized NS solutions in the hyperbolic theory. For example, in the top panel of Fig. 2.8 the $\beta = 10$ curve clearly does not have stable solutions different from GR. In other words, sufficiently small values of β only lead to deviations from GR when the ρ_c is large and in the black region of Fig. 2.7 and would undergo gravitational collapse. When $\beta = 40$ there exists a clear set of solutions different from GR that would indeed be stable up to the turning point, which we indicate with a circle in the figure for clarity. The values of $\beta_{\rm min}$ are listed in Table 2.3 for all EoSs studied.

There also appears to be an asymptotic branch of solutions in the limit $\beta \to \infty$, a qualitative feature occurring in each EoS studied. Starting from $\beta = 0$, increasing β initially induces dramatic changes in the corresponding branch of solutions; however, for $\beta \gtrsim 40$ for the ENG EoS, the relative change between solution branches changes only slightly even when β is increased by an order of magnitude. This idea can be explained by again referring back to the structure of $\alpha(\varphi)$ in Fig. 2.2. As $\beta \to \infty$ we find that $\alpha(\varphi) \to 1/\sqrt{3}$ exponentially. Therefore, as long as φ does not identically vanish everywhere, the coupling to matter is saturated, and thus, there will exist a branch of solution representing this maximal coupling case, which we see in Fig. 2.8 as β increases. This is a feature absent in the exponential theory because $\alpha(\varphi)$ is linear in β and therefore it has no asymptotic limit, meaning that the scalar field's coupling to matter can never be saturated.

Stability arguments [64, 84] indicate that there exists a maximum mass, and therefore a maximum stable scalar charge, on each branch of solutions determined by β. However, the bottom panel of Fig. 2.8 indicates that the scalar charge grows monotonically as the central density increases. Using the turning point criterion allows us to extract the most massive stable solution and hence the corresponding scalar charge of that solution. The points marked in Fig. 2.8 correspond to identical solutions in each panel and for $\beta \gtrsim 40$ we see that the maximum stable scalar charge on each solution branch decreases with increasing β. There actually exists a $\beta_{\rm max}$ where $\alpha_{\rm \,sc,max}(\beta)$ peaks, which is evident in Fig 2.1 and whose values appear in Table 2.3.

Figure 2.1 shows the maximum stable scalar charge as a function of β for all EoSs

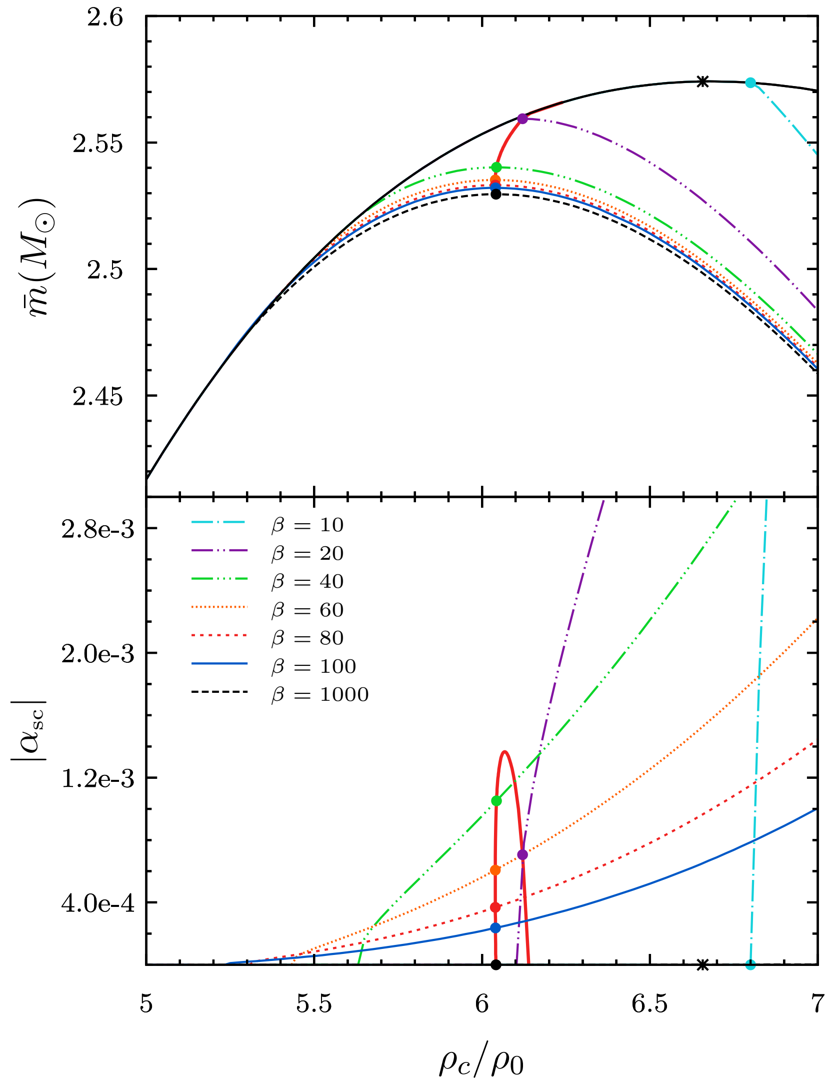

Figure 2.8: **Top:** Baryonic mass as a function of central baryonic density for a wide range of β. There exists an asymptotic solution as $\beta \to \infty$ (as β increases the branches only experience small changes from one to the next). Solid points indicate the maximum mass that is stable and the solid red line connects all maximum mass solutions for all β. **Bottom:** The scalar charge as a function of the central baryonic density for the same set of β's as in the top panel. Solid points here correspond to the same solutions at the solid points in the top panel, with the solid red curve showing how these values change as a function of β. Even though the scalar charge grows monotonically there exists a maximum value that it can take for stable NS solutions. For large β, increasing β continues to decrease the maximum stable scalar charge, though it does not cause the charge to vanish.

in Table 2.3. There is a general trend that EoSs that allow for larger compactness have large values of scalar charge. This complements the results presented in Ref. [80] where the author demonstrated a relation between the compactness and the onset of scalarization for the same set of EoSs. We can also roughly quantify how rapid the scalar field "turns on" [7] by measuring the slope of the charge in the bottom panel of Fig. 2.8 near the maximum stable solutions, i.e. the ones marked with points. Figure 2.9 shows the value of this slope, which we denote $\alpha'_{\text{sc,max}} = \partial\alpha_{\text{sc,max}}/\partial\rho_c$, as a function of β. For small β there is no change in the charge because, as we previously stated, there are no stable scalarized solutions below β_{min}. As one may expect from Fig. 2.8 there is a clear monotonic decrease in $\alpha'_{\text{sc,max}}$ as we increase β. A decreasing $\alpha'_{\text{sc,max}}$ means that the scalar field grows much more gradually with central pressure as β becomes larger.

To understand why the maximum scalar charge decreases for large β we must return to the field equations, particularly Eq. (2.63) which we rewrite for convenience as

$$\begin{aligned}\psi' &= \frac{4\pi G r A^4(\varphi)}{(r_* - 2\mu)}\big[\alpha(\varphi)(\epsilon - 3p) + r_*\psi(\epsilon - p)\big] \\ &\quad -2\psi\frac{(1-\mu/r_*)}{(r_* - 2\mu)}\ .\end{aligned}$$

This equation describes the curvature of the scalar field profile, with the first term in square brackets identified with $(-\alpha(\varphi)T^*_{\text{mat}})$. This term will explicitly be negative near the center of the NS because $T^*_{\text{mat}} > 0$. Increasing β increases the value of $\alpha(\varphi)$, even though only slightly when β is large. This term then contributes to a more negative value of curvature, which causes the scalar field to decay faster inside the

[7]This activation, or "turn on", is not dynamical. We are simply referring to how rapid the charge increases as ρ_c increases.

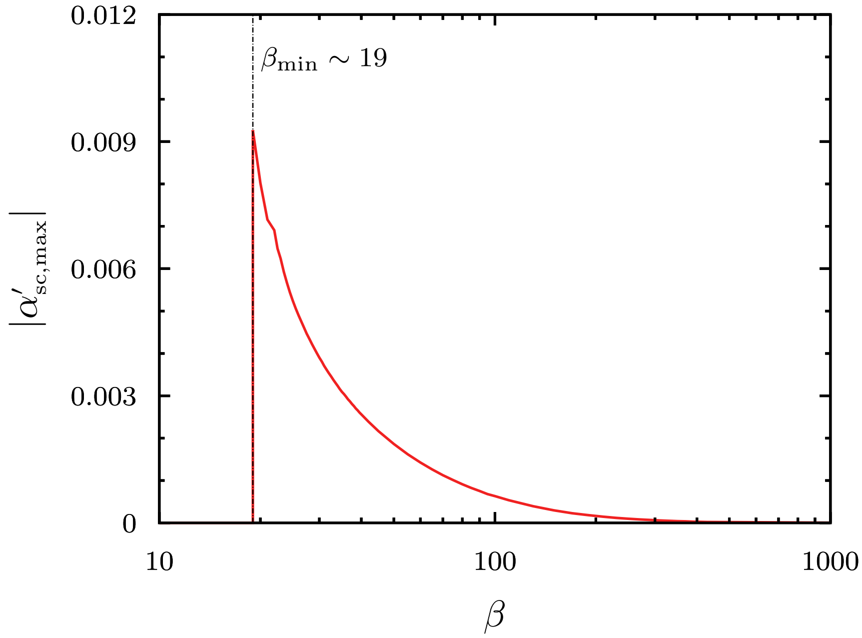

Figure 2.9: Rate of change of the scalar charge evaluated at the maximum mass solutions (solutions identified by points in Fig. 2.8) as a function of β for the ENG EoS. There are no values for $\beta \lesssim 19$ because there are no stable solutions with scalar charge, c.f. the discussion in the text. Notice that the "rapidity" of the increase of scalar charge monotonically decreases with increasing β. The apparent kink near $\beta = 25$ is a result of numerical error due to the fact that we only have limited precision and must interpolate between different solution branches.

star as β increases. Numerically, we find that the NS solutions appearing in Fig. 2.1 have nearly identical central scalar field values for $\beta > 100$. Because the scalar field decays faster inside the star there will exist a smaller value of ω from Eq. (2.68) upon matching boundary conditions at the surface and therefore a smaller scalar charge.

2.5 Conclusion

Our calculations show that theories with an exponential conformal factor (identical to the ones first studied by Damour and Esposito-Farèse [37, 38]) and theories with a hyperbolic conformal factor (motivated from quantum field theory [24, 44, 80]) always pass Solar System constraints provided that $\beta \lesssim \beta_{\text{crit}} = 24$ and $\beta \lesssim \beta_{\text{crit}} = 17$ respectively for all initial conditions consistent with BBN constraints. By considering a random distribution of initial conditions below the BBN constraint, these bounds can be relaxed to $\beta_{\text{crit}} \sim 34$ and $\beta_{\text{crit}} \sim 25$ respectively. These results tell us that Solar System constraints place a rather tight bound on the β parameter if one wishes to avoid fine-tuning the initial conditions at the time of BBN.

Recent work has suggested that scalarization is still possible in STTs with $\beta > 0$ if the star becomes dense enough such that the trace of the matter stress-energy tensor becomes positive inside the star, which is only possible for certain EoSs [41, 80, 81]. However, neutron stars in STTs with an exponential conformal factor have recently been shown to undergo gravitational collapse when $\beta > 0$ [41]; therefore, only NSs with $T^{\text{mat}} = -\rho + 3p < 0$ would exist in this theory and these would not scalarize. After verifying the results in these recent studies, we constructed NSs in a theory with hyperbolic coupling and $\beta > 0$ for β regions consistent with Solar System observations. Our results show that there exists a minimum value of β, denoted β_{min} in Table 2.3, for which there exist *stable* scalarized NS solutions that are distinct from GR. However, in every EoS that we considered, all of these values of β_{min} were larger than the upper bound on β placed with Solar System observations when one saturates BBN initial conditions.

The fact that $\beta_{\text{crit}} < \beta_{\text{min}}$ for many EoSs does not mean that no scalarized NSs can exist. Indeed, one can choose more finely-tuned initial conditions at the time of BBN, thus making β_{crit} slightly larger. The larger one wishes to make β_{crit}, the more one will need to fine-tune the initial conditions. Eventually, such a large fine-tuning of initial conditions would have to be justified through a theoretical physics mechanism that currently does not exist. Alternatively, one can pick a value of $\beta > \beta_{\text{crit}}$ such that Solar System constraints are satisfied today but fail in the future. In this case, the likelihood of the existence of stable, scalarized NSs becomes smaller the larger β is above $\beta_{\rm crit}$, as the bands of allowed β thin out and become more sparse as β increases.

The results presented here and in Ref. [82] may beg the question of whether or not it is possible to engineer a conformal factor in massless STTs that generally passes Solar System tests and, furthermore, leads to scalarization in neutron stars. Solar System tests demand that, at least locally, the conformal coupling potential have positive curvature, i.e. $\beta(\varphi) > 0$ in general, and therefore one must have an EoS that allows $T^{\rm mat} > 0$ in order to have scalarized neutron stars. It seems that having $\beta(\varphi) > 0$ and $T^{\rm mat} > 0$ only allows for a scalar charge of $\mathcal{O}(10^{-3})$, where as in the $\beta(\varphi) < 0$ case the charge is of $\mathcal{O}(10^{-1})$. Therefore, these consistency between Solar System observations and the cosmological evolution of the scalar field may limit the maximum size of the scalar charge that can occur in NSs for a large class of massless STTs. A promising avenue for future research would be the study of massive STTs [68, 85] in this context or to perform an analysis like the one in this paper on tensor-multiscalar theories.

If consistency between the bounds from Solar System tests and scalarized NSs were achieved, then NSs in these theories would have a different mass and radius than that predicted in GR and only deviate from GR after a critical density (or compactness) is achieved such that the trace of the stress-energy tensor is positive. A direct observation of such a system, perhaps with NASA's NICER telescope [86, 87], in conjunction with gravitational wave observation of such systems, may allow further constraints to be placed on STTs. Both observations would be necessary in order to break degeneracies between the mass-radius relation, the tidal deformabilities and our ignorance of the equation of state through approximately universal relations [88–91]. Such studies would provide useful information on what the actual form of the conformal factor may be. We have seen that some models, like the exponential one, do not allow for scalarized NSs, while others, like the hyperbolic one, do. Therefore, any observation of neutron stars that could shed some light on the functional form of the conformal factor would be valuable.

Similarly, it would also be interesting to investigate dynamical and induced scalarization in hyperbolic STTs with $\beta > 0$ with an eye out for gravitational wave tests with ground-based instruments [92–94]. Given the results obtained in the spontaneous scalarization case, we expect the scalar charge to be dynamically generated in binaries, but its magnitude to be significantly smaller than in the exponential $\beta < 0$ case. The latter case, however, is already ruled out by Solar System observations, while we showed here that hyperbolic STTs with $\beta > 0$ can still be consistent. Studying scalarization in these theories would allow us to predict the signatures that would imprint on the gravitational waves emitted in neutron star binaries. Presumably, the activation of the scalar field will induce dipole radiation, which in turn will speed up the inspiral of the binary, leaving a signature on the gravitational waves emitted. If so, gravitational wave observations with advanced LIGO could place the first meaningful constraints on such theories in the context of NSs.

2.6 Acknowledgments

We thank Emanuele Berti, Enrico Barausse, Norbert Wex, Hector Okada da Silva, Raissa Mendes, and Nestor Ortiz for useful discussions on neutron stars in scalar-tensor theories, and for reading our manuscript carefully and providing useful suggestions. N.Y. acknowledges support from the NSF CAREER grant PHY-1250636 and NASA grant NNX16AB98G.

CHAPTER THREE

SCALAR CHARGES AND SCALING RELATIONS IN MASSLESS SCALAR-TENSOR THEORIES

Contribution of Authors and Co-Authors

Manuscript in Chapter 2

Author: David Anderson

Contributions: Developed and implemented the design study. Developed numerical code necessary for the project. Wrote the first draft of the manuscript.

Co-Author: Nicolás Yunes

Contributions: Provided feedback on analysis and comments on draft of the manuscript.

Manuscript Information Page

David Anderson, Nicolás Yunes

Status of Manuscript:

__x__ Prepared for submission to a peer-reviewed journal

____ Officially submitted to a peer-reviewed journal

____ Accepted by a peer-reviewed journal

____ Published in a peer-reviewed journal

Manuscript will be ready for submission to Classical Quantum Gravity after minor revisions and subsequent review from authors.

Abstract

The timing of binary pulsars allows us to place some of the tightest constraints on modified theories of gravity. Perhaps some of the most interesting and well-motivated extensions to General Relativity are scalar-tensor theories, in which gravity is mediated by the metric tensor and a scalar field. These theories predict large deviations from General Relativity in the presence of neutron stars through a phenomenon known as scalarization. Neutron stars in scalar-tensor theories develop scalar charges, which directly enter the timing model for binary pulsars. In this paper, we calculate and tabulate these scalar charges in two popular, massless scalar tensor theories for a collection of neutron star equations of state that are compatible with constraints placed by the recent, gravitational wave observations of a binary neutron star coalescence. We then study these scalar charges and explore analytic scaling relations that allow us to predict their value in a large region of parameter space. Our results allow for the quick evaluation of the scalar charge in a large region of scalar-tensor theory parameter space, which has applications for gravitational wave tests of scalar-tensor theories, as well as binary pulsar experiments.

3.1 Introduction

Gravitational waves observations from aLIGO [1–6] and the high precision timing of binary pulsars [7–10] has allow us to test Einstein's theory of General Relativity (GR) in the most extreme environments [12,13]. With more NS-NS merger events, we will be able to tightly constrain the equation of state (EOS) and other properties of neutron stars (NS) [14,15]. Furthermore, as radio astronomers continue to monitor binary pulsars systems, the errors in the timing model parameters will continue to decrease and help place tighter constraints on modified theories of gravity. Nonetheless, in order to investigate how these future observations will help us further test gravity, we first must understand the precise details of how observable predictions are modified.

A popular class of theories in the literature are scalar-tensor theories (STT) of gravity, in which gravity is not only mediated by the metric tensor but also by a long-range scalar field that is non-minimally coupled. Each theory in this class is defined by the choice of conformal coupling function, which mediates the degree of violation of the strong equivalence principle (SEP). Such theories were first studied by Jordan [33, 34], Fierz [35], Brans [36], and Dicke (JFBD) as the most natural alternatives to GR, and were later extended By Damour and Esposito-Farése (DEF) [37, 38] to include higher order effects. A more recent extension of these theories was introduced by Mendes and Ortiz [41] (MO), which introduce a conformal coupling that replicates the behavior of including higher order scalar-field terms in the action [42–45].

Solar system observations, like that of the perihelion shift of Mercury and of the Shapiro time delay, are able to place tight bounds on the parameters of STTs [16, 61]. However, these are only measurements in the weak field regime where the gravitational potential is small. STTs are able to satisfy weak field constraints and still produce strong field deviations from GR through a phenomenon known as scalarization [37, 38, 52, 53]. Thus, one needs observations that probe the strong field, regions where non-linear effects like scalarization occur, in order to place tight constraints on STTs. While gravitational waves observations of binary NS coalescences with aLIGO and other detectors will be able to accomplish this regularly in the future, binary pulsar experiments are already able to probe and constrain STTs in the strong field to extremely high precision. By modeling the time of arrival (TOA) of pulses emitted from pulsar systems [39, 95, 96], one can take the observed data and place constraints on the underlying theory of gravity governing the motion of the binary. For this reason, binary pulsars are currently one of the best available testbeds for gravity.

To perform any test, however, one must first know precisely how observables are modified in STTs, and this depends on the so-called scalar charges, i.e. scalar quantities that determine how strongly a scalar field is sourced by an isolated neutron star. For example, the scalar charges enter directly into the parameterized-post-

Keplerian (PPK) parameters used in testing STTs [39, 42, 50, 70, 97] with binary pulsars. To find these scalar charges, one must numerically obtain NS solutions in STTs, subject to certain physical boundary conditions at the core of the star and at spatial infinity. This numerical process is, at first sight, simple, yet in practice it need not be, mainly for the following two reasons.

First, some of these charges can be numerically challenging to compute. The dominant scalar charge can indeed be read out easily from the leading 1/r piece of the scalar field at spatial infinity, given any numerical solution. Other scalar charges, however, depend on derivatives of the dominant charge with respect to the gravitational mass of the neutron star. During scalarization, the dominant scalar charge can change quite abruptly with respect to the asymptotic value of the scalar field, holding the baryonic mass of the star constant. This, in turn, leads to large spikes in the derivatives, which can be difficult to resolve if one is not careful.

Second, tests of STTs requires knowledge of the scalar charges everywhere in parameter space, and this can be computationally costly. Markov-Chain Monte-Carlo (MCMC) methods that explore the posterior probability distribution of parameters requires the evaluation of the likelihood function hundreds of thousands to millions of times. Every evaluation requires the scalar charges, and if these have to be numerically computed every time the likelihood is needed, the MCMC exploration becomes computationally prohibitive. Clearly then, the MCMC exploration of parameter space in STTs would greatly benefit from a "bank" of calculated scalar charges.

In this paper, we study, calculate, tabulate, and analytically explore the three main scalar charges (α_A, β_A, and k_A [42]) that enter the PPK parameters of binary pulsar observations. We carry out this calculation both in the STT proposed by Damour-Esposito-Farése [37, 38] and the one studied by Mendes-Ortiz [41] (hereafter referred to DEF theory and MO theory respectively). We explore a very large region of the parameter space spanned by the two coupling constants of these theories, using 11 different equations of state that are all consistent with neutron stars heavier than $2M_{\odot}$, including a few that are also consistent with the recent gravitational wave observation of a neutron star coalescence [6].

Our main result is the construction of an accurate bank of scalar charges in these two theories that can now be used used in Bayesian model selection and parameter estimation studies of tests of STTs with binary pulsar observations. This bank is constructed both through direct numerical calculations, as well as through the exploration of certain analytic scaling relations. We determine the regime of parameter space in which the latter hold, and when they do, we use them to greatly accelerate the calculation of scalar charges in these regions of parameter space. The end result is a numerically accurate and dense bank of scalar charges that can be interpolated if necessary to provide charges everywhere in parameter space.

The remainder of this paper presents the details of the calculation summarized above. Section 3.2.1 covers the basics of STTs along with observational constraints and includes a discussion of the scalar charges. Section 3.3 describes how NSs behave in STTs and begins to set up our numerical scheme to solve for the scalar charges. Section 3.4 details the calculations behind the scalar charges and what numerical techniques are needed to accurately explore the parameter space. Section 3.5 provides a detailed description of our publicly available data files, along with instructions for how to use them and what their limitations are. Section 3.6 concludes with a discussion of future work.

3.2 Scalar-Tensor Theories

In this section, we introduce the basics of the class of STTs that we consider and establish the notation to be used in the rest of the paper. For completeness we present this class of theories from first principles using an action and provide a summary of the calculations needed to reach the field equations; we refer the reader to [73] for further details. We then describe the two STTs we study in this paper and present the current constraints on these theories. We conclude this section with a discussion of scalarization and the definition of scalar charges in these theories.

3.2.1 Background and field equations

In general, the massless STTs that we consider can be described in the *Jordan frame* by an action of the form $\tilde{S} = \tilde{S}_g + \tilde{S}_{\text{mat}}$, with the gravitational part taking the form

$$\tilde{S}_g = \int \frac{d^4x}{c} \frac{\sqrt{-\tilde{g}}}{4\kappa} \left[\phi \tilde{R} - \frac{\omega(\phi)}{\phi} \partial_\mu \phi \partial^\mu \phi \right] , \tag{3.1}$$

where $\tilde{g}$ and $\tilde{R}$ are the determinant and Ricci scalar of the metric $\tilde{g}_{\mu\nu}$ respectively, ϕ is a scalar field, $\omega(\phi)$ is a coupling function of the scalar field, and $\kappa = 4\pi G/c^4$ with G the bare gravitational constant. The matter part of the action, $\tilde{S}_{\text{mat}}[\chi, \tilde{g}^{\mu\nu}]$, is a functional of the matter fields χ that couple directly to the Jordan-frame metric. Therefore, the STTs we study in this paper are metric theories, and as such, laboratory clocks and rods measure time intervals and distances associated with $\tilde{g}_{\mu\nu}$.

While STTs can be completely described using the Jordan-frame action above, it is far more convenient to perform a conformal transformation that puts the action in a form reminiscent of the Einstein-Hilbert action. Let us then consider the transformation $\tilde{g}_{\mu\nu} = A(\varphi) g_{\mu\nu}$, where $g_{\mu\nu}$ is the *Einstein-frame* metric[1], so that the action becomes

$$S = \int \frac{d^4x}{c} \frac{\sqrt{-g}}{4\kappa} \left[R - 2g^{\mu\nu} \partial_\mu \varphi \partial_\nu \varphi \right] + S_{\text{mat}} \left[\chi, A^2(\varphi) g_{\mu\nu} \right] , \tag{3.2}$$

[1]From this point on, we use an overhead tilde to represent quantities that are specifically in the Jordan frame. Quantities without overhead tildes should be assumed to be in the Einstein frame.

where g and R are the now the determinant and Ricci scalar associated with the Einstein-frame metric $g_{\mu\nu}$. Notice that the matter fields now couple to $A^2(\varphi)g_{\mu\nu}$, and therefore, matter no longer falls along geodesics of the metric $g_{\mu\nu}$, but rather it is now also influenced by the scalar field φ.

The conformal transformation that takes Eq. (3.1) into Eq. (3.2) requires the conformal factor

$$A(\varphi) = \phi^{-1} \ , \tag{3.3}$$

which then leads to a direct relation between φ and ϕ, given explicitly as

$$\alpha(\varphi)^2 \ = \ \left(\frac{d\ \ln A(\varphi)}{d\varphi}\right)^2 \ = \ \frac{1}{3+2\omega(\phi)} \ . \tag{3.4}$$

One can think of $\alpha(\varphi)$ as the gradient of some "conformal potential" [40, 55, 82, 98], defined by $V_\alpha \equiv \ln A(\varphi)$, and one can denote the "curvature" of this potential as $\beta(\varphi) = d\alpha/d\varphi$. The conformal potential is a simple way to understand and visualize the coupling between matter and the scalar field, which will be directly quantified by its slope and curvature in the field equations. Clearly then, the choice of $A(\varphi)$, or any of the above quantities for that matter, defines a particular member of this general class of STTs, which is ultimately a choice of exactly how the scalar field affects matter.

The variation of the Einstein-frame action with respect to the dynamical fields, $g_{\mu\nu}$ and φ, yields the field equations

$$R_{\mu\nu} \ = \ 2\partial_\mu\varphi\partial_\nu\varphi + 2\eta\left(T^{\rm mat}_{\mu\nu} - \frac{1}{2}g_{\mu\nu}T^{\rm \ mat}\right) \ , \tag{3.5}$$

$$\Box\varphi \ = \ -\kappa\alpha(\varphi)T^{\rm \ mat} \ , \tag{3.6}$$

where the Einstein frame stress-energy tensor is defined by

$$T_{\mu\nu}^{\text{ mat}} \equiv \frac{2c}{\sqrt{-g}} \left(\frac{\delta S_{\text{ mat}}}{\delta g^{\mu\nu}} \right) \ , \tag{3.7}$$

and $T^{\text{ mat}} \equiv g_{\mu\nu} T_{\mu\nu}^{\text{ mat}}$ is its trace. The stress-energy tensor in the Einstein frame can be related to its Jordan-frame counterpart via the relation $T_{\mu\nu}^{\text{ mat}} = A^2(\varphi)\tilde{T}_{\mu\nu}^{\text{ mat}}$ by applying the conformal transformation to Eq. (3.7). Assuming a perfect fluid description of the stress-energy tensor [see e.g. Eq. (3.30) below] allows one to derive the relations $\epsilon = A^4\tilde{\epsilon}$ and $p = A^4\tilde{p}$ between the energy density and pressure of the fluid in the different frames.

3.2.2 Scalar-tensor models

Scalar-tensor theories of the form described in the previous subsection allow for deviations from GR because of the new coupling that exists between matter and the scalar field. The particular choice of the conformal factor $A(\varphi)$, and likewise the formal coupling $\alpha(\varphi)$, defines the theory and plays a crucial role in understanding the observable modifications a theory predicts. The first model we consider is DEF theory and it is defined by

$$A(\varphi) = e^{\beta_0\varphi^2/2} \ , \tag{3.8}$$

$$V_\alpha(\varphi) = \frac{1}{2}\beta_0\varphi^2 \ , \tag{3.9}$$

$$\alpha(\varphi) = \beta_0\varphi \ , \tag{3.10}$$

$$\beta(\varphi) = \beta_0 \ , \tag{3.11}$$

where β_0 is a free coupling parameter. Aside from the JFBD theory in which $A(\varphi) = e^{\alpha_0\varphi}$, this is the simplest massless STT one can consider. One notices that the conformal potential is exactly a parabola whose curvature is precisely determined by the free parameter β_0.

The other model we consider, which has gained attention in the past few years, is MO theory and it is defined by

$$\begin{aligned} A(\varphi) &= \left[\cosh\left(\sqrt{3}\,\beta_0\varphi\right)\right]^{1/(3\beta_0)} , & (3.12)\\ V_\alpha(\varphi) &= \frac{1}{3\beta_0}\ln\left[\cosh\left(\sqrt{3}\,\beta_0\varphi\right)\right] , & (3.13)\\ \alpha(\varphi) &= \frac{\tanh\left(\sqrt{3}\,\beta_0\varphi\right)}{\sqrt{3}} , & (3.14)\\ \beta(\varphi) &= \beta_0\,\mathrm{sech}^2\left(\sqrt{3}\,\beta_0\varphi\right) , & (3.15) \end{aligned}$$

where again β_0 is a free coupling parameter. The MO theory was introduced as an analytic approximation to a more fundamental theory that includes quadratic terms of the scalar field coupled to curvature in the action [24, 41–43, 45]. This theory is functionally equivalent to DEF theory in the limit that $\varphi \to 0$, but it has strictly different behavior when the combination $\beta_0\varphi \neq 0$. Therefore, these theories have distinctly different properties, and therefore, modify observables in different ways [41, 98].

3.2.3 Solar System Constraints

In principle, observations we make, whether they be in the solar system [16, 61] or of binary pulsar systems [8, 10, 70], constrain the free parameters of the theory. Let us then consider how observables are modified in STTs. As an example, let us first consider the local value of Newton's gravitational constant. This quantity is given by

$$G_N = G\left[A_\infty^2\left(1+\alpha_\infty^2\right)\right] . \tag{3.16}$$

where G is the bare gravitational constant appearing in the action, and an ∞ subscript denotes quantities evaluated at $\varphi = \varphi_\infty$, e.g. $A_\infty = A(\varphi_\infty)$. The correction to the gravitational constant causes bodies to accelerate differently depending on the magnitude of scalar field, the parameters of the theory, and the bodies' composition through violations of the strong-equivalence principle.

The choice of coupling parameter also determines the local value of the parameterized post-Newtonian (PPN) parameters [30, 71, 72]. Scalar-tensor theories are a class of fully conservative theories and therefore only pose modifications to the $\gamma_{\,\mathrm{PPN}}$ and $\beta_{\,\mathrm{PPN}}$ parameters [16, 73]. The former is given by

$$|1 - \gamma_{\,\mathrm{PPN}}| = \frac{2\alpha_\infty^2}{1+\alpha_\infty^2}\,, \tag{3.17}$$

while the latter is given by

$$|1 - \beta_{\,\mathrm{PPN}}| = \frac{\beta_\infty \alpha_\infty^2}{2\left(1+\alpha_\infty^2\right)^2}\,, \tag{3.18}$$

where as before $\alpha_\infty = \alpha(\varphi_\infty)$ and $\beta_\infty = \beta(\varphi_\infty)$. The $\gamma_{\,\mathrm{PPN}}$ parameter is a measure of the spatial curvature induced by a unit rest mass, while the $\beta_{\,\mathrm{PPN}}$ parameter is a measure of the amount of non-linearity in the superposition law for gravity. The $\gamma_{\,\mathrm{PPN}}$ parameter has been measured from the Shapiro time delay observed by the Cassini spacecraft [16, 61], and it is constrained to $|1 - \gamma_{\,\mathrm{PPN}}| \lesssim 2.3 \times 10^{-5}$. The $\beta_{\,\mathrm{PPN}}$ parameter is measured from observations of the perihelion shift of Mercury [16], and it is constrained to $|1 - \beta_{\,\mathrm{PPN}}| \lesssim 8 \times 10^{-5}$.

The notation we have used above is slightly different from what is found in the literature so let us clarify this here. Typically, instead of using α_∞ and β_∞, some papers that studied DEF theory used a different set of parameters $\{\alpha_0,\, \beta_0\}$. This is because if one modifies Eq. (3.10) in DEF theory to

$$\alpha(\varphi) = \alpha_0 + \beta_0 \varphi \ , \tag{3.19}$$

and sets $\varphi_\infty = 0$, then $\alpha(\varphi_\infty) = \alpha_0$ and $\beta(\varphi_\infty) = \beta_0$, and all observables can be entirely parameterized by the set $\{\alpha_0, \beta_0\}$. This parameterization is identical to our description of DEF theory appearing in Eq. (3.8), provided that one enforces $\varphi_\infty = \alpha_0/\beta_0$ [70], which is the choice we make in this paper. When considering MO theory, however, $\alpha(\varphi_\infty) \neq \alpha_0 = \varphi_\infty \beta_0$ and $\beta(\varphi_\infty) \neq \beta_0$, as one can easily see from Eqs. (3.12)-(3.15).

In this paper, we want both theories to share the same free parameters $\{\alpha_0,\, \beta_0\}$ and, therefore, the quantities that enter the PPN parameters, $\{\alpha_\infty,\, \beta_\infty\}$, are different functions of $\{\alpha_0,\, \beta_0\}$ in the two theories. These functions are

$$\alpha_\infty^{\rm DEF} = \alpha_0 \ , \tag{3.20}$$

$$\beta_\infty^{\rm DEF} = \beta_0 \ , \tag{3.21}$$

in DEF theory, and

$$\alpha_\infty^{\rm MO} = \tanh\left(\sqrt{3}\,\alpha_0\right)/\sqrt{3} \ , \tag{3.22}$$

$$\beta_\infty^{\rm MO} = \beta_0\,{\rm sech}^2\left(\sqrt{3}\,\alpha_0\right) \ . \tag{3.23}$$

in MO theory. These choices have the advantage of reducing $(\alpha_\infty, \beta_\infty)$ to the known relations of DEF theory, while properly generalizing them to MO theory.

3.2.4 Scalarization and binary pulsar constraints

Solar system observations have the ability to place tight constraints on STTs through weak field observations [16]. STTs, however, are able to satisfy these constraints and still deviate substantially from GR inside and near NSs [37,38,52,53]. The strong field deviations are caused by a phenomenon known as scalarization, in which the scalar field can grow rapidly towards order unity inside NSs even when the asymptotic value, that which is constrained by Solar System observations, approaches zero.

The key behind this rapid growth is the existence of an instability in the field equations when a star reaches a sufficiently large compactness. The onset of this instability is analogous to spontaneous magnetization in ferromagnets [42]. To understand this, consider the external scalar field far from a neutron star, labeled A, $\varphi = \varphi_\infty + G\,\omega_A/r + \mathcal{O}(1/r^2)$, where ω_A is a type of "charge" that is energetically conjugate to the external scalar field,

$$\omega_A = -\frac{\partial m_A}{\partial \varphi_\infty} \,, \tag{3.24}$$

with m_A the total gravitational mass of the NS. When one considers a sequence of neutron stars of masses m_A, ω_A can become suddenly non-zero at a critical value of the mass or compactness of the star. This sudden activation of the scalar field is what is referred to as spontaneous scalarization. When a NS is scalarized, $\omega_A \neq 0$ and the scalar field is excited above its background value, leading to local gravitational effects that will generically be different than those in GR.

For binary pulsar tests, it is convenient to introduce certain quantities that enter the PPK parameters of the binary pulsar timing model. We call these parameters *scalar charges* in this paper, the first of which is defined by

$$\alpha_A = -\frac{\omega_A}{m_A} = \left.\frac{\partial \ln m_A}{\partial \varphi_\infty}\right|_{\bar{m}_A} , \tag{3.25}$$

which plays the role of an effective coupling between the scalar field and the Ath NS in the binary. The baryonic mass must be held constant because this signifies that we are considering the same NS, i.e. the baryonic mass of a NS will not change due to fluctuations of φ_∞. This quantity is the strong field counterpart of the α_∞ parameter introduced in the previous section. Similarly, there is a strong field counterpart to the β_∞ parameter of the previous section, namely

$$\beta_A = \left.\frac{\partial \alpha_A}{\partial \varphi_\infty}\right|_{\bar{m}_A} , \tag{3.26}$$

which encodes higher order effects associated with the exchange of multiple scalar particles between the binary components. Lastly, there is one more charge that enters the PPK parameters, namely

$$k_A = \left.\frac{\partial \ln I_A}{\partial \varphi_\infty}\right|_{\bar{m}_A} , \tag{3.27}$$

where I_A is the moment of inertia of the NS. Similarly to how α_A was an effective coupling between the mass of the NS and the scalar field, this quantity acts as a coupling between the field and the star's spin angular momentum, and it describes how the NS's inertia reacts to the presence of an external scalar field. All of these scalar charges must be calculated while holding the baryonic mass of the star constant, as they measure the "sensitivity" of a star to the external scalar field. The main goal of this work is to calculate these scalar charges and make them publicly available. As such, we will provide the details of these calculations later in §3.4 after we introduce the relevant framework needed to understand NSs in STTs.

3.3 Compact Stars in Scalar-Tensor Gravity

In this section we discuss how compact stars behave in STTs and introduce some of the basics of scalarization from an analytic perspective. We focus our attention on isolated, slowly-rotating stars because the binary pulsar systems that we wish to provide scalar charges for are widely separated. We begin with a discussion of the interior spacetime of slowly-rotating compact stars and then discuss the exterior spacetime and how one connects it to the interior. Following the discussion of the field equations, we discuss the different types of equations of state one can use and conclude with an analytic discussion of scalarization in the different regions of parameter space.

Before we begin, however, let us discuss how we will describe compact stars in STTs. We focus on a stationary, axisymmetric spacetime, which allows for a description of a star that is slowly rotating. Following closely the work of [42], we make the metric ansatz proposed by Hartle [99]

$$\begin{aligned} ds^2 &= g_{\sigma\delta}\, dx^\sigma dx^\delta \;=\; -e^{\nu(\rho)}c^2 dt^2 + e^{\lambda(\rho)} d\rho^2 + \rho^2 d\theta^2 \\ &\quad + \rho^2 \sin^2\theta \left(d\phi + [\omega(\rho,\theta) - \Omega]\, dt\right)^2 \;, \end{aligned} \tag{3.28}$$

in which one only keeps terms to first order in the star's angular velocity $\Omega = u_\phi/u_t$, where u^μ is the fluid's four velocity. In this ansatz, the metric functions (ν, λ) are zeroth-order in rotation and functions of the radial coordinate ρ only, while the metric function ω is first-order in rotation and depends both on ρ and the polar angle θ. For practical and physical convenience, we also redefine the g_{rr} component of the metric through the interior mass function $\mu(\rho)$ defined via

$$e^{\lambda(\rho)} = \left(1 - \frac{2\mu(\rho)}{\rho}\right)^{-1} . \tag{3.29}$$

Moreover, we model the NS matter with a perfect fluid stress-energy tensor given by

$$T_{\mu\nu} = (\epsilon + p)u_\mu u_\nu + p g_{\mu\nu} , \tag{3.30}$$

where ϵ is the fluid's energy density and p is the pressure, both in the Jordan frame.

3.3.1 Interior Spacetime

The scalar-tensor field equations with this metric ansatz are similar to those in GR. At zeroth-order in rotation, the field equations for the diagonal components of the metric are identical to those in the spherical case, which have already been studied in detail in the literature [42]. At first order in rotation, one finds a second-order equation for the ω metric function, which can be converted into an ordinary, second-order differential equation in ρ through a Legendre decomposition in θ [42]. Such a decomposition reveals that only the $\ell = 1$ mode in the Legendre decomposition has support. In particular, the field equations can be written in the first-order form [42]

$$\mu' = \kappa\rho^2 A^4(\varphi)\tilde{\epsilon} + \frac{1}{2}\rho(\rho - 2\mu)\psi^2 \ , \tag{3.31a}$$

$$\nu' = 2\kappa\frac{\rho^2 A^4(\varphi)\tilde{p}}{\rho - 2\mu} + \rho\psi^2 + \frac{2\mu}{\rho(\rho - 2\mu} \ , \tag{3.31b}$$

$$\varphi' = \psi \ , \tag{3.31c}$$

$$\psi' = \kappa\frac{\rho A^4(\varphi)}{\rho - 2\mu}\left[\alpha(\varphi)(\tilde{\epsilon} - 3\tilde{p}) + \rho\psi(\tilde{\epsilon} - \tilde{p})\right] - \frac{2(\rho - \mu)}{\rho(\rho - 2\mu)}\psi \ , \tag{3.31d}$$

$$\tilde{p}' = -(\tilde{\epsilon} + \tilde{p})\left[\frac{\nu'}{2} + \alpha(\varphi)\psi\right] \ , \tag{3.31e}$$

$$\bar{m}' = 4\pi G\tilde{\rho}A^3(\varphi)\frac{\rho^2}{\sqrt{1 - 2\mu/\rho}} \ , \tag{3.31f}$$

$$\omega' = \varpi \ , \tag{3.31g}$$

$$\varpi' = \kappa\frac{\rho^2}{\rho - 2\mu}A^4(\varphi)(\tilde{\epsilon} + \tilde{p})\left(\varphi + \frac{4\omega}{\rho}\right) + \left(\rho\psi^2 - \frac{4}{\rho}\right)\varpi \ , \tag{3.31h}$$

where primes denote derivatives with respect to the radial coordinate ρ. Notice that we have also included an equation for the enclosed baryonic mass of the star $\bar{m}(\rho)$, which gives the total baryonic mass through $\bar{m}_A = \bar{m}(R) = \int \tilde{\rho}\, u^t\sqrt{-\tilde{g}}\, d^3x$, where R marks the surface of the star, where by definition the pressure vanishes. In Eq. (3.31) we have explicitly used the Jordan-frame fluid variables $\tilde{\epsilon}$, $\tilde{\rho}$, and $\tilde{p}$ since these are the physical quantities that are measured by observations and appear in the EOSs that are discussed below.

From a numerical standpoint these equations pose a problem near the center of the star at $\rho = 0$ since the equations diverge there. The proper way to deal with this is to expand the equations about $\rho = 0$ and start the numerical integration at some arbitrary small distance away from the center, say $\rho_{\rm min}$. Expanding Eqs. (3.31) and evaluating at $\rho_{\rm min}$ gives the boundary conditions

$$\mu(\rho_{\rm min}) = 0 \,, \tag{3.32a}$$

$$\nu(\rho_{\rm min}) = 0 \,, \tag{3.32b}$$

$$\varphi(\rho_{\rm min}) = \varphi_c \,, \tag{3.32c}$$

$$\psi(\rho_{\rm min}) = \left(\frac{\rho_{\rm min}}{3}\right) \eta A^4(\varphi_c)\alpha(\varphi_c) \left[\tilde{\epsilon}_c - 3\tilde{p}_c\right] \,, \tag{3.32d}$$

$$\tilde{\rho}(\rho_{\rm min}) = \tilde{\rho}_c \,, \tag{3.32e}$$

$$\bar{m}(\rho_{\rm min}) = 0 \,, \tag{3.32f}$$

$$\omega(\rho_{\rm min}) = 1 \,, \tag{3.32g}$$

$$\varpi(\rho_{\rm min}) = \left(\frac{4}{5}\rho_{\rm min}\right) \eta A^4(\varphi_c)\alpha(\varphi_c) \left[\tilde{\epsilon}_c - 3\tilde{p}_c\right] \,, \tag{3.32h}$$

where $\tilde{\epsilon}_c = \tilde{\epsilon}(\tilde{\rho}_c)$ and $\tilde{p}_c = \tilde{p}(\tilde{\rho}_c)$ are the central values of the Jordan-frame energy density and pressure respectively and are defined by the EOS. The values of φ_c and $\tilde{\rho}_c$ are chosen independently and define a particular solution to the field equations. Equations (3.31) and (3.32) allow one to integrate the field equations from $\rho = \rho_{\rm min}$ to any arbitrary radius, even outside the star as the field equations describe the entire spacetime. A more computationally efficient method, however, is to use an analytic solution in vacuum that is valid in the exterior of the star, and then, match it to the interior solution at $\rho = R$, as we describe in the next section.

3.3.2 Exterior spacetime

The exterior solution to the field equations [Eqs.(3.31)] were found by Just in the late 1950s [100]. In the coordinates introduced by Just, the exterior metric takes the form

$$ds^2 \;=\; -e^{\nu}c^2dt^2 + e^{-\nu}\left[dr^2 + (r^2 - ar)(d\theta^2 + \sin^2\theta\, d\phi^2)\right] \;, \tag{3.33}$$

where one has

$$e^{\nu(r)} \;=\; \left(1 - \frac{a}{r}\right)^{b/a} \;, \tag{3.34}$$

while the scalar field takes the form

$$\varphi(r) \;=\; \varphi_0 + \frac{d}{a}\,\ln\left(1 - \frac{a}{r}\right) \;, \tag{3.35}$$

where a, b, and d are integration constants and are constrained by the relation $a^2 - b^2 = 4d^2$. The integration constants can all be expressed in terms of the gravitational mass of the star m_A and some effective coupling constant α_A, which in this context plays the role of the scalar charge in Eq. (3.25). These relations take the form

$$b \;=\; 2\frac{G}{c^2}m_A \;, \tag{3.36a}$$

$$\frac{a}{b} \;=\; \sqrt{1 + \alpha_A} \;, \tag{3.36b}$$

$$\frac{d}{b} \;=\; \frac{1}{2}\alpha_A \;. \tag{3.36c}$$

The coordinates used in the Just spacetime above are not the same as those used in the Hartle ansatz of the interior metric. Comparing the two line elements, one finds that

$$\rho \;=\; r\left(1 - \frac{a}{r}\right)^{\frac{a-b}{2a}} \;, \tag{3.37a}$$

$$e^{\lambda(\rho)} = \left(1 - \frac{a}{r}\right)\left(1 - \frac{a+b}{2r}\right)^{-2} . \tag{3.37b}$$

Given these relations, we can now read off the total gravitational mass of the star m_A from the $1/\rho$ behavior of g_{tt}, or $g_{\rho\rho}$, and the star's z-component of the total angular momentum J_A from the $1/\rho^2$ portion of $g_{t\phi}$. We can recast the later in terms of the $1/\rho^3$ behavior of ω as

$$\omega = \Omega - \frac{G}{c^2}\frac{2J_A}{\rho^3} + \mathcal{O}\left(\rho^{-4}\right) , \tag{3.38}$$

in which case the moment of inertia follows as

$$I_A = \frac{J_A}{\Omega} . \tag{3.39}$$

By directly integrating the equation for $\omega(\rho)$ and inserting Eqs. (3.37) into Eqs. (3.31), we arrive at a set of relations that are valid at the stellar surface [42] (with a subscript s denoting values at the surface of the star), namely

$$R \equiv \rho_s \ , \tag{3.40a}$$

$$\nu'_s \equiv R\psi_s^2 + \frac{2\mu_s}{R(R-2\mu_s)} \ , \tag{3.40b}$$

$$\alpha_A \equiv \frac{2\psi_s}{\nu'_s} \ , \tag{3.40c}$$

$$Q_1 \equiv \sqrt{1+\alpha_A^2} \ , \tag{3.40d}$$

$$Q_2 \equiv \sqrt{1-2\mu_s/R} \ , \tag{3.40e}$$

$$\hat{\nu}_s \equiv -\frac{2}{Q_1}\tanh^{-1}\left(\frac{Q_1}{1+2/(R\nu'_s)}\right) \ , \tag{3.40f}$$

$$\varphi_0 \equiv \varphi_s - \frac{1}{2}\alpha_A\hat{\nu}_s \ , \tag{3.40g}$$

$$\frac{G}{c^2}m_A \equiv \frac{1}{2}\nu'_s R^2 Q_2 \exp\left(\frac{1}{2}\hat{\nu}_s\right) \ , \tag{3.40h}$$

$$\frac{G}{c^2}J_A \equiv \frac{1}{6}\varpi_s R^4 Q_2 \exp\left(-\frac{1}{2}\hat{\nu}_s\right) \ , \tag{3.40i}$$

$$\begin{aligned}\Omega \equiv\ & \omega_s - \frac{c^2}{G^2}\frac{3J_A}{4m_A^3(3-\alpha_A^2)}\left\{e^{2\hat{\nu}_s} - 1 + \frac{4Gm_A}{Rc^2}e^{\hat{\nu}_s}\right. \\ & \left. \times\left[\frac{2Gm_A}{Rc^2} + e^{\hat{\nu}_s/2}\cosh\left(\frac{1}{2}Q_1\hat{\nu}_s\right)\right]\right\} \ ,\end{aligned} \tag{3.40j}$$

These set of relations allow us to extract important observables at $\rho = \infty$ by simply knowing their appropriate values at the surface of the star.

3.3.3 Equations of State

The description of the problem is not complete without first knowing how the fluid properties $\{\tilde{\rho}, \tilde{p}, \tilde{\epsilon}\}$ depend on one another. This is accomplished by an EOS and it allows us to close the system of equations. In this subection we describe the three types of EOSs considered in this paper in detail.

3.3.3.1 Polytropes The most simple EOS to consider for NSs is a polytropic equation of state in which the the pressure and baryonic density are related through a power law, i.e.

$$\tilde{p} = K\tilde{\rho}_0 \left(\frac{\tilde{\rho}}{\tilde{\rho}_0}\right)^{\Gamma} , \tag{3.41}$$

where K is the polytropic constant and Γ is the adiabatic index of the fluid. A particular choice for K and Γ define the EOS as well as some macroscopic properties of the NS, such as the maximum mass and compactness. In [42], a polytropic EOS was used in the calculation of the "gravitational form factors" (what we call the scalar charges in this paper) and therefore we will use the same polytropic EOS here to validate our computational algorithm. In particular, we will choose

$$\Gamma = 2.34 \quad , \quad K = 0.0195 , \tag{3.42}$$

with a fiducial baryonic mass density $\tilde{\rho}_0 = 1.66 \times 10^{14}$ g cm^{-3}, to make comparisons to the results in that paper, which we present later in Fig. 3.3.

The baryonic mass density only appears in the integral for calculating the baryonic mass of the star, and therefore, we need another relation relating pressure and baryonic density to the total energy density. The first law of thermodynamics provides such a relation:

$$\tilde{\epsilon} = \tilde{\rho} + \frac{\tilde{p}}{\Gamma - 1} . \tag{3.43}$$

Equations (3.42) and (3.43) can now be inserted directly into Eqs. (3.31) to provide a complete description of the interior of the NS.

While polytopes are very simple analytic EOSs that facilitate quick numerical calculations, they are an oversimplification of the true microphysics occurring inside the NS. Polytropes assume the same functional dependence between pressure and density throughout the entire star and do not account for any real differences that exist in different density regimes. Due to this reason, we only use polytopes as a proof of concept for the existence of scalarization and to make valid comparison between our results and those presented in Ref. [42] to ensure numerical consistency.

3.3.3.2 Tabulated Equations of state A complete description of the microphysics occurring inside NSs requires the full modeling of N-body quantum systems at extremely high pressures and densities. The calculations required to solve for these relations is very expensive and not practical on the fly for every density and pressure inside a NS. Moreover, because NS type densities cannot be observed in laboratories on Earth there is uncertainty on what physics is actually taking place at these densities. There have been numerous models proposed to describe matter at supra-nuclear densities and they have been tabulated such that one can interpolate them as needed.

For the purpose of this paper, we consider a wide range of tabulated EOSs that produce NSs with masses that are consistent with observations, most notably that of a near $2M_\odot$ pulsar in J0348+0432. We consider 11 different tabulated EOS [101] that satisfy this constraint: AP3-4 [102], ENG [103], H4 [104], MPA1 [105], MS0 [106], MS2 [106], PAL1 [107], SLy4 [108] [2] , and WFF1-2 [109]. All but one (H4) of these EOSs contain plain nuclear matter and *do not* contain any form of strange matter. Because these EOS arise from numerical calculations that include true microphysics (or at least various justified approximations) we consider these to be the most physically relevant of the EOSs that we consider and are the ones we use for our main results. More importantly, however, many of these EOSs are consistent with aLIGO's constraints placed from the observation of coalescing NSs [14].

[2]The SLy4 EOS we use here is commonly denoted as simply SLy in the literature.

3.3.3.3 Piecewise Polytropes A useful compromise between the simple polytropic and tabulated EOSs is a piecewise polytropic model that stitches together multiple polytropes in different density regions inside the NS. In particular, we consider the piecewise polytropic EOSs studied in Ref. [83] in which the authors developed a parameterized model that can accurately capture the feature of tabulated EOS. Of the 34 EOSs that the authors fit their model to, 8 of them overlap with the set of tabulated EOSs that we consider in this paper[3]. While these approximations have been used extensively in the literature for their convenience, we later investigate how these approximations affect the scalar charges that are developed in NSs. Hence, let us briefly discuss these EOSs, referring to Ref. [83] for a more detailed and complete description.

Similarly to the standard polytropic EOS, the various regions inside of the NS are described by a polytrope of the form

$$\tilde{p} = K_i \, \tilde{\rho}^{\Gamma_i} \,, \tag{3.44}$$

where now Γ_i is the adiabatic index for the ith region of the NS and K_i is the polytopic constant chosen to ensure continuity at the boundaries between regions. Similarly to the single polytrope case, the first law of thermodynamics in Eq. (3.43) is used to find the energy density in each region

$$\tilde{\epsilon}_i = (1 + a_i)\tilde{\rho}_i + \frac{1}{\Gamma_i - 1} K_i \tilde{\rho}_i^{\Gamma_i} \,, \tag{3.45}$$

[3]One might notice that, aside from the PAL1 EOS that is explicitly not contained in Ref. [83], there are 10 EOSs listed in the previous section that correspond to the EOSs that were fit in this paper. The data we received from Norbert Wex came from the original work by Lattimer and Prakash [101] and in fact the EOSs labeled MS0 and MS2 are *different* from those of the same name appearing in Ref. [83]. There appears to be a mismatch in nomenclature that we feel is worth pointing out.

where

$$a_i = \frac{\tilde{\epsilon}(\tilde{\rho}_{i-1})}{\tilde{\rho}_{i-1}} - 1 - \frac{K_i}{\Gamma_i - 1}\tilde{\rho}_{i-1}^{\Gamma_i - 1} \ , \tag{3.46}$$

is an integration constant that must be present in order to ensure that all fluid variable are continuous across the boundaries between regions. For the single polytrope case, the requirement that $\tilde{\epsilon}/\tilde{\rho} = 1$ in the limit that $\tilde{\rho} \to 0$ forces $a = 0$ and thus reduces Eq. (3.45) to Eq. (3.43).

We adopt a low-density EOS for the crust of the NS that is identical to the one presented in Table II of Ref. [83] where the SLy (SLy4 as appearing in this paper) is independently fit for $\tilde{\rho} \lesssim 10^{12}$ g/cm^3. The boundary between the crust and high-density EOS is then determined by the intersection of the respective polytropes and is ultimately determined by the value of Γ_1. Then, at a fixed baryonic density of $\tilde{\rho} = 10^{14.7}$ g/cm^3 and best fit pressure $\tilde{p}_1 = \tilde{p}(\tilde{\rho}_i)$ the first region is matched to a second region with adiabatic index of Γ_2 and polytropic constant K_2. Another match is then performed at another boundary $\tilde{\rho} = 10^{15}$ g/cm^3 to an even higher density region with constants Γ_3 and K_3. The complete set of parameters $\{\log(\tilde{p}), \Gamma_1, \Gamma_2, \Gamma_3\}$ represents the best fit values found in Table III of Ref. [83]. For our purposes, we focus exclusively on the approximations of AP3 and SLy4 to compare scalar charges between tabulated and piecewise polytropic EOSs.

3.4 Calculating the Scalar Charges

Now that we have a full description of the problem at hand, we solve the equations numerically to obtain the relevant scalar charges appearing in Eqs (3.25)-(3.27). We begin this section with an analytic description of the scalar charges, and then proceed with a description of our numerical methods for solving the field equations and extracting the various scalar charges. We then recap, but in more detail, the different regions of parameter space that we are concerned with and discuss their importance. We first present a comparison between some of our results and those originally found in Ref. [42], and then discuss our full results in each region of parameter space.

3.4.1 Analytic investigation of scalarization

The phenomenon of scalarization has been well studied in the literature over the past decades, particularly in the context of spontaneous scalarization occurring when $\beta_0 \lesssim -4.3$. However, it is useful to review what happens outside of this regime as well since there are still non-linear effects coming into play, particularly when $\beta_0 \gtrsim -3.5$. In this subsection we review the analytics that help guide our calculations in the different regions of parameter space.

Scalarization can be understood from an analytic standpoint when one makes a few simple approximations. In both theories we consider here, the conformal coupling takes the form $\alpha(\varphi) = \beta_0\varphi + \mathcal{O}(\varphi^2)$ in the limit that $\beta_0\varphi$ is relatively small compared to unity. Let us now consider the field equation for the scalar field in Eq. (3.6), but instead of considering the full nonlinear equation, we make a weak field approximation such that $\Box \to \delta_{ij}\nabla_i\nabla_j \to \nabla_r^2$ with the last term being the radial portion of the flat space Laplacian in spherical coordinates. We assume that $T_{\rm mat}$ is constant since we are considering weakly gravitating systems. As mentioned in [38], we do not expect the trace of the stress-energy tensor to be negative for weakly gravitating systems, but it is fruitful to leave its sign general and consider the full breadth of parameter space with the same analytics.

The assumptions made thus far allow one to write the equation of motion for the scalar field as

$$\nabla_r^2\varphi \;=\; -C^2\varphi\,\mathrm{sign}(\beta_0\,T_{\rm mat})\;, \tag{3.47}$$

where we have introduced the constant $C^2 = \kappa|\beta_0 T_{\rm mat}|$ for $r < R$, which vanishes when $r > R$. The field equation is still subject to the same boundary conditions as before, and thus, $\varphi(r=0) = \varphi_c$ and $\varphi'(r=0) = 0$ to ensure regularity at the center and to ensure the scalar field is continuous and differentiable at the surface.

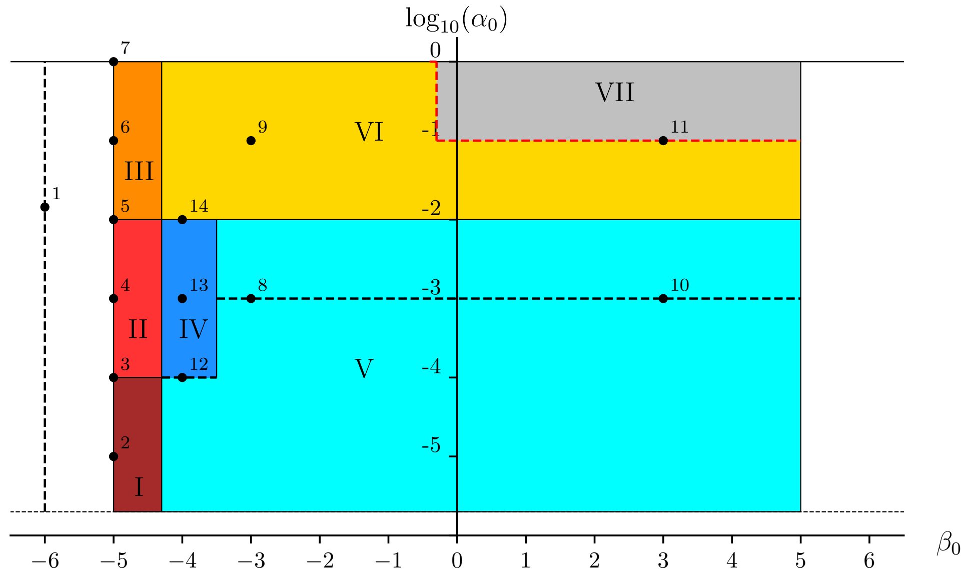

Figure 3.1: A breakdown of the parameter space we explore. Each colored region, labeled also by Roman numeral, has a different numerical grid associated with it that is explain in detail throughout the text. The numbered points appearing here represent points in parameter we use to estimate the error in our numerical calculations, the details of which can be found in Appendix 3.A.

Now we must solve Eq. (3.47) inside and outside the star, subject to the boundary conditions above. The exterior solution takes the form

$$\varphi = \varphi_\infty + \frac{G\omega_A}{r} + \mathcal{O}\left(\frac{1}{r^2}\right) \ , \tag{3.48}$$

where φ_∞ and ω_A are integration constants. There are two interesting scenarios that can occur within the star, namely when the product $\beta_0 T_{\rm mat}$ is positive and when it is negative. In the positive case, the interior solution for the scalar field takes the form

$$\varphi(r < R) \;=\; \frac{\varphi_\infty}{\cos{(CR)}} \frac{\sin{(C\,r)}}{C\,r} \;. \tag{3.49}$$

The asymptotic value of the scalar field at infinity φ_∞ can be chosen to be arbitrarily small, but even in the case of $\varphi_\infty \to 0$, the central value of the scalar field can still be non-zero if $\cos(CR) \to 0$ at the same rate. While this is an over-simplified description of the problem, one in which we essentially are assuming a constant density inside the star and ignoring non-linear effects, it does demonstrate that there can be non-trivial scalar field solutions even when one forces the asymptotic value of the scalar field to vanish.

In the situation where the product $\beta_0\,T_{\,\rm mat}$ is negative, there exists an opposite effect inside the star: any deviations from GR are exponentially suppressed. The negative case leads to an interior solutions of the form

$$\varphi(r < R) \;=\; \frac{\varphi_\infty}{\cosh{(CR)}} \frac{\sinh{(C\,r)}}{C\,r} \;, \tag{3.50}$$

in which case any non-vanishing value of φ_∞ is suppressed even further by $\cosh{(CR)}$. The suppression mechanism drives the STT solution to GR inside the star when $\beta_0\,T_{\,\rm mat} < 0$.

In this linear φ regime, the quantity $G\omega_A$ appearing in Eq. (3.48) can be expressed as

$$G\omega_A \;=\; -\varphi_\infty \left(R - \frac{\tan(CR)}{C} \right) \;, \tag{3.51}$$

in the case of $\beta_0\,T_{\,\rm mat} > 0$ and with the tangent exchanged for a hyperbolic tangent when $\beta_0\,T_{\,\rm mat} < 0$. Recalling from Sec. 3.2 that $\alpha_A \;=\; -\omega_A/m_A$ and that $\varphi_\infty = \alpha_0/\beta_0$

one finds that $\alpha_A \propto f(\beta_0, m_A){\alpha_0}^4$, as long as one can neglect non-linear interactions of the scalar field. While many of the most interesting effects of STTs, like spontaneous scalarization, occur in the most non-linear regions of parameter space, this simple relations provides valuable insight into the types of solutions one would expect in other regions of parameter space.

3.4.2 A classification of parameter space

Let us now use the analytic insight described above to guide us in our numerical exploration of the $\{\alpha_0,\, \beta_0\}$ parameter space shown in Fig. 3.1. We will break our investigation into six distinct regions in parameter space, each of them having distinct features that need to be handled differently when solving for the scalar charges numerically. In all of these regions we must set up some numerical grid in α_0, β_0, and m_A, and these grids are precisely how each of these regions differ from one another. We discuss the various regions in Fig, 3.1 in detail below, relying on the analytic insight above and our numerical results, and in the next subsections we will present the numerical techniques used in each region and our results.

There exist three regions, I–III (brown, red, and orange respectively) in Fig. 3.1 in which spontaneous scalarization occurs, i.e. when $\beta_0 \leq -4.3$. In all of these regions there exists a phase transition in the scalar field, with the sharpness of the transition being determined by the value of α_0 (lower values leading to more steep transitions). Due to the varying level of steepness in the phase transitions and the numerical limitations of taking derivatives, we have broken this region of β_0 into 3 distinct subregions in which we use different numerical techniques to most efficiently

[4]Technically, this relation should read $\alpha_A \propto f(\beta_0, m_A)\alpha_\infty$ as the scalar charge should always reduce to its weak field counter part α_∞ in the absence of strongly self-gravitating matter. However, these relations are already derived under weak field assumptions and in both theories $\alpha_\infty \approx \alpha_0$ in this regime.

explore the parameter space. In short, region I in Fig. 3.1 contains the sharpest transitions, and therefore requires a finer numerical grid in m_A to resolve the relevant features of interest. Region II contains less sharp transitions and it can be accurately explored with less grid points. Regions I and II both contain the same grid spacing in $\log_{10}(\alpha_0)$ and β_0, but a different spacing in m_A. Lastly, region III contains the same grid spacing in m_A and β_0 as region II, but it contains more grid points in α_0 to allow us to accurately calculate the numerical derivatives necessary for the scalar charges.

Region V (cyan) in Fig. 3.1 is where the non-linearity of the scalar field can effectively be neglected and hence the scalar charge turns out to scale as in Eq. (3.51). When we solve the full set of field equations we make no approximations, but the resulting scalar charges do indeed follow the scaling relation $\alpha_A \propto f(\beta_0, m_A)\alpha_0$. Thus, in region V we solve for a single set of solutions at a single value of α_0, lying on the black dashed lines in Fig. 3.1 at $\alpha_0 = 10^{-3}$ for $\beta_0 > -3.5$ and $\alpha_0 = 10^{-4}$ for $\beta_0 < -3.5$, and we use the scaling relation to populate the entire region. We numerically verify in Sec. 3.A.2 that these scaling relations are indeed accurate when compared to the full numerical exploration of this region of parameter space. This scalable region does not cover the entire parameter space where spontaneous scalarization does not occur. We have found numerically that the scaling does not hold when $\beta_0 < -3.5$ and when $\alpha_0 \in (10^{-4}, 10^{-2})$, which is why we have isolated this part of parameter space to region IV. In this region, we investigate the solutions as if we expected spontaneous scalarization.

For region VI in Fig. 3.1 we find that the scaling relations previously discussed no longer exist because of how large α_0 can become. The lack of quasi-analytic solutions here should not come as a surprise because this region has such large values of α_0 that STT modifications can be easily constrained with solar system observations. For completeness, however, we still investigate this region extensively as some parts of this parameter space are actually useful when placing binary pulsar constraints[5]. We have also removed a portion, region VII in gray, from the parameter space because we are not able to calculate NS solutions here. This has been noted in the literature before when considering DEF theory [41, 98], but in those papers, the authors only investigate small values of α_0 and focused on values of β_0 considerably larger than what we consider here. Nonetheless, we find results very similar in this gray region of parameter space for both DEF and MO theory and it becomes impossible to extract any useful information from our numerical calculations. Therefore, since binary pulsar typically do not probe this region and Solar System tests have already ruled it out, we are justified in neglecting it.

The final point to discuss regarding the parameter space is the vertical dashed line and numbered points appearing in Fig. 3.1. The black vertical dashed line at $\beta_0 = -6$ marks a set of special solutions we have calculated to compare our results to those original found in Ref. [42]. While we do not explore this region of parameter space in depth it provides a useful comparison to validate our code and make comparisons between known results in DEF theory and new results in MO. Details about the numbered points in Fig. 3.1 can be found in Table 3.3 and they represent a set of points we use to investigate the error in our numerical results. The details of this error analysis can be found in Sec. 3.A.

3.4.3 Numerical methodology

We parameterize our NS solutions by a choice of $\{\tilde{\rho}_c, \alpha_0, \beta_0\}$ which ultimately determines the star's gravitational mass m_A, baryonic mass $\bar{m}_A$, and the asymptotic

[5]In Ref. [7], for example, there exists a region near $\beta_0 \sim -2$ in which constraints on scalar dipole radiation fail to constrain STTs better than Cassini and other weak field tests. This "horn" appearing in the binary pulsar constraints occurs for NS-WD binaries in which the quantity $(\alpha_{NS} - \alpha_{WD})^2 \sim (\alpha_{NS} - \alpha_0)^2$ vanishes, which tends to happen near $\beta_0 \sim -2$.

value of the scalar field $\varphi_\infty = \alpha_0/\beta_0$. We take the approach of solving Eqs. (3.31) starting from the center of the NS, using Eqs. (3.32) to start our numerical integration away from the singularity at $\rho = \rho_{\min}$. We follow the methods employed in Refs. [82, 98] and use MATHEMATICA's default ODE solver[6] to integrate the equations to the surface of the NS where we then use Eqs. (3.40) to extract values at spatial infinity.

In order to begin the integrations, however, we must make a choice of $\tilde{\rho}_c$ and φ_c as these are the two independent parameters appearing in the boundary conditions. It is near impossible to guess the correct value of φ_c that correspond to a given $\varphi_\infty = \alpha_0/\beta_0$ to within a small tolerance. Therefore, we use a Newton-Raphson shooting method to converge onto the correct value of φ_c. In particular, we solve the equations again with a new central value of the scalar field $\varphi_{c,n+1} = \varphi_{c,n} + \Delta\varphi_c$, which gives a slightly different value of φ_∞. The difference of the extracted values of φ_∞ allow us to construct a simple difference equation

$$\varphi_{c,n+1} \;=\; \varphi_{c,n} - \Delta\varphi_c \frac{\varphi_{\infty,n} - \alpha_0/\beta_0}{\varphi_{\infty,n+1} - \varphi_{\infty,n}} \;, \tag{3.52}$$

where n is the iteration number. The equation above allows us to predict a new value of φ_c that gives a value of φ_∞ that is closer to the desired result, and we iterate this process until the resulting value of φ_∞ is equivalent to α_0/β_0 to within some numerical tolerance. At the subsequent point in $\tilde{\rho}_c$ we use the previous value of φ_c as the starting point for the shooting, which typically allows convergence to within numerical tolerance in about 2-3 iterations.

The method described above provides NS solutions corresponding to a single combination of $\{\tilde{\rho}_c,\, \alpha_0,\, \beta_0\}$ for any choice of theory and EOS. It is convenient that

[6]The default method used is LSODA which is a variant of the original LSODE (Livermore Solver for Ordinary Differential Equations) approach to solving a wide class of differential equations.

the scalar charge α_A can be extracted directly from the boundary conditions at the surface. The quantities β_A and k_A, however, must be calculated by taking derivatives across multiple solutions while keeping the baryonic mass constant. The most accurate way to take these derivatives would involve parameterizing the NS solutions by $\{\bar{m}_A,\, \alpha_0,\, \beta_0\}$ instead and shooting in *both* $\tilde{\rho}_c$ and φ_c. Such an approach would allow one to construct multiple NS solutions with identical values of $\bar{m}_A$ and varying values of φ_∞, corresponding to different values of α_0, which is required for the derivatives needed to calculate β_A and k_A. While this approach works extremely well, it is very computationally expensive since one must now shoot in two dimensions multiple times just to calculate the scalar charges for a single combination of $\{\bar{m}_A,\, \alpha_0,\, \beta_0\}$. To completely populate the parameter space of interest one must compute the charges for roughly 10^5 combinations of $\{\bar{m}_A,\, \alpha_0,\, \beta_0\}$ just for a single EOS and theory choice. This quickly becomes cumbersome from a computational standpoint so we decided to take a different approach.

Our computational method is as follows. We continue to parameterize the NS solutions with $\{\tilde{\rho}_c,\, \alpha_0,\, \beta_0\}$, but rather than focusing on a single value of $\bar{m}_A$, we calculate an entire mass-radius (MR) curve of solutions, corresponding to a set of $\{\tilde{\rho}_{c,i}\}$, for a large discrete set of $\{\alpha_0,\, \beta_0\}$ values. This approach allows us to then interpolate the scalar charge α_A as a function of the baryonic mass, thus generating curves like those in Fig. 3.2. Because we have a finely discretized grid in $\bar{m}_A$, we can interpolate between points and extract $\alpha_A(\bar{m}_A)$ for *any* value of baryonic mass, and we can do the same for every curve we calculate. Therefore, we can compute numerical derivatives of the scalar charge (or any other quantity) at any value of baryonic mass in a computationally efficient way. While this method is prone to more numerical error than the previous one, it allows us to sample the entire parameter space very finely and it can be carried out orders of magnitude faster. A discussion of the errors associated with our methods is presented in Sec. 3.A.2

Method	-4	-3	-2	-1	0	1	2	3	4
central	—	—	1/12	-2/3	0	2/3	-1/12	—	—
forward	—	—	—	—	-25/4	4	-3	4/3	-1/4
backward	1/4	-4/3	3	-4	25/4	—	—	—	—

Table 3.1: The finite difference coefficients found in Eqs. (3.53)-(3.55). For every method (central, forward, or backward) the columns denote the value of the coefficient for the corresponding subscripts found in Eqs. (3.53)-(3.55) .

Let us now discuss the way we take numerical derivatives. We choose to use a fourth-order accurate finite difference scheme to calculate the derivatives in Eqs. (3.26)-(3.27). For reasons discussed below, we have to use central, forward, and backward finite difference schemes in order to most effectively utilize our numerical grid, and they take the forms

$$\left(\frac{dF}{d\varphi_0}\right)_c = \frac{c_{\text{-}2}F_{\text{-}2} + c_{\text{-}1}F_{\text{-}1} + c_0F_0 + c_{+1}F_{+1} + c_{+2}F_{+2}}{\Delta\varphi_0}\,, \tag{3.53}$$

$$\left(\frac{dF}{d\varphi_0}\right)_f = \frac{f_0F_0 + f_{+1}F_{+1} + f_{+2}F_{+2} + f_{+3}F_{+3} + f_{+4}F_{+4}}{\Delta\varphi_0}\,, \tag{3.54}$$

$$\left(\frac{dF}{d\varphi_0}\right)_b = \frac{b_{\text{-}4}F_{\text{-}4} + b_{\text{-}3}F_{\text{-}3} + b_{\text{-}2}F_{\text{-}2} + b_{\text{-}1}F_{\text{-}1} + b_0F_0}{\Delta\varphi_0}\,, \tag{3.55}$$

where $F_{\pm n} = F(\varphi_0 \pm n\Delta\varphi_0)$, and c_i, f_i, and b_i are the corresponding finite difference coefficients for central, forward, and backward derivatives respectively found in Table 3.1.

Let us now briefly discuss the numerical grid in parameter space. Each region of parameter space in Fig. 3.1 uses a different numerical grid in $\{m_A,\, \alpha_0,\, \beta_0\}$. The spacing in α_0 is determined by the level of accuracy we want when using the various finite difference schemes for the derivatives. Since $\Delta\varphi \propto \Delta\alpha_0$ we need to choose our spacing such that $\Delta\alpha_0$ between consecutive solutions branches is not too large.

Finally, the β_0 grid is determined strictly by the presence of spontaneous scalarization. Therefore, if $\beta < -4.3$, the grid spacing is $\Delta\beta_0 = 0.02$ and otherwise it is $\Delta\beta_0 = 0.1$. The details of the grids in each subspace are presented in the next subsection.

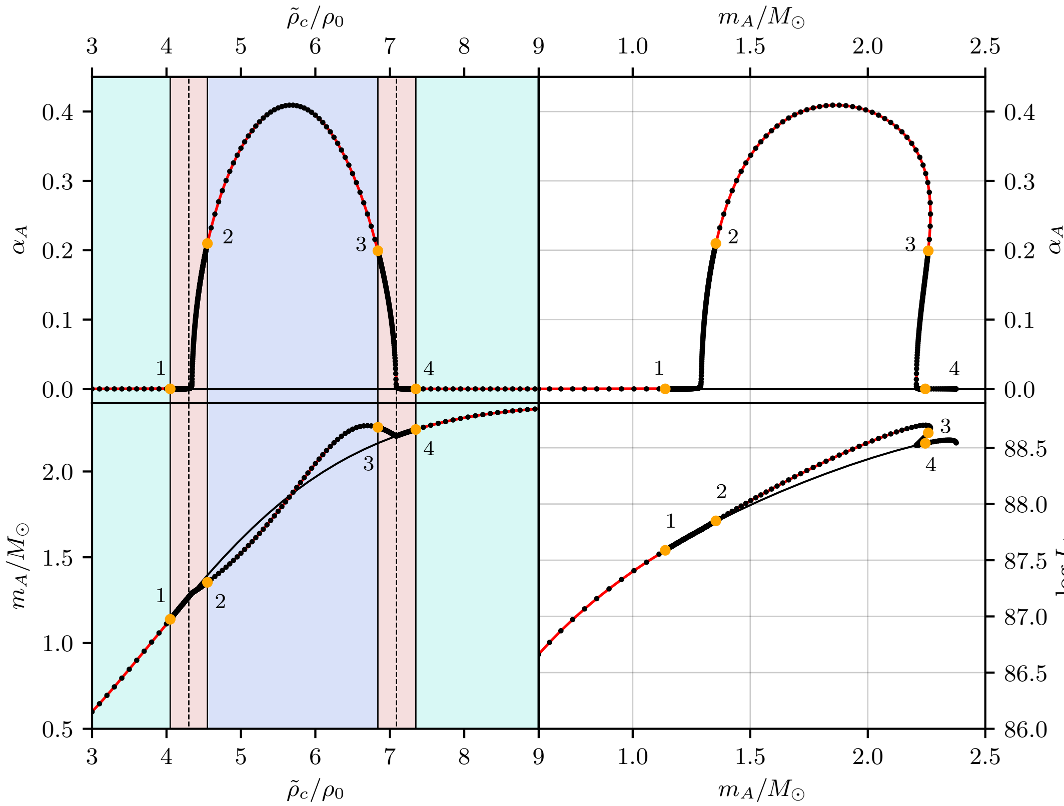

Figure 3.2: As example of the numerical grid we use and the resulting solutions for m_A for DEF theory and AP3 EOS with $\beta_0 = -5.0$ and $\alpha_0 = 10^{-5}$. Starting counter-clockwise from the top-left: $\alpha_A(\tilde{\rho}_c)$, $\alpha_A(m_A)$, $\log_{10} I_A(m_A)$, and $m_A(\tilde{\rho}_c)$. The orange points marked 1–4 represent the same NS solution on each of the panels and the solid black curves appearing in each panel represents the GR solution. The green regions represent the lowest resolution, followed by the blue region, and with th red regions being most dense, as described in detail in the text. The vertical dashed lines represent the critical values of central density at which point spontaneously scalarization "turns on" and "turns off".

The spacing in m_A in each region is determined by the presence of any sharp features that may appear in the solutions, such as spontaneous scalarization. The green regions appearing in the left panels of Fig. 3.2 represent the lowest resolution portions of our grid, in which we have a grid point every $0.1\rho_0$; we call this value $\Delta\rho_c^{GR}$ since it is dense enough to accurately reproduce a MR curve in GR. Spontaneous scalarization turns "on" and "off" in the red regions in Fig. 3.2, and in order to capture the phase transition effectively, we increase our resolution to $\Delta\rho_c^{PT} = \Delta\rho_c^{GR}/800$, where PT stands for phase transition[7]. The blue region in Fig. 3.2 between the phase transitions is where there are no sharp features, but where we still want increased resolution since non-linear effects do come into play; in these regions, we use a grid spacing $\Delta\rho_c^{scal} = \Delta\rho_c^{GR}/20$ where *scal* stands for scalarization. Figure 3.2 illustrates the density of grid points in these different regions by the number of orange circles appearing along each curve. We limit our solutions to values of $\tilde{\rho}_c$ that give a $0.5M_\odot$ NS in GR and the $\tilde{\rho}_c$ that predicts the maximum mass NS in GR, for each EOS we consider. As in the (α_0, β_0) grid spacing case, the details of the $\tilde{\rho}_c$ grid are presented in the next subsection.

3.4.4 Numerical results

3.4.4.1 Code Verification: the $\beta_0 = -6.0$ case

With a basic idea of our numerical grid and numerical methods for solving NS solutions in hand, let us present a comparison between our results and the ones found in [42]. In that study, the authors used the polytropic equation of state described in Sec. 3.3.3.1 and they show results for the $\beta_0 = -6$ and $|\varphi_\infty| = 2.4 \times 10^{-3}$ (or $\alpha_0 = 1.44 \times 10^{-2}$ in our framework) case, which corresponds to point 1 in Fig. 3.1. In addition to using the polytropic EOS of [42], we will also show here results for the tabulated and piecewise polytropic

[7] We only increase this resolution by a factor of 800 when we consider $\alpha_0 \leq 10^{-4}$ and $\beta_0 < -4.3$. When $\alpha_0 > 10^{-4}$, we find that we do not need to sample as many points to fully capture the features of the phase transition, hence we allow $\Delta\rho_c^{PT} = \Delta\rho_c^{GR}/200$. In regions where spontaneous scalarization does not occur, i.e. $\beta > -4.3$, there is no phase transition and we simply use $\Delta\rho_c = \Delta\rho_c^{GR}/20$ everywhere.

versions of AP3 for both the DEF and MO STTs.

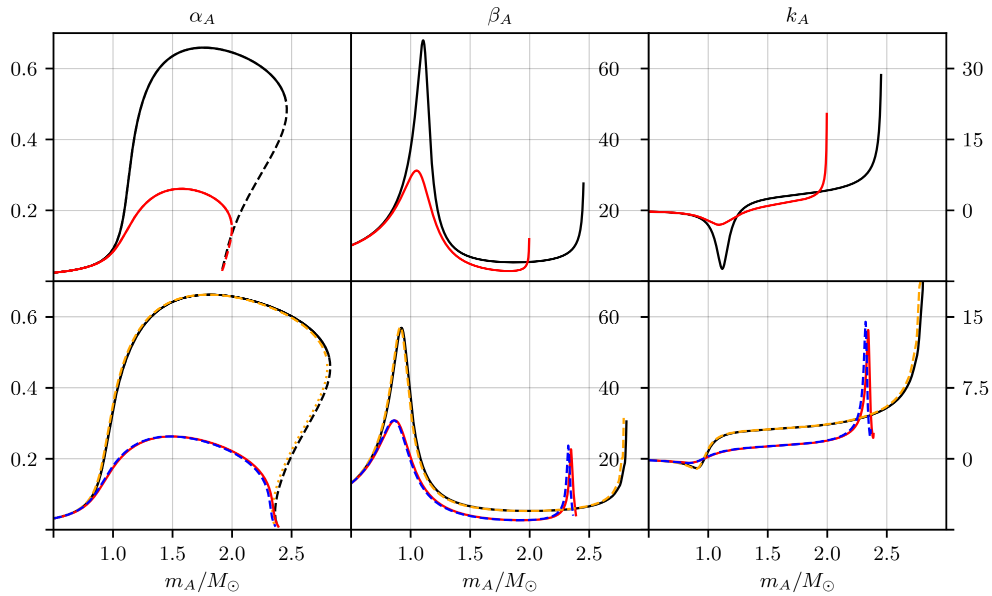

Figure 3.3: The different scalar charges α_A, β_A, and k_A, appearing in the first, second, and third column respectively, as function of the gravitational mass of the NS for $\beta_0 = -6$ and $\alpha_0 = 1.44 \times 10^{-2}$. The top row was obtained using the polytropic equation of state in Sec. 3.3.3.1, with black curves corresponding to DEF theory and red curves to MO theory. The bottom row was obtained using the tabulated AP3 EOS (black and red) and its piecewise polytropic approximant (orange and blue) where black and orange curves are for DEF theory and red and blue for MO theory.

Let us first take a look at the top row of Fig. 3.3. Comparing our result to those in [42], we see that the black curves, those for DEF theory, are in great agreement[8]. The red curves in Fig. 3.3 are the results for the MO theory and we see that in every case the magnitude of the charge is less than those of DEF theory and that they also do not reach very high masses. This feature is general for MO theory, i.e. this feature is not a result of a special choice of α_0 and β_0. The reasoning behind this is that the curvature of the conformal potential appearing in Eq. (3.13) is not as large as that of

[8]Noticed that we have used gravitational mass instead of baryonic mass on the horizontal axis.

DEF theory, and therefore, the excitation of the scalar field is never as strong once the instability occurs. The curves for β_A and k_A formally diverge at higher masses, a phenomenon due to the fact that these are derivatives of quantities that "turn over" on themselves, e.g. in the right panels Fig. 3.2 one can see that the slope in α_A and $\log_{10} I_A$ become infinite at some point as the mass increases.

The bottom row in Fig. 3.3 shows the same scalar charges but for realistic equations of state, namely AP3 here, and its piecewise polytropic approximate. The maximum values of α_A are very weakly affected by the EOS in both theories. There is, however, a strong dependence on the EOS when it comes to the location of the critical mass, $m_{\rm crit}$, at which spontaneous scalarization occurs, and the maximum mass above which stable NSs do not exist. The other scalar charges, β_A and k_A, are quite different between the different EOSs and theories. The phase transition is now less sharp, and therefore, the magnitude of β_A is smaller than in the polytropic case. Moreover, it happens to be the case here that in MO theory there is no formal divergence in β_A at large masses. Finally, the "negative spike" in k_A that usually occurs is greatly suppressed for realistic EOSs.

The piecewise polytropic EOS leads to scalar charges that are very similar to those found with a tabulated EOS. Aside from a very slight shift in the masses, the structure and magnitude of the scalar charges are nearly identical. The small differences are likely due to the fact that polytropes are just too simple to accurately capture the different physics that occurs at different densities inside NSs, which can over/under exaggerate features we find in the scalar charges. Using the piecewise polytropes, however, can speed up numerical calculations immensely since they are analytic. A more detailed investigation of the differences between tabulated and piecewise polytrope results can be found in Sec. 3.A.3

3.4.4.2 Spontaneous scalarization: $\beta_0 \leq -4.3$ As is well-known in the literature, spontaneous scalarization occurs in STTs when $\beta < -4.3$ regardless of the EOS. As demonstrated in the previous section, there exists a m_{crit} at which a phase transition of the scalar field occurs, but the precise value of this mass, however, depends on the theory, the EOS, and the value of β_0. These dependencies require that we determine what this critical mass is, and to place a finer grid in $\tilde{\rho}_c$ centered near this location to ensure we capture the details of the phase transition with enough accuracy and precision to calculate the scalar charges at these points, cf. Fig. 3.2. Spontaneous scalarization occurs in regions I–III (brown, red, and orange) of Fig. 3.1, each of which has a slightly different grid that we discuss in detail next.

Region I (Brown):

This region has the finest grid in $\tilde{\rho}_c$ because the phase transition is most sharp here, and near the transition we decrease our spacing in $\tilde{\rho}_c$ by a factor of 800 relative to $\Delta\rho_c^{GR}$, as mentioned earlier. This level of resolution requires around 600 NS solutions in total for each value of α_0 and β_0. In this region, we use $\alpha \in \{1.2, 1.1, \cdots, 0.2\} \times 10^{\text{mag}}$ where $\text{mag} \in \{-4, -5\}$, and a spacing in β_0 of $\Delta\beta_0 = 0.02$. Spacing α_0 in this manner gives a spacing in φ of $\Delta\varphi = 10^{\text{mag}-1}/\beta_0 \sim 2 \times 10^{\text{mag}}$ for this range of β_0. Since our finite difference schemes are all fourth-order accurate, our spacing in α_0 is small enough to confidently calculate the needed derivatives[9]. This particular spacing allows us to use the central finite difference scheme for mantissa of α_0 from 1.0 to 0.4, the forward finite difference scheme for 0.2 and 0.3, and the backward scheme for 1.2 and 1.1. Since we need to calculate 1.2, 1.1, 0.3, and 0.2 for using the central finite difference scheme, we automatically get the derivatives at these extra points for free

[9] Going to smaller values of α_0 is difficult because we can never let it change signs when calculating the derivatives. This means that $\Delta\alpha_0$ *must* always be smaller than α_0, and it is computationally expensive to calculate solutions with enough accuracy and precision for $\Delta\alpha_0 \lesssim 10^{-6}$.

just by changing the finite differencing.

Region II (Red):

In this region, we are able to use only a factor of 200 more points near the transition regions, i.e. $\Delta\rho_c^{GR}/200$. We use the same grid in β_0 here as in region I above, i.e. $\Delta\beta_0 = 0.02$. Our grid in α_0 is set up in a similar way as well, i.e. $\alpha \in \{1.2,\, 1.1,\, \cdots,\, 0.2\} \times 10^{\text{mag}}$ where $\text{mag} \in \{-2,\, -3\}$, and are both set up to make efficient use of the finite differences introduced above. As one can see in Fig. 3.3 for example, the phase transitions are not as sharp in this region as they are in region I (see Fig. 3.2), and this allows us to confidently under-sample m_A relative to these smaller values of α_0.

Region III (Orange):

In this region, the spacing in α_0 is finer than what we used before. Overall, we adopt a similar scheme as before, but we now require a finer grid centered around the main values of α_0 we are interested in. Here we use $\alpha_0 \in \{1.0,\, 0.9,\, \cdots,\, 0.2\} \times 10^{\text{mag}}$ with $\text{mag} \in \{0,\, -1\}$ as the main grid points, and around each of these grid points we choose the set $\alpha_0 \in \{+2, +1, -1, -2\} \times 10^{\text{mag}-3}$ to give us the other necessary points needed for the finite differences. These choices roughly enforce the same level of accuracy in our results when compared to the grids used for smaller values of α_0.

Region IV (Blue):

This region of Fig. 3.1 extends to larger values of β_0 than where spontaneous scalarization occurs, but there are still non-linear effects here that come into play and prevent us from using the quasi-analytic relations. In this region, we only sample in intervals of $\Delta\beta_0 = 0.1$, but we must sample α_0 on a grid like that used in region I. Thus, region IV is essentially a transition region between spontaneous scalarization and the rest of parameter space, and thus it requires special consideration.

Scalar Charges:

Some representative results for the various scalar charges in MO theory can be found in Fig. 3.4, for multiple values of α_0 and β_0 described in the caption. The first three rows in Fig. 3.4 show the behavior of the scalar charges for $-5 \leq \beta_0 \leq -4.0$, ranging from most red to most blue respectively, and three orders of magnitude in α_0. Notice that as α_0 decreases, the growth of α_A becomes more rapid as the phase transition of the scalar field becomes more sudden. As a result of this, the peaks in β_A and k_A increase in magnitude and decrease in width because higher order effects become more localized in m_A. One also notices that the location of $m_{\text{ crit}}$, the mass at which spontaneous scalarization turns "on", moves towards larger masses as β_0 become less negative, as one would expect [42].

The maximum value of β_A at $m_{\text{ crit}}$ decreases as we decrease $|\beta_0|$, while the max values of the k_A tends to increase. A possible explanation for this is related to the location of $m_{\text{ crit}}$. For the situations where $m_{\text{ crit}}$ is larger, the NSs at this mass have a larger moment of inertia, and therefor, it is possible the the NS's inertia is more sensitive to the external scalar field, and hence the increase in k_A. This reasoning also explains why the right peaks of k_A are larger than the left peaks[10]. We have determined numerically that the max values $\beta_{A,\max}$ and $k_{A,\max}$ follow simple linear relations in $\log_{10}$ space for α_0 and a *fixed* β_0. The coefficient of these relations remain

[10]The appearance of this second peaks is somewhat unique to MO theory for this range of β_0. As one can see in Fig. 3.3, β_A and k_A diverge for high masses in DEF theory but not in MO. For more negative values of β_0, however, MO theory also exhibits such divergences for large masses.

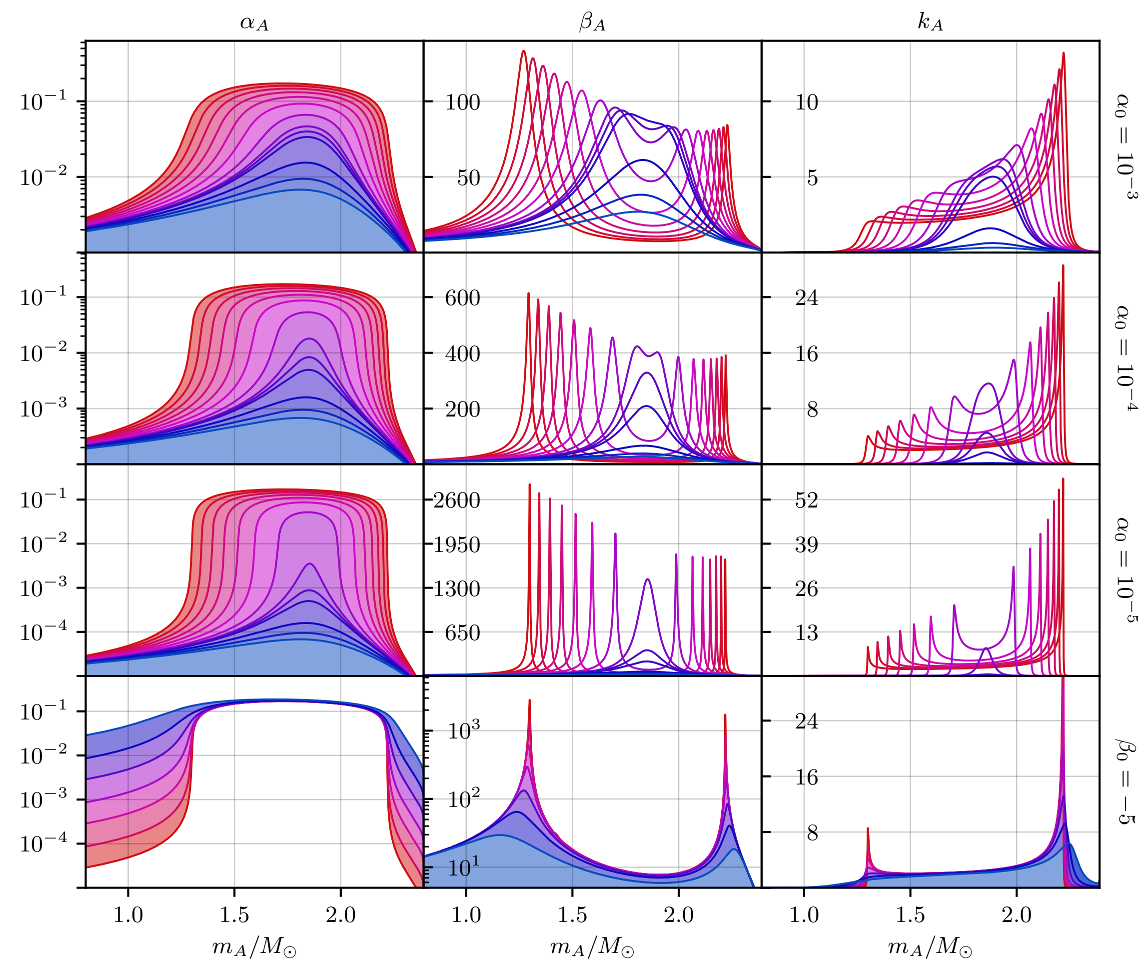

Figure 3.4: The behavior of the scalar charges as one changes α_0 and β_0. Here we have used MO theory with AP3 EOS. The first three rows correspond to constant values of α_0 (show on the right) for $-5.0 \leq \beta_0 \leq -4.0$, ranging in color from most red to most blue respectively. The bottom row corresponds to $\beta_0 = -5$ and $-5 \leq \log_{10}\alpha_0 \leq -2$, with colors from red to blue respectively. The shaded regions represent the smooth transitions in the solutions from one curve to the next and they continue to follow these trends as one continues to change the parameters α_0 and β_0.

EOS and theory dependent, but they take the general form

$$\log_{10}\beta_{A,\mathrm{max}} = B_0(\beta_0) + B_1(\beta_0)\log_{10}\alpha_0 \ , \tag{3.56}$$

$$\log_{10}k_{A,\mathrm{max}} = K_0(\beta_0) + K_1(\beta_0)\log_{10}\alpha_0 \ , \tag{3.57}$$

where B_0, B_1, K_0, and K_1 are coefficients that depend on the value of β_0. It is worth pointing out that B_1 and K_1 are always negative for *all* values of β_0 that we consider, and there is no reason to think that this would be different for more negative values of β_0. This means that $\beta_{A,\mathrm{max}}$ and $k_{A,\mathrm{max}}$ *always* increase(decrease) with decreasing(increasing) α_0 as one might expect. Moreover, for our data we find that B_1 is always less than 2, and is typically less than unity. This is important because the combination $\alpha_0^2\beta_A$ appears directly in the PPK parameter $\dot{\omega}$ for binary pulsars with a companion white dwarf. While is it hard to numerically investigate regions of parameter space with $\alpha_0 < 10^{-5}$, these linear relations tell us that the combination $\alpha_0^2\beta_A$ will always decrease with decreasing α_0 and have negligible effect on the PPK parameters. These relations only hold for $\alpha_0 < 10^{-2}$ but they provide a convenient way to estimate the maximum value of the scalar charges without numerically solving the field equations.

The bottom row of Fig. 3.4 shows the behavior of the charges for a constant $\beta_0 = -5$, but multiple orders of magnitude in α_0, red corresponding to the smallest values and blue to the largest. As one may expect, the overall magnitude of α_A is determined by the values of β_0, while its growth rate near the critical mass is determined by α_0 and is correlated directly with the magnitude of β_A. A similar statement can be made for k_A in that α_0 determines how sudden the growth of the scalar field is, and therefore, it leads to larger values of k_A near the critical mass at which these transitions occur.

3.4.4.3 No Spontaneous Scalarization: $\beta_0 > -4.3$

Region V (Cyan):

This region of parameter space is perhaps the simplest and easiest to explore numerically. As mentioned in Sec. 3.4.1, as long as α_0 is not too large, there exist scaling relations that we can use to calculate the scalar charges. Reiterating what we explained in that section, in this region of parameter space we can assume the scalar charge α_A takes the form

$$\alpha_A = \alpha_0 f(\beta_0, m_A) \ , \tag{3.58}$$

which then allows us to derive simple relations for the other scalar charges. Taking the derivative of this scalar charge, and applying the chain rule to the definition of β_A, we find

$$\beta_A = \frac{\partial \alpha_A}{\partial \alpha_0} \left(\frac{\partial \varphi_\infty}{\partial \alpha_0} \right)^{-1} = \beta_0 \, f(\beta_0, m_A) = \frac{\alpha_A}{\varphi_\infty} \ . \tag{3.59}$$

Equation (3.59) tells us that, for any value of β_0, $\beta_A(m_A)$ is the same for all values of $\alpha_0 \lesssim 10^{-2}$. Moreover, this equation also tells us that β_A is always directly proportional to α_A, meaning that we technically do not even need to take any derivatives to determine it.

We can find a similar relation to that in Eq. (3.58) for the inertial charge k_A, but the derivation is slightly more complicated. Starting with Eqs. (3.40i)-(3.40j) and assuming weak fields everywhere such that $e^{\hat{\nu}} \sim 1$ one finds that the moment of inertia becomes

$$I = \frac{J}{\Omega} \approx \frac{Gm^2 R(3 - \alpha_A^2)}{3c^2} \ , \tag{3.60}$$

where we have also neglected terms of order $(Gm/Rc^2)^2$. Using this in the definition for k_A in Eq. (3.27) we find

$$k_A \approx \alpha_A \left(2 + \frac{m}{R} \frac{\partial R}{\partial m} - \frac{2}{3} \beta_A \right) \ , \tag{3.61}$$

where we have made use of the definitions of the other scalar charges α_A and β_A.

Then, making use of Eqs. (3.58)-(3.59) we find that

$$k_A \;=\; \alpha_0\, g(\beta_0, m_A) \;, \tag{3.62}$$

where g is a function independent of α_0.

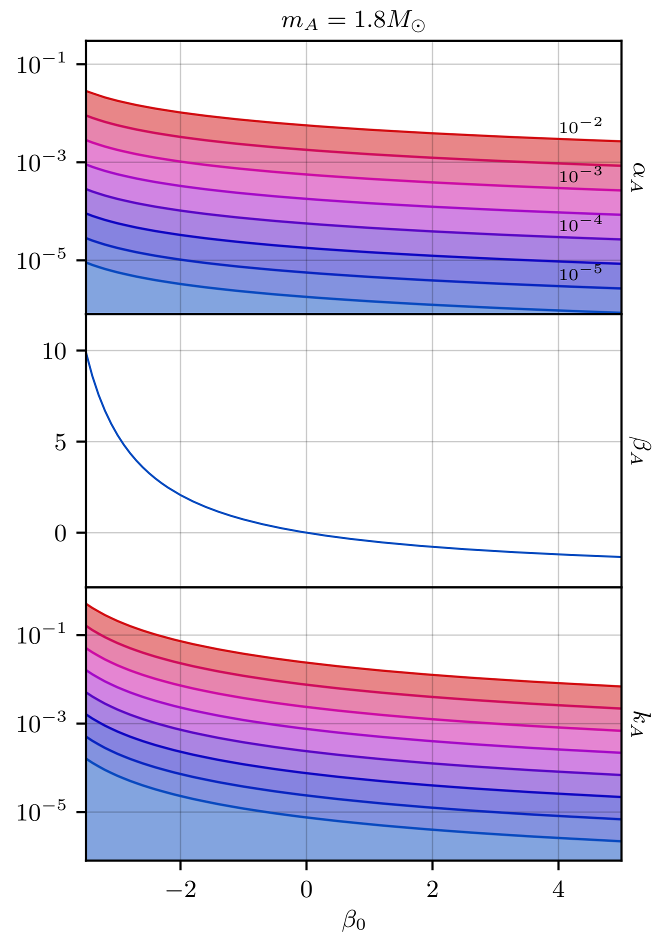

Figure 3.5: An example of the scaling relations described in the text for MO theory and AP3 EOS. The scalar charges α_A and k_A do indeed scale directly with α_0 and β_A behaves independent of the value of α_0.

The scaling relations we have introduced make the exploration of this region in β_0 almost trivial. We simply calculate the three scalar charges for points in parameter space lying on the horizontal dashed lines of Fig. 3.1 (at $\alpha_0 = 10^{-4}$ and $\alpha_0 = 10^{-3}$), and then, we rescale the results to find the charges for any other point in region V, holding β_0 constant. For the solutions we do calculate directly, we use a grid in β_0 given by $\Delta\beta_0 = 0.01$ and a grid in $\tilde{\rho}_c$ given by $\Delta\rho_c^{GR}/20$. Because there are no sharp features in the scalar charges in this region of parameter space, we sample considerably less central densities when compared to when spontaneous scalarization occurs.

Region VI (Yellow):

This region presents the same numerical difficulties as region III, expect that there is a lack of spontaneous scalarization in region VI. We use the same grids in β_0 and α_0 as those used in region III, and the same grid in $\tilde{\rho}_c$ as that used in region V. Note, however, the the gray region in Fig. 3.1 cuts out a significant portion of region VI. As we mentioned earlier, this is because we cannot find stable NS solutions in the gray region, and we must thus omit them from our analysis since they are extremely unlikely to affect binary pulsars constraints.

Scalar Charges:

Some representative results of the scalar charges in region V are shown in Fig. 3.5. In this figure, we hold m_A constant and plot the scalar charges as a function of β_0 spanning the entire region for $\beta_0 \geq -3.5$. Each curve in Fig. 3.5 represents a different value of α_0 and it becomes clear that $\log_{10}\alpha_A$ and $\log_{10}k_A$ scale *directly* with $\log_{10}\alpha_0$, showing that the relations in Eqs. (3.58) and (3.62) are indeed accurate. Moreover, the value of β_A shown in the middle panel of Fig. 3.5 shows no dependence on α_0, verifying that Eq. 3.59 holds.

3.5 Using the data file

Now that we have discussed how we calculate the charges and presented some of the results, let us discuss how one can use the end product of this analysis: the data generated for all the scalar charges. This section explains how the master data file is generated, what its properties and limitations are and

3.5.1 The generation of the master data file

We first set up our numerical grid according to Sec. 3.4 and subsections therein. From each NS solution we extract the boundary conditions in Eqs. (3.40) and save them to file for post-processing. The previous step requires the bulk of the computational time, as we need to calculate on the order of 10^5 different NS solutions (1 for each combination of $\{\tilde{\rho}_c,\, \alpha_0,\, \beta_0\}$) for *each* combination of theory (DEF or MO) and EOS in Sec. 3.3.3.2.

With the full set of data in hand for a theory-EOS combination, we now process it to extract the scalar charges. As we mentioned in Sec. 3.4, we interpolate the raw data in order to extract information from more masses than we actually sampled. To do this interpolation, however, we need to proceed with caution when dealing with NS that spontaneous scalarize, like those in Fig. 3.3. One notices that α_A “turns over” on itself for large masses. While this feature is not present for every set of NSs that undergoes spontaneous scalarization, it does present a problem for interpolation since the function is multi-valued. To avoid this issue, we remove any data past the point when the slope of α_A becomes infinite and simply interpolate the data up until this point.

For some EOSs in DEF theory, specifically AP4, ENG, WFF1, and WFF2, α_A becomes double valued at masses that are less than $2.1 M_\odot$. This is not a real issue, but the method we described above does not work for these EOSs, since we want to require that our data *at least* go up to $2M_\odot$, and preferably $2.1M_\odot$. Therefore, rather than removing the data past the "turn over" point, we remove *only* the points that lie on the unstable branch of solutions, i.e. the ones that coincidentally make α_A double valued (cf. the dashed points in the top left panel of Fig. 3.3). This is possible because, at least when spontaneous scalarization occurs, there is *always* NS solutions that reach maximum masses that are *at least* as large as the maximum mass in GR[11]. With the unstable points of the solution removed we simply continue with the interpolation as described in the previous paragraph.

In total we must interpolate 4 separate functions to give us the data we need for constructing the data files, which are $\{m_A(\bar{m}_A),\, \bar{m}_A(m_A),\, \alpha_A(\bar{m}_A),\, \log I_A(\bar{m}_A)\}$. We need α_A and $\log I_A$ as function of the baryonic mass for each φ_∞ in order to take the relevant derivatives in Eqs. (3.25)-(3.27) and we need $\{m_A(\bar{m}_A),\, \bar{m}_A(m_A)\}$ in order to freely switch back and forth between baryonic and gravitational mass[12]. For the two masses, we interpolate them with a simple linear method to remove any possible artifacts that arise from the interpolation itself. For α_A we implement different interpolation schemes depending on if spontaneous scalarization occurs. If spontaneous scalarization is absent, we simply use a cubic spline on α_A and this does great since the curves are smooth and generally free of any numerical anomalies. If spontaneous scalarization is present, however, then we use a cubic spline on $\log_{10} \alpha_A$ as this helps us better handle the rapid growth of the scalar field, especially when

[11] This can be seen from a mass-density curve like that in Fig 3.2, in which case the scalarized branch of solutions "departs" from the GR curve and eventually "return" for larger values of $\tilde{\rho}_c$. Therefore, even if the scalarized branch does not produce a NS with mass greater than the maximum mass in GR, the GR branch will.

[12] The gravitational mass is the one appearing in parameterized-post-Keplerian parameters that get constrained from binary pulsar experiments. Therefore, we need the baryonic mass to take the appropriate derivatives for the scalar charges, and the gravitational mass to link our results to binary pulsar experiments.

α_A	β_A	k_A	$\bar{m}_A$	m_A	α_0	$\log_{10}\alpha_0$	β_0
0.444979	0.270288	0.931259	1.16903	1.000	1.	0.	-5.00
0.444787	0.270318	0.931345	1.17155	1.002	1.	0.	-5.00
0.444595	0.270350	0.931432	1.17408	1.004	1.	0.	-5.00
$\vdots$	$\vdots$	$\vdots$	$\vdots$	$\vdots$	1.	0.	-5.00
0.331799	0.410289	1.101105	2.67262	2.100	1.	0.	-5.00
0.440000	0.314515	0.925646	1.15792	1.000	0.9	-0.045757	-5.00
0.439811	0.314451	0.925772	1.16041	1.002	0.9	-0.045757	-5.00
$\vdots$	$\vdots$	$\vdots$	$\vdots$	$\vdots$	$\vdots$	$\vdots$	-5.00
0.120843	10.909670	4.323983	2.50472	2.100	0.000002	-5.69897	-5.00
0.444997	0.270390	0.931196	1.16931	1.000	1.	0.	-4.98
$\vdots$	$\vdots$	$\vdots$	$\vdots$	$\vdots$	$\vdots$	$\vdots$	$\vdots$
$\vdots$	$\vdots$	$\vdots$	$\vdots$	$\vdots$	$\vdots$	$\vdots$	$\vdots$
0.0000004	1.062219	-0.000001	2.50430	2.100	0.000002	-5.69897	5.00

Table 3.2: An example of the layout of the data file for MO theory and AP3 EOS. For a given value of β_0 we tabulated the data for every value of α_0, of which for every value of α_0 we tabulate data for all values of m_A using the grid described in the text. This pattern repeats for all values of $-5 \leq \beta_0 \leq +5$ that we sampled. The definitions of the quantities in the columns is described in the text.

$\alpha_0 < 10^{-4}$. We find that the errors, discussed in Sec. 3.A.1, are significantly smaller when we interpolate $\log_{10}\alpha_A$ instead of just α_A. Lastly, we interpolate $\log I_A$ with a cubic spline as well, and while this may introduce some error for low masses, it better suites the data for larger masses, c.f Sec. 3.A.1 for a discussion.

What follows after the interpolation of the raw data is the calculation of the scalar charges β_A and k_A according to Eq. (3.26) and Eq. (3.27) respectively, making use of the various finite difference schemes in Eqs. (3.53)-(3.55). At this point we are able to produce the data we have shown in our figures thus far, and we have the ability to sample our results as finely as we need to in m_A in order to produce the most accurate results. However, when producing the master data files for each theory-EOS combination we do not have the luxury of over sampling in m_A otherwise each individual data file would be far too large in size. Therefore, we decided to sample in the region $1M_\odot < m_A < 2.1M_\odot$[13], with a spacing $\Delta m_A = 0.002M_\odot$, since this is a generous mass range in which we expect to observe pulsars.

3.5.2 Properties of the master data file

The data files we have generated contain nine columns of data and they have the structure that appears in Table 3.2. The first three columns of the data correspond to the scalar charges α_A, β_A, and k_A respectively. The fourth and fifth columns contain the values for baryonic mass and gravitational mass respectively, the latter of which falls on the grid described in the previous paragraph. Columns six and seven contain α_0 and $\log_{10}\alpha_0$, of which the former lay on the grid described in section Sec. 3.4.4.2. Column eight contains the value of β_0, which ranges from $-5 \leq \beta_0 \leq +5$ and lies on a grid with spacing $\Delta\beta_0 = 0.02$ for $\beta_0 < -4.3$ and $\Delta\beta_0 = 0.1$ for $\beta_0 > -4.3$. The ninth column in the master data file contains a flag that is either 0 or 1 and has no relevant purpose for actually using the data.

The files we have generated can be used in a variety of fields where scalar charges appear, not just binary pulsar experiments, although this is the primary target of this work. The data can be accessed though a git repository [**?**] and is structured on a uniform grid such that one can either use the data as is, or interpolate it if desired. For interpolation purposes, we have also included three separate files containing the grid points in $\{m_A, \alpha_0, \beta_0\}$ that we used and are labeled appropriately in the git repository. We have included both a Python and Mathematica script that is capable of reading in the data, setting up the numerical grid, and interpolating the data using SciPy's `RegularGridInterpolator` function for Python and Mathematica's native

[13]This is higher than the maximum mass that some of the EOS, SLy4 ($2.03M_\odot$) and H4 ($2.04M_\odot$), are able to produce for GR. In these cases we only sample up to a maximum gravitational mass of $2M_\odot$.

`Interpolation` function, both of which make use of a linear order method for three-dimensional data.

Recall that for the gray region of parameter space in Fig. 3.1 we were not able to find NS solutions that were of any use. As we have mentioned earlier, excluding this data from our investigation is not necessarily a shortcoming since these regions of parameter space are so heavily constrained by solar system observations and they are generally excluded from any analysis. However, for the sake of enforcing that *all* data lie on a uniform grid and can therefore be interpolated with ease, we found it beneficial to include this region of parameter space in our data. To do this, we artificially give values to the three scalar charges as a sort of place holder in the data. Since these regions of parameter space are generally excluded by observations we have given the scalar charges all an unphysical value of 10^5. We chose this value more out of convenience in an effort to force, say, an MCMC to avoid these points in parameter space because NSs do not exist and therefore the charges technically do not exist either.

3.5.3 Comparison to full data

One questions we need to concern ourselves with is whether or not the data in these files accurately reproduces the raw data from which they came since we have had to, in some cases, undersample the data in m_A. Here we discuss how the data recovers the results presented in Sec. 3.4, which were produced with full numerical data. The points in parameter space we consider here lie on our numerical grid and therefore should show great agreement with the full data, provided we sampled the charges finely enough in m_A. A more detailed discussion of the limitations of our data can be found in Appendix 3.B where we point out some known issues.

Figure 3.6 shows a comparison between some of the full data found in Fig. 3.4,

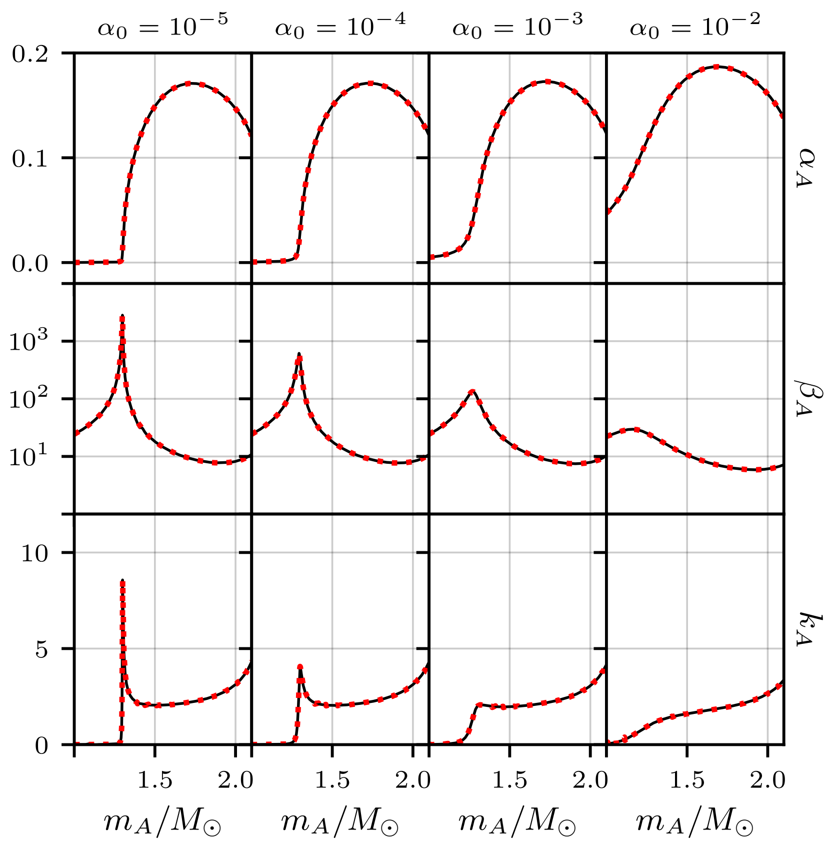

Figure 3.6: Comparison between the charges from our data files (dotted red) to the full raw data used to make the files (black) for points 2-5 in Table 3.3. There is excellent recovery for the full data, even in this extremely non-linear part of parameter space, suggesting that we have indeed sampled the solutions fine enough in m_A.

i.e. points labeled 2-5 in Table 3.3, and the data file for MO theory and AP3 EOS. As one can see, there is remarkable consistency between the two data sets, even in the most non-linear regions of parameter space, e.g. $\beta_0 = -5$ and $\alpha_0 = 10^{-5}$. In fact, the only real error that is noticeable is in β_A for these parameters, and only near the sharpest part of the peak does the data files deviate from the full data.

Even deviations as large as 10% should not have a significant effect on binary pulsar constraints, and the reason is threefold. First, the peaks in β_A are extremely isolated in m_A and there may not be a pulsar with that particular mass. Second, even if this value of m_A were important, the value of β_A is still so large that it would be immediately ruled out. Third, this error only occurs in the regions of parameter space that are already tightly constrained [7,42,82,98]. The astute reader may point out that the location of the peaks in β_A depend on the EOS and β_0, which would make it quite possible for an observed pulsar to lie on one of these peaks at some points in the $\{\alpha_0,\, \beta_0\}$ plane. While this is true, our second point above still holds and, in fact, the differences between the tabulated and full data tends to decrease as β_0 becomes less negative and α_0 becomes larger.

3.6 Conclusion

We have extended the original work in Ref. [42] and calculated the scalar charges $\{\alpha_A,\, \beta_A,\, k_A\}$ for a large region of the $\{\alpha_0,\, \beta_0\}$ parameter space, for gravitational masses $1m_\odot \leq m_A \leq 2.1M_\odot$, with 11 physical equations of state, in two distinct scalar tensor theories (that of Damour-Esposito-Farése and Mendes-Ortiz). We have presented the numerical schemes we implemented to complete these calculations and presented our results. Our goal was to calculate the scalar charges and tabulate them so that they could be of use in the future, particularly in the application of binary pulsar tests of gravity. We have investigated both the error of our numerical solutions, as well as the ability of certain scaling relations to reproduce full numerical results. Through this paper, the data is made fully available to the community.

Future work that utilizes this data include tests of STTs with binary pulsars and gravitational waves. In particular, this data makes it possible to perform a Bayesian analysis on the PPK parameters of binary pulsar system. Such analysis would require the use of an MCMC in which case one would need knowledge of the scalar charges in order to compute the likelihood. Instead of calculating the scalar charges on the fly, which we have demonstrated to extremely computationally expensive, one can make use of the data file provided in this paper to significantly speed up these likelihood evaluations. We intend to perform such an investigation in future work.

LIGO and VIRGO will inevitably detect more NS mergers in the future, some of which are likely to be NS-BH systems. Such systems are ideal for testing STTs because BHs do not develop scalar charges in these theories and therefore the emission of dipolar GWs would be maximized in these scenarios. The data provided in this paper would again be necessary for one to perform a Bayesian analysis of the data through MCMC simulations. Furthermore, if one wishes to study the constraints the future GW detectors can place on STTs, high resolution calculations of the scalar charges would be a crucial for such an analysis.

3.7 Acknowledgments

We would like to thank Norbert Wex, Hector O' Silva, and Travis Robson for useful insight and discussions. DA would like to thank Paulo Freire and the Max-Planck-Institut für Radioastronomie for their hospitality during part of this work. We would also like to acknowledge the support of the Research Group at Montana State University through their High Performance Computer Cluster Hyalite. NY and DA acknowledge support from NSF grant PHY-1759615 and NASA grants NNX16AB98G and 80NSSC17M0041.

3.A Error Analysis of Results

Here we attempt to quantify the numerical error in our results. We start with an investigation of the error associated with our grid spacing in $\tilde{\rho}_c$ and show that we can trust our results to within 1% in the worst of cases for the regions of parameter space that we have explored. We then look into how reliable the scaling relations are and how much error we introduce by using these rather than populating the entire parameter space fully numerically. We then finish with a discussion of the effects of using piecewise polytrope versus their tabulated counterparts. For our analysis, we focus on the numbered points appearing in Fig. 3.1, which we have detailed below in Table 3.3. For each of the analyses we perform, we investigate the error at these points in parameter space in detail in an attempt to quantify our errors across the entire parameter space.

#	β_0	α_0	$\alpha_A(\tilde{\rho}_c)$	$\beta_A(\tilde{\rho}_c)$	$k_A(\tilde{\rho}_c)$
1	-6	1.44×10^{-2}	—	—	—
2	-5	10^{-5}	10^{-2}	10^{0}	10^{0}
3	-5	10^{-4}	10^{-2}	10^{0}	10^{-1}
4	-5	10^{-3}	10^{-3}	10^{-2}	10^{-2}
5	-5	10^{-2}	10^{-3}	10^{-3}	10^{-3}
6	-5	10^{-1}	10^{-3}	10^{-1}	10^{-1}
7	-5	10^{-0}	10^{-3}	10^{-1}	10^{-1}
8	-3	10^{-3}	10^{-6}	10^{-5}	10^{-2}
9	-3	10^{-1}	10^{-5}	10^{-2}	10^{-2}
10	3	10^{-3}	10^{-6}	10^{-5}	10^{-1}
11	3	10^{-1}	10^{-5}	10^{-2}	10^{-1}
12	-4	10^{-4}	10^{-5}	10^{-4}	10^{0}
13	-4	10^{-3}	10^{-5}	10^{-4}	10^{-2}
14	-4	10^{-2}	10^{-5}	10^{-5}	10^{-3}

Table 3.3: Numbered points appearing in Fig. 3.1 and there associated relative errors as determined by Eq. (3.63). The columns with $\tilde{\rho}_c$ in parentheses are the errors determined in Sec. 3.A.1. Recall that Eq. (3.63) actually yields the percent error in the solutions, therefore 10^0 actually represents a 1% error, which is the highest error we find from our results.

3.A.1 Grid in central density

In order to obtain the most accurate and precise results from our numerical calculations one would have to use an infinitely dense grid in central density $\tilde{\rho}_c$ such that interpolating between points in Fig. 3.2 leaves no room for error. However, this is not computationally feasible, and thus, by reducing the number of points in this grid we introduce numerical error that is not associated with our methods of solving the field equations. The grid we have used in the end, for each individual region of parameter space, was chosen to achieve sufficient confidence in our results for the amount of computation time needed for the calculations. While we are confident in the grids we have chosen, there is still numerical error associated with our choices and we quantify those here.

In order to assess our errors we decided to double the number of points in our central density grid and calculate the relative errors between these solutions and the ones we have calculated using our original grids, which we have done for every point in parameter space detailed in Table 3.3. While we analyzed each of these points in detail, we only discuss the results for the points with the worst errors and give explanation for why the errors arise. For concreteness, to calculate relative percent error for any of the scalar charges, denoted by "χ" here, we use

$$\frac{\Delta_{\rm rel}\,\chi(\alpha_0,\beta_0,m_A)}{100} = \left|\frac{\chi_2(m_A)-\chi_1(m_A)}{\chi_2(m_A)}\right|_{\alpha_0,\beta_0}\,, \tag{3.63}$$

where χ_2 is the solution with twice as many grid points as χ_1. We evaluate this for all values of m_A for the specific combination of α_0 and β_0 and quote the largest values of relative error in the columns of Table 3.3 with $\tilde{\rho}_c$ in parentheses.

Figure 3.7 shows a representative sample of our errors, including points labeled 2, 8, 10, and 13 as they show special features worth discussing. The first row in

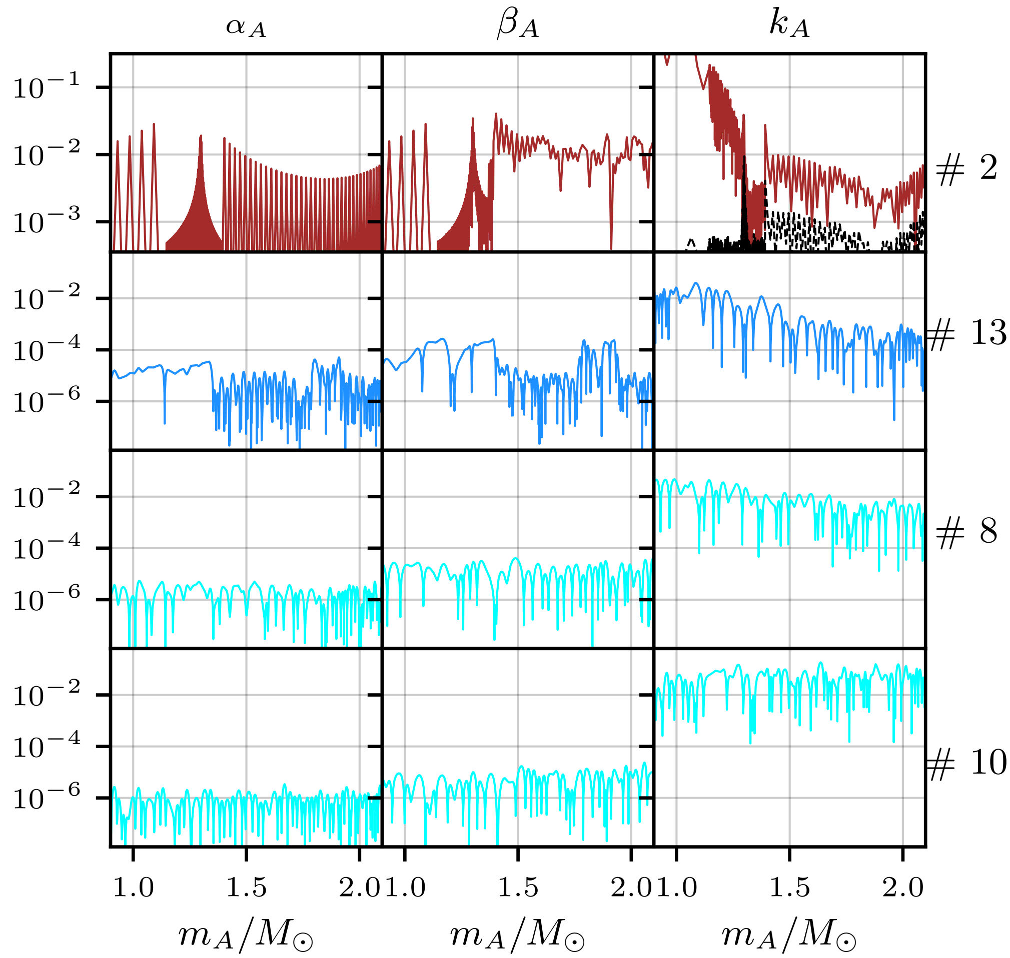

Figure 3.7: The percent error in the scalar charges α_A, β_A, and k_A for points labeled 2, 8, 10, and 13 in Table 3.3. These results are for MO theory and using AP3 for the EOS.

Fig. 3.7, showing the errors in the charges for point 2 in Table 3.3, represents what we consider to be one of the most error prone regions of parameter space. Spontaneous scalarization occurs here, and since α_0 is so small the phase transition in the scalar field is extremely sharp. However, our results for α_A are good to withing 0.01%, with some of the worst error appearing exactly when the phase transition occurs ($\sim 1.3 M_\odot$). The errors in β_A are slightly worse as one might expect since a numerical derivative is involved, but surprisingly enough the largest error is not associated with the phase transition. The spike in the error at $\sim 1.4 M_\odot$ is related to a mishap in the interpolation of the finer grid data, and while this does not happen often, our solutions are sometimes prone to this type of error in this part of parameter space.

The error in k_A may seem alarming at first for low masses, but this only occurs because $k_A \sim 0$ here and even tiny numerical noise in the results can generate a large relative error in the solution. This error is not a consequence of our numerical grid, but rather is an error associated with a the fact that numerical integration has finite precision and how we interpolate our results. For comparison we have also included the absolute error for k_A plotted by a dashed red line in Fig. 3.7. An obvious downfall here might be that we should have used a finer grid for the low masses, which would have most certainly increases the accuracy of our interpolations somewhat. The other issue, however, could be the method of interpolation we used. As described in Sec. 3.5, when calculating k_A we must interpolate $\log I_A(\bar{m}_A)$ for multiple values of α_0 in order to calculate derivatives, and we use a cubic spline to do so. Using a cubic spline on potentially noisy data like this is a good way to introduce extra error, which is what we are seeing here. However, switching to a linear order interpolation method significantly increases our errors for larger masses, precisely in the more interesting regions of parameter space where pulsar masses tend to lie. For this reason, we sacrifice precision on the lower end of masses in order to increase it elsewhere for more relevant masses.

The second, third, and fourth rows of Fig. 3.7 tell a different story than the first. For all these points in parameter space we find great agreement between solutions and therefore very small relative error. As expected, error in α_A are extremely small and this is due to the fact that there is no spontaneous scalarization and it is easy to extract α_A from the NS solutions. The errors in β_A are slightly worse than those of

α_A but still show exceptional agreement. As we saw with the with point 1, the errors in k_A tend to be much worse than those of the other scalar charges.

3.A.2 Analytic Scaling

One of the greatest properties about the cyan region of parameter space in Fig. 3.1 is that we can make use of the scaling relations presented in Sec. 3.4.4.3 to significantly reduce the number of NS solutions needed to explore this region. There is, however, some error associated with these scaling relations since we are, effectively, ignoring some of the non-linearities that appear in the field equations. While we expect these relations to hold in the small α_0 regime, we need to show numerically that this is indeed the case. To investigate this particular kind of error we have decided to explore the cyan region of parameter space with the same numerical grid for the blue region, described in Sec. 3.4.4.2, but only for AP3 and SLy4 EOS to get a sense of the error.

To make use of the scaling relations, we simply calculate all the scalar charges on the dashed horizontal lines in Fig. 3.1 and use Eq. (3.58) to find the function $f(\beta_0, m_A)$. Once we have found $f(\beta_0, m_A)$, then α_A can be solved for all other $\alpha_0 < 10^{-2}$ by substituting f and the new α_0 back into Eq. (3.58). Since we have already calculated the actual, unscaled scalar charges for the AP3 and SLy4 EOSs can can compare the scaled versions to the full numerically solved ones.

Figure 3.8 shows some of the results from our error analysis for $\beta_0 = \pm 3$, where the scaling relations are expected to hold. We see that the relations have the most error for solutions with $\alpha_0 = 10^{-2}$ (blue curves) but are never more than 1%. For all values of $\alpha_0 < 10^{-2}$ the error continues to decrease and would presumably go to zero in the limit that $\alpha_0 \to 0$ if we had infinite precision in our numerics. In general, we find errors of the same order of magnitude as the ones presented in Fig. 3.8 across

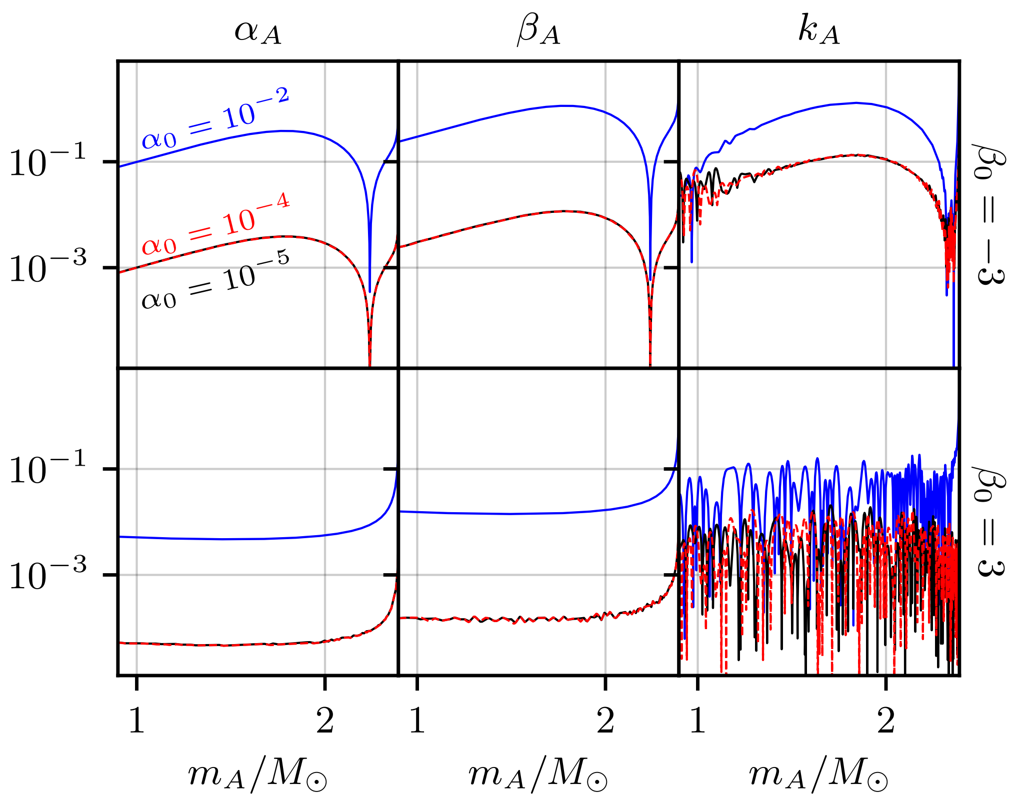

Figure 3.8: The percent error in the scalar charges α_A, β_A, and k_A for points labeled 8 10 in Table 3.3 when comparing scaled charges to their fully numerical counterparts. Blue curves correspond to $\alpha_0 = 10^{-2}$, red to $\alpha_0 = 10^{-4}$, and black to $\alpha_0 = 10^{-5}$. These results are for MO theory and using AP3 for the EOS. The results for DEF theory and AP3 looked nearly identical but the errors are overall slightly smaller.

the entire cyan region of parameter in Fig. 3.1, with the errors being slightly larger in MO theory than in DEF theory. One notices that the errors for α_A and β_A look very similar, and they should be this way according to Eq. (3.59) since β_A is a derivative of α_A. The inertial charge k_A also has a similar structure to the other charges but is polluted with more numerical noise, which is extremely evident for $\beta_0 = +3$. The distinct difference in the function form of the errors between $\beta_0 = -3$ and $\beta_0 = +3$ can be attributed to the fact that the effects of the non-linearities in the scalar field are more prominent for negative values of β_0.

3.A.3 Piecewise Polytropes

The piecewise polytropic approximation to tabulated EOSs in Ref. [83] allows one to considerable speed up numerical calculations involving NSs because of their analytic nature. The data files we provide were all generated using the full tabulated data, but for others who wish to perform future calculation, it would be nice to have an idea how these approximations affect the final results. In Fig. 3.3 we briefly compared how charges calculated using the piecewise polytropes compare to those calculated with the full tabulated EOS, and one can see that aside from slight apparent shifts in the masses, the curves seem nearly identical. We have verified, using the points in Table 3.3 as a representative sample, that this is indeed consistent across the entire parameter space. The similarity between the charges should not come as a surprise considering how well the piecewise polytropes match the actual data, c.f Table III in Ref. [83]. For all of the equations of state we consider here, the residuals in Ref. [83] for both the mass and moment of inertia of the NSs are less than 2%, which are the two most important quantities when calculating the scalar charges. Having such small deviations between tabulated and approximated EOSs leads to very small deviations when calculating α_A, β_A, and k_A from Eqs. (3.25)-(3.27).

3.B Limitations of Data Files

We have discovered a few limitations of the data we have provide and these are discussed in this appendix. We should point out, however, that these complications arise when one wishes to interpolate the data files we have generated, in order to determine that charges for points that *do not* lie on our numerical grid. As far as we are able to tell, the data files are able to reproduce the full numerical data used to make the files to great level of accuracy (see Sec. 3.5) for all points that lie on our grid.

Figure 3.9 shows how the interpolation of the data behaves for points that lie on (solid) and off (dashed) numerical grid we have established for α_0 and β_0. One notices that the solid curves appear as expected, according to the results presented in Figs. 3.3 and 3.4; α_A experiences a smooth rapid growth while β_A and k_A have peaks near m_{crit} for which spontaneous scalarization turns "on" and "off". However, the dashed curves, which lie off the numerical grid, have somewhat significantly different features. The curves for α_A appear to be good, but one notices that the dashed curves develop slight instantaneous "discontinuities" in the slope during the growth of the scalar field. As a result of this apparent discontinuities, β_A develops a double peak near the critical mass at which the phase transition occurs. Likewise, a very similar feature develops in k_A in which the single peak that is present in the solid curves turns into two peaks that are not as large in magnitude.

The issue we are seeing in Fig. 3.9 is a direct consequence of the nature of the scalar charges, particularly the presence of the phase transition, and trying to interpolate them. Consider β_A for example, in which case we expect the magnitude of the peak at the critical mass to decrease as β_0 becomes less negative, cf. the plots of β_A in Fig. 3.4. We also expect the critical mass to shift to higher masses as we allow β_0 to become less negative. Therefore, there are multiple features changing in the solutions with the variation of just a single parameter, in this case β_0. Because of this dependence, the linear interpolator has issues when it tries to interpolate between these peaks because the algorithm considers changes in β_0 and m_A at the same time, which physically are in effect co-dependent on each other in a non-linear way. As it might be expected, it is hard to interpolate any function with extremely sharp features like we have here and taking the log of the data does not seem to improve anything in this situation.

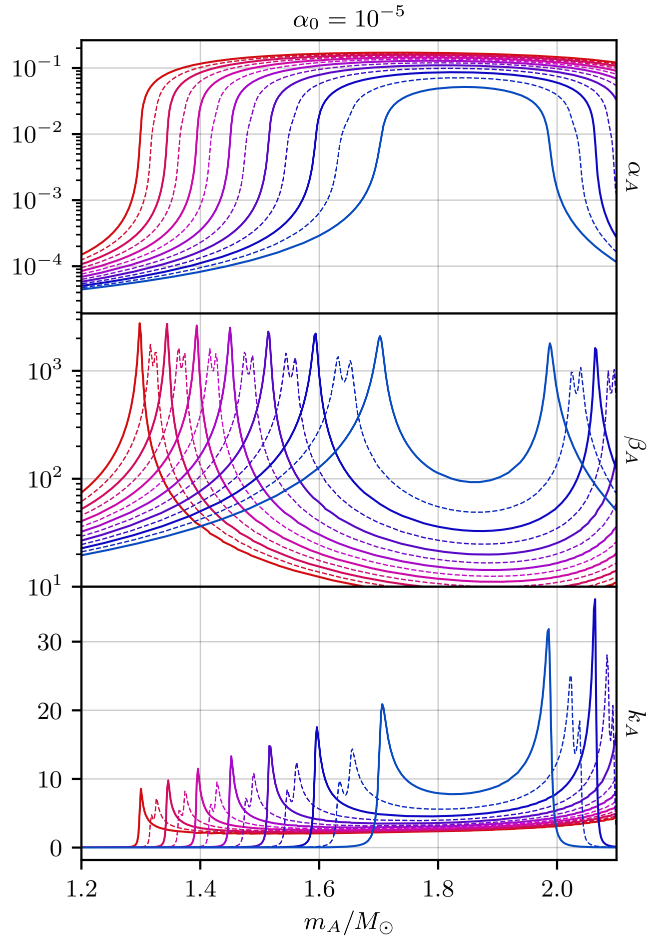

Figure 3.9: Comparison between the charges for points that lie on our $\{\alpha_0, \beta_0\}$ numerical grid (solid lines) and points the we have to interpolate to find (dashed lines). Similar to Fig 3.4, we use a constant value of $\alpha_0 = 10^-5$ and $-5.0 \leq \beta_0 \leq -4.4$, ranging in color from most red to most blue respectively. One notices that the interpolated point acquire a double peaked feature, the details of which are described in the text.

The features described thus far are most prominent in the $\alpha_0 \leq 10^{-5}$ case since the peaks are the most narrow here. However, this artifact of the interpolation does arise for other values of α_0 when spontaneous scalarization, but since the effects are less localized, i.e. the phase transition is more smooth for larger values of α_0, the discrepancy is less severe. Once out of the regime of spontaneous scalarization these artifacts no longer appear to be present and the interpolation of the data does an excellent job of giving us information between our grid points.

CHAPTER FOUR

BINARY PULSAR CONSTRAINTS ON MASSLESS SCALAR-TENSOR THEORIES USING BAYESIAN STATISTICS

Contribution of Authors and Co-Authors

Manuscript in Chapter 4

Author: David Anderson

Contributions: Developed and implemented the design study. Developed numerical code necessary for the project. Wrote the first draft of the manuscript.

Co-Author: Paulo Freire

Contributions: Provided feedback on analysis and comments on draft of the manuscript. Provided the pulsar data need for this project and valuable information related to testing gravity with binary pulsars.

Co-Author: Nicolás Yunes

Contributions: Provided feedback on analysis and comments on draft of the manuscript. Wrote second draft of the manuscript.

Manuscript Information Page

David Anderson, Paulo Freire, Nicolás Yunes

Status of Manuscript:

__x__ Prepared for submission to a peer-reviewed journal

____ Officially submitted to a peer-reviewed journal

____ Accepted by a peer-reviewed journal

____ Published in a peer-reviewed journal

Manuscript will be ready for submission to Classical Quantum Gravity after the inclusion of a final section and subsequent review from all authors.

Abstract

Binary pulsars provide some of the tightest current constraints on modified theories of gravity and these constraints will only get tighter as radio astronomers continue timing these systems. These binary pulsars are particularly good at constraining scalar-tensor theories in which gravity is mediated by a scalar field in addition to the metric tensor. Scalar-tensor theories can predict large deviations from General Relativity due to the fact that they allow for violation of the strong-equivalence principle through a phenomenon known as scalarization. This effect appears directly in the timing model for binary pulsars, and as such, it can be tightly constrained through precise timing. In this paper, we investigate these constraints for two scalar-tensor theories and a large set of realistic equations of state. We calculate the constraints that can be placed by saturating the current 1σ bounds on single post-Keplerian parameters, as well as employing Bayesian methods through Markov-Chain-Monte-Carlo simulations to explore the constraints that can be achieved when one considers all measured parameters simultaneously. Our results demonstrate that both methods are able to place similar constraints and that they are both indeed dominated by the measurements of the orbital period decay. The Bayesian approach, however, allows one to simultaneously explore the posterior distributions of not only the theory parameters but of the masses as well.

4.1 Introduction

General Relativity (GR) has been the most successful theory of gravity over the last century, passing all current tests with great success. Our ability to test gravitational theories is becoming even stronger [13, 110] with the recent observations of gravitational waves (GW) [1, 5, 6] and the continued monitoring of binary pulsars (PSRs) [7, 8, 111]. As more neutron star (NS) systems are discovered through gravitational wave observations we will be able to pin down the nuclear equation of state (EOS) and other NS properties [14, 15]. Such observations can help break the degeneracy that arise between EOS effects and those introduced by modified theories of gravity.

Even with the success of GR, there are many theoretical reasons to consider modified theories. Some of the most well-motivated modified theories are scalar-tensor theories (STTs) of gravity, in which gravity is mediated by the metric tensor *and* a dynamical scalar field. These theories are defined by a choice of conformal coupling function that dictates the manner in which the scalar field couples to matter, and ultimately the level at which the strong-equivalence principle (SEP) is violated. Originally proposed by Jordan [33, 34], Fierz [35], Brans [36], and Dicke (JFBD) as some of the most natural alternatives to GR, STTs were later extended by Damour and Esposito-Farése (DEF) to include higher order terms in the conformal coupling, as well as multiple scalar fields [37]. Recently, a slight variation on this theory, proposed by Mendes and Ortiz (MO) [41], has gained some attention as it arises from more fundamental considerations.

While Solar System observations have the ability to tightly constrain STTs, these weak field constraints do not always translate to tight restrictions in the strong field regime. In particular, STTs give rise to a phenomenon in NSs known as scalarization in which the scalar field can become excited far above its background (weak field) value. Neutron stars in STTs can acquire a so-called scalar charge which quantifies the $1/r$ behavior of the scalar field in a far field expansion from the NS. Such modifications to NS spacetimes directly affect observables, particularly those that can be probed with binary PSR observations. The scalar charges that NSs can develop appear directly in the timing model that is used to predict when we should observe pulses from binary PSRs. Astronomers are able to time PSRs so precisely that even slight deviations from the GR predictions are highly constrained, thus providing some of the best constraints on STTs.

Typically, constraints on STTs are placed through the observed rate of decay of the orbital period of the binary. STTs predict dipolar gravitational radiation, which enters at lower post Newtonian (PN) order relative to the typical quadrupole radiation predicted by GR, and thus, speeds up the orbital decay rate. Since observations seem to suggest the absence of this extra dipole effect, STTs can be constrained from the observation of the orbital decay rate with precision that can exceed that of Solar System observations. However, STTs predict that *all* post-Keplerian (PK) parameters [39] are modified from the GR prediction. Thus, observations of post-Keplerian parameters other than the orbital period decay can in principle be combined to allow for even tighter constraints.

In this paper we investigate the type of constraints that can be placed on STTs, particularly the theories proposed by DEF and MO, by using multiple post-Keplerian parameters, as well as multiple PSR systems. We use a combination of PSR-white-dwarf systems and PSR-NS systems with a wide range of PSR masses to explore the effects of scalarization and place constraints in a self-consistent manner. We also explore the effects of the NS EOS and how it affects the strength of such constraints. Such studies are carried out with Bayesian methods through Markov-Chain-Monte-Carlo simulations that explore the *full* parameter space and determine which values of the STT parameters are most consistent with observations. This approach allows us to accurately take into account any correlations between observed post-Keplerian parameters and ensures that the constraints we place are self-consistent.

Using the data for scalar charges provided in [112], we are able to reproduce the constraints that are typically placed on STTs through just the orbital period decay. We show that the EOS has relatively little impact on these types of parameters and does not change the relative strength of any constraints placed from different PSRs. We find that other post-Keplerian parameters, like the rate of periastron advance, are, in some case, able to place tighter constraints on STTs for PSR-NS systems. When we take a Bayesian approach to place constraints we find very similar results.

We start with a description of STTs and the timing model in Sec. 4.2 in order to lay down the foundation for the rest of the paper. Here we discuss the current constraints on STTs from Solar System observations, as well as the details of the various post-Keplerian parameters appearing in the timing model. In Sec. 4.3 we investigate the various constrains that can be placed on STTs, first through the standard method that is employed in the literature, and then through MCMC methods in §4.4. We then conclude in Sec. 4.5 with a discussion of our results and future work. Throughout this paper, we follow the conventions of [69].

4.2 Timing binary PSRs in STTs

In this section we will introduce the basics of STTs and the post-Keplerian parameters that appear in the timing model. We will discuss the particular theories we consider in this paper and the current constraints that Solar System observations place on these theories. We give a brief discussion of the scalar charges and how they are calculated, and discuss their importance for timing binary PSRs. For completeness we provide a summary of the timing model and present the various post-Keplerian parameters in the context of STTs.

4.2.1 Scalar-tensor theories

In this paper we will focus explicitly on massless STTs in which there exists a single scalar field non-minimally coupled to the metric tensor $g_{\mu\nu}$. These theories can be derived from an action in the so called *Einstein frame* given by [37, 38, 42]

$$S = \int \frac{d^4x}{c} \frac{\sqrt{-g}}{4\kappa} \left[R - 2g^{\mu\nu}\partial_\mu\varphi\partial_\nu\varphi\right] + S_{\rm mat}\left[\chi, A^2(\varphi)g_{\mu\nu}\right] \,, \tag{4.1}$$

where g and R are the determinant and Ricci scalar associated with the metric $g_{\mu\nu}$, $\kappa = 4\pi G/c^4$, χ are any matter fields, and $A(\varphi)$ is a conformal factor that determines how the scalar field φ couples to matter.

The field equations resulting from variation of action above with respect to $g_{\mu\nu}$ and φ are given by

$$\begin{aligned} R_{\mu\nu} &= 2\partial_\mu\varphi\partial_\nu\varphi + 2\eta\left(T^{\,\text{mat}}_{\mu\nu} - \frac{1}{2}g_{\mu\nu}T^{\,\text{mat}}\right) , && (4.2) \\ \Box\varphi &= -\kappa\alpha(\varphi)T^{\,\text{mat}} , && (4.3) \end{aligned}$$

where the stress-energy tensor is defined by

$$T^{\,\text{mat}}_{\mu\nu} \equiv \frac{2c}{\sqrt{-g}}\left(\frac{\delta S_m}{\delta g^{\mu\nu}}\right) , \tag{4.4}$$

and $T^{\,\text{mat}} \equiv g_{\mu\nu}T^{\,\text{mat}}_{\mu\nu}$ is its trace.

In addition to the $A(\varphi)$ function that appears in the action, it is also convenient to introduce a couple of additional quantities. Let us then define

$$\alpha(\varphi) = \frac{\partial \ln A(\varphi)}{\partial\varphi} , \tag{4.5}$$

which we designate the conformal coupling, as it appears directly in the equations of motion for the scalar field. Another quantity that appears directly in the parameterized-post-Newtonian (PPN) and parameterized-post-Keplerian (PPK) formalisms is the derivative of this quantity, namely,

$$\beta(\varphi) = \frac{\partial\alpha(\varphi)}{\partial\varphi} , \tag{4.6}$$

and quantifies the non-linear behavior of $A(\varphi)$.

A particular STTs is defined by one's choice of the conformal factor $A(\varphi)$, or likewise $\alpha(\varphi)$, and will ultimately determine how the scalar field reacts to the presence of matter, or likewise the gravitational potential generated by such matter. In this paper, we consider two models that exhibit similar behavior when $\varphi \ll 1$ but allows for much different behavior elsewhere. The first model we consider is DEF theory [37,38], which is defined by

$$
\begin{aligned}
A(\varphi) &= e^{\beta_0\varphi^2/2} , && (4.7)\\
\alpha(\varphi) &= \beta_0\varphi , && (4.8)\\
\beta(\varphi) &= \beta_0 , && (4.9)
\end{aligned}
$$

where β_0 enters directly as a free parameter. The other model we consider is MO theory [41], which is defined by

$$
\begin{aligned}
A(\varphi) &= \left[\cosh\left(\sqrt{3}\,\beta_0\varphi\right)\right]^{1/(3\beta_0)} , && (4.10)\\
\alpha(\varphi) &= \frac{\tanh\left(\sqrt{3}\,\beta_0\varphi\right)}{\sqrt{3}} , && (4.11)\\
\beta(\varphi) &= \beta_0\,\mathrm{sech}^2\left(\sqrt{3}\,\beta_0\varphi\right) , && (4.12)
\end{aligned}
$$

where, again, β_0 enters directly as a free parameter.

Both theories are subject to a boundary condition at spatial infinity such that the scalar field has a cosmologically determined background value φ_∞. This quantity then becomes another free parameter of these theories and must be chosen to satisfy weak-field constraints, like those from Solar System observations. However, we choose the parameterization $\varphi_\infty = \alpha_0/\beta_0$ and let α_0 become our second free parameter appearing in both theories. A more detailed description of this parameterization of STTs can be found in Refs. [70, 112]. It is worth pointing out, however, the this parameterization enforces certain relations when one inserts φ_∞ into Eqs. (4.8)-(4.9), namely

$$\alpha_\infty^{\rm DEF} = \alpha(\varphi_\infty) = \alpha_0 \ , \tag{4.13}$$

$$\beta_\infty^{\rm DEF} = \beta(\varphi_\infty) = \beta_0 \ , \tag{4.14}$$

in DEF theory, and when using Eqs. (4.11)-(4.12)

$$\alpha_\infty^{\rm MO} = \tanh\left(\sqrt{3}\,\alpha_0\right)/\sqrt{3} \ , \tag{4.15}$$

$$\beta_\infty^{\rm MO} = \beta_0\,{\rm sech}^2\left(\sqrt{3}\,\alpha_0\right) \ , \tag{4.16}$$

in MO theory.

The quantities in Eqs. (4.13)-(4.16) appear directly in the weak field predictions made by these theories. The choice of parameters (α_0, β_0) will determine the local value of the gravitational constant via the relation

$$G_N = G\left[A_\infty^2\left(1+\alpha_\infty^2\right)\right] \ , \tag{4.17}$$

as well as the PPN parameters $\gamma_{\,\rm PPN}$ and $\beta_{\,\rm PPN}$ [16, 73]. The former is given by

$$\bar{\gamma} = |1-\gamma_{\,\rm PPN}| = \frac{2\alpha_\infty^2}{1+\alpha_\infty^2} \ , \tag{4.18}$$

while the latter is given by

$$\bar{\beta} = |1-\beta_{\,\rm PPN}| = \frac{|\beta_\infty|\alpha_\infty^2}{2\left(1+\alpha_\infty^2\right)^2} \ , \tag{4.19}$$

The $\gamma_{\,\rm PPN}$ parameter is a measure of the spatial curvature induced by a unit rest mass and has been measured from the Shapiro time delay observed by the Cassini spacecraft [16,61], being constrained to $|1-\gamma_{\,\mathrm{PPN}}| \lesssim 2.3\times10^{-5}$. The $\beta_{\,\mathrm{PPN}}$ parameter is a measure of the amount of non-linearity in the superposition law for gravity, and it is constrained from observations of the perihelion shift of Mercury [16] to be $|1-\beta_{\,\mathrm{PPN}}| \lesssim 8\times10^{-5}$. From these relations we infer constraints on α_∞ and β_∞, namely

$$\alpha_\infty^2 \lesssim \frac{\bar{\gamma}}{2-\bar{\gamma}} \ , \tag{4.20}$$

from Eq. (4.18), and

$$\alpha_\infty^2(\beta_0) \lesssim \frac{|\beta_\infty|}{\bar{\beta}} - 1 - \frac{1}{4\bar{\beta}}\sqrt{|\beta_\infty|(|\beta_\infty| - 8\bar{\beta})} \ , \tag{4.21}$$

from Eq. (4.19), which only places tighter constraints for $|\beta_\infty| \gtrsim 14$.

4.2.2 Scalarization of neutron stars

While STTs can be constrained rather tightly from Solar System observations they are still able to produce significant deviations from GR near strongly self-gravitating matter like NSs. These strong field effects are a result of a well-studied phenomenon known as scalarization [37, 38, 42] . When the coupling parameter β_0 is sufficiently negative ($\lesssim -4.3$) the scalar field can grow rapidly inside the NS even when the cosmologically determined background value of the field approaches zero. This is precisely how STTs satisfy Solar System constraints but produce observable deviations from GR in the strong field regime.

The effects of scalarization can be quantified by quantities known as scalar charges and they enter directly into the timing model presented in the next section. There are three scalar charges that appear, the first of which is defined via

$$\alpha_A = \left.\frac{\partial \ln m_A}{\partial \varphi_\infty}\right|_{\bar{m}_A} \ , \tag{4.22}$$

for the Ath NS of a system and where the derivative must be taken with the baryonic mass held constant. This scalar charge measures the "sensitivity" of the NS's mass to variations in the background scalar field, and thus, it represents an effective coupling between the NS and the scalar field. This quantity is the strong field counterpart to the weak field parameter α_∞. The second relevant scalar charge is the strong field equivalent to β_∞, and thus, it is a derivative of Eq. (4.22), i.e.

$$\beta_A = \left.\frac{\partial \alpha_A}{\partial \varphi_\infty}\right|_{\bar{m}_A}, \tag{4.23}$$

where again the baryonic mass must be held constant. This scalar charge encodes non-linear interactions between the binary component. The final scalar charge of interest is linked to the NS's moment of inertia I_A, and it is defined as

$$k_A = \left.\frac{\partial \ln I_A}{\partial \varphi_\infty}\right|_{\bar{m}_A}, \tag{4.24}$$

with the baryonic mass once more held fixed. Similar to the relations between α_A and the NS's mass, k_A quantifies the sensitivity of the NS's moment of inertia to the scalar field. This quantity becomes most relevant when a NS is in a binary system with another NS. As the NSs orbit one another, they will move through each other's gravitational potential, effectively altering the local value of the scalar field. The NS's moment of inertia will then fluctuate throughout the orbit and produce an additional time delay that is measurable in principle.

Calculating these scalar charges is not very difficult but can be numerically expensive over large regions of the (α_0, β_0) parameter space. For the Bayesian methods used in this paper, it would be nearly impossible to compute these quantities as often as they would be needed for millions of likelihood calculations. However, these quantities have recently been calculated over a large region of parameter space and for a wide range of EOS [112], consistent with the PSR mass in J0348+0432 and the recent constraints placed from LIGO and VIRGO [14]. In this paper, we make use of this data in order to avoid solving for the scalar charges on the fly during our MCMC simulations.

4.2.3 Timing model in STTs

In order to use binary PSRs to place constraints on a gravitational theory, one must work out how that theory predicts modifications to the motion of a binary system. Therefore, one must develop a timing formula that captures the relativistic effects of the theory by relating the observed time of arrival (TOA) of the pulse to the time the pulse was emitted. Blandford and Teukolsky (BT) [113] originally developed such a formula to explain the, then recent, discovery by Hulse and Taylor of the the first binary PSR B1913+16 [114]. Later, Damour and Deruelle (DD) developed a full 1PN description of the two-body problem in a way that allowed for a parameterized description of the timing model, encapsulating all relativistic effects in GR. This model was then extended by Damour and Taylor [39] in a phenomenological manner such that the DD model could be used generically to constrain any conservative theory of gravity. The parameters of the Damour-Taylor model are the two masses (m_A and m_B) of the binary, the standard Keplerian orbital parameters $\{P_b, n = 2\pi/P_b,\, T_0,\, \omega_0,\, e_0,\, x_0\}$ (orbital period, orbital frequency, time of periastron passage, location of periastron, eccentricity, and projected semi-major axis), and a set of post-Keplerian parameters. In this section we will review the timing formula of DD and present the relevant post-Keplerian parameters of Damour and Taylor in the context of scalar-tensor theories.

The timing model is traditionally (BT and DD) written as

$$D\tau_a = T_e + \Delta_R + \Delta_E + \Delta_S + \mathcal{O}(c^{-4}) \ , \tag{4.25}$$

where τ_a is the infinite frequency barycenter arrival time, T_e is the proper time of emission, and D is a Doppler factor accounting for center of mass motion between the binary and the Solar System barycenter. Using τ_a here means that one must have accurately accounted for the time delays associated with dispersion from the interstellar medium and corrections that transform this barycenter arrival time to the time kept at the observatory on Earth's surface [115, 116]. The Doppler factor D is an inconsequential constant that can be transformed out of the timing formula through a redefinition of units, and restored later if needed [39]. The last three terms in Eq. (4.25) account for all other time delays occurring between the binary and the Solar System barycenter. The Römer delay Δ_R is simply the classical light travel across the binary and depends on the PSR's position in its orbit. The magnitude of this time delay is determined by the projected semi-major axis along the line of sight.

The Einstein delay Δ_E arises from relating coordinate time of emission to the proper time of emission, and thus, it depends on the metric component g_{00}. This time delay takes the form

$$\Delta_E = \gamma \sin u \ , \tag{4.26}$$

where γ is a post-Keplerian parameter and u is an eccentric anomaly like variable that is the function of T_e found by solving

$$u - e \sin u = n \left[(T_e - T_0) - \frac{\dot{P}_b}{2p_b}(T_e - T_0)^2 \right] \ . \tag{4.27}$$

with $\dot{P}_b$ being another post-Keplerian parameter describing the change in orbital period, which we will discuss later. The coefficient γ is determined when one accounts for the gravitational redshift of the companion and the second-order Doppler shift from the PSR's motion in the line element, using Kepler's equations to integrate.

There is also an additional effect described by the Einstein delay that is related to violation of the SEP. Theories that violate the SEP will allow the PSR's moment of inertia to change throughout the orbit as it moves through the gravitational potential of the companion. This means that the PSR's rotational frequency will vary throughout its orbit in order to conserve angular momentum. Such effects add another time delay to the timing formula and are directly proportional to $\sin u$, and therefore, they are included in the definition of γ [39, 73].

The final time delay appearing in Eq. (4.25) is the Shapiro delay Δ_S resulting from the fact that light must travel in the curved background of the binary. This term can be thought of as the first relativistic correction to Δ_R and is most easily measured when one observes the binary edge on. The magnitude of the Shapiro delay is denoted by a post-Keplerian parameter r and is labeled the "range" of the Shapiro delay. Another post-Keplerian parameter, $s \equiv \sin \iota$, representing the "shape" of the Shapiro delay, and enters here to characterize how this time delay is effected by the orbit's inclination relative to the line of sight.

While Eq. (4.25) captures the delays associated with the pulse traveling in the curved spacetime between the PSR and the Solar System barycenter, it does not account for any secular variations in the Keplerian parameters of the binary. Thus, in principle, one must also account for three other post-Keplerian parameters, i.e. $\dot{x}$,

$\dot{e}$, and $\dot{\omega}$, via

$$x = x_0 + \dot{x}(T_e - T_0) \ , \tag{4.28}$$

$$e = e_0 + \dot{e}(T_e - T_0) \ , \tag{4.29}$$

$$\omega = \omega_0 + \dot{\omega}(T_e - T_0) \ , \tag{4.30}$$

and insert these back into the timing formula of Eq. (4.25). In practice, however, the rate of periastron advance $\dot{\omega}$ is usually the only one of these parameters that can be measured consistently and its theoretical value can be determined by the methods in [39, 95].

Thus far, we have worked in a theory independent framework and we have parameterized the various time delays with a set of measurable post-Keplerian parameters $\{\dot{\omega},\, \gamma,\, r,\, s\}$. In GR, these four parameters take on simple forms that are a function of the two masses and the Keplerian parameters. In other theories of gravity, however, one must determine their functional form using the formalism in [39]. Thus, in the context of STTs [37, 39, 70, 97], the post-Keplerian parameters that are typically measured are given by

$$\gamma = \frac{e}{n}\frac{X_B}{1+\alpha_A\alpha_B}\left(\frac{G_{AB}Mn}{c^3}\right)^{2/3}\left[X_B(1+\alpha_A\alpha_B)+1+\alpha_B k_A\right] \ , \tag{4.31}$$

$$\dot{\omega} = \frac{3n}{1-e^2}\left(\frac{G_{AB}Mn}{c^3}\right)^{2/3}\left[\frac{1-\alpha_A\alpha_B/3}{1+\alpha_A\alpha_B} - \frac{X_A\beta_B\alpha_A^2 + X_B\beta_A\alpha_B^2}{6(1+\alpha_A\alpha_B)^2}\right] \ , \tag{4.32}$$

$$r = \frac{G(1+\alpha_\infty\alpha_B)m_B}{c^3} \ , \tag{4.33}$$

$$s = \frac{na\sin\iota}{cX_B}\left(\frac{G_{AB}Mn}{c^3}\right)^{-1/3} \ , \tag{4.34}$$

in which we have made use of the notation in [39], where M is the total mass and $X_{A,B} = m_{A,B}/M$. One will notice that the scalar charge $(\alpha_A,\, \beta_A,\, k_A)$ described earlier appear directly in these definitions.

The effects we have incorporated thus far do not capture radiative effects such as gravitational wave emission. The orbital period derivative, $\dot{P}_b$, accounts for these radiative effects, along with others, and in general has the contributions [39]

$$\dot{P}_b = \dot{P}_b^{\rm Acc} + \dot{P}_b^{\rm Shk} + \dot{P}_b^{\dot{M}} + \dot{P}_b^{T} + \dot{P}_b^{\dot{G}} + \dot{P}_b^{\rm \,int} \,. \tag{4.35}$$

The quantity $\dot{P}_b^{\rm Acc}$ is due to the relative acceleration between the binary and the Solar System barycenter along the line of sight. The quantity $\dot{P}_b^{\rm Shk}$ is the so-called Shklovskii effect and is due to centrifugal acceleration between the two binary components. The quantity $\dot{P}_b^{\dot{M}}$ accounts for mass loss of the system, and finally $\dot{P}_b^{T}$ accounts for any tidal effects. The term $\dot{P}_b^{\dot{G}}$ accounts for a possibly varying gravitational constant which generally happens on cosmological time scales, if for example the scalar field evolves in a cosmological potential and influences the gravitational constant.

The intrinsic orbital period derivative, $\dot{P}_b^{\rm \,int}$, is of most interest for constraining STTs and can be found directly from the orbital energy that is lost due to gravitational radiation. In the context of STTs, $\dot{P}_b^{\rm \,int}$ has the following contributions

$$\dot{P}_b^{\rm \,int} = \dot{P}_b^{\varphi,\rm mon} + \dot{P}_b^{\varphi,\rm dip} + \dot{P}_b^{\varphi,\rm quad} + \dot{P}_b^{g,\rm quad} \,. \tag{4.36}$$

Each of these pieces can be calculated from a multipole expansion of the energy fluxes for the scalar field and the metric, which yield [37]

$$\dot{P}_b^{\varphi,\mathrm{mon}} = -\frac{3\pi X_A X_B}{1+\alpha_A\alpha_B}\left(\frac{G_{AB}Mn}{c^3}\right)^{5/3}\frac{e^2(1+e^2/4)}{(1-e^2)^{7/2}} \tag{4.37}$$

$$\times\left[\frac{5}{3}(\alpha_A+\alpha_B)-\frac{2}{3}(\alpha_A X_A+\alpha_B X_B)+\frac{\beta_A\alpha_B+\beta_B\alpha_A}{1+\alpha_A\alpha_B}\right]^2 , \tag{4.38}$$

$$\dot{P}_b^{\varphi,\mathrm{dip}} = -\frac{2\pi X_A X_B}{1+\alpha_A\alpha_B}\left(\frac{G_{AB}Mn}{c^3}\right)\frac{(1+e^2/2}{(1-e^2)^{7/2}}(\alpha_A-\alpha_B)^2 , \tag{4.39}$$

$$\dot{P}_b^{\varphi,\mathrm{quad}} = -\frac{32\pi X_A X_B}{5(1+\alpha_A\alpha_B)}\left(\frac{G_{AB}Mn}{c^3}\right)^{5/3}$$

$$\times(1-e^2)^{-7/2}\left(1+\frac{73}{24}e^2+\frac{37}{96}e^4\right)\left[X_B\alpha_A+X_A\alpha_B\right] , \tag{4.40}$$

$$\dot{P}_b^{g,\mathrm{quad}} = -\frac{192\pi X_A X_B}{5(1+\alpha_A\alpha_B)}\left(\frac{G_{AB}Mn}{c^3}\right)^{5/3}(1-e^2)^{-7/2}\left(1+\frac{73}{24}e^2+\frac{37}{96}e^4\right) \tag{4.41}$$

In GR only the quadrupolar term survives, but in STTs, both monopole and dipole radiation exist as well, the latter entering at -1 PN order relative to the GR term. In practice, the dipolar contribution from the scalar field will dominate the energy loss, followed by the quadrupolar terms. Thus, we will neglect the monopole contribution and the higher PN order contributions to the dipolar radiation in our calculations. The set of parameters $\{\dot{P}_b, \gamma, \dot{\omega}, r, s\}$ will be referred to as the post-Keplerian parameters from now on and will be the main set of parameters we use to constrain STTs.

4.2.4 Systems Considered

Typically, PSR-WD systems provide the tightest constraints on STTs due to the predicted dipolar contribution to $\dot{P}_b$, which has the largest effect when the binary components have very different scalar charges (as is the case with PSR-WD systems). However, one of the goals of this paper is to investigate how other post-Keplerian parameters affect the $(\alpha_0,\, \beta_0)$ parameter space. Therefore, we are also particularly interested in PSR-NS systems that have multiple post-Keplerian parameters measured to high precision. While the dipolar radiation is generally suppressed in such systems, $\dot{\omega}$ and γ can become very large (and therefore inconsistent with observations) due to the presence of the scalar charges $\beta_{A,B}$ and κ_A, which can take values $\sim 10^2$ and even $\sim 10^3$ in some cases [112].

The set of PSRs in [94] satisfy our first criteria for PSR-WD systems with mass measurements. These PSRs include J1738+0333 [7, 117], J2222-0137 [118, 119], J1012+5307 [120], and J1909-3744 [121][1]. In one way or another, there have been measurements of $\dot{P}_b$, the companion mass m_B, and the mass ratio $q \equiv m_A/m_B$, thus allowing us to pin down the masses of the system. In the case of J1738+0333 and J1012+5307, there have been independent mass measurements from optical observations of the white dwarf companions, and thus, there are no correlations between any of the parameters. For J2222-0137 and J1909-3744, there exist measurements of the Shapiro parameters r and s, which provide the extra information needed to pin down the masses. These systems also contain a diverse set of PSR masses that allow us to probe the (α_0, β_0) parameter space of STTs over a wide range of masses in which strong field effects like scalarization behave differently.

In terms of PSR-NS systems, we study J0737-3039A [111,122] and B1913+16 [9], as these PSRs have been precisely timed and there exists measurements of multiple post-Keplerian parameters. Table 4.1 summarizes the Keplerian and post-Keplerian parameters associated with each of these PSRs. For B1913+16 there are measurements of all 5 post-Keplerian parameters introduced in Sec. 4.2.3. J0737-3039A is part of a double PSR system, and there are measurements of all 5 post-Keplerian as well. But here there is also an independent measurement of the mass ratio from the

[1]We exclude J0348+0432 due to the large mass ($\sim 2M_\odot$) of the PSR in this system. The scalar charges in [112] only go up to $2.1M_\odot$ ($2M_\odot$ for some EOS), and thus, this makes it difficult for our MCMC runs to adequately explore the neighboring parameter space for a $2M_\odot$ NS

orbital velocities of the two PSRs, providing a total of 6 parameters that can be used to place constraints.

	J1738+0333	J1012+5307	J2222-0137	J1909-3744
P_b (d)	0.3547907398724(13)	0.60467271355(3)	2.44576469(13)	1.533449474406(13)
x (s)	0.343429130(17)	0.5818172(2)	10.8480239(6)	1.89799118
e	$3.5(1.1) \times 10^{-7}$	$1.2(3) \times 10^{-6}$	0.000380967(30)	$1.14(10) \times 10^{-7}$
m_A ($M_\odot$)	1.47(7)*	1.64(22)*	1.76(6)*	1.47(3)*
m_B ($M_\odot$)	0.181(8)	0.16(2)	1.293(25)*	0.208(2)
$q \equiv m_A/m_B$	8.1(2)	10.5(5)	—	—
$\dot{P}_b^{\,\rm int}$ (fs s^{-1})	-25.9(3.2)	-15(15)	-60(90)	—
$\dot{\omega}$ (deg yr^{-1})	—	—	0.1033(29)	—
$s \equiv sin\iota$	—	—	0.99559	0.99771
r ($T_\odot$)	—	—	1.293(25)	—

	J0737-3039A	B1913+16	B1534+12
P_b (d)	0.10225156248(5)	0.322997448918(3)	0.420737298879(2)
x (s)	1.415032(1)	2.341776(2)	3.7294636(6)
e	0.0877775(9)	0.61713404(4)	0.27367752(7)
m_A ($M_\odot$)	1.3381(7)*	1.438(1)*	1.3330(2)*
m_B ($M_\odot$)	1.2489(7)*	1.390(1)*	1.3455(2)*
$q \equiv m_A/m_B$	1.0714(11)	—	—
$\dot{P}_b^{\,\rm int}$ (fs s^{-1})	-1252(17)	-2398(4)	—
$\dot{\omega}$ (deg yr^{-1}	16.89947(68)	4.226585(4)	1.7557950(19)
γ (ms)	0.3856(26)	4.307(4)	2.0708(5)
$s \equiv sin\iota$	0.99974(39)	0.68(10)	0.97772
r (μs)	6.21(33)	9.6(3.5)	6.6(2)

Table 4.1: The Keplerian and post-Keplerian parameters measured for the systems we consider in this paper. Values with and asterisks are derived quantities assuming GR as the underlying theory. The values in parentheses represent the 1σ errors associated with each quantity. Note that the Shaprio parameter r is measured in units of $T_\odot = GM_\odot/c^3 = 4.925490947\mu$s for J2222-0137.

4.3 Constraints on STTs from binary PSRs: 1σ Constraints

In this section we will focus on placing constraints on the STT parameters α_0 and β_0 by saturating the bounds on individual post-Keplerian parameters. As we have mentioned, some of the tightest constraints on STTs come from the lack of observed dipolar radiation in binary PSRs. In principle, if one has measured the orbital decay rate to be $\dot{P}_{b,\rm obs}$ up to some uncertainty $\delta\dot{P}_b$ and found that it is consistent with the GR prediction, then Eq. (4.36) can be used to place constraints on the scalar charges $\alpha_{A,B}$, and therefore, the theory parameters (α_0, β_0). The connection between $\alpha_{A,B}$ and the theory parameters, however, is dependent on the equation of state used to calculate the scalar charges. These constraints, therefore, must assume a particular EOS, and then be repeated for all possible choices. We investigate how these constraints behave when using a large number of EOSs, and how they can be improved when using measurements of other post-Keplerian parameters, considering both DEF and MO theories.

4.3.1 Constraints from $\dot{P}_b^{\rm int}$

To place constraints using measurements of $\dot{P}_b$, we evaluate Eq. (4.36) for the entire region of parameter space investigated in [112], i.e. $-5.5 \lesssim \log_{10}(\alpha_0) \lesssim 0$ and $-5 \lesssim \beta_0 \lesssim 5$. While the masses are measured to a finite precision, we evaluate the dipole term at the best fit value of the masses for the moment, and returning to this point later. Then, by determining if these predicted values of $\dot{P}_b^{\rm int}$ lie with the range $\dot{P}_{b,\rm obs} \pm \delta\dot{P}_b$ we can determine if that point in parameter space is consistent or inconsistent with observations.

Figure 4.1 shows such constraints for multiple PSR systems that have accurate measurements of $\dot{P}_b$ for both DEF theory (left panel) and MO theory (right panel)

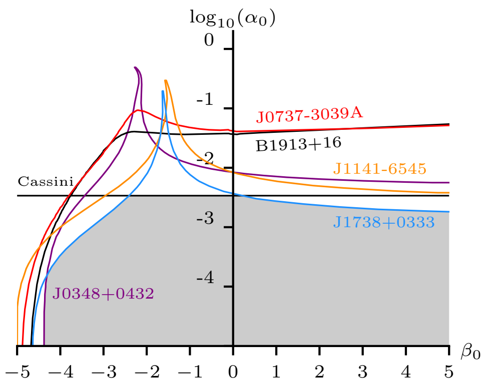

Figure 4.1: Constraints on (α_0, β_0) from a variety of binary PSRs on DEF theory (left) and MO theory (right) with the AP3 EOS [102]. The left panel confirms the results in [7] and the right panel places the first stringent constraints with binary PSRs on MO theory. Observe that the constraints on DEF and MO theory are comparable. The horns appearing near $\beta_0 = -2$, however, are more pronounced in MO theory, because these theories are very different in this region of parameter space. The shaded gray regions are still allowed by current PSR and Solar System (Cassini [61]) observations.

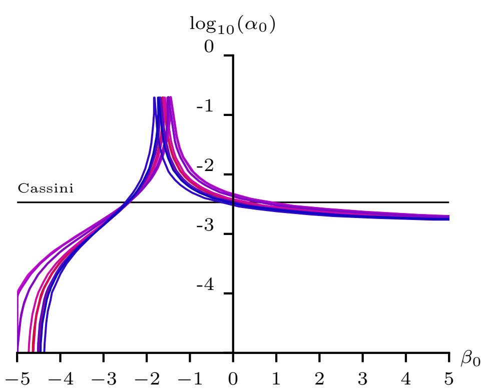

Figure 4.2: Same as Fig. 4.1 but using only PSR J1738+0333 and varying over 11 different EOSs [94, 112]. While the EOSs tend to shift the curves horizontally, the relative strength of all the constraints are consistent with one another.

with the AP3 EOS [102]. Let us first focus on the constraints on DEF theory. These constraints confirm the results first presented in [7]. The only difference between those results and the ones found here arises because the scalar charges have been here calculated much more finely in (α_0, β_0) space, allowing us to resolve the structure of the "horn" constraints more accurately. These horns arise because there are certain values of α_0 and β_0 for which the dipole term is significantly suppressed, thus preventing any constraint.

The constraints presented on the right panel of Fig. 4.1 on MO theory are new. Observe that the strength of the constraints in the two theories is roughly the same. This is mostly because these theories are nearly identical to each other in the limit $\varphi \ll 1$, and therefore, they only differ substantially from each other when β_0 is very negative and/or $\alpha_0 \gtrsim 0.01$. Indeed, we see that the main difference between the constraints on the different theories is the "horns" that appear in Fig. 4.1 for large values of α_0 and $\beta_0 < 0$.

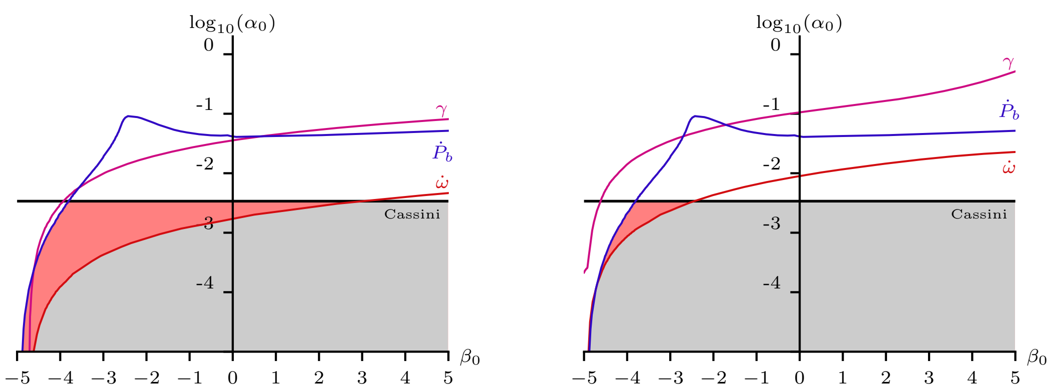

Figure 4.3: One sigma constraints on (α_0, β_0) from multiple post-Keplerian parameters using B1913+16 (left) and J0737-3039 (right) and the AP3 EOS [102]. For both of these PSRs, the constraints placed from γ and $\dot{\omega}$ are tighter than the one placed from $\dot{P}_b$ in certain regions, with $\dot{\omega}$ consistently placing the tightest constraints over the entire parameter space. The shaded gray regions are those permitted by *all* current constraints, while the red regions are those that have been excluded upon including other post-Keplerian parameters.

The EOS affects the magnitude of the scalar charges, and thus, the mass at which spontaneous scalarization occurs, and the constraints that can be obtained from observations of $\dot{P}_b$. Let us then repeat the analysis presented above, but this time using 11 different EOSs, namely the ones previously studied in Refs. [94, 112]: AP3-4 [102], ENG [103], H4 [104], MPA1 [105], MS0 [106], MS2 [106], PAL1 [107], SLy4 [108], and WFF1-2 [109]. Figure 4.2 illustrates the effect that the EOS has on the constraints placed by J1738+0333. As one can see, the EOS simply shifts the location of the horns left and right. This is because different EOS predict different masses at which scalarization kicks in, modifying the values of (α_0, β_0) at which the dipole term is suppressed. Aside from this modification, the variation of the EOS does not affect the overall strength of the constraints much, especially in regions where spontaneous scalarization does not occur, confirming previous results from [7, 94]. Although one ought to marginalize over our ignorance of the EOS, as we will discuss in the next section, the above analysis suggests that the constraints placed on DEF theory in the past [7] are robust to this ignorance.

4.3.2 Constraints from other Post-Keplerian parameters

For most systems, measurements of $\dot{P}_b$ place the tightest constraints on STTs since the dipolar contribution to Eq. (4.36) enters at -1 PN order relative to the quadrupole terms, and is therefore dominant. However, for double NS systems, the other post-Keplerian parameters can be significantly affected by the scalar charges, even though the dipolar contribution to Eq. (4.36) can be negligible. Thus, using the same methods used above for ${\dot{P}_b}^{\rm int}$, we here investigate the constraints that can be placed from other post-Keplerian parameters in these double NS systems. More precisely, for any one post-Keplerian parameter $d^i_{\rm obs}$ measured with 1σ accuracy δd^i, we calculate the values of (α_0, β_0) for which the predicted value of $d^i_{\rm th}$ lies inside $d^i_{\rm obs} \pm \delta d^i$.

Figure 4.3 shows the relative strength of the constraints on (α_0, β_0) from

B1913+16 and J0737-3039 using the post-Keplerian parameters $\dot{P}_b$, $\dot{\omega}$, and γ. In both cases, the observations of $\dot{\omega}$ place significantly tighter constraints on STTs than measurements of $\dot{P}_b$, especially for $\beta_0 < 0$. This may come as a surprise but it can be understood by the functional form of $\dot{\omega}$. The equation for $\dot{\omega}$ contains the higher-order scalar charge β_A, which can take on significantly large values when $\beta_0 < 0$. Typically, however, these effects are suppressed by a factor of α_0^2 for PSR-WD systems, which is enough to make these effects completely negligible [112]. However, when the companion is another NS, α_B^2 can be of order unity, making these contributions large and lead to confrontation with observations as we are seeing in Fig. 4.3.

These constrains, particularly the ones places by $\dot{\omega}$, are very sensitive to the masses used in Eq. (4.32), especially when the error is small. Consider B1913+16 in GR, for instance, in which $\dot{\omega}$ has been measured to very high precision. The current measurements of $\dot{\omega}$ are so precise that the total mass of the binary in GR can be determined to one part in 10^6. However, the individual masses cannot be constrained this well from the other parameters, which means that one is not well-justified in using the best-fit masses into the equations to place the above constraints. Moreover, these plots should not be taken as a hard upper limit on (α_0, β_0), but rather more as a guideline of what constraints could be placed.

There are two ways to address these types of constraints in a more consistent manner and that are not prone to issues described above. One such way is to perform an analysis similar to the one in Ref. [51] in which one calculates the theoretical values of the post-Keplerian parameters and their errors for every combination of α_0 and β_0. Then, that point in parameter space is only excluded if there does not exist a pair of masses (m_A, m_B) that lies in the intersection of these curves. Another method, however, involves using an MCMC to investigate these constraints and it not limited to only exploring the 1σ constraints of this section. Thus, in the next section, when we use Bayesian methods to investigate these constraints in a more informative and self-consistent manner.

4.4 Bayesian inference

Thus far we have considered the tightest possible 1σ constraints that can be placed on STTs using individual PSRs. However, we have not investigated how these constraints are affected by possible covariances between the post-Keplerian parameters, or by marginalizing over our ignorance on the EOS. Thus, in this section we will employ Bayesian methods through MCMC simulations to address these short comings.

4.4.1 Basics of Bayesian Inference

In Bayesian statistics, given a data set d_n and some hypothesis H (playing the role of the theory in this case), the posterior distribution on the parameters of the hypothesis are determined by Bayes' theorem

$$P(\vec{\lambda}|d_n, H) = \frac{P(\vec{\lambda}|H)P(d_n|\vec{\lambda}, H)}{P(d_n|H)} , \tag{4.42}$$

where $P(\vec{\lambda}|H)$ is the *prior* probability density of the parameters $P(d_n|\vec{\lambda}, H)$ is the *likelihood* of the data given the model H and parameters $\vec{\lambda}$, and $P(d_n|H, I)$ is the model evidence that plays the role of a normalization factor here. Therefore, if one has the priors and the likelihood, then in principle the posterior distribution of $\vec{\lambda}$ can be calculated. In order to explore these posterior distributions efficiently, we use MCMC simulations for each data set d_n, corresponding to the independent observations of each PSR.

For our purposes, $\vec{\lambda} = \{\xi_i, m_A,\, m_B,\, \log_{10}(\alpha_0),\, \beta_0\}$, and we enforce uniform priors for all parameters. The discrete parameter ξ_i represents a given EOS and can take integer values from 0 to 10, with 0 corresponding to AP3 and 10 to WFF2 (ordered alphabetically). For the masses, the priors ranges are $0.01M_\odot < m < 1.44M_\odot$ if the mass corresponds to a WD and $1M_\odot < m < 2M_\odot$ if the mass corresponds to a NS[2]. The STTs parameters have the prior ranges $-5.5 < \log_{10}\alpha_0 < -1$ and $-5 < \beta_0 < 5$. The priors we have chosen are primarily constrained by the information we have available about the scalar charges today. Despite being able to, we *do not* allow $\log_{10}\alpha_0$ to reach 0, nor do we allow the NS mass to exceed $2M_\odot$. We restrict $\log_{10}\alpha_0$ simply because we find that our MCMC chains never explore these regions (as one might expect given the results of Sec. 4.3.1. We restrict the masses of the NSs to be less than $2M_\odot$ because not all of the EOS we consider can achieve masses much larger than this.

For our logarithmic likelihood we use a multivariate Gaussian distribution given by

$$\ln\mathcal{L}(\vec{\lambda}) = -\frac{1}{2}[d^i_{\rm th}(\vec{\lambda}) - d^i_n]\,\mathbb{C}^{-1}_{ij}\,[d^j_{\rm th}(\vec{\lambda}) - d^j_n]\,, \tag{4.43}$$

where d^i_n are the post-Keplerian parameters of the nth data set (or nth PSR), $d^i_{\rm th}(\vec{\lambda})$ are the theoretical prediction for the same post-Keplerian parameters given the parameters $\vec{\lambda}$, and $\mathbb{C}^{-1}_{ij}$ is the inverse of the correlation matrix associated with the data set d_n. This likelihood has a maximum when the theoretical post-Keplerian parameters are precisely equal to their observed values and adequately handles the covariances that exist between the observed post-Keplerian parameters. The likelihood contains the theoretical predictions of the post-Keplerian parameters $d^i_{\rm th}$, given in Eqs. (4.31)-(4.34) and Eqs. (4.36)-(4.41), which in turn all depend explicitly

[2]We have restricted our investigation to this range of NS masses because it becomes numerically complicated to deal with the scalar charges above this range. For our study, however, this does not limit our investigation because we do not include PSR systems with large NS masses and indeed these priors do not affect our final results.

on the scalar charges ($\alpha_{A,B}$, $\beta_{A,B}$, k_A). For any WD companions, the charges reduce to $\alpha_B = \alpha_\infty$ and $\beta_A = \alpha_A/\varphi_\infty = \beta_\infty$ since WD are weakly self gravitating. For NSs on the other hand, the scalar charges are functions of the NS mass, α_0, and β_0 and must be solved numerically. To avoid this last step, we linearly interpolate the data from [112] for the scalar charges, allowing the quick computation of the likelihood over the entire prior range of the parameters.

We start our MCMC chains near the binary masses predicted by GR, with EOS AP3, $\log_{10}\alpha_0 = -2$, $\beta_0 = -2$. While we start the chains near the expected peaks of the posterior distributions, the chain are allowed to explore the entire prior range, and we find that, after a burn-in phase, the chains always find these peaks regardless of where we start them. The parameter space is then explored through a proposal distribution that is equivalent to a random draw from a Gaussian distribution, with a variance that is different for each of the parameters. The variances are chosen to ensure decent acceptance ratios and autocorrelation lengths, and in practice they are different for each PSR..

Proposed jumps are accepted or rejected based on the Metropolis-Hastings algorithm. The Metropolis ratio for symmetric proposal distributions is just the ratio of the posterior distributions, namely

$$r = \frac{P(\vec{\lambda}_{new}|H)\ P(d_n|\vec{\lambda}_{new}, H)}{P(\vec{\lambda}_{old}|H)\ P(d_n|\vec{\lambda}_{old}, H)} \,, \tag{4.44}$$

where we used Bayes theorem from Eq. (4.42) to rewrite this ratio in terms of the priors and likelihoods. The acceptance probability is then defined via $a(\vec{\lambda}_{old}, \vec{\lambda}_{new}) = \min(1, r)$, which determines whether or not the proposed set of parameters is accepted by the chain or not. This is accomplished by drawing a random number u between 0 and 1 and comparing it to the acceptance probability, i.e. if $a \geq u$ the jump is made,

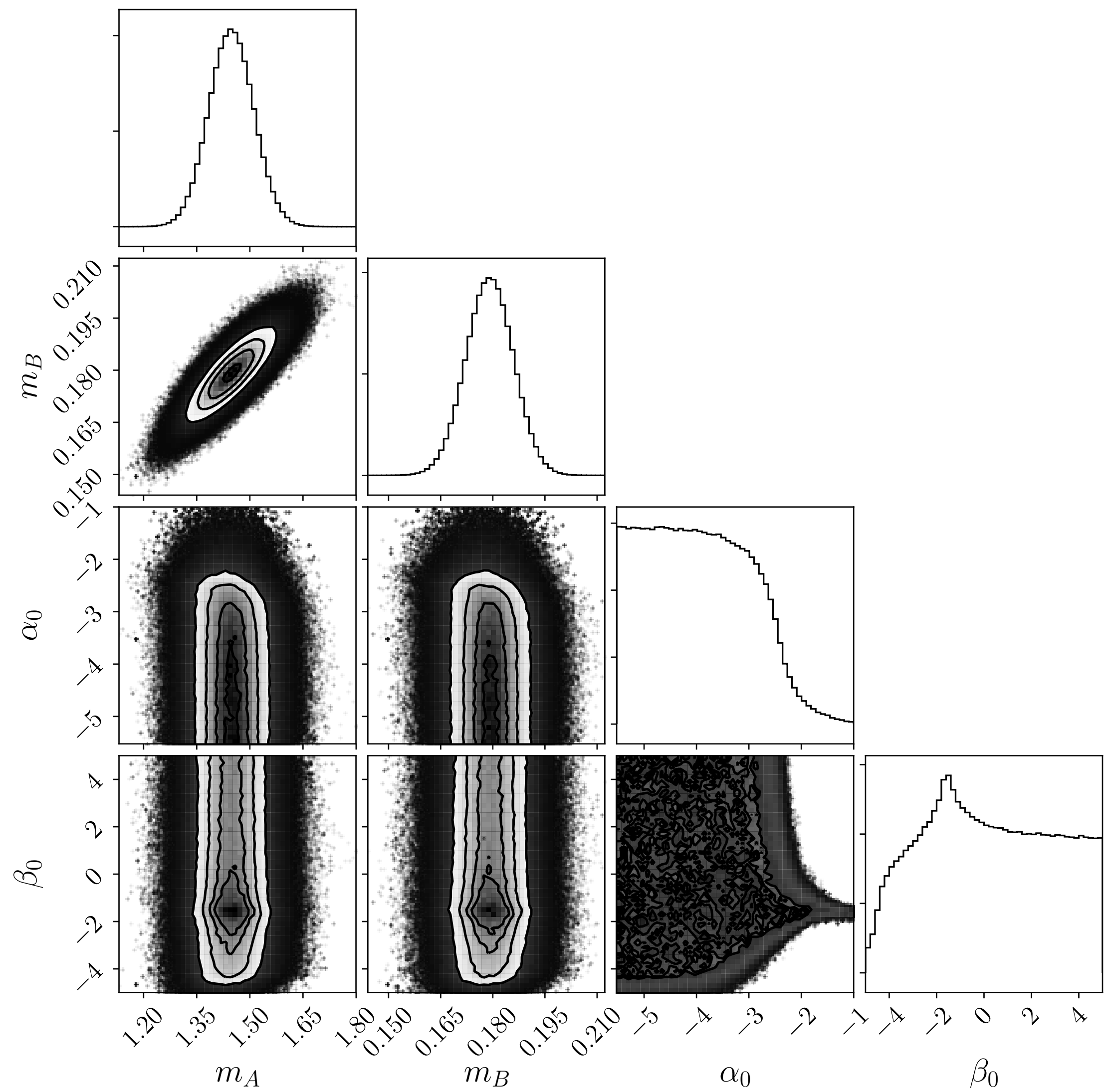

Figure 4.4: Corner plot with the marginalized posteriors distributions for (m_A, m_B, $\log_{10}\alpha_0$, β_0) from MCMC simulations using observations of post-Keplerian parameters from J1738+0333 for DEF theory.

and otherwise it is not. If the proposed jump leads to a larger likelihood, the jump is always accepted, but even if the new likelihood is smaller, there is still a chance that the proposal will be accepted. We repeat this process millions of time for each PSR to ensure convergence and good exploration of the posterior distributions.

The result of an MCMC is the joint posterior distribution on all parameters $\vec{\lambda}$. To obtain information about a single parameter, say β_0, we *marginalize*, or integrate, over all other parameters $\vec{\theta}$, for instance

$$P(\beta_0|d_n, H) = \int P(\vec{\lambda}|d_n, H)d\vec{\theta}\,. \tag{4.45}$$

In practice, this is equivalent to creating a histogram of the likelihood evaluations over the parameter that is being marginalized.

4.4.2 Bayesian Results

Figure 4.4 shows the marginalized posteriors on the parameters (m_A, m_B, $\log_{10}\alpha_0$, β_0) for J1738+0333. The marginalized posteriors on ξ_i for the EOS is uniform, meaning that the MCMC showed no preference toward any particular EOS and thus we do not show it because it is uninformative. We recover mass distributions that are consistent with observations and the predictions of GR. The posteriors on α_0 and β_0 behave as one would expect. Lower values of α_0 (towards GR) are preferred and the posteriors on β_0 have a nearly identical form as the constraints placed by $\dot{P}_b$ in the previous section. The latter makes sense since we are not enforcing Solar System priors on the parameters, and thus, the MCMC spends more time exploring regions that are less constrained, i.e. near $\beta_0 = -2$.

The joint posterior on α_0 and β_0 are presented in Fig. 4.5, where we also include an overlay of the constraints placed from the previous section. This figure is really a heat plot of the posterior distribution, with brighter (darker) colors representing low (high) posterior probabilities. Therefore, the dark regions are unconstrained by our Bayesian analysis, while the bright regions are excluded. We see great consistency between the Bayesian constraints and the constraints from the previous subsection.

Thus far we have only discussed results involving single PSRs with associated

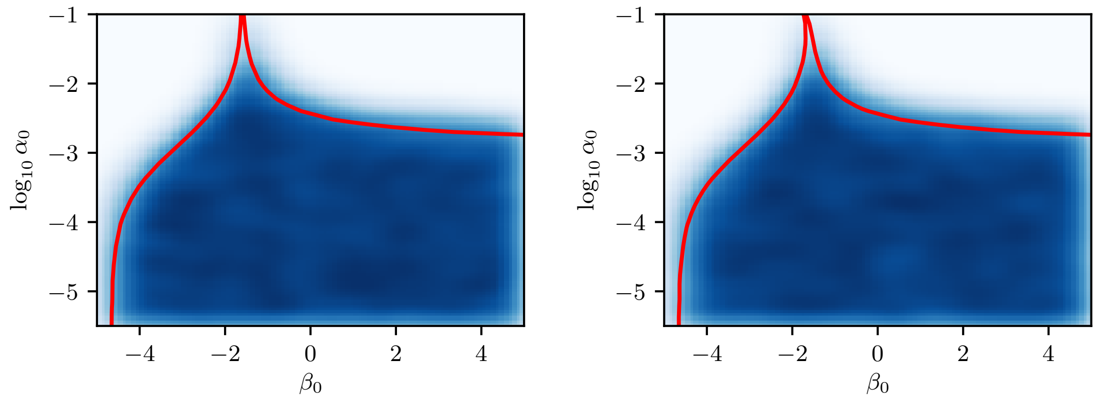

Figure 4.5: Marginalized posteriors distributions for $(\log_{10}\alpha_0,\ \beta_0)$ from MCMC simulations of the post-Keplerian parameters extracted from J1738+0333, using DEF theory (left) and MO theory (right), with the AP3 EOS. We overlay the constraints found in Sec. 4.3.1 in red for comparison. One can see that the MCMCs predict marginalized posteriors that are consistent with the 1σ constraints.

data d_n, so let us now combine the constraints from multiple observations in two different ways. The first involves constructing a new log likelihood that contains information from *all* of the PSRs we consider. This is equivalent to simply adding the log likelihoods (multiplying the actual likelihoods) associated with each individual PSR and running a new MCMC with a new parameter vector given by $\vec{\lambda}_{\rm total} = \{\sum_n m_{A,n}, \sum_n m_{B,n},\ \xi_i\,,\alpha_0,\ \beta_0\}$ where n stands for the nth binary system. One would then marginalize the likelihood over all parameters that are not (α_0, β_0) to find the new joint posterior. This is quite possible but it requires us to effectively recompute the posteriors we have already found.

Another way to combine information is to carefully "stack" the joint posteriors on the parameters $\vec{\sigma} = (\xi_i,\ \alpha_0,\ \beta_0)$ that we have already calculated[3]. In this case the total posterior distribution is just the product of the individual posteriors. To do

[3]It is impossible to stack posteriors on single parameters simply because the operations of integration and multiplication do not commute. Thus, we are only able to stack marginalized posteriors if we have marginalized over parameters that are not shared in different observations, like the masses in this case.

this we start with Bayes theorem in Eq. (4.42) with total data D from N systems, and we note that the priors are identical with the likelihood following the relation

$$\frac{P(D|\vec{\sigma})}{P(D|H)} = \prod_{n=1}^{N} \frac{P(d_n|\vec{\sigma}, H)}{P(d_n|H)} = \prod_{n=1}^{N} \frac{P(\vec{\sigma}|d_n, H)}{P(\vec{\sigma}|H)} \ , \tag{4.46}$$

Putting this information back into Bayes theorem for the total posterior we find the relation

$$P(\vec{\sigma}|D, H) = P(d_n|\vec{\sigma}, H)^{1-N} \prod_{n=1}^{N} P(\vec{\sigma}|d_n, H) \ . \tag{4.47}$$

Therefore, we are able to take the individual joint posteriors on $\vec{\sigma}$ that we have already calculated and multiply them in this manner to find the total posterior we would have found had we done a new MCMC simulation with all PSRs included.

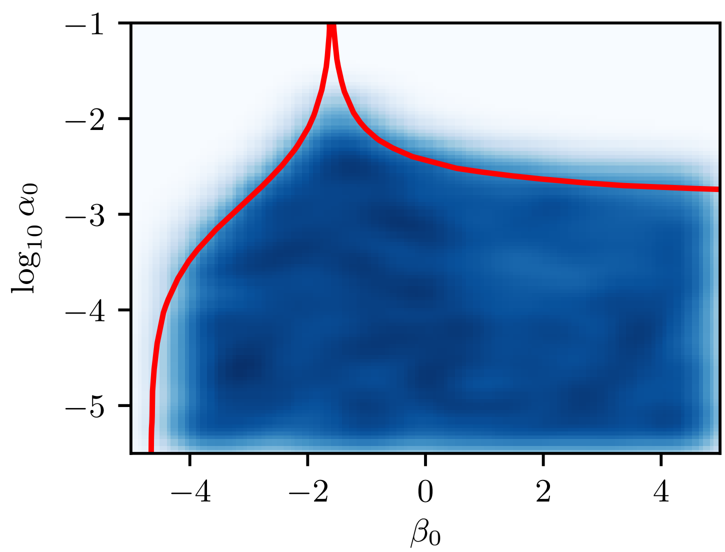

Figure 4.6: Same as Fig. 4.5 but stacked over information from PSRs J1738+0333, J2222+0137, J1012+5307, J1909-3744, and B1913+16, in DEF theory using the AP3 EOS. Again, we overlay the constraints found in Sec. 4.3.1 for J1737+0333 in red for comparison. Since J1737+0333 places the tightest constraints in Sec. 4.3.1 it makes sense that the stacked posterior is consistent with these constraints.

Figure 4.6 shows the total joint posterior on (α_0, β_0), marginalized over the EOS, after combining the posteriors from the PSRs J1738+0333, J2222-0137, J1909-3744, J1012+5307, and B1913+16 via Eq. (4.47). The overall effect of this "stacking" of the posteriors does not produce a significant effect but it does visibly reduce the probability of the larger values of α_0 near $\beta_0 \sim -2$. This results makes sense when compared to results found in Sec. 4.3.1. Each PSR tends to place different constraints in this region of parameter space, and the Bayesian methods we have employed here allow us to take these multiple constraints into consideration simultaneously.

Rather than assuming flat priors for the STTs parameters we can enforce constraints that have been placed from other tests, like Solar System tests, through different priors. The Solar System constraint on the post-Keplerian parameters appear in Eqs. (4.18)-(4.21), and numerically, these constraints turn into $\alpha_\infty \leq 0.003391$. As we have pointed out in Sec. 4.2, this constraint on α_∞ technically translates to different constraints on α_0 in each theory. However, for practical purposes the constraints on α_0 are identical in both DEF and MO theory because of the small magnitude of α_∞.

The effect of more stringent priors is to tighten the posteriors on all parameters. These priors effectively remove the posterior distributions on α_0 larger than 0.003391 that we have presented thus far and therefore reduce the parameter space that the MCMC explores. This results in tighter posteriors for the masses of the systems, as well as more stringent constraints on (α_0, β_0) as shown in Fig. 4.7.

4.5 Conclusion

We have investigated the constraints that binary PSRs can place on the parameters α_0 and β_0 that appear in scalar-tensor theories, particular in DEF theory and in MO theory. We show for the first time in MO theory the type of constraints that one can place on STTs using observed orbital period decay $\dot{P}_b$. Then, using

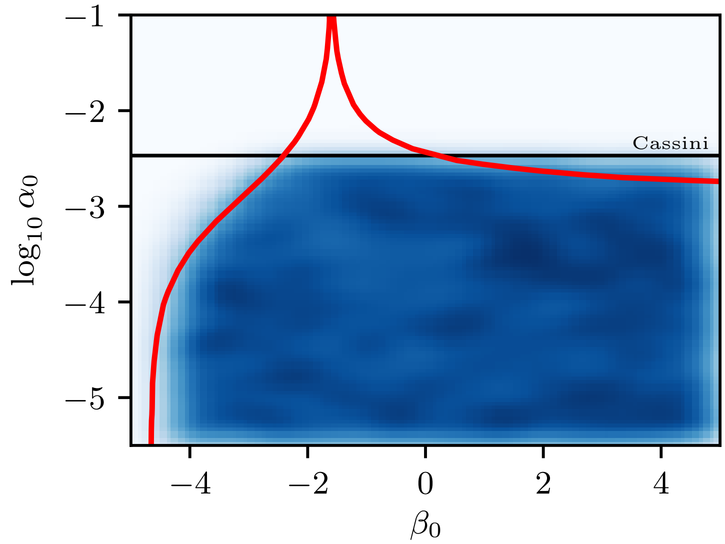

Figure 4.7: Same as Fig. 4.6 but where we have enforced Solar System constraints on α_0 through priors.

other post-Keplerian parameter we demonstrate that for certain systems, like double NS systems, even tighter constraints can be place on the (α_0, β_0) parameter space of STTs. We find consistency with these results when we use Bayesian methods to investigate the posterior distributions of the parameters and find that the dominant effects the dictate the overall constraints is indeed $\dot{P}_b$.

This work has been one of the first attempts to apply an MCMC to explore the constraints on STT parameter space from binary PSRs, and therefore, it should be considered a first step towards a more in depth Bayesian study. For example, we have only used the quoted values of the post-Keplerian parameters, along with the correlations, to construct our likelihood functions and explore the posterior distributions of α_0 and β_0. Such a method introduces systematic errors because we are not able to incorporate covariances between the normal Keplerian parameters, even though these parameters are measured to extremely high precision. Our analysis also potentially suffers from having a limited number of data points, i.e. the post-

Keplerian parameters here.

A more complete study, and one we hope to perform in the future, would involve using more sophisticated MCMC techniques like parallel tempering, to allow us to explore potentially multi-modal posteriors, or like those implemented in the emcee_hammer package available for Python. Moreover, one could argue that the most correct way to analyze the PSR data is to incorporate the TOAs directly into the likelihood and allow an MCMC to perform the fits for the Keplarian and post-Keplerian parameters, essentially performing the computations that timing packages like TEMPO and TEMPO2 handle. This would allow one to easily fit the TOAs given any gravitational theory, like GR and STTs, that have a well developed timing formula. The benefit of handling the TOA directly is that it removes any systematics and inconsistencies that arise in our study, i.e. trying to analyze data that has already been processed. This is quite a large endeavor, however, and would take years of work from multiple groups to accomplish.

4.6 Acknowledgments

We would like to thank Norbert Wex for useful discussions on constraining STTs and Neil Cornish and Travis Robson for useful discussions on Bayesian statistics. DA would like to thank Paulo Freire and the Max-Planck-Institut für Radioastronomie for their hospitality during part of this work. NY and DA acknowledge support from NSF grant PHY-1759615 and NASA grants NNX16AB98G and 80NSSC17M0041.

CONCLUSION

With more detections of gravitational waves becoming a reality and the continued timing of millisecond pulsars in binary systems, more high sensitivity tests of gravity will become available in the near future. Thus it is important to determine the predictions made by theories of gravity other than GR such that one can place constraints on these theories once these observations become available. In this work I have focused my investigation on the study of scalar-tensor theories of gravity and the various predictions they make in both the weak- and strong-field regimes. This work represents the first comprehensive studies of scalar-tensor theories in the regimes of cosmology, Solar System observations, and binary pulsars in which constraints are placed on these theories in a self-consistent manner across these three, very different, physical systems.

In chapters 1 and 2 we study the effects that the cosmological evolution of the scalar field has on current observational constraints that can be placed from Solar System observations. We modified the conformal coupling of these theories to include higher order terms to determine whether or not this change corrected the inconsistencies between the cosmological evolution of the scalar field and the Solar System. We found that one can indeed achieve this by modifying the coupling function, however, these modifications suppress the effects of scalarization that occur in neutron stars. We then studied the cosmological evolution of the scalar field in regions of parameter space that were thought to be consistent with Solar System observations. We found, however, that only a small subset of this parameter space is actually consistent with such observations and that one must carefully select valid initial conditions for the scalar field in order to increase the volume of this parameter space subset. Moreover, the effects of scalarization are suppressed here as well, demonstrating the one can only consistently satisfy Solar System constraints if one only allows for regions of parameter space that do not permit spontaneous scalarization.

In chapters 3 and 4 we address strong field tests of gravity involving binary pulsar systems. In order to place constraints from binary pulsar observations we first needed an accurate description of the motion of the pulsar that is predicted by scalar-tensor theories, which is described by the timing model of Damour and Deruelle. In order to make use of this in the context of scalar-tensor theories we needed high-resolution calculations of the so-called scalar charges that appear directly in the timing model. We perform these exact calculations in chapter 3 over a large region of parameter space that can be explored with binary pulsar observations. Moreover, we find and investigate certain scaling relations that these scalar charges obey in some regions of parameter space that greatly accelerate their calculation. The data generated in this work for these scalar charges is a necessity for future strong-fields test of gravity involving scalar tensor theories.

With these scalar charges in hand we are able to place constraints on scalar-tensor theories using binary pulsar data in chapter 4. We determine constraints that can be placed on two popular scalar tensor theories by saturating 1σ bounds on measured post-Keplerian parameters , using the data above. Moreover, for the first time we investigate the effects of realistic equations of state on these constraints, determining that they do not change any relative features. The results suggest, however, that one should investigate these effects more carefully, and thus we employ Bayesian methods through Markov-Chain-Monte-Carlo simulations to explore the posterior distributions of the scalar-tensor theory parameters. Our results show consistency between these methods and one previously used by radio astronomers but suggests the need for future investigations using our methods in order to reduce potential errors in our calculations.

REFERENCES CITED

[1] B. P. Abbott *et al.*, "Observation of Gravitational Waves from a Binary Black Hole Merger," *Phys. Rev. Lett.*, vol. 116, no. 6, p. 061102, 2016.

[2] B. P. Abbott *et al.*, "GW151226: Observation of Gravitational Waves from a 22-Solar-Mass Binary Black Hole Coalescence," *Phys. Rev. Lett.*, vol. 116, no. 24, p. 241103, 2016.

[3] B. P. Abbott *et al.*, "GW170104: Observation of a 50-Solar-Mass Binary Black Hole Coalescence at Redshift 0.2," *Phys. Rev. Lett.*, vol. 118, no. 22, p. 221101, 2017. [Erratum: Phys. Rev. Lett.121,no.12,129901(2018)].

[4] B. P. Abbott *et al.*, "GW170608: Observation of a 19-solar-mass Binary Black Hole Coalescence," *Astrophys. J.*, vol. 851, no. 2, p. L35, 2017.

[5] B. P. Abbott *et al.*, "GW170814: A Three-Detector Observation of Gravitational Waves from a Binary Black Hole Coalescence," *Phys. Rev. Lett.*, vol. 119, no. 14, p. 141101, 2017.

[6] B. Abbott *et al.*, "GW170817: Observation of Gravitational Waves from a Binary Neutron Star Inspiral," *Phys. Rev. Lett.*, vol. 119, no. 16, p. 161101, 2017.

[7] P. C. C. Freire, N. Wex, G. Esposito-Farese, J. P. W. Verbiest, M. Bailes, B. A. Jacoby, M. Kramer, I. H. Stairs, J. Antoniadis, and G. H. Janssen, "The relativistic pulsar-white dwarf binary PSR J1738+0333 II. The most stringent test of scalar-tensor gravity," *Mon. Not. Roy. Astron. Soc.*, vol. 423, p. 3328, 2012.

[8] M. Kramer, "Pulsars as probes of gravity and fundamental physics," *Int. J. Mod. Phys.*, vol. D25, no. 14, p. 1630029, 2016.

[9] J. M. Weisberg, D. J. Nice, and J. H. Taylor, "Timing Measurements of the Relativistic Binary Pulsar PSR B1913+16," *Astrophys. J.*, vol. 722, pp. 1030–1034, 2010.

[10] N. Wex, "Testing Relativistic Gravity with Radio Pulsars," *ArXiv e-prints*, Feb. 2014.

[11] E. Fonseca, I. H. Stairs, and S. E. Thorsett, "A Comprehensive Study of Relativistic Gravity using PSR B1534+12," *Astrophys. J.*, vol. 787, p. 82, 2014.

[12] E. Berti *et al.*, "Testing General Relativity with Present and Future Astrophysical Observations," *Class. Quant. Grav.*, vol. 32, p. 243001, 2015.

[13] N. Yunes and X. Siemens, "Gravitational-Wave Tests of General Relativity with Ground-Based Detectors and Pulsar Timing-Arrays," *Living Rev. Rel.*, vol. 16, p. 9, 2013.

[14] B. P. Abbott *et al.*, "GW170817: Measurements of neutron star radii and equation of state," 2018.

[15] B. P. Abbott *et al.*, "Properties of the binary neutron star merger GW170817," 2018.

[16] C. M. Will, "The Confrontation between General Relativity and Experiment," *Living Rev. Rel.*, vol. 17, p. 4, 2014.

[17] T. Clifton, P. G. Ferreira, A. Padilla, and C. Skordis, "Modified Gravity and Cosmology," *Phys. Rept.*, vol. 513, pp. 1–189, 2012.

[18] S. Alexander and N. Yunes, "Chern-Simons Modified General Relativity," *Phys. Rept.*, vol. 480, pp. 1–55, 2009.

[19] A. G. Riess *et al.*, "Observational evidence from supernovae for an accelerating universe and a cosmological constant," *Astron. J.*, vol. 116, pp. 1009–1038, 1998.

[20] S. Perlmutter *et al.*, "Measurements of Omega and Lambda from 42 high redshift supernovae," *Astrophys. J.*, vol. 517, pp. 565–586, 1999.

[21] Y. Sofue and V. Rubin, "Rotation curves of spiral galaxies," *Ann. Rev. Astron. Astrophys.*, vol. 39, pp. 137–174, 2001.

[22] G. Bertone and D. Hooper, "History of dark matter," *Rev. Mod. Phys.*, vol. 90, no. 4, p. 045002, 2018.

[23] S. Weinberg, "Effective Field Theory for Inflation," *Phys. Rev.*, vol. D77, p. 123541, 2008.

[24] N. D. Birrell and P. C. W. Davies, *Quantum Fields in Curved Space.* Cambridge Monographs on Mathematical Physics, Cambridge, UK: Cambridge Univ. Press, 1984.

[25] J. Polchinski, *String theory. Vol. 1: An introduction to the bosonic string.* Cambridge Monographs on Mathematical Physics, Cambridge University Press, 2007.

[26] M. J. Duff, "Kaluza-Klein theory in perspective," in *The Oskar Klein centenary. Proceedings, Symposium, Stockholm, Sweden, September 19-21, 1994*, pp. 22–35, 1994.

[27] L. Randall and R. Sundrum, "A Large mass hierarchy from a small extra dimension," *Phys. Rev. Lett.*, vol. 83, pp. 3370–3373, 1999.

[28] L. Randall and R. Sundrum, "An Alternative to compactification," *Phys. Rev. Lett.*, vol. 83, pp. 4690–4693, 1999.

[29] R. V. Wagoner, "Scalar tensor theory and gravitational waves," *Phys. Rev.*, vol. D1, pp. 3209–3216, 1970.

[30] K. Nordtvedt, Jr., "PostNewtonian metric for a general class of scalar tensor gravitational theories and observational consequences," *Astrophys. J.*, vol. 161, pp. 1059–1067, 1970.

[31] P. G. Bergmann, "Comments on the scalar tensor theory," *Int. J. Theor. Phys.*, vol. 1, pp. 25–36, 1968.

[32] M. Salgado, "The Cauchy problem of scalar tensor theories of gravity," *Class. Quant. Grav.*, vol. 23, pp. 4719–4742, 2006.

[33] P. Jordan, *Schwerkraft und Weltall.* Braunschweig, F. Vieweg, 1955.

[34] P. Jordan, "The present state of Dirac's cosmological hypothesis," *Z. Phys.*, vol. 157, pp. 112–121, 1959.

[35] M. Fierz, "On the physical interpretation of P.Jordan's extended theory of gravitation," *Helv. Phys. Acta*, vol. 29, pp. 128–134, 1956.

[36] C. Brans and R. H. Dicke, "Mach's principle and a relativistic theory of gravitation," *Phys. Rev.*, vol. 124, pp. 925–935, 1961. [,142(1961)].

[37] T. Damour and G. Esposito-Farese, "Tensor multiscalar theories of gravitation," *Class. Quant. Grav.*, vol. 9, pp. 2093–2176, 1992.

[38] T. Damour and G. Esposito-Farese, "Nonperturbative strong field effects in tensor - scalar theories of gravitation," *Phys. Rev. Lett.*, vol. 70, pp. 2220–2223, 1993.

[39] T. Damour and J. H. Taylor, "Strong field tests of relativistic gravity and binary pulsars," *Phys. Rev.*, vol. D45, pp. 1840–1868, 1992.

[40] T. Damour and K. Nordtvedt, "General relativity as a cosmological attractor of tensor scalar theories," *Phys. Rev. Lett.*, vol. 70, pp. 2217–2219, 1993.

[41] R. F. P. Mendes and N. Ortiz, "Highly compact neutron stars in scalar-tensor theories of gravity: Spontaneous scalarization versus gravitational collapse," *Phys. Rev.*, vol. D93, no. 12, p. 124035, 2016.

[42] T. Damour and G. Esposito-Farese, “Tensor - scalar gravity and binary pulsar experiments,” *Phys. Rev.*, vol. D54, pp. 1474–1491, 1996.

[43] M. Salgado, D. Sudarsky, and U. Nucamendi, “On spontaneous scalarization,” *Phys. Rev.*, vol. D58, p. 124003, 1998.

[44] W. C. C. Lima, G. E. A. Matsas, and D. A. T. Vanzella, “Awaking the vacuum in relativistic stars,” *Phys. Rev. Lett.*, vol. 105, p. 151102, 2010.

[45] P. Pani, V. Cardoso, E. Berti, J. Read, and M. Salgado, “The vacuum revealed: the final state of vacuum instabilities in compact stars,” *Phys. Rev.*, vol. D83, p. 081501, 2011.

[46] D. D. Doneva, S. S. Yazadjiev, N. Stergioulas, and K. D. Kokkotas, “Rapidly rotating neutron stars in scalar-tensor theories of gravity,” *Phys. Rev.*, vol. D88, no. 8, p. 084060, 2013.

[47] H. Sotani, “Slowly Rotating Relativistic Stars in Scalar-Tensor Gravity,” *Phys. Rev.*, vol. D86, p. 124036, 2012.

[48] H. O. Silva, H. Sotani, E. Berti, and M. Horbatsch, “Torsional oscillations of neutron stars in scalar-tensor theory of gravity,” *Phys. Rev.*, vol. D90, no. 12, p. 124044, 2014.

[49] T. Damour and G. Esposito-Farese, “Gravitational wave versus binary - pulsar tests of strong field gravity,” *Phys. Rev.*, vol. D58, p. 042001, 1998.

[50] G. Esposito-Farese, “Binary pulsar tests of strong field gravity and gravitational radiation damping,” in *On recent developments in theoretical and experimental general relativity, gravitation, and relativistic field theories. Proceedings, 10th Marcel Grossmann Meeting, MG10, Rio de Janeiro, Brazil, July 20-26, 2003. Pt. A-C*, pp. 647–666, 2004.

[51] G. Esposito-Farese, “Motion in alternative theories of gravity,” *Fundam. Theor. Phys.*, vol. 162, pp. 461–489, 2011. [,461(2009)].

[52] C. Palenzuela, E. Barausse, M. Ponce, and L. Lehner, “Dynamical scalarization of neutron stars in scalar-tensor gravity theories,” *Phys. Rev.*, vol. D89, no. 4, p. 044024, 2014.

[53] E. Barausse, C. Palenzuela, M. Ponce, and L. Lehner, “Neutron-star mergers in scalar-tensor theories of gravity,” *Phys. Rev.*, vol. D87, p. 081506, 2013.

[54] L. Sampson, N. Yunes, N. Cornish, M. Ponce, E. Barausse, A. Klein, C. Palenzuela, and L. Lehner, “Projected Constraints on Scalarization with Gravitational Waves from Neutron Star Binaries,” *Phys. Rev.*, vol. D90, no. 12, p. 124091, 2014.

[55] T. Damour and K. Nordtvedt, "Tensor - scalar cosmological models and their relaxation toward general relativity," *Phys. Rev.*, vol. D48, pp. 3436–3450, 1993.

[56] A. Coc, K. A. Olive, J.-P. Uzan, and E. Vangioni, "Big bang nucleosynthesis constraints on scalar-tensor theories of gravity," *Phys. Rev.*, vol. D73, p. 083525, 2006.

[57] A. Coc, K. A. Olive, J.-P. Uzan, and E. Vangioni, "Non-universal scalar-tensor theories and big bang nucleosynthesis," *Phys. Rev.*, vol. D79, p. 103512, 2009.

[58] R. H. Cyburt, B. D. Fields, K. A. Olive, and E. Skillman, "New BBN limits on physics beyond the standard model from ^4He," *Astropart. Phys.*, vol. 23, pp. 313–323, 2005.

[59] J.-P. Uzan, "Varying Constants, Gravitation and Cosmology," *Living Rev. Rel.*, vol. 14, p. 2, 2011.

[60] B. D. Fields, "The primordial lithium problem," *Ann. Rev. Nucl. Part. Sci.*, vol. 61, pp. 47–68, 2011.

[61] B. Bertotti, L. Iess, and P. Tortora, "A test of general relativity using radio links with the Cassini spacecraft," *Nature*, vol. 425, pp. 374–376, 2003.

[62] J. Alsing, E. Berti, C. M. Will, and H. Zaglauer, "Gravitational radiation from compact binary systems in the massive Brans-Dicke theory of gravity," *Phys. Rev.*, vol. D85, p. 064041, 2012.

[63] L. Blanchet, "Gravitational radiation from post-Newtonian sources and inspiralling compact binaries," *Living Rev. Rel.*, vol. 9, p. 4, 2006.

[64] T. Harada, "Neutron stars in scalar tensor theories of gravity and catastrophe theory," *Phys. Rev.*, vol. D57, pp. 4802–4811, 1998.

[65] M. Shibata, K. Taniguchi, H. Okawa, and A. Buonanno, "Coalescence of binary neutron stars in a scalar-tensor theory of gravity," *Phys. Rev.*, vol. D89, no. 8, p. 084005, 2014.

[66] K. Taniguchi, M. Shibata, and A. Buonanno, "Quasiequilibrium sequences of binary neutron stars undergoing dynamical scalarization," *Phys. Rev.*, vol. D91, no. 2, p. 024033, 2015.

[67] M. Ponce, C. Palenzuela, E. Barausse, and L. Lehner, "Electromagnetic outflows in a class of scalar-tensor theories: Binary neutron star coalescence," *Phys. Rev.*, vol. D91, no. 8, p. 084038, 2015.

[68] F. M. Ramazanoğlu and F. Pretorius, "Spontaneous Scalarization with Massive Fields," *Phys. Rev.*, vol. D93, no. 6, p. 064005, 2016.

[69] C. W. Misner, K. S. Thorne, and J. A. Wheeler, *Gravitation.* San Francisco: W. H. Freeman, 1973.

[70] T. Damour, "Binary Systems as Test-beds of Gravity Theories," in *6th SIGRAV Graduate School in Contemporary Relativity and Gravitational Physics: A Century from Einstein Relativity: Probing Gravity Theories in Binary Systems Villa Olmo, Como, Italy, May 17-21, 2005*, 2007.

[71] C. M. Will and K. Nordtvedt, Jr., "Conservation Laws and Preferred Frames in Relativistic Gravity. I. Preferred-Frame Theories and an Extended PPN Formalism," *Astrophys. J.*, vol. 177, p. 757, 1972.

[72] K. J. Nordtvedt and C. M. Will, "Conservation Laws and Preferred Frames in Relativistic Gravity. II. Experimental Evidence to Rule Out Preferred-Frame Theories of Gravity," *Astrophys. J.*, vol. 177, pp. 775–792, 1972.

[73] C. Will and C. M, *Theory and Experiment in Gravitational Physics.* Cambridge University Press, 1993.

[74] http://www.lorene.obspm.fr.

[75] Wolfram Research Inc., *Mathematica 10.4.0*, 2016.

[76] B. P. Abbott *et al.*, "Tests of general relativity with GW150914," *Phys. Rev. Lett.*, vol. 116, no. 22, p. 221101, 2016. [Erratum: Phys. Rev. Lett.121,no.12,129902(2018)].

[77] M. B. Green, J. H. Schwarz, and E. Witten, *SUPERSTRING THEORY. VOL. 1: INTRODUCTION.* Cambridge Monographs on Mathematical Physics, 1988.

[78] V. Faraoni, *Cosmology in scalar tensor gravity*, vol. 139. 2004.

[79] J. Martin, C. Schimd, and J.-P. Uzan, "Testing for w¡ -1 in the solar system," *Phys. Rev. Lett.*, vol. 96, p. 061303, 2006.

[80] R. F. P. Mendes, "Possibility of setting a new constraint to scalar-tensor theories," *Phys. Rev.*, vol. D91, no. 6, p. 064024, 2015.

[81] C. Palenzuela and S. L. Liebling, "Constraining scalar-tensor theories of gravity from the most massive neutron stars," *Phys. Rev.*, vol. D93, no. 4, p. 044009, 2016.

[82] D. Anderson, N. Yunes, and E. Barausse, "Effect of cosmological evolution on Solar System constraints and on the scalarization of neutron stars in massless scalar-tensor theories," *Phys. Rev.*, vol. D94, no. 10, p. 104064, 2016.

[83] J. S. Read, B. D. Lackey, B. J. Owen, and J. L. Friedman, "Constraints on a phenomenologically parameterized neutron-star equation of state," *Phys. Rev.*, vol. D79, p. 124032, 2009.

[84] T. Harada, "Stability analysis of spherically symmetric star in scalar - tensor theories of gravity," *Prog. Theor. Phys.*, vol. 98, pp. 359–379, 1997.

[85] T. A. de Pirey Saint Alby and N. Yunes, "Cosmological Evolution and Solar System Consistency of Massive Scalar-Tensor Gravity," *Phys. Rev.*, vol. D96, no. 6, p. 064040, 2017.

[86] D. Psaltis, F. Ozel, and D. Chakrabarty, "Prospects for Measuring Neutron-Star Masses and Radii with X-Ray Pulse Profile Modeling," *Astrophys. J.*, vol. 787, p. 136, 2014.

[87] Z. Arzoumanian *et al.*, "The neutron star interior composition explorer (NICER): mission definition," in *Proceedings of the SPIE* (T. Takahashi, J.-W. A. den Herder, and M. Bautz, eds.), pp. 914420–914420–9, NASA Goddard Space Flight Ctr. (United States), SPIE, July 2014.

[88] K. Yagi and N. Yunes, "I-Love-Q," *Science*, vol. 341, pp. 365–368, 2013.

[89] K. Yagi and N. Yunes, "I-Love-Q Relations in Neutron Stars and their Applications to Astrophysics, Gravitational Waves and Fundamental Physics," *Phys. Rev.*, vol. D88, no. 2, p. 023009, 2013.

[90] K. Yagi and N. Yunes, "Binary Love Relations," *Class. Quant. Grav.*, vol. 33, no. 13, p. 13LT01, 2016.

[91] K. Yagi and N. Yunes, "Approximate Universal Relations for Neutron Stars and Quark Stars," *Phys. Rept.*, vol. 681, pp. 1–72, 2017.

[92] K. G. Arun and A. Pai, "Tests of General Relativity and Alternative theories of gravity using Gravitational Wave observations," *Int. J. Mod. Phys.*, vol. D22, p. 1341012, 2013.

[93] X. Zhang, J. Yu, T. Liu, W. Zhao, and A. Wang, "Testing Brans-Dicke gravity using the Einstein telescope," *Phys. Rev.*, vol. D95, no. 12, p. 124008, 2017.

[94] L. Shao, N. Sennett, A. Buonanno, M. Kramer, and N. Wex, "Constraining nonperturbative strong-field effects in scalar-tensor gravity by combining pulsar timing and laser-interferometer gravitational-wave detectors," *Phys. Rev.*, vol. X7, no. 4, p. 041025, 2017.

[95] T. Damour and N. Deruelle, "General relativistic celestial mechanics of binary systems. I. The post-Newtonian motion.," *Ann. Inst. Henri Poincaré Phys. Théor., Vol. 43, No. 1, p. 107 - 132*, vol. 43, pp. 107–132, 1985.

[96] T. Damour and N. Deruelle, "General relativistic celestial mechanics of binary systems. II. The post-Newtonian timing formula.," *Ann. Inst. Henri Poincaré Phys. Théor., Vol. 44, No. 3, p. 263 - 292*, vol. 44, pp. 263–292, 1986.

[97] M. W. Horbatsch and C. P. Burgess, "Model-Independent Comparisons of Pulsar Timings to Scalar-Tensor Gravity," *Class. Quant. Grav.*, vol. 29, p. 245004, 2012.

[98] D. Anderson and N. Yunes, "Solar System constraints on massless scalar-tensor gravity with positive coupling constant upon cosmological evolution of the scalar field," *Phys. Rev.*, vol. D96, no. 6, p. 064037, 2017.

[99] J. B. Hartle, "Slowly rotating relativistic stars. 1. Equations of structure," *Astrophys. J.*, vol. 150, pp. 1005–1029, 1967.

[100] M. W. Horbatsch and C. P. Burgess, "The Motion of Mercury According to the theory of Thiry and Lichnerowicz," *Zeitschrift Naturforschung Teil*, vol. 14a, p. 751, 1959.

[101] J. M. Lattimer and M. Prakash, "Neutron star structure and the equation of state," *Astrophys. J.*, vol. 550, p. 426, 2001.

[102] A. Akmal, V. R. Pandharipande, and D. G. Ravenhall, "The Equation of state of nucleon matter and neutron star structure," *Phys. Rev.*, vol. C58, pp. 1804–1828, 1998.

[103] L. Engvik, G. Bao, M. Hjorth-Jensen, E. Osnes, and E. Ostgaard, "Asymmetric nuclear matter and neutron star properties," *Astrophys. J.*, vol. 469, p. 794, 1996.

[104] B. D. Lackey, M. Nayyar, and B. J. Owen, "Observational constraints on hyperons in neutron stars," *Phys. Rev.*, vol. D73, p. 024021, 2006.

[105] H. Muther, M. Prakash, and T. L. Ainsworth, "The nuclear symmetry energy in relativistic Brueckner-Hartree-Fock calculations," *Phys. Lett.*, vol. B199, pp. 469–474, 1987.

[106] H. Mueller and B. D. Serot, "Relativistic mean field theory and the high density nuclear equation of state," *Nucl. Phys.*, vol. A606, pp. 508–537, 1996.

[107] M. Prakash, T. L. Ainsworth, and J. M. Lattimer, "Equation of state and the maximum mass of neutron stars," *Phys. Rev. Lett.*, vol. 61, pp. 2518–2521, 1988.

[108] F. Douchin and P. Haensel, "A unified equation of state of dense matter and neutron star structure," *Astron. Astrophys.*, vol. 380, p. 151, 2001.

[109] R. B. Wiringa, V. Fiks, and A. Fabrocini, "Equation of state for dense nucleon matter," *Phys. Rev.*, vol. C38, pp. 1010–1037, 1988.

[110] N. Yunes, K. Yagi, and F. Pretorius, "Theoretical Physics Implications of the Binary Black-Hole Mergers GW150914 and GW151226," *Phys. Rev.*, vol. D94, no. 8, p. 084002, 2016.

[111] M. Kramer and N. Wex, "The double pulsar system: A unique laboratory for gravity," *Class. Quant. Grav.*, vol. 26, p. 073001, 2009.

[112] D. Anderson, "private communication."

[113] R. Blandford and S. A. Teukolsky, "Arrival-time analysis for a pulsar in a binary system.," *Astrophys. J.*, vol. 205, pp. 580–591, Apr. 1976.

[114] R. A. Hulse and J. H. Taylor, "Discovery of a pulsar in a binary system," *Astrophys. J.*, vol. 195, pp. L51–L53, 1975.

[115] R. T. Edwards, G. B. Hobbs, and R. N. Manchester, "Tempo2, a new pulsar timing package. 2. The timing model and precision estimates," *Mon. Not. Roy. Astron. Soc.*, vol. 372, pp. 1549–1574, 2006.

[116] D. Lorimer and M. Kramer, *Handbook of Pulsar Astronomy.* Cambridge Observing Handbooks for Research Astronomers, Cambridge University Press, 2005.

[117] J. Antoniadis, M. H. van Kerkwijk, D. Koester, P. C. C. Freire, N. Wex, T. M. Tauris, M. Kramer, and C. G. Bassa, "The relativistic pulsar-white dwarf binary PSR J1738+0333 I. Mass determination and evolutionary history," *Mon. Not. Roy. Astron. Soc.*, vol. 423, p. 3316, 2012.

[118] D. L. Kaplan, J. Boyles, B. H. Dunlap, S. P. Tendulkar, A. T. Deller, S. M. Ransom, M. A. McLaughlin, D. R. Lorimer, and A. T. Stairs, "A 1.05 $M_{\odot}$ Companion to PSR J2222-0137: The Coolest Known White Dwarf?," *Astrophys. J.*, vol. 789, p. 119, 2014.

[119] I. Cognard *et al.*, "A Massive-born Neutron Star with a Massive White Dwarf Companion," *Astrophys. J.*, vol. 844, no. 2, p. 128, 2017.

[120] K. Lazaridis *et al.*, "Generic tests of the existence of the gravitational dipole radiation and the variation of the gravitational constant," *Mon. Not. R. Astron. Soc.*, vol. 400, pp. 805–814, 2009.

[121] D. J. Reardon *et al.*, "Timing analysis for 20 millisecond pulsars in the Parkes Pulsar Timing Array," *Mon. Not. Roy. Astron. Soc.*, vol. 455, no. 2, pp. 1751–1769, 2016.

[122] M. Kramer *et al.*, "Tests of general relativity from timing the double pulsar," *Science*, vol. 314, pp. 97–102, 2006.